Micromechanical Analysis of Geosynthetic-Soil Interaction under Cyclic Loading

By

Anil Bhandari

B.E., Tribhuvan University, Nepal, 2003
M.E., Asian Institute of Technology, Thailand, 2006

Submitted to graduate degree program in Civil, Environmental, and Architectural Engineering and the Graduate Faculty of the University of Kansas School of Engineering in partial fulfillment of the degree requirements for the degree of Doctor of Philosophy

Dr. Jie Han, Chairperson

_____

Committee members Dr. Anil Misra

_____

Dr. Robert L. Parsons

_____

Dr. Steven D. Schrock

_____

Dr. W. Lynn Watney

Date defended**:** _____

The Dissertation Committee for Anil Bhandari certifies

that this is the approved version of the following dissertation:

Micromechanical Analysis of Geosynthetic-Soil Interaction

under Cyclic Loading

Dr. Jie Han, Chairperson

_____

Committee members Dr. Anil Misra

_____

Dr. Robert L. Parsons

_____

Dr. Steven D. Schrock

_____

Dr. W. Lynn Watney

Date Approved**:** _____

ABSTRACT

Granular materials are commonly used in the construction of civil engineering infrastructure. Geosynthetics have been used to improve the performance of these structures in many projects. The interaction between geosynthetics and soil is an important factor that governs the performance of the geosynthetic-reinforced structures. Previous studies on geosynthetic-soil interaction using laboratory and continuum based numerical approach were beneficial for studying the overall behavior of the system, however those investigations did not provide insight into microscale response. To improve the understanding of the geosynthetic reinforcement mechanisms, geosynthetic-soil interaction was studied under a monotonic and a cyclic loading using a micromechanical approach.

The micromechanical parameters of the granular materials and reinforcements were calibrated using a biaxial test and a tensile test, respectively. The behavior of granular materials was evaluated under a monotonic and a cyclic loading and analyzed from force and fabric orientation perspectives. Using the calibrated micromechanical parameters, benchmark trapdoor experiments were simulated to establish the simulation techniques for geosynthetic-soil interaction. The micromechanical studies of three practical problems involving geosynthetic-soil interaction were conducted. The practical problems were: geosynthetic-reinforced embankments overlying voids, Geosynthetic-Reinforced Pile-Supported (GRPS) embankments, and geosynthetic-reinforced bases.

In the biaxial test simulation of soil, porosity of the soil showed profound influence on the shear strength of soil. Particle gradation had a limited influence on the shear strength under the monotonic loading; however, the particle gradation had a strong influence on the resilient modulus computed under the cyclic loading. In the trapdoor experiments, soil arching was

observed as an essentially meta-stable condition. The inclusion of reinforcement in the embankments reduced the settlements measured on the top of the embankments. Geosynthetic reinforcement increased the load transfer to the piles and reduced the load on the compressible soils. The anchorage failure of the reinforcement also controlled the load transfer particularly in the low embankments. In the geosynthetic-reinforced base simulation, the density of base course had a profound effect on a rut depth. The tensile stresses developed in the geosynthetic reinforcement helped distribute the contact forces wider. A relatively small tensile stress developed in the reinforcement; therefore, a very stiff reinforcement was not necessary to improve the performance of the base. An optimum ratio between the aperture sizes to the aggregate diameter was identified for the improved performance of the geogrid-reinforced base.

ACKNOWLEDGMENT

The author wishes his profound gratitude to his adviser, Prof. Jie Han, for his continuous and consistent advice, suggestions, encouragements, and criticisms about the work from the very beginning towards its end. I was shown the creative thinking ways to approach the research problems and the need to be persistent to accomplish the goal. Without his sincere help, this work would not have been materialized. Beyond this research scope, his lessons and examples to help/support individuals with his best capacity are highly impressive. Those lessons are and will be influential to my life.

The author expresses his sincere thanks and appreciations towards Prof. Anil Misra, Dr. Robert L. Parsons, Dr. Steven D. Schrock, and Dr. W. Lynn Watney for kindly serving as committee members. Their regular concerns and suggestions gave an impetus on the work, and are highly appreciated. In addition to their mentor in this research work, I benefitted from their excellent courses offered at the CEAE department. Similarly the gratitude is extended to Prof. Karan Surana, Prof. Cristine Jensen Sunderstorm, and Dr. Atanas Stefanov for their wonderful teachings on Mechanical Engineering, Writings Skills, and Mathematics respectively. All the courses significantly sharpened my research skills.

This research was partly supported by the University of Kansas, Transportation Research Institute from Grant # DT0S59-06-G-00047, provided by the US Department of Transportation – Research and Innovative Technology Administration, the University of Kansas, General Research Fund, and the Geosynthetic Institute under its GSI Fellowship Program. Additional support was provided by the CEAE department. These supports are acknowledged.

I would like to thank the fellow members of KUGS (University of Kansas Geotechnical Society) for their companions, advices, and supports. Similarly, I would like to thank WoanJing, Chris, and George. They were always supportive and never left this author to fall down emotionally during the hours of anxiety and frustration. They are always appreciated for their noble company.

The author is heartfelt to his parents and sisters for their support he enjoyed during his stay at the University of Kansas. Their overwhelming love is everything for him that he treasures in this planet. He heartily dedicates this piece of work towards his parents.

TABLE OF CONTENTS

LIST OF TABLES

LIST OF FIGURES

CHAPTER ONE

INTRODUCTION

Granular materials are commonly used in the construction of civil engineering infrastructure ranging from pavements, to foundations, to embankments to dams. In their design life, these structures are subjected to both monotonic and cyclic loads. Geosynthetics have been used to improve the performance of these structures in many projects. The properties of geosynthetics and the interaction between geosynthetics and granular materials often govern the extent of improvement. Laboratory, field, and numerical approaches have been adopted by researchers in the past three decades to understand the mechanisms of improvement in the mechanical properties of granular materials due to the inclusion of geosynthetics. Most numerical studies so far have treated granular materials as continuous media that do not have a particulate nature. The DEM, also a micromechanical approach, has an ability to better simulate the behavior of granular materials under different loading conditions based on the principles of physics (Bardet 1998).

Early research on granular materials can be traced back to Coulomb, who deduced the law of friction for granular materials in 1785. The statics and kinematics of granular materials have been extensively investigated in physics, chemical engineering, and geotechnical engineering. A closed-form stiffness tensor of a random packing was obtained considering a microstructural continuum approach (Chang and Misra 1989; 1990; Misra 1991). Using a similar microstructural continuum approach, Bathurst and Rothenburg (1990) expressed an angle of friction at a macro level in terms of the coefficient of contact orientations under a large strain. On the other hand, significant research has been done to understand

the fundamental properties of granular materials with a particular emphasis on strain localization and shear band formation at the particle level (Gardiner and Tordesillas 2005; Pena *et al.* 2007; Wang *et al.* 2007; Zhang and Thornton 2007). However, very few practical problems have been analyzed using DEM approaches primarily beacause of limitations on the number of particles that can be modeled in a reasonable time with an acceptabale accuracy.

1.1 Statement of Problem

The macromechanical properties (mainly shear strength and stiffness) of granular materials depend on factors, such as packing density, particle shape, size, and gradation, confinement pressure, and stress history. Skermer and Hillis (1970) and Lekarp *et al.* (2000) found through their experimental studies that the particles with an appropriate gradation showed the maximum shear strength and stiffness. However, Selig and Roner (1987) observed a constant shear strength of the coarse-grained soils tested at the same void ratio but with different gradations in the laboratory. These contradictory findings regarding the influence of aggregate gradation on its shear strength and stiffness are evident because of the fact that more than one variable (for example gradation and shape) affect the shear strength of the granular materials and they are difficult to account for seperately in a natural material like soil. A micromechanical study of granular materials may offer explanations to these contradictory findings in an elegant way as evidenced by Rothenburg and Bathurst (1993). Rothenburg and Bathurst (1993) showed that the friction angle of a granular material had strong positive correlation with particle eccentricity.

In numerical studies, the behavior of granular materials is often described by constitutive laws derived from the concepts of continuum mechanics, where variables (displacements

and stresses) are assumed to vary continuously in space. The use of continuum-based finite element software is beneficial for studying the overall behavior of the system; however, this software does not provide insight into microscale response. On the other hand, many parameters are used in constitutive modeling to replicate the response of the system. For example, Saad *et al.* (2006) have used three constitutive models for four materials: namely, the linear elastic model for asphalt concrete and geosynthetic reinforcement, the Drucker Prager model for granular base materials, and the Cam Clay model for subgrade materials to study the effects of geosynthetic reinforcement on fatigue and rutting strain of the pavement. Each of these models involves more than one variable. In addition, many constitutive relationships used in continuum mechanics are obtained from clever curve fitting of experimental data so that the related parameters lack physical meanings (Bardet 1998). Geosynthetic-soil interaction is often modeled using an interface element in the continuum mechanics analysis, which may not accurately simulate the interlocking between geogrid and soil particles. Furthermore, the discrete nature of granular materials challenges the mathematical formualtion based on continuum mechanics. In addition, the continuum approach does not account for the effects of aggregate angularity and sliding on the performance of geosynthetic-reinforced earth structures.

The discontinuum approach addresses major drawbacks of the finite element approach discussed above. In the discontinuum approach, the force displacement law is applied to individual grains and very few parameters are required to replicate the response of the materials under different loading conditions. These parameters have physical meanings. Therefore, a micromechanical study of the interaction between geosynthetics and soil particles is needed to understand the mechanisms and identify key influence factors. This

research proposes the use of the DEM, based on the discontinuum approach to investigate the geosynthetic-soil interaction problems.

In many geotechnical engineering applications, soil arching is an ubiquitous phenomenon and has been studied for the past seven decades since Terzaghi (1943). The details of soil arching and the governing factors can be found in Giroud *et al.* (1990), McKelvey (1994), Han and Gabr (2002), Jenck *et al.* (2007), and Chen *et al.* (2008). Several governing differential equations have been proposed based on experimental observations at a macro level which led to a lack of consensus method for designing a structure that inolves soil arching. Understanding this phenomenon at a microscale can improve the design methods. Soil arching can be studied at microscale using Photoelastic Discrete Simulation (PDS) and or the DEM simulation. To observe the soil arching at a micro level, PDSs were successfully used in a laboratory (Tien 2001). Tien (2001) concluded that soil arching develops at a small movement (2 mm) of the trapdoor and particle translations contribute to the soil arching formation more than particle rotations. However, no similar mechanism studies at a micro level have been conducted for the geosynthetic-reinforced structures where a soil arch develops for example, geosynthetic-reinforced embankments over voids and geosnthetic-reinforced pile-supported embankments. This research proposes the use of the DEM to investigate the mechanisms of soil arching in the geosynthetic-reinforced structures.

1.2 Objectives of the Study

The main objective of this study is to understand the interaction between geosynthetic and soil subjected to monotonic and/or cyclic loading from the micromechanical perspectives.

However, the focus of this study is on the behavior under cyclic loading. The above objective was achieved through the following tasks:

1) Conducting a literature review of previous studies related to the interaction between geosynthetic and soil.
2) Calibrating micromechanical parameters of granular materials and reinforcements for numerical simulation and evaluating the behavior of the granular materials under a monotonic and a cyclic loading. The numerical simulations were conducted using Particle Flow Code (PFC2D) developed by Itasca based on the discrete element model (Cundall and Strack, 1979).
3) Conducting benchmark trapdoor experiments involving granular materials and simulating these experiments using the micromechanical parameters to validate the calibration and simulation techniques. A trapdoor experiment system was designed and fabricated at Department of Civil, Environmental, and Architectural Engineering at the University of Kansas. Trapdoor experiments were conducted with monitoring the displacements in the embankments and strains in the reinforcements. Numerical simulations of those experiments were performed.
4) Performing numerical DEM studies of Geosynthetic-Reinforced Pile-Supported (GRPS) embankments to understand load transfer mechanisms at a micro level using the validated simulation techniques. Stresses and displacements in the embankments were studied that varied as a consequence of the sub-soil settlement. Force-fabric orientations were calculated to understand the soil arching mechanisms at a micro level.
5) Performing numerical DEM studies of geosynthetic-reinforced bases under cyclic loading to understand improvement mechanisms of geosynthetics at a

micro level using the validated simulation techniques. Laboratory tests of geotextile-reinforced bases were simulated. The displacements (translational as well as rotational) and the force chains within the granular media were studied to understand the mechanisms of geosynthetic reinforcement for performance improvement.

1.3 Organization of This Dissertation

This dissertation consists of seven chapters including the introduction chapter.

Chapter Two: This chapter reviews on the literature pertinent to this study. The fundamentals of geosynthetic-soil interactions, GRPS embankments, geosynthetic-reinforced bases, and their DEM simulations were reviewed and summarized.

Chapter Three: This chapter focuses on the calibration and assessment of micromechanical parameters of granular materials and geosynthetic reinforcements. Calibrations of sand, analogical soil (aluminum bars), geosynthetic, and paper (used as a reinforcement in the trapdoor experiment) were conducted. Biaxial simulations of the graded analogical soil were performed. The contributions of small and large particles were analyzed for sharing external loads at different stress conditions from the force-fabric perspectives. The effect of particle gradation on the resilient modulus of the granular medium was also studied.

Chapter Four: This chapter describes on the benchmark trapdoor experiments involving granular media. The experiments included unreinforced and paper-reinforced embankments. Embankments at two heights were tested. Soil arching due to different trapdoor displacements was studied. Numerical simulations of the experiments were

performed using the calibrated micromechanical parameters in Chapter Three. The simulation results were compared with the measured displacements of the embankments and the measured strains in the paper-reinforcement.

Chapter Five: This chapter focuses on the numerical study of GRPS embankments. The stresses and displacements in the embankments were analyzed. Force-fabric orientations were calculated to understand the soil arching mechanisms at a micro level. A cyclic vertical load was applied at the top of the embankments to study the effect of cyclic loading on soil arching.

Chapter Six: This chapter discusses the numerical study of geosynthetic-reinforced bases. A suitable dimension of a geogrid-reinforced base was identified and numerical simulations of the base under a vertical cyclic load were performed. Experimental studies of geotextile-sand interaction tests were simulated for a limited number of cyclic loads. The effect of porosity (packing density) on the performance of the geotextile-reinforced sand was investigated. An optimum ratio between the geogrid aperture size and the particle diameter was identified based on the performance of the geogrid-reinforced base. The geogrid strains and the particle rotations were studied to explain the reinforcement mechanism at a micro level. Comparisons of the numerical simulation results were made with the published research data.

Chapter Seven: This chapter provides the conclusions from this research and recommendations for future study.

CHAPTER TWO

LITERATURE REVIEW

Geosynthetics have been successfully used to improve mechanical properties of granular materials. This chapter reviews the applications and relevant research of geosynthetics in embankments and roadways. The mechanisms of geosynthetic reinforcement and the parameters of geosynthetics which govern the performance of geosynthetic-reinforced earth structures are reviewed and summarized. While experimental research has been valuable in this area, numerical modeling can provide insight views of mechanisms and efficiently supplement experimental research thus is increasingly used. Because of its ability to model particle movement and large deformations anticipated in geosynthetic-soil interaction, the DEM is the research tool chosen in this study. Salient features of the DEM and modeling pertinent to geosynthetic-soil interaction are included.

2.1 Types of Geosynthetics

Geosynthetics are used in civil engineering for five major functions: separation, reinforcement, filtration, drainage, and containment (Koerner 1998). Although geotextiles, geogrids, geocells, geonets, geomembranes, geosynthetic clay liners, geopipes, and geocomposites are all in the family of geosynthetics, geotextiles and geogrids are of interest to this study because of their capacity to improve the performance of embankments and roadways. Geotextiles and geogrids are also used to increase the bearing capacity, and reduce the total and differential settlements of foundations. Nonwoven geotextiles are usually used for separation, filtration, and drainage while woven geotextiles are usually used for reinforcement. Geogrids are typically used for soil reinforcement. Geotextiles

and geogrids are planar structures while geocells are three-dimensional structures. Geocells are also used for reinforcement, but they provide reinforcement by all-around confinement, which is different from geotextiles and geogrids.

2.2 Geosynthetic-Soil Interaction

The interaction of geosynthetic and soil depends upon the size, shape, and gradation of soil particles and the openings of the geosynthetic. There is an optimum ratio of the apparent opening size (AOS) of the geotextile to the mean particle size of sand (D_{50}) for the maximum interface bond resistance in the geotextile-reinforced sand (Athanasopoulos 1993). Raymond (2002) found that geosynthetics had more improvement in the performance of rounded particles than angular particles (Raymond 2002). The self interlocking of angular particles, which would otherwise be improved by geosynthetics, is the reason for the difference in performance improvement. For the same reason, well-graded particles would have less improvement with geosynthetics than poorly-graded particles (Han *et al.* 2008a).

Embedment depth of the geosynthetic also governs the interaction of geosynthetic and soil. Experimental tests and numerical simulations of geosynthetic-reinforced foundations showed that the optimum embedment depth of the geosynthetic layer was governed by the soil friction angle (Hatami and Raymond 2006). Raymond (2002) found that the geosynthetic improved a weak foundation more effectively than an already strong foundation. For a weaker foundation, the optimum embedment depth of the geosynthetic was found closer to the footing.

The interaction behavior of geosynthetic and soil has been investigated under monotonic and cyclic loading conditions (Raju and Fannin 1997; 1998; Ling *et al.* 2008). In geogrid pullout tests, Raju and Fannin (1997) observed that the accumulation of plastic deformation diminished within the first five load cycles so that they recommended the use of ten load cycles to describe the interface behavior of geosynthetic and soil. The results obtained by Ling *et al.* (2008) using direct shear box tests showed that the interface strength between geosynthetic and soil was not affected significantly by cyclic loading. Thus, the interface behavior, evaluated using a monotonic loading test, is equally relevant for the design of geosynthetic-reinforced structures subjected to cyclic loading.

The interaction between geosynthetic and soil is equally important in minimizing grain crushing. Grain crushing is identified as one of the major causes for progressive degradation of aggregates under cyclic loading (Indraratna and Salim 2003). When a large particle is subjected to an excessive load, the particle may break into smaller fragments. Repeated breakage of an angular particle leads to the formation of rounded particle. Using a box test apparatus, Raymond (2002) concluded that rounded aggregates underwent minimum particle breakage while the angular aggregates underwent maximum particle breakage. Raymond (2002) demonstrated the use of geogrid reinforcement to reduce the particle breakage for angular aggregates thereby increasing the aggregate longevity. This phenomenon is particularly significant in roadways construction, as crushed angular particles undergo smaller plastic deformations than rounded particles (Allen 1973; Barksdale and Itani 1989). The interlocking of angular particles is the reason behind this phenomenon. Multiple layers of reinforcement were beneficial for further reduction in the particle breakage. The effectiveness of a geosynthetic in reducing grain crushing depends upon the strength of aggregate (McDowell and Stickley 2006). McDowell and Stickley

(2006) reported that the use of a geosynthetic was more beneficial on reducing the grain crushing for strong ballast as compared with weak ballast. It can be inferred that the use of geogrids in pavement construction provides double benefits: restraining the particle movement, and reducing the particle breakage.

The size, shape, and gradation of soil particles are all important in the geosynthetic-soil interaction; the size and gradation of soil particles are of particular interest to this research. The influence of embedment depth on the geosynthetic-soil interaction is studied under a cyclic loading condition.

2.3 Experimental Study of Geosynthetic-Soil Interaction

Numerous experimental studies have been conducted to evaluate the interface behavior between geosynthetic and soil, bearing capacities of geosynthetic-reinforced foundations, and permanent deformations of geosynthetic-reinforced bases (Fannin and Sigurdsson 1996; Adams and Collin 1997; Chang *et al.* 2000; DeMerchant *et al.* 2002; Nogami and Yong 2003; Raymond and Ismail 2003; Abu-Farsakh *et al.* 2006; Almohd *et al.* 2006; Hufenus *et al.* 2006; Abu-Farsakh *et al.* 2007; Brown *et al.* 2007; Subaida *et al.* 2008; Liu *et al.* 2009). Different test methods for geosynthetic-soil interaction are reviewed below.

2.3.1 Direct shear tests

The interface friction angle between geotextile and soil depends upon the apparent opening size (*AOS*) of geotextile, the average particle size of soil (D_{50}), and the normal stress (σ_n) for a soil at a given relative density as shown in Fig. 2.1 (Athanasopoulos 1993). The direct shear test results of the geotextile vertically embedded in sand showed that a maximum δ_a/ϕ ratio was achieved when a ratio of AOS/D_{50} was 1.6. Here ϕ denotes the

friction angle of soil and δ_a denotes the interface friction angle between geotextile and soil. Athanasopoulos (1993) also found that the δ_a/ϕ ratio consistently decreased with an increase of the normal stress.

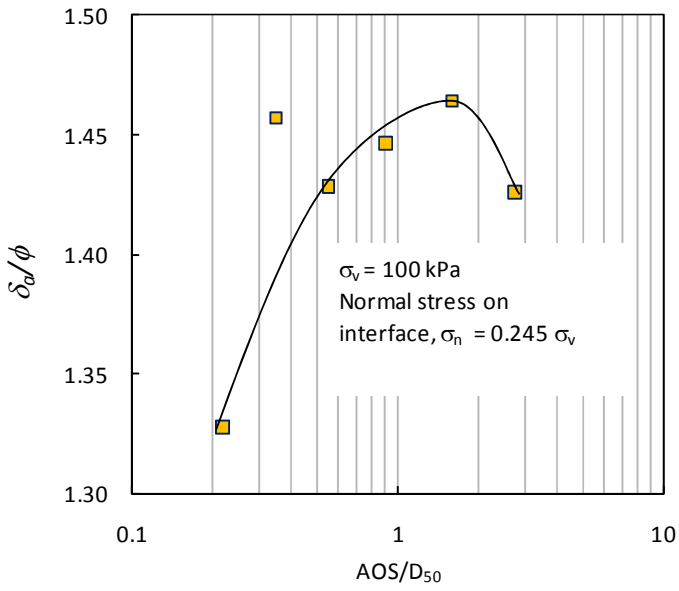

Fig. 2.1 Effect of the AOS to particle diameter ratio on the ratio of δ/ϕ at σ_v= 100 kPa (after Athanasopoulos 1993)

The interface efficiency or interaction coefficient (C_i) is defined as the ratio of the shear strength of the geosynthetic-soil interface to the soil internal shear strength at the same normal stress as follows (Cowell and Sprague 1993):

$$C_i = \frac{C_a + \sigma_n tan\delta_a}{C + \sigma_n tan\phi} \qquad \text{Eq. 2.1}$$

For a coarse-grained soil (cohesionless), Eq. 2.1 reduces to:

$$C_i = \frac{tan\delta_a}{tan\phi} \qquad \text{Eq. 2.2}$$

where, c_a=adhesion between geosynthetic and soil;

c = cohesion of soil;

σ_n =overburden stress;

δ_a = friction angle between the geosynthetic and soil;

ϕ =friction angle of the soil.

Abu-Farsakh *et al.* (2007) found that the interaction coefficient (C_i) from the direct shear tests depended upon soil type, geosynthetic type, and vertical stress. For a coarse-grained soil, they obtained that C_i varied from 0.74 to 0.94; whereas, for a fine grained soil, it varied from 0.64 to 0.89. In their study, C_i increased with an increase of vertical stress. This finding is different from that obtained by Athanasopoulos (1993), in whose tests the geotextiles were vertically placed in the direct shear box. The boundary condition in the Athanasopoulos (1993) study is closer to that in the pullout tests than the direct shear tests. It is well established that C_i decreases with an increase of normal stress in pull-out tests (Mallick *et al.* 1996).

Nakamura *et al.* (2003) investigated the behavior of the geogrid-sand interface in direct shear tests under two loading conditions: nominal constant pressure (NCP) and constant pressure (CP). In the nominal constant pressure test, a constant vertical load was applied to the sample. In the constant pressure test, a varying vertical load was applied to maintain a constant normal pressure at the geogrid-sand interface using a feedback from a load cell installed at the bottom of the lower box. The test results in Fig. 2.2 show that these two test methods resulted the same peak and residual failure envelopes (Nakamura *et al.* 2003). This study indicated that the direct shear test apparatus, which provides a constant pressure

during the entire test, is adequate for evaluating the interface strengths of geosynthetic and soil.

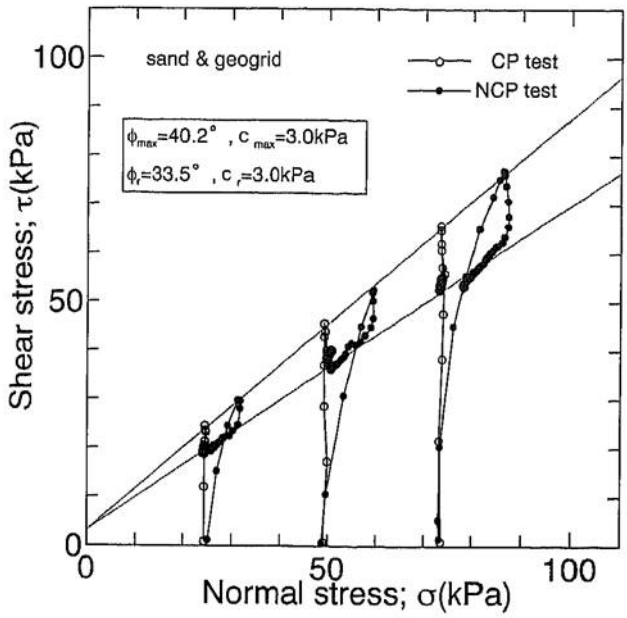

Fig. 2.2 Effect of normal stress loading methods (after Nakamura *et al.* 2003)

2.3.2 Pull-out tests

The interface properties between geosynthetic and soil are best evaluated by pull-out tests for the applications involving shallow rotational failure of a geosynthetic-reinforced slope where the geosynthetics are subjected to pull-out forces (Mallick *et al.* 1996). Synthesizing the previous researchers, Farrag *et al.* (1993) showed that the efficiency factors obtained from pull-out tests are generally larger than those obtained from direct shear tests (Fig. 2.3).

Using a modular pull-out test facility where the dimension of the test box can be changed easily, Farrag *et al.* (1993) studied the influence of the box size, the soil density, the vertical pressure, and the loading rate on the pull-out strength of the geosynthetic-soil interface. The authors recommended a pull-out rate of 6 mm/min. The increased density of the soil facilitated improved interlocking and resulted in higher pull-out strength. The load-deformation curves in the pull-out tests depend upon the strength of the geosynthetics (Almohd *et al.* 2006). Almohd *et al.* (2006) observed bilinear curves for relatively weaker geosynthetics and non-linear curves for stronger geosynthetics.

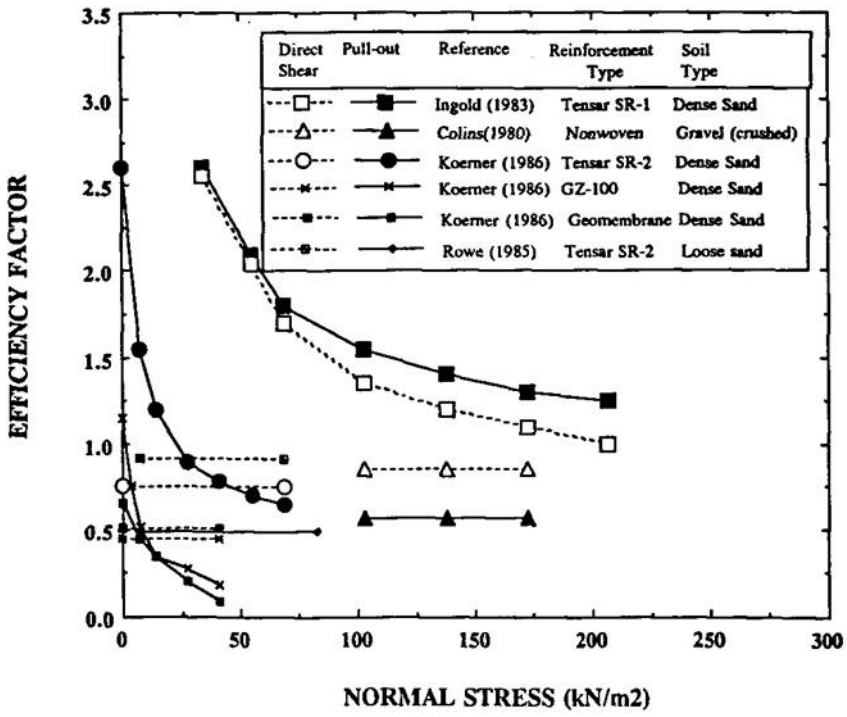

Fig. 2.3 Comparison of efficiency factors obtained from for soil-geosynthetic systems in direct shear and pull-out boxes (after Farrag *et al.* 1993)

2.3.3 Triaxial tests

Triaxial tests are often used to study the geosynthetic-soil reinforcement, probably because the apparatus is commonly available in most research institutes, and these tests allow for the stress controlled conditions. Using two sample sizes: 38-mm and 100-mm in diameter, Haeri *et al.* (2000) studied the benefits of geotextile reinforcement on sand. They considered the four arrangements of geotextiles by altering layer numbers and placement heights. The number of geotextile layers placed inside the sample and their proper locations, which can intercept the failure plane, were crucial for maximizing the benefits. Also, the benefits of geotextiles diminished as the confining pressure increased. This study proves that geotextiles provide lateral confinement to the sample. From their experiments, it was observed that the stiffness of the reinforced samples was correlated to the stiffness of the geotextile and was higher than that of the unreinforced sample.

Equal amounts of geosynthetics, arranged in different shapes, can provide different levels of improvement (Latha and Murthy 2007). When soil was reinforced with discrete fibers, the soil showed marginal benefits. On the other hand, soil reinforced with planar or cellular-type geosynthetics showed 2 times to 5.5 times strength increase depending on the type of geosynthetic and the level of confining pressure. Figure 2.4 shows the typical triaxial test results of the strength ratio (the strength of a reinforced sample divided by that of an unreinforced sample) for the geotextile-reinforced sand using different geosynthetic shapes. The benefit of geotextile reinforcement diminished with an increase of the confining pressure, which is consistent with the findings of Haeri *et al.* (2000). In Latha and Murthy's study, the geotextile cell resulted in a lower strength ratio than the multiple layers of geotextiles. It should be noted that, the geotextile cell was prepared by stitching geotextiles into a cylindrical form which has lower seam strength (approximately 7 % of

the parent geotextile materials) than the commercial geocells. In this author's opinion, if the seam had have the same strength as the geotextile, the geocell would give the maximum strength ratio because of the all-around confinement effects compared to eight layers of planar reinforcement. Further, Latha and Murthy (2007) compared the performance of polyester film to the geotextile. The polyester film performed better than the geotextile as sand particles penetrated into the polyester film which increased surface roughness and resulted in enhanced interlocking effects.

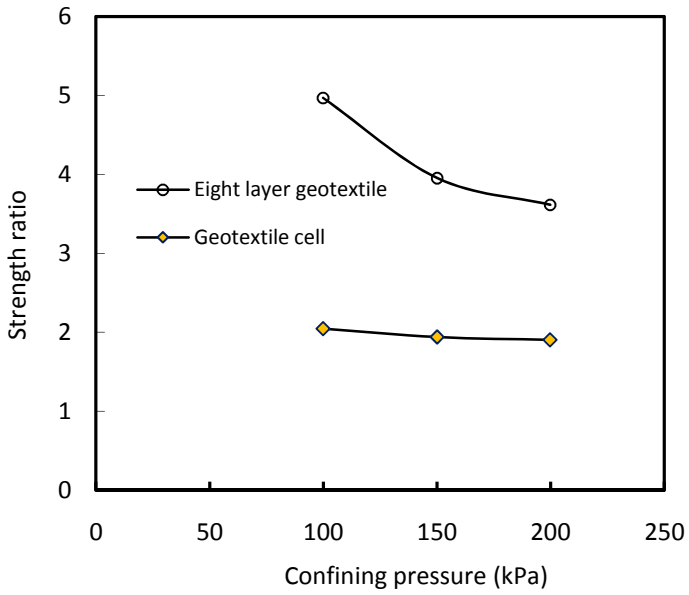

Fig. 2.4 Variation of strength ratio with confining pressure for sand reinforced with different forms of geotextile (after Latha and Murthy 2007)

2.3.4 Anisotropic consolidation tests

The conventional triaxial tests of the geosynthetic-reinforced soil, which is conducted by isotropically consolidating the soil, cannot represent the performance of reinforced soil

(Ling and Tatsuoka 1992). The isotropic consolidation induces compressive strains in geosynthetics that must be overcome by increasing the axial stress for which a significant lateral tensile strain in the soil is required. Similarly, the triaxial tests are not suitable for studying the interaction between bi-directional geogrid and soil because of different alignments between the principal plane and the stronger stiffness direction of the geogrid. Subsequent studies by Ling and Tatsuoka (1994) using anisotropic consolidation demonstrated that the value of *K* (defined as the coefficient of the lateral earth pressure) influenced the interaction between geosynthetics and soil. When *K* equaled to unity, there was no benefit by using geosynthetics since the boundary conditions restricted any interaction between geosynthetic and soil. At a lower *K* value (0.15), the geosynthetic interacted with the soil right from the beginning of the test, and restrained soil movement. Ling and Tatsuoka (1994) also studied the influence of geosynthetic stiffness on the performance of the geosynthetic-reinforced soil. They reported that the effect of the variation in *K* was more prominent than the variation in the geosynthetic stiffness for the performance of the geosynthetic-reinforced soil.

2.4 Geosynthetics in Embankments

Geosynthetics have been successfully used in pile-supported embankments as a basal reinforcement to improve the load transfer mechanism to the piles. This construction technique has been referred as the Geosynthetic-Reinforced Pile-Supported (GRPS) embankments technique (Han and Gabr 2002). GRPS embankments are an economic and effective solution to solve total and differential settlement problems encountered in the construction of earth structures over a compressible soil when limited construction time is available and limited deformation is permissible (Han and Gabr 2002). This construction

technique is equally useful for addressing the challenges posed by an existing large sinkhole under a proposed highway alignment (Wang *et al.* 2009).

Reid and Buchanan (1984) reported the early construction of a GRPS embankment using a single layer of geomembrane for a bridge approach embankment in Scotland in 1983. The geosynthetic reinforcement helped minimize the differential settlement and prevented the formation of a bump between the embankment and the bridge. The success of the earlier projects led to a widespread use of GRPS embankments in Europe, U.S., and Asia (Han and Gabr 2002; Van Eekelen *et al.* 2003; Chen *et al.* 2008). Soil arching caused by the differential movement in soil and the tension in the geosynthetic are the key mechanisms for the load transfer to the piles.

2.4.1 Soil arching

At a macroscopic scale, soil arching is the transfer of stress from a yielding area onto adjoining stationary areas through the development of shear stresses in the soil. This concept was proposed by Terzaghi based on his observation in a trapdoor experiment (1943). In Terzaghi's study, a trapdoor (7.3 cm wide and 46.3 cm long) was mounted on the base of a bin containing a layer of sand approximately 31 cm thick. The test results indicated that the shear stress induced by soil arching increased with an increase in the displacement. When the soil layer was thick enough, a plane of equal settlement developed at the height of 1.5 to 2.5 times the width of the trapdoor. The pressure on the trapdoor became constant when the deflection reached 10% the width of the trapdoor.

McNulty (1965) performed similar trapdoor experiments in an axisymmetric arrangement. In addition to the self weight of sand, air pressure was applied on the surface of the dry

sand over the trapdoor. These results indicated that with an axisymmetric arrangement, a lower height of the plane of equal settlement was required. The height of the plane of equal settlement varied between 1.0 to 1.5 times the diameter of the trapdoor. No soil arching or reduction of vertical stresses above this plane was observed. Also the pressure on the trapdoor became constant at a lower percentage (approximately 3%) of trapdoor deflection. McNulty (1965) defined a soil arching ratio as the ratio of the pressure on the trapdoor to that far away from the trapdoor (equal to an overburden stress), and he found that the soil arching ratio decreased with an increase of the ratio of the fill thickness (H) to the trapdoor diameter (B).

2.4.2 Governing equation for soil arching

Terzaghi (1943) proposed a theoretical solution for calculating the average vertical stress on the yielding part. This solution assumed that vertical slip planes develop in soil and the shear stresses along the planes reduce the average vertical stress applied onto the yielding part (Fig. 2.5). The observation in the trapdoor experiment motivated these assumptions.

Considering the vertical equilibrium of the soil element in Fig. 2.5 and using the appropriate boundary conditions as shown in Fig. 2.5, Terzaghi (1943) derived the following expressions for the vertical stress within the soil arching region and the soil arching ratio.

$$\sigma_v = \frac{B\left(\gamma - \frac{c}{B}\right)}{Ktan\emptyset}\left(1 - e^{-\frac{Kztan\emptyset}{B}}\right) + q\, e^{-\frac{Kztan\emptyset}{B}} \qquad \text{Eq. 2.3}$$

$$\rho = \frac{\sigma_v}{\gamma H + q} = \frac{B\left(\gamma - \frac{c}{B}\right)}{(\gamma H + q)Ktan\emptyset}\left(1 - e^{-\frac{Kztan\emptyset}{B}}\right) + \frac{q\, e^{-\frac{Kztan\emptyset}{B}}}{\gamma H + q} \qquad \text{Eq. 2.4}$$

where, σ_v =vertical stress at depth z;

K =coefficient of lateral earth pressure;

$2B$ =width of the trapdoor;

c =cohesion of soil;

$\emptyset$ =friction angle of soil;

z = depth below the equal settlement plane;

ρ = soil arching ratio.

Terzaghi (1943) suggested that K varied from 1 to 1.5 and the equal settlement plane was located at a height above 2.5 times the width of trapdoor.

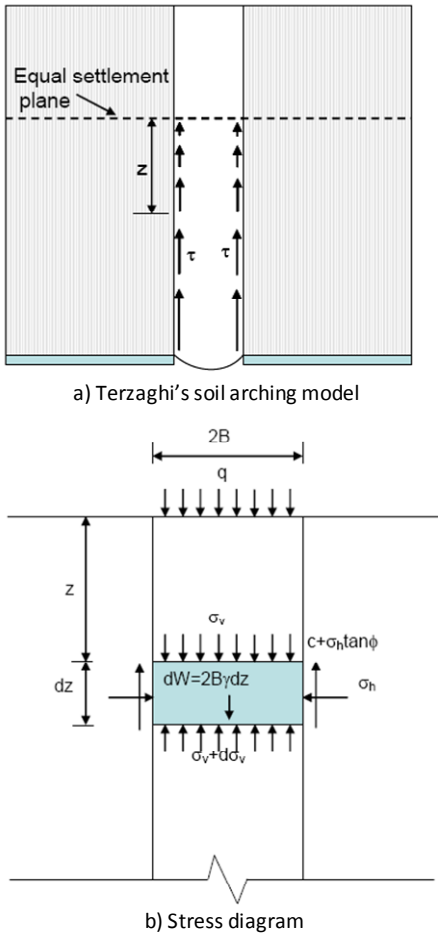

Fig. 2.5 Terzaghi's soil arching model

Hewlett and Randolph (1988) conducted a small-scale test of piled embankments using dry sand as a fill, wooden blocks as piles, and a bed of rubber chips as a compressible subsoil. They noticed soil arching formed in a semi-cylindrical shape as shown in Fig. 2.6 in a plane strain condition. Beneath the arches and in the cusps between the arches, the soil was in an isotropic stress condition without mobilizing any shear strength. Considering the weightless soil within the arch and assuming that the zone located at the crown first reached the limit equilibrium, the following differential equation was proposed for a radial equilibrium:

$$\frac{d\sigma_r}{dr} + \frac{\sigma_r - \sigma_\theta}{r} = 0 \qquad \text{Eq. 2.5}$$

Substituting the boundary conditions, the expressions for the vertical stress in the interior of soil arching (σ_i) and the soil arching ratio (ρ) are:

$$\sigma_i = \gamma \left(H - \frac{s}{2}\right) \left(\frac{s-b}{s}\right)^{(K_p - 1)} \qquad \text{Eq. 2.6}$$

$$\rho = \frac{\sigma_i}{\gamma H} = \frac{1}{H} \left(H - \frac{s}{2}\right) \left(\frac{s-b}{s}\right)^{(K_p - 1)} \qquad \text{Eq. 2.7}$$

where, b = width of the support;

s = center to center spacing between the neighborhood supports;

K_p = coefficient of passive earth pressure;

H = height of the embankment.

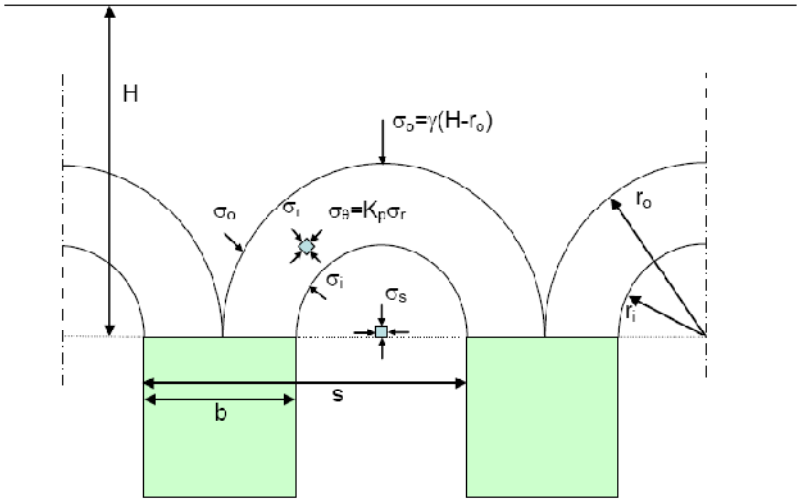

Fig. 2.6 Soil arching in the plane strain condition (after Hewlett and Randolph 1988)

Hewlett and Randolph (1988) also considered the development of soil arching above a grid of piles which is relevant for embankments supported over piles. In the case of soil arching above the grids, a failure at the crown may not necessarily be the design criteria. For a limited area of support at the pile caps, the bearing failure of the embankments at the pile caps may control the design. Hewlett and Randolph (1988) suggested the evaluation of load transfer to the pile caps based on the failure criteria at the crown and the pile caps; the smaller load transfer to the pile caps should be considered for the design.

The German design methodology (Kempfert *et al.*, 2004) for GRPS embankments adopted the radial soil arch proposed by Hewlett and Randolph (1998). The other commonly cited design methods include the BS8006 (BSI 1995) and the Swedish Standard Method (Carlson 1987; Rogbeck *et al.* 1998). All of these methods consider soil arching and tension membrane effect independently. The vertical stress applied on the geosynthetic is calculated based on one of the governing equations (for example, Terzaghi 1943, Hewlett and Randolph 1988) for soil arching. Therefore, different solutions are inevitable

depending on the selection of design methodology. The variations in the design solutions are further compounded since some methods consider the subsoil support (e.g. the German method) while others neglect the subsoil support (e.g. the BS8006 and the Swedish Standard Method).

2.4.3 Tension in geosynthetics

When a geosynthetic is used to bridge the supports over the weaker zone (e.g. voids, compressible soils), the geosynthetic is stretched and mobilizes a portion of its strength. This phenomenon is often called a tensioned membrane effect. Depending upon the size of the weaker zone and the stiffness of the geosynthetic, the geosynthetic may come to the bottom of the weaker zone (in the case of a small weaker zone) and transfer some of the load to the weaker zone or support the load without touching the bottom of the weaker zone (in the case of a large weaker zone and a strong and stiff geosynthetic) (Giroud *et al.* 1990).

Analytical solutions are available to compute the tension in the geosynthetic bridging over the weaker zone (Giroud *et al.* 1990, BS8006). In the Giroud *et al.* (1990) method, the membrane was assumed to deform in a circular shape and the load was applied in the normal direction to the membrane. The geosynthetic spanning outside the weaker zone was assumed not to stretch and a uniform strain developed only in the portion of geosynthetic overlying the weaker zone. In the BS8006 method, the membrane was assumed to deform in a parabolic shape, and the load was distributed horizontally along the bridged span instead of the deformed length.

2.5 Geosynthetics in Roadways

Geosynthetics have been widely used in roadway construction since their introduction in the 1970s. Geosynthetics are used to reduce the permanent surface deformation for a given pavement thickness or to reduce the pavement thickness for a given allowable permanent surface deformation. For a sound design of the roadways, it is imperative to understand the underlying mechanisms of geosynthetic-soil interaction and identify key parameters that govern the mechanisms. The mechanical properties of geosynthetics are crucial to the performance of a geogrid-reinforced base (Webster 1992). Although established methods are available to evaluate these geosynthetic properties significant to the behavior of the reinforced base, the interaction between soil and geosynthetic is more relevant to the performance of the reinforced base (Han *et al.* 2008a). The interaction between geosynthetic and soil depends upon several factors: the tensile strength and stiffness of the geosynthetic and its geometry, and the mechanical properties of soil, and the loading conditions.

2.5.1 Reinforcement mechanisms

Previous studies have identified three key mechanisms for performance improvement when geosynthetics are used for roadway applications. They are separation, lateral confinement, and tensioned membrane effect (Selig 1987; Bourdeau 1989; Miura *et al.* 1990). The geosynthetics, in particular geotextiles, separate the base or sub-base layer from subgrade layer and prevent their intermixing. The lateral confinement developed when an applied vertical load induces lateral forces in the base that have a tendency to cause soil particles move laterally. The frictional interaction between the geosynthetic and the soil through the interlocking of soil particles restrains the particle movement in the

lateral direction. At a large rut depth on a road surface after a sufficient number of repeated loads, the geosynthetic can deform into a curved shape and act as a tensioned membrane. The upward forces exerted by the geosynthetic help support the wheel load and reduce vertical stresses on the subgrade (Perkins and Ismeik 1997). While the lateral confinement mechanism does not require a significant rut depth; to realize the tensioned membrane effect, a significant rut depth is needed. The individual contributions of these mechanisms to the performance improvement of the roadway are difficult to measure from the experiments; therefore, the DEM simulation of the geosynthetic-reinforced bases is essential to understand the individual contributions of these mechanisms.

2.5.2 Plate load tests

A plate load test is commonly used to evaluate the bearing capacity and stiffness of foundation layers. In this test, a steel plate (typically 305 mm in diameter) is placed over the foundation layer and a monotonic or a cyclic load is applied. The resulting settlement due to the applied load is measured, and the bearing capacity and stiffness of the foundation layer are evaluated. This test has also been used to evaluate the benefits of placing a geosynthetic on subgrade or within a base course (Douglas and Valsangkar 1992; Kelly *et al.* 1995; Tingle and Jersey 2005, Han *et al.* 2008b, Pokharel *et al.* 2009, Qian *et al.* 2010). Tingle and Jersey (2005) conducted a series of cyclic plate load tests in a large steel box (1.83 m x 1.83 m x 1.37 m) facility to study the benefits of geosynthetics on the performance of unbound roadways by. They tested four geosynthetic-reinforced sections, one control section with the same thickness as the reinforced sections, and another unreinforced base section with larger thickness. Most plate load tests demonstrated that the use of geosynthetics can improve the performance of roadways. The improvement by geosynthetics depends on the geosynthetic-soil interaction and the stiffness of the

geosynthetic for a given soil. The use of high-stiffness geosynthetics does not necessarily outperform the low-stiffness geosynthetics for all conditions. For example, plate load tests conducted on shale lightweight aggregates by DeMerchant *et al.* (2002) showed that the stiffer geogrids were less beneficial at a small displacement ($\delta < 6.0$ mm) than the flexible geogrids. Clearly more research work is needed to explain these observations, which can be done by a micromechanical analysis

2.5.3 Full scale trafficking tests

Full scale trafficking tests involve the construction of roadways and subsequent traffic loading. In the trafficking tests, the performance of the unreinforced and geosynthetic-reinforced roadways is evaluated. These tests are often used to propose and/or verify the design guidelines for roadways construction. An extensive study was performed by Hufenus *et al.* (2006) to investigate the effects of geosynthetics on compaction, bearing capacity, and rut depth of unbounded roadways over a weak subgrade of CBR from 0.5 to 4 % and strain development in the geosynthetics due to compaction and trafficking using full scale field tests. Recycled rubbles derived from crushing concrete and brickwork were used as a fill material. It was observed that the geosynthetics eased compaction over a weak subgrade (approximately 3% CBR) and reduced the rut depth and the ratio of unloading Young's modulus to loading Young's modulus. A reduction in the ratio of unloading Young's modulus to loading Young's modulus, because of the geosynthetic reinforcement, illustrates the benefits of reinforcing roadways with the geosynthetics. The geosynthetic reinforcement was effective for a base thickness of less than 0.4 m. The test results revealed that in general the use of geosynthetics can reduce the required pavement thickness by 30%. Based on the strain measurements as well as the subgrade profile

records, they found that the geosynthetics underwent low strains in range of 1-3 % and tensile forces of 8 to 15 kN/m. Given the range of tensile forces (8 to 15 kN/m) in the geosynthetics, Hufenus *et al.* (2006) concluded that an extremely stiff reinforcement was unnecessary. Further, it was noticed that placing geogrid and geotextile together formed a weaker interlocking between geogrid and aggregates and created a sliding plane for the geogrid over the geotextile. Hufenus *et al.* (2006) recommended the use of the geotextile for separation and the placement of the geogrid 5 cm above the geotextile within the aggregates to avert this negative effect.

Perkins and Cortez (2005) studied the performance of geosynthetic-reinforced flexible pavements using four full-scale test sections constructed in an indoor facility under a controlled environmental condition. One control section and three geosynthetic-reinforced sections were constructed. The test sections had a subgrade with a target CBR of 1 %, a base course, and an asphalt layer with the asphalt content ranging from 4.8 to 7%. For the asphalt layer, the nominal maximum aggregate sizes were 19.0 mm and 9.5 mm for the top and bottom layers respectively. The test sections were loaded with a standard dual tire truck. The degree of improvement in the performance of pavement sections, evaluated as the Traffic Benefit Ratio (TBR). TBR is defined as the ratio between the numbers of traffic passes between a reinforced and an unreinforced section for a particular rut depth. The TBRs followed the same sequence as that from cyclic plate loading tests conducted previously by Perkins (1999). The test results showed that stiff geosynthetics provided the maximum improvement. However, the stationary plate tests yielded better improvement in the performance compared to the trafficking tests. This difference was attributed to the loading sequence of test sections and the generation of pore water pressure

2.6 Numerical Modeling

Engineering problems are often analyzed using numerical methods, which can be classified into continuum mechanics-based and discrete element approaches. In the continuum approach, material properties are averaged over a finite integral volume and the domain is discretized into finite zones to evaluate nodal strains and stresses (Munjiza 2004). On the other hand, in the discontinuum approach, the individual particles and their interactions are considered explicitly. Though engineering materials are discontinuous in nature, many problems can be easily solved by approximating them as continuum materials when the sizes of individual particles are small compared to the characteristic volume. When the sizes of individual particles continue reduced, the discrete element solution approaches the continuum mechanics solution. Hence, the continuum mechanics-based approach can be considered as a subset of the DEMwhen the sizes of individual particles are negligibly small compared to the characteristic volume (Munjiza 2004). However, the continuum approach cannot be employed when the assumption of continuity of media is violated and/or macroscopic properties are represented by a summation of individual properties rather than the integration of properties over the characteristic volume. Many engineering problems dealing with large deformation and collapse of structures can be better analyzed using the discrete element method.

2.6.1 Discrete Element Method

The DEM, a discontinuum approach, is an increasingly popular tool for studying the behavior of particles by representing them as an assembly of disks and spheres. This method uses an explicit numerical scheme to solve Newton's equation of motion for each particle. The particles are modeled as rigid bodies interacting at soft contacts. The force-

deformation relationship at the contact points is modeled using contact laws. The numerical scheme demands a short time step such that any disturbance during a single time step only affects the immediate neighboring particles. Any perturbations should have enough time to achieve a quasi-static equilibrium in DEM analysis. For example, O'Sullivan *et al.* (2008) and Zhang et al (2008) observed that an axial stress applied on a given material strongly depended upon the loading rate in a biaxial simulation of the granular media. Since a critical time step in DEM simulation depends upon the stiffness and masses of the particles, the loading rate differs considerably and should be investigated on a case-by-case basis. A critical velocity for a strain-controlled test should be small enough that a further reduction on the velocity should not have any effects on the simulation results.

An experimental verification of the DEM could use an optically sensitive material where the contact forces of interacting particles can be determined. Cundall and Strack (1979) performed tests on an assembly of discs reported by Josselin de Jong and Verruijt (1969); the contact forces among the particles and their displacements and rotations were independently verified. A comparison of the results from the DEM and the photo-elastic disc tests indicated that the numerical model may be used to replace tests on photo-elastic discs. The initial comparisons were qualitative and relied on the visual comparison of the contact forces. Nonetheless, the correspondence of the force vectors between the numerical and photo-elastic experiments laid a foundation for the DEM as a potential tool in research.

A software program for DEM should have two attributes: (1) it should be capable of allowing the finite displacements and rotations of discrete bodies including complete detachment and (2) it should be able to update new contacts as calculation progresses. The

following four classes of computer programs meet these requirements for the DEM (Cundall and Hart 1992):

1. Distinct element methods

2. Modal methods

3. Discontinuous deformation analysis methods

4. Momentum-exchange methods.

These methods and the evolution of the DEMis described by Cundall and Hart (1992) as

> *"… the distinct element programs use explicit, time marching to solve the equations of motion directly. Bodies may be rigid or deformable; contacts are deformable. Modal methods are similar to the distinct element method in the case of rigid bodies, but for deformable bodies, modal superposition is used. In discontinuous deformation analysis, contacts are rigid, and bodies may be rigid or deformable. In momentum-exchange methods, both the contacts and bodies are rigid; momentum is exchanged between two contacting bodies during an instantaneous collision".*

2.7 Introduction to PFC2D

PFC^{2D}, a commercial DEM software program developed by *ITASCA*, uses a rigid body and a soft contact approach. The soft contact approach allows the calculation of deformation only at the contacts. The assumption is acceptable since sliding movement along interfaces and rotation of individual particles account for most of the deformation which is significantly higher than the deformation of an individual particle. Therefore, precise modeling of particle deformation is not necessary to obtain a good approximation of the mechanical behavior. In PFC^{2D}, circular particles are used with provisions to use clumps to model the angular shape of the particles. Salient features of the program are discussed in proceeding sections with the aim of outlining the key issues for producing satisfactory numerical results rather than to describe the DEM methodology.

2.7.1 Computational scheme

PFC^{2D} utilizes two successive cycles to compute the forces and displacements of the particles (Fig. 2.7). At each step, the motions of all particles are calculated from the resultant contacts and body forces using a double integration of Newton's 2nd law of motion. The new positions are then used to compute the contacts and body forces on particles and the walls using the force-displacement law (Itasca 2004). The solution scheme is identical to that used by the explicit finite-difference method for a continuum analysis.

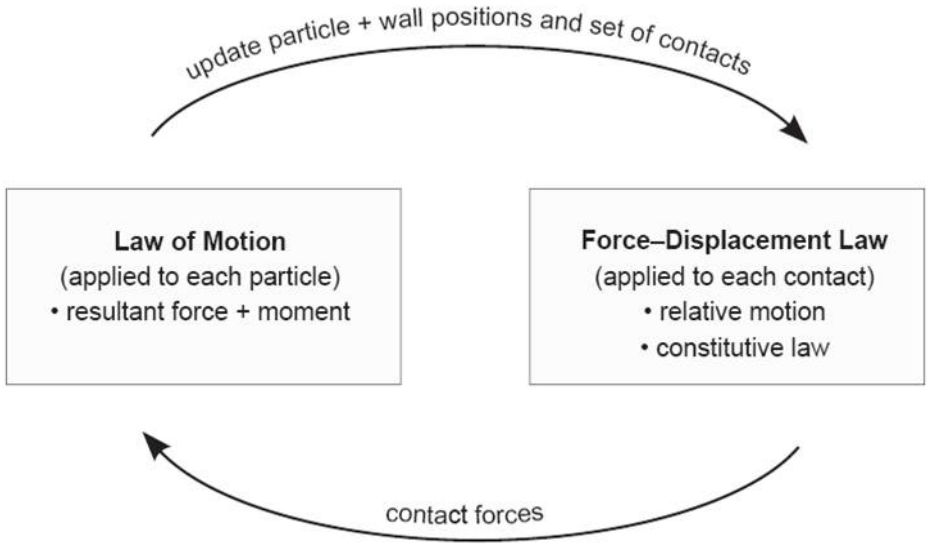

Fig. 2.7 Calculation cycle in PFC^{2D} (after Itasca, 2004)

2.7.2 Contact Models

The contact behavior of particles is described using three constitutive models: the contact stiffness model, the slip and separation model, and the bonding model. These models are

activated when the two interacting particles overlap with each other, but the three models are not necessarily all active at a given contact point.

Stiffness models

The PFC^{2D} has a library for two contact stiffness models: linear and simplified Hertz-Mindlin models. A contact stiffness model can also be written in C++ and linked to the PFC^{2D} as a function that can be executed from the command line. In the linear model, a total normal contact force is based on a normal stiffness via a total normal displacement. Similarly, an incremental shear force is related to a shear tangent stiffness via an incremental shear displacement (Cheng 2004). The normal and shear tangent stiffness are computed from the stiffness of the two contacting particles assuming that they act in series. The calculation of stiffness is further discussed in Chapter 3.

$$K^n = \frac{k_n^{[A]} k_n^{[B]}}{k_n^{[A]} + k_n^{[B]}} \qquad \text{Eq. 2.8}$$

$$K^s = \frac{k_s^{[A]} k_s^{[B]}}{k_s^{[A]} + k_s^{[B]}} \qquad \text{Eq. 2.9}$$

where, K^n = effective normal stiffness;

K^s = effective shear contact stiffness;

$k_n^{[A]}$ and $k_n^{[B]}$ = normal stiffness of particles A and B respectively;

$k_s^{[A]}$ and $k_s^{[B]}$ = shear stiffness of particles A and B respectively.

The forces and displacements are linearly related by the constant stiffness in the linear model (Fig. 2.8). In the Hertz-Mindlin model, the particle shear modulus and Poisson's

ratio are specified and a non-linear force displacement relationship governs the contact behavior. The normal compressive force increases linearly with an overlap, and there is no limit on the force.

Slip and separation model

In the PFC^{2D}, a slip model is mutually exclusive to a contact bond. In absence of the contact bond, the slip model limits the maximum shear force between the two interacting particles using a simple frictional law. In other words, slippage between two particles can occur only when the particles are not bonded or the bond is already broken. Slippage will occur if the shear force exceeds the maximum shear resistance given by Eq. 2.10.

$$F^s_{\max} = \mu \left| F^n \right| \qquad \text{Eq. 2.10}$$

where, $F^s_{\max}$ = the maximum allowable shear resistance;

μ = the minimum coefficient of friction of two interacting particles;

F^n = the normal component of contact forces at the contact points.

When the two interacting particles are separated by a finite distance, the normal force does not exist and this model is not implemented.

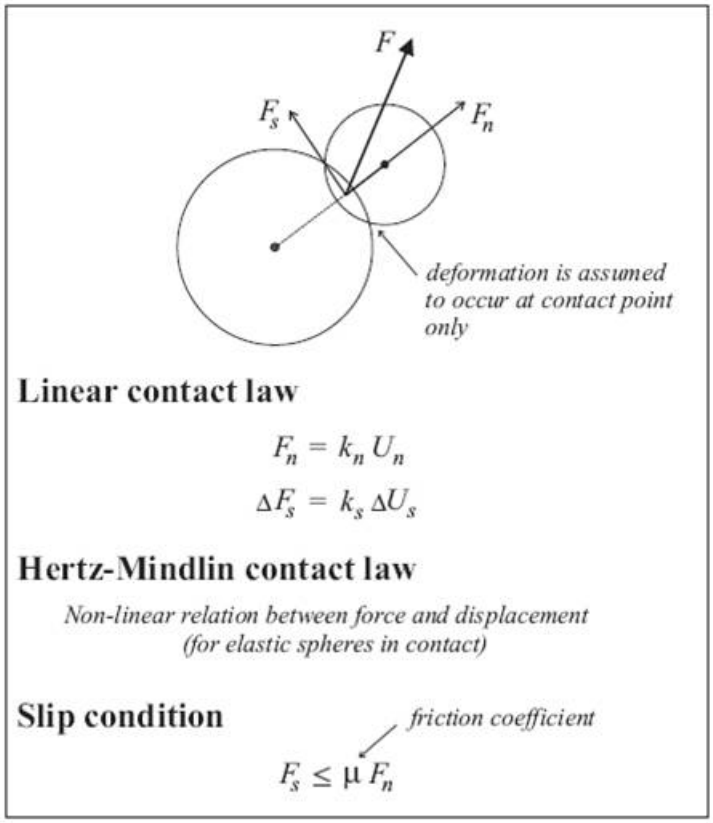

Fig. 2.8 Contact logic (after Itasca 2004)

Bonding models

A contact bond and a parallel bond are available in the PFC^{2D} to model the cohesion and cementation between two particles. The contact bonds act over a vanishingly small area and can be envisioned as a pair of elastic springs at a point of glue. No slippage occurs at the contact bond though the particles can rotate. The parallel bond can resist both the forces and moments (Fig. 2.9). The contact bond serves as a cut-off tool for the tensile normal force and the contact shear force. The contact bond breaks when either of these two forces exceeds the prescribed bond strengths. The normal tensile force is limited to its bond strength.

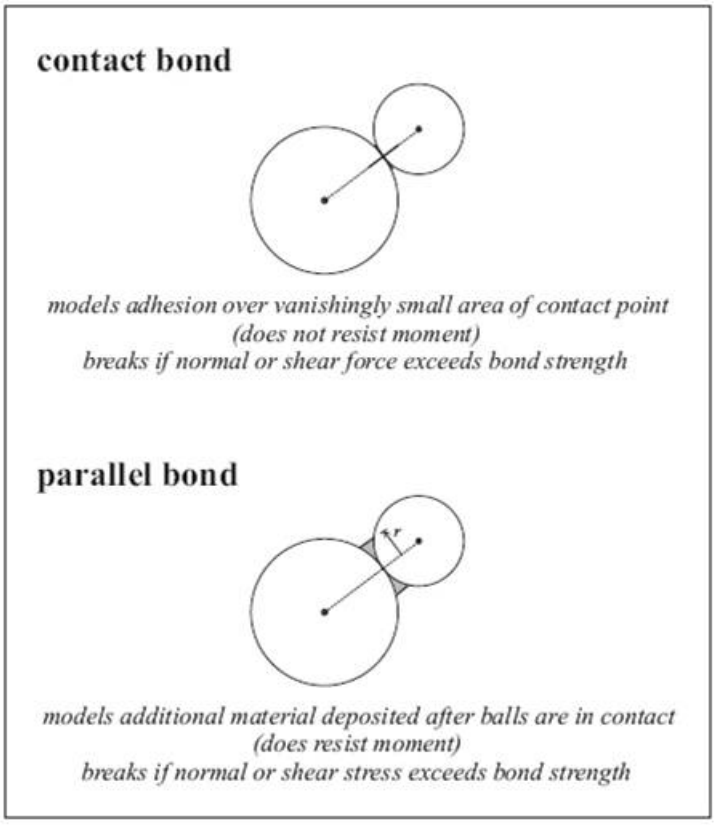

Fig. 2.9 Contact and parallel bonds in PFC^{2D} (after Itasca 2004)

The shear behavior of an interface is governed by the slip model in absence of the contact bond. If a contact bond exists, there should be sufficient tensile or compressive force at a contact to break the bond first. Then, the two spheres rearrange to attain the equilibrium compressive and shear forces. New shear and normal displacements are calculated using the updated forces.

2.7.3 Damping

PFC^{2D} implements two methodologies to dissipate energy; namely frictional sliding and damping. The friction dissipation of the energy is a real phenomenon and occurs during sliding when the absolute value of the shear force at any contact exceeds its limit. For a

given stiffness of the material, frictional dissipation of energy depends on the coefficient of friction between the interacting particles. On the other hand, damping is an artificially introduced phenomenon to dissipate the energy during collision to restore the equilibrium of the system within a reasonable number of iterations. The damping dissipates energy in the whole system following the equation of motion by adding a damping-force term. This form of damping only acts on accelerating motion and no force arises from steady-state motion. The damping constant is non-dimensional and frequency independent, therefore, the regions of different natural periods in an assembly damp equally. The damped equation of motion can be written as:

$$F_i + {F_i}^d = M_i A_i \qquad ; i = 1, 2, 3 \qquad \text{Eq. 2.11}$$

$$M_i A_i = \begin{cases} m\ddot{x}_i & \text{for } i = 1, 2 \\ I\dot{w}_i & \text{for } i = 3 \end{cases} \qquad \text{Eq. 2.12}$$

$${F_i}^d = -\alpha |F_i| \, sign(V_i) \qquad ; i = 1, 2, 3 \qquad \text{Eq. 2.13}$$

where, F_i = components of generalized force;

M_i =generalized mass;

A_i =generalized components of acceleration;

${F_i}^d$= damping force

α =damping constant;

V_i =generalized components of velocity;

$sign(V_i)$ = step function of generalized velocity.

Cundall (1987) observed that the particulate system is always under-damped when using this scheme; that is, decaying oscillations are observed. When optimum damping is used, the numerical solution scheme converges faster. The suggested value of damping constant is 0.7 in PFC^{2D} (Itasca 2004).

2.8 Application of PFC^{2D} in Geosynthetic-Soil Interactions

The reinforcement of soil with geosynthetic enhances its tensile and shear strengths. Researchers have been using laboratory tests (i.e. direct shear tests, triaxial tests, and pullout tests) to study this phenomenon. The DEM can supplement the understanding of the mechanisms and is an ideal tool for studying the interaction between geosynthetic and soil (Konietzky *et al.* 2004). The past studies on the geosynthetic-soil interaction using the DEM are reviewed in the following paragraphs.

2.8.1 Direct shear test

The influence of a microscopic contact friction on the friction angle of sand is well documented by Hainbuchner *et al.* (2003) using DEM simulation (PFC^{2D}) of direct shear tests. The authors concluded that the macroscopic friction angle can be adjusted in a range of 30^{o} to 35^{o} for loose sand and 40^{o} to 45^{o} for dense sand by merely changing the contact friction. However, the simulations of the Jenike shear tests using PFC^{3D}, found different dependence values for the macroscopic friction angles on microscopic contacts (Hartl and Ooi 2008). For a wide microscopic contact friction coefficient ranging from 0.05 to 2.0, the macroscopic friction angle varied between 17^{o} to 38^{o}. The macroscopic friction angle is contributed by inter-particle friction as well as geometrical interaction among particles. A three-dimensional simulation allows the true interaction of particles which lacks in a

two-dimensional simulation. For this reason, the three-dimensional simulation could obtain a reasonable friction angle even for a low microscopic contact.

The ASTM standard (D 3080-04) of the direct shear test recommends the specimen width (L) should be ten times greater than the maximum particle diameter (d). This guideline is based on the fact that a narrow shear band may form during the direct shear test. There must be the particle rearrangement in its neighborhood to form a shear band. Jacobson *et al.* (2007) reported the DEM simulation results of direct shear box tests. Their results showed that a visible shear band formed at a large deformation (x/L = 0.09, x is cumulative horizontal translation of each particles and L is specimen width) when the specimen width to the particle diameter ratio (L/d) equals to 19 (Fig. 2.10). In Fig. 2.10, y is initial vertical position of the particles and h is the specimen height. If the shear band formation is expected during the test, the ASTM recommendation of L/d equals to 10 should be increased. However, it should be noted that the DEM simulation by Jacobson *et al.* (2007) was based on the uniform distribution of particles in a narrow range of diameters between 0.6 mm and 0.8 mm, and the conclusion should be used cautiously. A summary of the direct shear tests conducted by various researchers is given in Table 2.1.

The DEM model of a direct shear test can also be used to study the grain crushing of granular materials. Though PFC^{2D} does not allow grain crushing, it can be implemented by replacing the particles subjected to a higher tensile contact stress than their tensile strength with fragmented smaller particles. A failure criterion based on coordination numbers can be used to scan the particles that are vulnerable to the crushing (Guerrero and Vallejo 2005; Hossain *et al.* 2007). The DEM model of a direct shear test can also be used to study the interface behavior of geosynthetic and soil, although no research has been conducted so far.

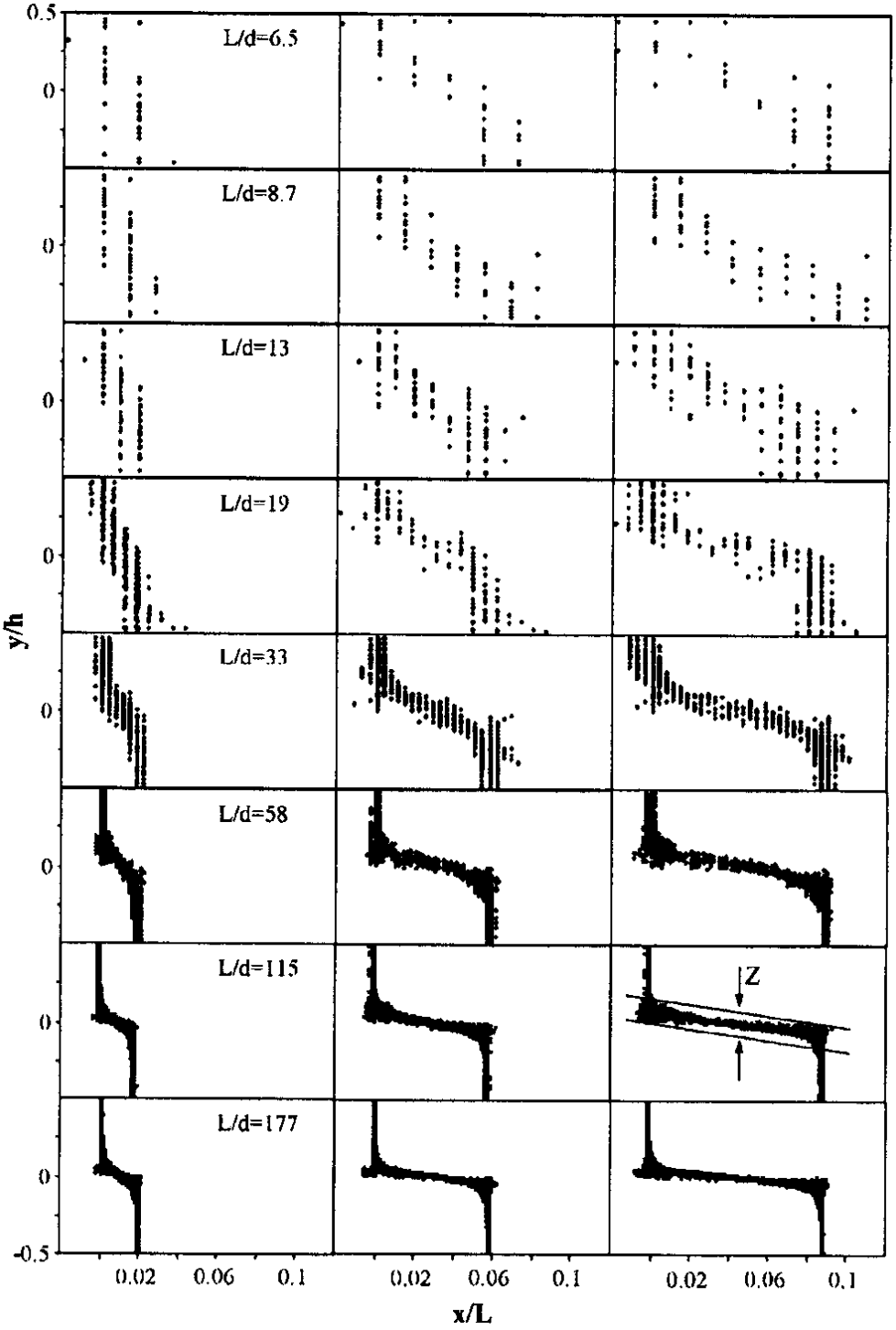

Fig. 2.10 Particle translation data for direct shear tests with $6.5 \leq L/d \leq 177$ sheared to X/L = 0.02 (left), 0.06 (center), and 0.09 (right) (after Jacobson *et al.* 2007)

Table 2.1 Summary of direct shear test modeling using DEM

Investigator	Year	Particles size	k_n (N/m)	k_s (N/m)	μ	Porosity	Summary
Jacobson *et al.*	2007	0.6 - 0.8 mm	1E8	7E7	0.3	0.150	2D study at150 kPa normal stress. Circular assembly, ratio of specimen width to particle diameter studied.
Zhang and Thornton	2007	30, 40, 50, 60, 70, 80, 90 μm	-	-	0.5	-	2D study focused on shear zone and comparison between strength evolution using boundary and particles.
Guerrero and Vallejo	2005	3 mm	1E8	1E8	0.7	0.170	2D study on particle breakage using coordination number.
Thornton and Zhang	2003	30, 40, 50, 60, 70, 80, 90 μm	-	-	0.5	-	2D study focused on shear strength development using particle contact forces in shear zone.
Hainbuchner *et al.*	2003	5 mm to 70 mm	-	-	-	0.150, 0.190	2D DEM study compared well with lab results. Exhibiting peak, residual strengths and dilatancy of sand. Upscaling of particle sizes used to model shallow foundations.
Liu	2006	5 and 9 mm	5E9	1.5E8	0.27	0.163, 0.189	2D study to establish the relationship of internal friction and stress-dilatancy relationships.
Hartl *et al.*	2008	6 mm	-	-	0.2-2.0	0.38-0.45	3D study using rainfall filling method to study the effect of interparticle friction on bulk friction and porosity.

Note: k_n is normal stiffness; k_s is shear stiffness, and μ is coefficient of friction for particles

2.8.2 Pull-out test

The microscopic parameters of geosynthetic and soil can be calibrated using pull-out and other simple test data. A biaxial compression test and a geogrid pull-out test in a horizontal plane were used to derive the microscopic properties of soils and the geogrid-soil interface in PFC^{3D} to study the geogrid-anchorage mechanisms (Chareyre and Villard 2002). Using the calibrated parameters, Chareyre and Villard (2002) simulated the force-displacement curves for the geogrid anchorage in sand and silt using PFC^{3D}. Large fluctuations in the force were observed from the numerical results when the geogrid was anchored in sand, but the force-displacement curve was smooth with constant periodicity in force fluctuations when the geogrid was anchored in silty sand. The anchorage failure mechanism was qualitatively captured by the PFC^{3D} in both cases. Similar pull-out tests with different anchorage shapes of geotextiles were simulated numerically by Villard and Chareyre (2004). They considered an L- and a V-shaped anchorage in their laboratory models. The analytical, laboratory, and numerical models derived consistent anchorage failure mechanisms of the geotextile-reinforced slopes. Villard and Chareyre (2004) concluded that the failure of the geotextile-soil interface was dominant for cohesive soil while the instability of anchoring soil mass as well as the interface failure were dominant for cohesionless soil.

The interface strength between geosynthetic and soil is a key factor controlling the behavior of geosynthetic-reinforced soil. In DEM, the interface friction is conveniently adjusted by selecting the appropriate coefficients of friction (μ) for geosynthetic and soil. Since geosynthetic and soil have different sizes, their interface roughness and strength are dependent on their sizes (Chareyre and Villard 2005). Geosynthetics have been commonly

used using bonded particles, which pose difficulties in modeling large strain behavior of the geosynthetic because significant voids would be created at each contact between particles. To address this limitation, Chareyre and Villard (2005) introduced a new method called the Dynamic Spar Element Method (DSEM) to model the geosynthetic within the framework of the DEM. In this method, the geosynthetic is modeled as a set of spar elements connected at the nodes. The spar elements have finite thickness, and their interaction with other particles uses the same soft contact approach as in DEM. The flexibility of the spar element is ensured by allowing rotations at nodes. Chareyre and Villard (2005) indicated that the implementation of DSEM resulted in equivalence between the microscopic and macroscopic friction.

The interlocking effect of geogrid helps mobilize the intrinsic capacity of aggregates which depends upon the aperture size of geogrid and the diameter of aggregates. Using the PFC^{3D} model of laboratory pull-out tests, McDowell *et al.* (2006) demonstrated that the ratio of aperture size to aggregate diameter played an important role in the peak strength of the geogrid-reinforced aggregate and its corresponding displacement as shown in Fig. 2.11. For a tested sample with 40-mm diameter aggregates, the optimum interlock was observed at a ratio of 1.4. The distribution of the average shear force in the model showed that the interlocking effect of the geogrid was confined to a relatively narrow thickness of 10 cm below and above the geogrid. The ratio of the peak shear and normal forces at the end of the test to its initial values reached 10. This study clearly demonstrated the confinement effect of geogrids on aggregates (Fig. 2.11). A similar conclusion was drawn by Konietzky *et al.* (2004). For aggregates with a particle size distribution between 0.6 mm to 20 mm, a punched-drawn geogrid had a confinement influence zone of 10 cm on either side of the geogrid. Beyond this influence zone, the contact forces in aggregates did not

change significantly. Though this study was able to capture the force-displacement behavior and demonstrate the interlocking effects of geogrids in pull-out tests, this study did not investigate the effect of aggregate shape on the performance of the reinforced section.

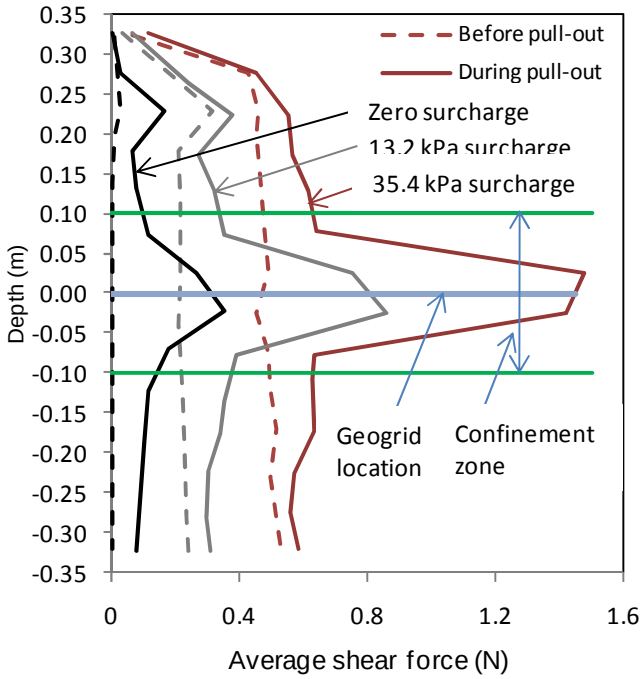

Fig. 2.11 Average shear force before and at end of the pull-out test (modified from McDowell *et al.* 2006)

2.8.3 Triaxial test

Konietzky *et al.* (2004) modeled triaxial tests using PFC^{3D} to study the confinement zone of a geogrid. The back analysis of triaxial tests conducted for the geogrid-reinforced aggregates showed that the resulted strength increase cannot be attributed solely to the tensile stress of the geogrid. The difference on the deviatoric stress between the reinforced

and unreinforced samples to produce same deviatoric strain was larger than the mobilized tensile stress of the geogrid. The additional strength of the reinforced sample must have been derived from the confinement effect of the geogrid.

Subsequent studies by McDowell *et al.* (2006) showed the importance of aggregate shape on the peak strength and dilatancy behavior of railway ballasts. They analyzed a 300 mm (diameter) x 600 mm (height) triaxial model in PFC^{3D}, which had the same dimensions as used in the lab. Clumps of overlapping spheres were used to represent the actual shape of aggregates (Fig. 2.12). The ability of the clumps to capture the peak strength and dilatancy behavior of the ballast demonstrated that the clumps are superior to the spheres for modeling ballast. The triaxial test simulation of aggregates was extended to study the geogrid confinement effect on aggregates by placing the geogrids at different heights in the model. In the model, three layers of geogrids at quarter, half, and three quarter height of the sample were considered, and the force distribution along the model height was used to quantify the improvement.

Figure 2.13 shows that the force ratio (β) is maximum at all geogrid locations. Force ratio (β) was defined as the ratio of the average contact force inside a cuboid enclosed by the four intact closed apertures at mid-depth and 1 cm above and below mid-depth to the average force in the same 2 cm height interval but across the entire cross-section enclosing the entire layer of geogrid. The effect was much more pronounced during an unloading process, and the finding is consistent with Konietzky *et al.* (2004).

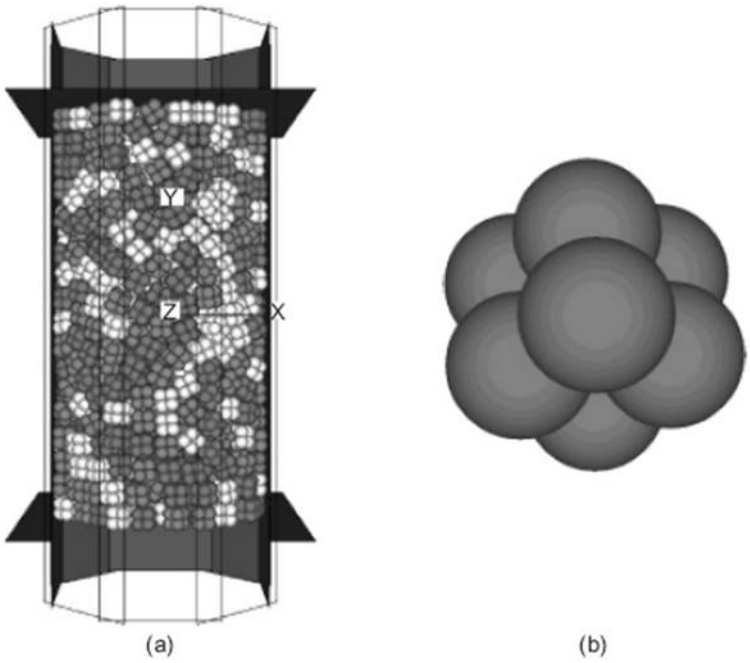

Fig. 2.12 PFC^{3D} model for triaxial test: (a) assembly of cubic clumps in the triaxial cell and (b) a cubic clump to model blast (after McDowell *et al.* 2006)

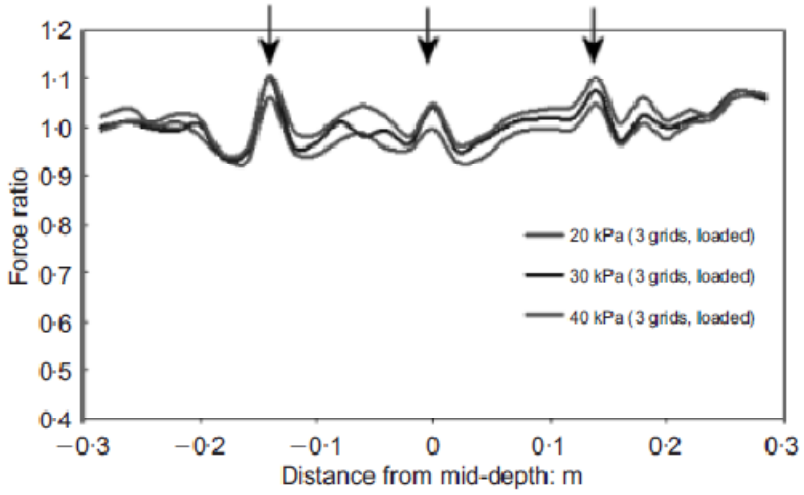

Fig. 2.13 Force ratio β during loading along the model height with the arrows indicating the geogrid locations (after McDowell *et al.* 2006)

McDowell *et al.* (2006) also investigated the effect of three layers of geogrids on the displacement of the model as compared with one layer of geogrid reinforcement. The numerical results showed that the single-layer geogrid-reinforced aggregate had 50% more axial and radial displacements compared to the three-layer geogrid-reinforced aggregate. This comparison indicated the benefit of multiple layers of geogrids on reinforcing the aggregates.

2.8.4 Plate loading test

DEM analyses were conducted to simulate plate loading tests, in which particle movement and contact forces between the interacting particles were investigated (Lim and McDowell 2005; Lu and McDowell 2007, Bhandari and Han 2009).

Lu and McDowell (2007) compared contact forces and particle movement using two shapes of particles: spheres and angular clumps of spheres. It was shown that the use of angular clumps increased the contact forces between particles and improved the rolling resistance that provided more interlocking among particles. Further, the use of properly shaped aggregates obtained a more realistic force-deformation response of ballast particles in the plate loading test. When the aggregates were simulated with smooth surfaces using spheres, the particles continued rolling even during an unloading step. On the other hand, when the aggregates were simulated with angular clumps, the particles rolled in the opposite direction during an unloading step compared to a loading step. The DEM model of a plate load test can also be used to study the interface behavior of geosynthetic and soil, although no research has been conducted so far.

2.8.5 Grain crushing

A large particle breaks into smaller fragments when it is subjected to unbalanced forces. The use of DEM has enriched our understanding of particle breakage. For instance, under a moving wheel load, Vallejo *et al.* (2006) found that particle crushing started at the interface between an asphalt layer and a granular base, and continued downward towards the bottom of the base layer. The DEM simulation of pile driving in a granular medium illustrated the significance of pile shapes on penetration resistance and grain crushing (Lobo-Guerrero and Vallejo 2007). A flat-ended pile induced the maximum grain crushing followed by an open-ended (hollow) pile and a triangular tip pile. The importance of grain crushing on the vertical deformation of a railway ballast subjected to cyclic loading was investigated by Lobo-Guerrero and Vallejo (2006). They found that the vertical deformation of the railway ballast increased substantially when grain crushing was allowed in the simulation. Similarly, Hossain *et al.* (2007) noticed two processes in their DEM analysis namely, a corner breakage and the splitting of an aggregate, under dilating and contracting conditions, respectively. The particle breakage occurs at a microscopic level and is manifested in the change in void ratio (the volume of voids to that of solids) (Cheng *et al.* 2004). They found the soil behavior was consistent with critical-state soil mechanics, only when the particle breakage was allowed. Without allowing the particle breakage, the soil appeared stronger and sustained a higher deviatoric stress before it yielded. Because particle breakage can occur only at higher stress levels, grain crushing is not an issue at low stress levels. Despite these findings, there is a lack of numerical studies on the particle breakage phenomenon when the aggregates are reinforced with geosynthetics.

2.9 Application of PFC^{2D} in Geosynthetic-Reinforced Pile-Supported Embankments

Soil arching is a key mechanism to transfer the load from the embankment weight and surface loading to the piles that would otherwise rely on the support from the soft soil or a void area. Different design methods for the load transfer platform above the piles have been proposed based on different assumptions of load transfer mechanisms of the embankment fill to the piles and the compressible soil. For example, Chen *et al.* (2008) compared three design methods based on Terzaghi (1943), Low *et al.* (1994), and BS8006 (1995) with the experimental results and found significant deviations in the calculated stress concentration ratios from the measured ones. Understanding the load transfer mechanisms of the pile-supported embankment is one of the keys to improve these design methods.

Recently, research has focused on a coupled finite-discrete model of the geosynthetic-reinforced embankment over piles. The coupled finite-discrete model accommodates the fibrous structure of geosynthetics including the tensioned membrane effect. Meanwhile, the discrete model of the embankment fill evaluates the force transfer between the particles at the particle contact levels which is the key mechanism of soil arching (Le Hello and Villard 2009; Villard *et al.* 2009). Le Hello and Villard (2009) observed that the stiffness of the geosynthetic had a minimum influence on the load transfer mechanism but governed the maximum geosynthetic deformation. This finding signifies that the load transfer to the pile caps due to soil arching develops at small particle movement in the embankments. The displacement vector of the particles in the embankments indicated a triangular shape of soil arching. Bhandari *et al.* (2009) also reported the triangular shape of soil arching.

Jenck *et al.* (2009) presented a two-dimensional small-scale model study as well as discrete and continuum-based numerical modeling of the pile-supported granular platform. Their study showed that the DEM model closely predicted the behavior of the platform, for example, the efficiency/efficacy (ratio of the load shared by piles to the total load of the platform), as compared with the continuum model even though both approaches over-predicted the experimental value. Note that "efficiency" and "efficacy" are used interchangeably in the literature. Furthermore, they pointed out that the stress and strain in the continuum model are coupled while the discrete model has less restriction on the stress and strain relationship. As a consequence, the increased friction angle of the platform material increased the efficiency and reduced the settlement in the continuum model. However, the reduction in the settlement in the discrete model was insignificant.

CHAPTER THREE

MICROMECHANICAL PARAMETER CALIBRATION AND ASSESSMENT

This chapter discusses some fundamental relationships involved and the background theory essential to this micromechanical study. The micromechanical parameters involved in modeling different geotechnical problems were calibrated against the experimental data. With the established parameters, numerical simulations were performed to study the effects of particle gradation on the shear strength of granular media under monotonic and cyclic loading. The behavior of granular media under these loading conditions was explained on the basis of fabric-force analysis. A micromechanical parameter calibration of planar reinforcements (paper, geotextile, and geogrid) was conducted to simulate the tensile load tests of these materials.

3.1 Relationship Between Modulus and Contact Stiffness

The relationship between a contact force and an inter-particle displacement is generally non-linear due to the variation in the contact area with the level of contact force. The contact normal secant stiffness (K_n) for a purely granular material can be expressed by the following Hertz-Mindlin model (Itasca 2004):

$$K_n = \left(\frac{2\prec G\succ\sqrt{2\check{R}}}{3(1-\prec\nu\succ)}\right)\sqrt{U_n} \qquad \text{Eq. 3.1}$$

where $\prec G \succ$ = the shear modulus of the particles;

$\check{R}$ = the radius of the particles;

$\prec \nu \succ$ = Poisson's ratio of the particles;

U_n = the overlap between the particles.

If particles of different sizes and materials are used, the material properties are appropriately weighted. When the contact force is large enough to cause a local yield at the contact, an elasto-plastic local constitutive model is needed to describe the contact force and inter-particle displacement. However, uncertainties arise when determining the contact area and the redistribution of pressure. Therefore, an equivalent shear modulus of the particle smaller than the elastic shear modulus can be assigned to account for the effect of local yielding (Chang and Misra 1989).

The mechanism of force transfer in the granular material can be approximated by a linear relationship between the contact force and the inter-particle displacement. Along the line of linear relationship, Bathurst and Rothenburg (1988) proposed the following equation to calculate the contact normal stiffness for a two-dimensional isotropic material:

$$K_n = \left(\frac{8\prec G\succ}{m_v \bar{l}_o \zeta(1+\lambda)}\right) \qquad \text{Eq. 3.2}$$

where $\prec G \succ$ = the shear modulus;

m_v = the contact density (the number of contacts per unit area);

λ = the ratio of tangential to normal contact stiffness ($i.e.,\ \lambda = K_s/K_n$).

$\boldsymbol{\zeta}$ = a constant which was not specified;

$\boldsymbol{\bar{l}_o}$ = the average contact length taken from all assembly contacts.

In this study, a linear contact model was used for the simulation of granular materials (sand, aggregate, and analogical soil at a dry condition). The linear contact model greatly economizes the computation effort in comparison to the non-linear Hertz-Mindlin model. Different from the Hertz-Mindlin model in which a constant shear modulus and Poisson's ratio can be used over a wide range of contact forces, the linear contact model should be calibrated for the level of the expected contact forces. A biaxial test of the particle assembly is useful when a routine calibration is performed. Utilizing the Hertzian contact law at a contact strain of 0.5% (i.e. $U_n/2R$ = 0.5%), Misra and Cheung (1999) proposed the following relationship between the contact normal stiffness and Young's modulus of the particle.

$$K_n = 0.094ER \qquad \text{Eq. 3.3}$$

where E = Young's modulus of the particle.

In the linear contact model, the normal contact stiffness of a particle can be related to Young's modulus at each particle-particle contact. The two interacting particles A and B acts in series and their deformability behavior can be envisioned as an elastic beam with its ends at the particle center (Fig. 3.1). Therefore, for identical particles, the axial stiffness of the beam ($K = Area*E_c/L$) is one half of the normal stiffness (k_n) of the interacting particles (Potyondy and Cundall 2004) as shown below:

$$\frac{k_n}{2} = \left(\frac{Area*E_c}{L}\right) = \left(\frac{LtE_c}{L}\right) = tE_c \qquad \text{Eq. 3.4}$$

where t = the thickness of the particle towards the plane of paper.

Equation 3.4 relates the normal stiffness of the particle to Young's modulus at contact (E_c). However, there is no direct link between Young's modulus at contact and the ensemble Young's modulus except that Young's modulus at contact is usually higher than the ensembled Young's modulus.

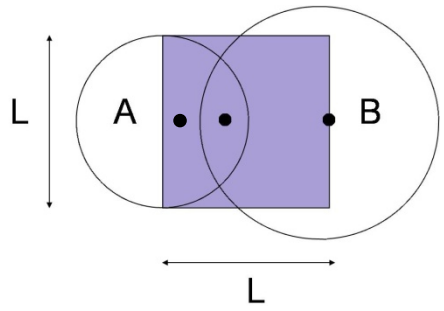

Fig. 3.1 Equivalent continuum material of the particle system (after Potyondy and Cundall 2004)

3.2 Calibration of Sand

The micromechanical parameters of materials are usually calibrated using known responses of the materials in a macro level. Numerical biaxial tests and shear tests are commonly used to evaluate the microscopic properties of geo-materials (Chareyre and Villard 2002; Zhang and Thornton 2007). In this study, biaxial tests were used to calibrate the micro-parameters of the sand.

Poorly-graded sub-rounded Kansas River Sand (KRS) with a mean particle size (d_{50}) of 2.6 mm in diameter was used for consolidated drained (CD) triaxial tests. The other properties of the sand were: G = 2.65, C_c = 0.98, C_u = 2.73, γ_{min} =16.4 kN/m^3, and γ_{max} = 19.5 kN/m^3. For the triaxial tests (Fig. 3.2a), the samples were prepared at a 72% relative

density. The peak angle of internal friction of the sand as obtained from CD triaxial tests was 39^{o} (Fig. 3.3).

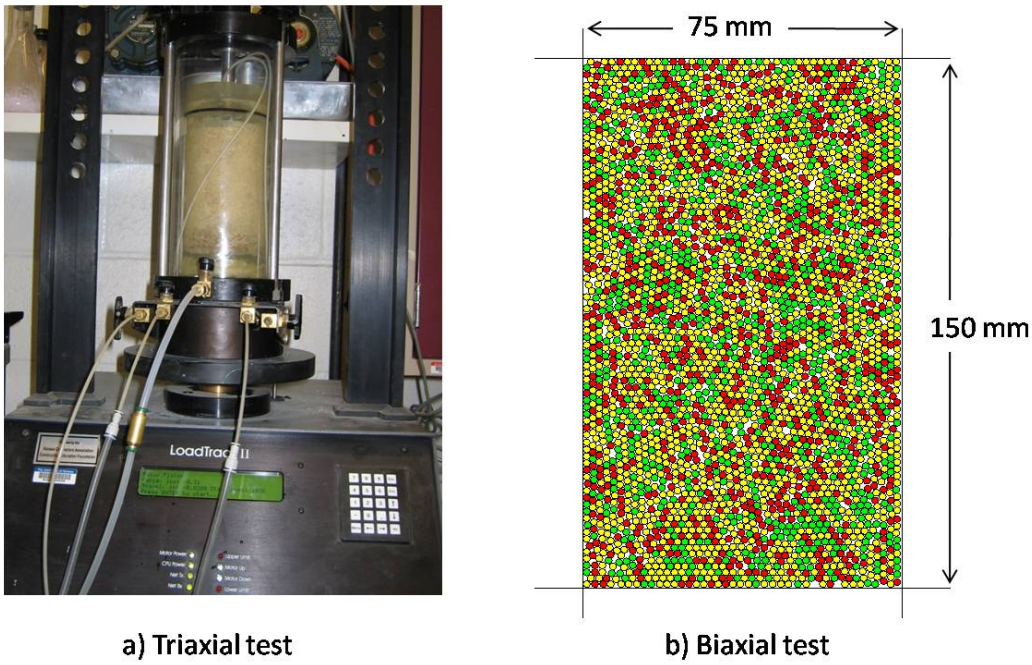

Fig. 3.2 Sample for: (a) experiment and (b) numerical simulation

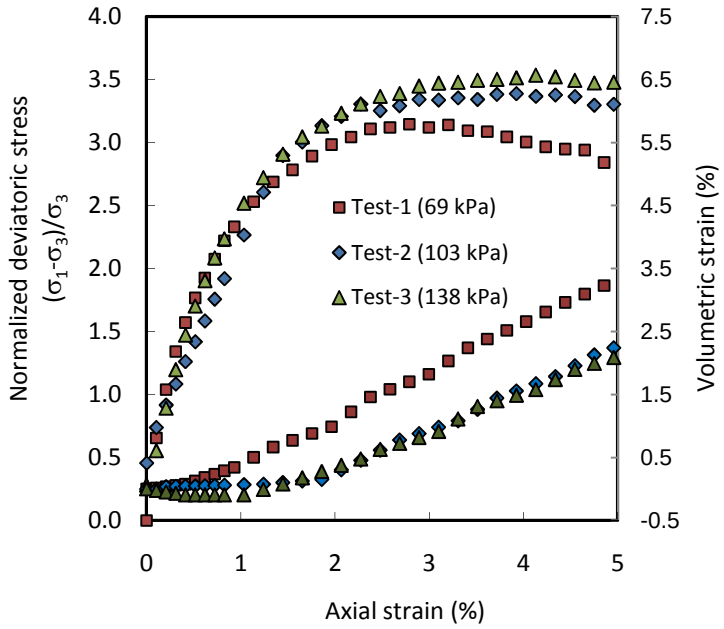

Fig. 3.3 Normalized deviatoric stress and volumetric strain vs. axial strain for KRS

Figure 3.2 b shows the dimensions of the biaxial test samples which had similar dimensions as those in the triaxial tests. Uniform particles of 2.6 mm (mean particle size of KRS) were generated within the enclosed wall at sixty percent of their final size. Initially, smaller size particles were prepared to facilitate their placement. These particles were expanded to achieve the required porosity of the assembly. The assembly was cycled for a mechanical equilibrium state of all particles. Note that a complete equilibrium of all particles indicated by a zero net force at each particle centroid is unattainable. Using a numerical servo control algorithm, the assembly was brought to an initial isotropic stress of 138 kPa. At this point, the vertical stress on the assembly was increased using a strain-controlled procedure to an axial strain of 5% without changing the lateral stress.

Figure 3.4 shows the effect of Young's modulus at the contact (E_c) and the friction coefficient of the interparticle contact (μ) on a normalized deviatoric stress. Figure 3.5 shows the similar effect on volumetric strain of the particle assembly. These results indicate the difficulty of replicating the deviatoric stress and volumetric strain of a real sand using idealized uniform particles in a biaxial assembly. However, considering the trends in the normalized deviatoric stress and volumetric strain, a legitimate choice of Young's modulus at the contact and the interparticle friction coefficient can be made (for example, E_c = 500 MPa, and μ =0.85). For the selected micromechanical properties (E_c = 500 MPa, and μ =0.85), the friction angle of the particle assembly was 30^o, which was less than the friction angle of the sand obtained from CD triaxial tests. The lower friction angle of the particle assembly was expected because other sizes and shapes of the sand particles were not considered in this numerical simulation.

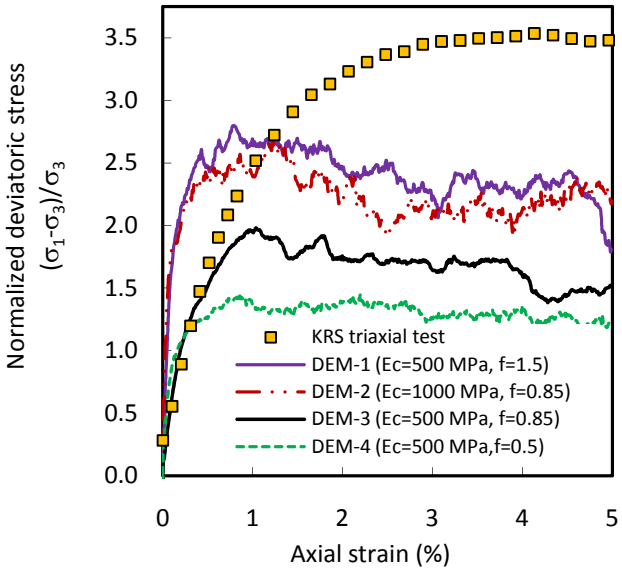

Fig. 3.4 Normalized deviatoric stress vs. axial strain (σ_3 =138 kPa)

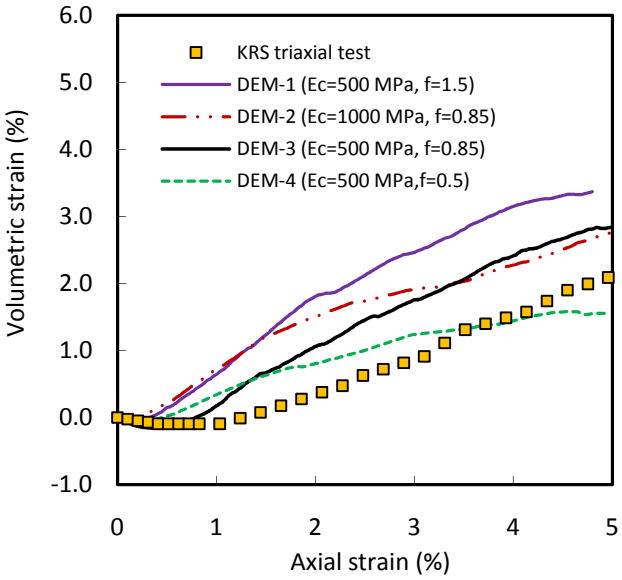

Fig. 3.5 Volumetric strain vs. axial strain (σ_3= 138 kPa)

The calibrated micromechanical properties are appropriate only if they are used for analyses at the corresponding confining stresses that mimic the field confining stresses for granular bases. Since a linear contact model was used in the simulation, Young's modulus

at the contact between the particles should be reduced when the assembly is confined at low stresses. In absence of a relationship for the change in Young's modulus of the linear contact model at different confining stresses, Eq. 3.2 can be used for an initial estimate. Note that the overlap between particles (U_n) is a function of the contact forces. The approach to evaluate the normal contact stiffness at different confining stresses is similar to the one proposed by Misra and Cheung (1999). Therefore, for the rest of the study, Young's modulus at the contact was reduced from 500 MPa (a legitimate choice at the confining stress of 138 kPa) to 150 MPa considering a low confining stress for the granular bases.

3.3 Calibration of Analogical Soil

The behavior of granular media is often studied using two-dimensional analogical soil in model tests (Matsuoka and Yamamoto 1994; Misra and Jiang 1997; Shahin *et al.* 2004; Shahin *et al.* 2006; Jenck *et al.* 2007; Sibille and Froiio 2007). In this approach, biaxial experiments with different size rods are conducted to determine the properties of granular materials. The calibration of these biaxial experiments results in the determination of the relevant parameters that can be used for the numerical simulations of different geotechnical problems. For example, Shahin *et al.* (2004; 2006) and Jenck *et al.* (2007) reported the biaxial tests along with the calibrations to determine the parameters for the continuum-based numerical simulations. Jenck *et al.* (2009) used biaxial tests to determine the parameters for the DEM simulation of the pile-supported granular platform.

A biaxial test conducted on aluminum bars with two diameters of 1.6 mm and 3.0 mm mixed at a ratio of 3:2 was used for calibration. Shahin *et al.* (2004) reported the details of the experiments. The published work of Shahin *et al.* (2004) was selected in this study

since the details of the experiments were available and the findings were also most representative of other research. The width of the numerical sample was 40 times the weighted diameter of the particles and the height of the numerical sample was twice the width. The ratio of the width of the rectangular box to the weighted diameter of the particles used in this study is larger than the ASTM specification but closely follows the recommendation of Jacobson *et al.* (2007) as a requirement for observing a shear band in a granular medium. The number of generated particles (4858) was sufficient to permit the development of a shear band. The particles were generated at the porosity (n) of 0.17. The biaxial test simulation procedure was conducted as described in Section 3.2. The stress ratio vs. the deviatoric strain and the volumetric strain vs. the deviatoric strain are shown in Figs. 3.6 and 3.7. The contraction of the sample was plotted as negative volumetric strain and the dilation of the sample was plotted as positive volumetric strain in Fig. 3.7. These plots were obtained at 20 kPa confining stress. The selected low confining stress was maintained same as that in the experiments.

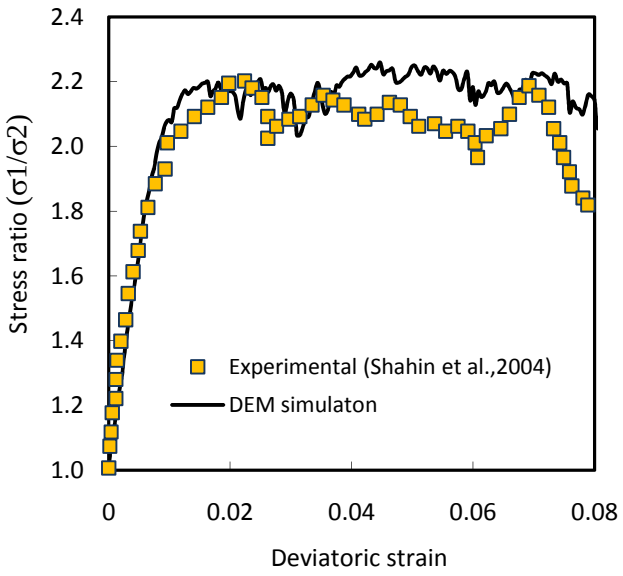

Fig. 3.6 Stress ratio vs. deviatoric strain at confining stress of 20 kPa

The stress ratio in the DEM simulation matched well with the experimental results conducted at the same porosity (n = 0.17). On the other hand, while the qualitative nature of the compression and dilation of the assembly was captured, the volumetric behavior was not quantitatively reproduced in the simulation.

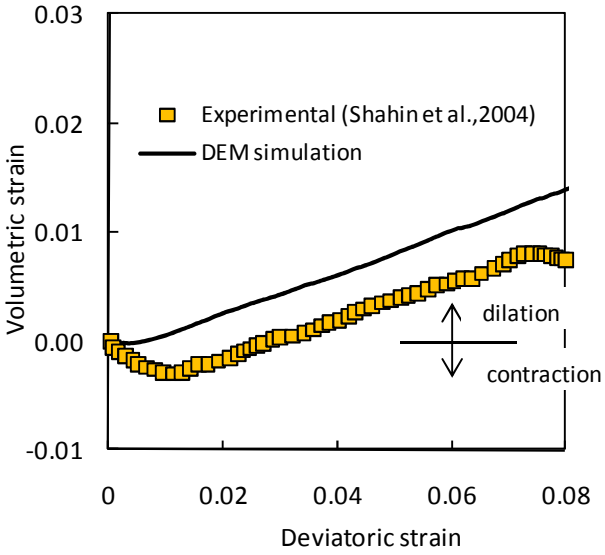

Fig. 3.7 Volumetric strain vs. deviatoric strain at the confining stress of 20 kPa

3.3.1 Effect of confining stress

The numerical analogical soil sample as described in the previous section was sheared at confining stresses of 5, 10, and 20 kPa. Figure 3.8 shows the effect of the confining stress on the deviatoric stress-strain plot. Note that the deviatoric stress was not normalized in order to show the distinct plots at different confining stresses. The experimental result of Shahin *et al.* (2004) was re-plotted accordingly. Figure 3. 9 shows the effect of confining stress on the friction angle of the analogical soil. The maximum friction angle was obtained at the least confinement (5 kPa). Such a reduction in the friction angle of the

granular material with the increase of the confining stress is a well-known phenomenon in geotechnical engineering.

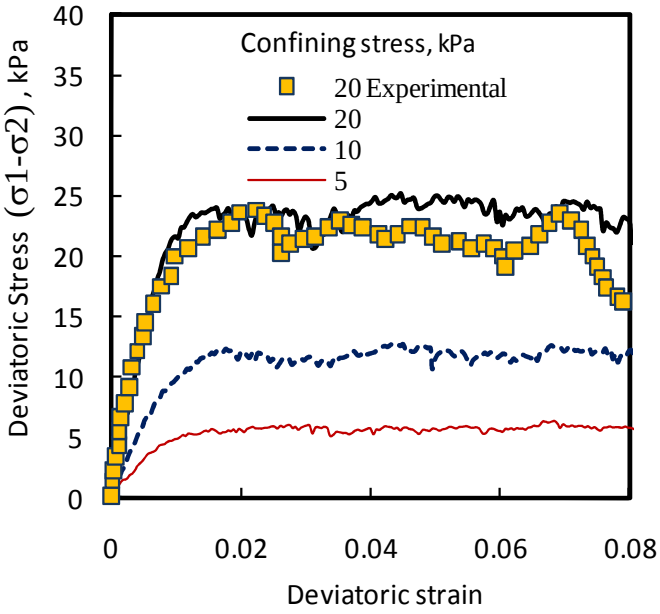

Fig. 3.8 Deviatoric stress vs. deviatoric strain at different confining stresses

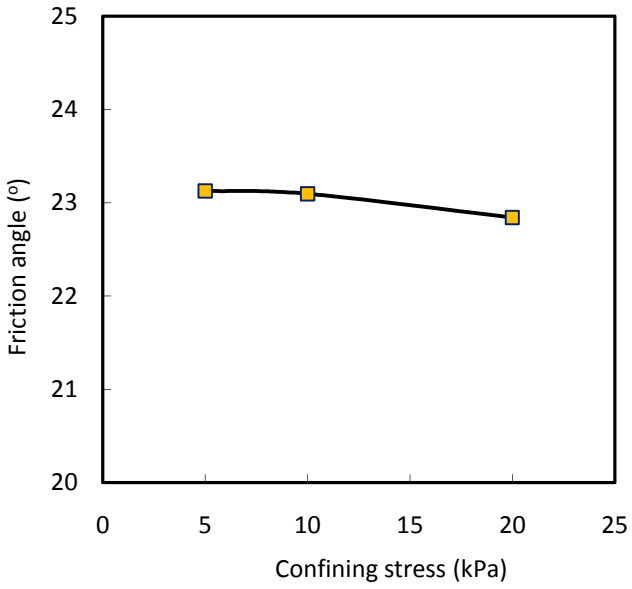

Fig. 3.9 Effect of the confining stress on the friction angle of the analogical soil

3.3.2 Effect of porosity

Porosity is an important physical property of granular materials. From a microscopic view, porosity indicates the number of contacts per particle known as the coordination number (Oda *et al.* 1980). The porosity of a granular material depends upon the packing configuration. It is obvious that the porosity in a three-dimensional packing is different from that in a two-dimensional packing. The porosity of the sample with the two-dimensional packing of equal-diameter particles without any overlap can be calculated from the geometry. For example, a sample with particles in a simple cubic arrangement in which each ball is in contact with four balls in the neighborhood has a porosity of 0.21. A sample in a hexagonal arrangement provides the closest possible regular packing in two dimensions with a porosity of 0.09. In this hexagonal arrangement, a particle is in contact with six neighboring particles.

The analogical soil samples (i.e., aluminum bars of 1.6 mm and 3.0 mm in diameter mixed at the ratio of 3:2) were generated at different porosities for the numerical biaxial simulations. Each of these samples was brought to an initial isotropic stress of 20kPa before applying the axial stress. During the process of isotropic compression, each sample experienced a change in its porosity as shown in Table 3.1 and Figure 3.10. Any point below the solid line with a slope of 45^{o} indicates that the sample compressed while achieving the isotropic stress condition. All samples generated at porosities of 0.17 and higher were compressed. On the other hand, the sample generated at a porosity of 0.14 dilated. For the selected particle diameters, the numerical results showed that the sample generated at a porosity of 0.16 would achieve the isotropic stress condition with little or no change in the porosity. This critical porosity should not be understood as a unique parameter. Rather, the porosity at an isotropic stress is a function of the porosity at

particle generation, the diameter of the particles, and the confining stress if all other micromechanical properties remain same. In general, it is not possible to control the porosity and the stress condition within the sample at the same time.

Table 3.1 Porosities of the analogical soil samples at different states

Sample No.	Porosity at particle generation	Porosity at an isotropic stress of 20kPa	Change in porosity (positive in compression)
1	0.250	0.190	0.060
2	0.200	0.180	0.020
3	0.180	0.170	0.010
4	0.167	0.160	0.007
5	0.140	0.157	-0.017

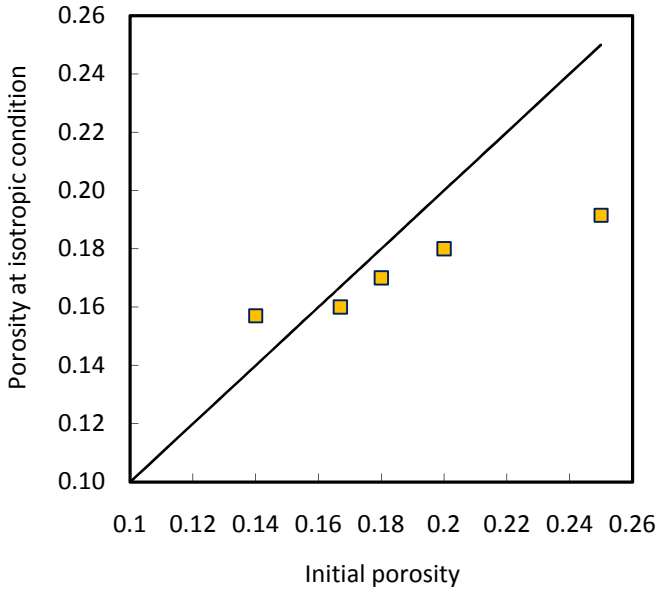

Fig. 3.10 Variations in porosities at the isotropic stress condition (σ_2 =20 kPa)

Figures 3.11 and 3.12 show the effect of porosity on the deviatoric stress or volumetric strain vs. the deviatoric strain. The deviatoric stress increased with the reduction in the

porosity in the assembly. Furthermore, it is shown that the assembly had a higher modulus at a low porosity. The dependence of Young's modulus on the packing structure (associated with the porosity) and the confining stress was derived by Chang and Misra (1990) in a closed-form solution for a isotropic packing confined at an isotropic stress as follows:

$$\tilde{E} = 2r^2 \frac{(5-4\nu)}{3(5-3\nu)} [9\sigma_o]^{\frac{1}{3}} \left[\frac{GN}{(1-\nu)V}\right]^{\frac{2}{3}} \quad \text{Eq. 3.5}$$

where, $\tilde{E}$ =Young's modulus of the assembly;

ν -=Poisson's ratio;

r = the radius of the spherical particle;

σ_o = the confining stress;

G = the shear modulus of the sphere;

N = the total number of contacts in the assembly of volume V.

This closed-form solution was derived for a three-dimensional packing and showed stronger dependence of Young's modulus on N than on σ_o.

The assemblies at porosities of 14%, 17%, 18%, and 20% showed an initial volumetric contraction followed by dilation. On the other hand, the assembly at 25% porosity showed contraction throughout the biaxial test simulation (Fig. 3.12). As expected, the samples showed increased dilation with the reduction in porosity.

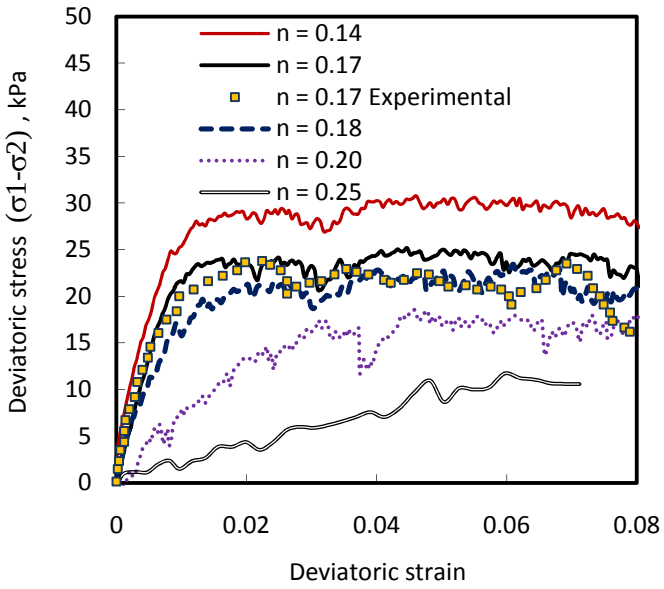

Fig. 3.11 Effect of porosity on deviatoric stress vs. strain (σ_2 =20 kPa)

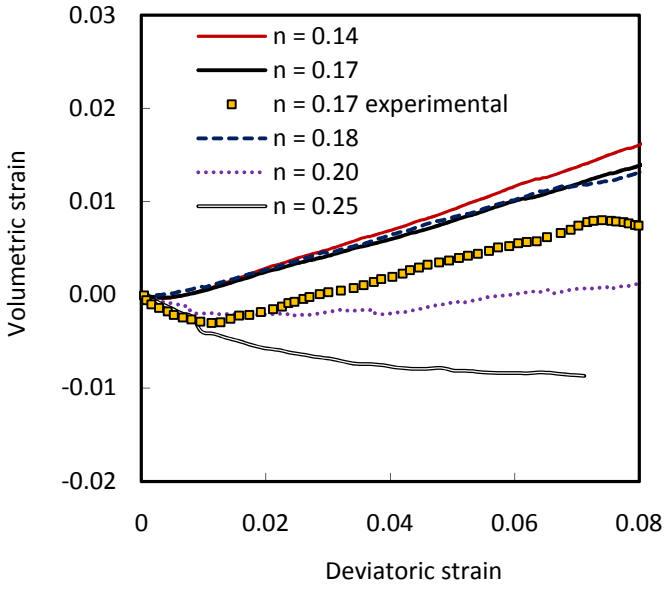

Fig. 3.12 Effect of porosity on volumetric vs. deviatoric strains (σ_2= 20 kPa)

The peak friction angle of the assembly decreased almost in a linear fashion with an increase of the porosity (Fig. 3.13). The peak friction angles were calculated based on the maximum deviatoric stresses observed within the simulation ranges. While the assemblies

at porosities other than 25% seemed to achieve the critical state, the assembly at 25% porosity was in a pre-peak state. Therefore, the peak friction angle of the assembly at the porosity of 25 % may be underestimated in this simulation.

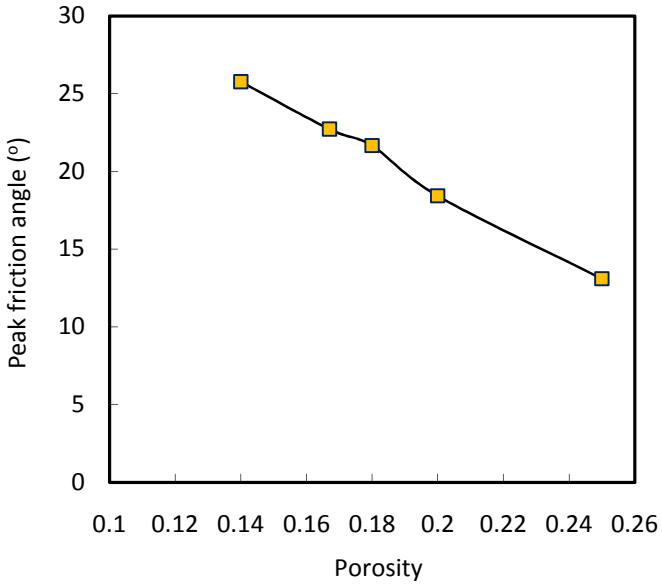

Fig. 3.13 Effect of porosity on friction angle (σ_2= 20 kPa)

3.3.3 Effect of particle gradation

Figure 3.14 shows the gradation of the particles used in the numerical study. Gradation A had uniform particles; Gradations B and C were both graded over a similar range of particle diameters. Particles larger than d_{50} followed the Fuller gradation in the case of Gradation B. Fuller's gradation is the gradation for particles to achieve the maximum density (Fuller and Thompson 1907):

$$P = \left(\frac{d}{D}\right)^n \qquad \text{Eq. 3.6}$$

where P= the percentage finer than the sieve size;

d= the aggregate size being considered;

D= the maximum aggregate size to be used;

n= the parameter for the maximum particle density (recommended as 0.45 by Federal Highway Administration (FHWA) in 1960).

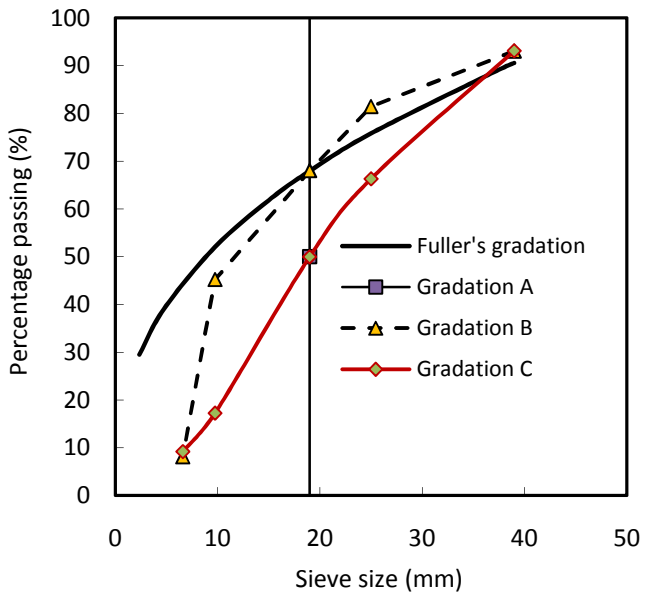

Fig. 3.14 Particle size distribution curve for the DEM study

The ratio of the maximum to minimum particle diameters for Gradation B was selected to seven to avoid excessive computational time during the numerical simulation. Therefore, the Fuller gradation could not be followed at the lower end (i.e., smaller particles) of the curve. Gradation C had the same range of particle sizes as Gradation B but followed a different distribution. The d_{50} of Gradation C was same as the d_{50} of Gradation A.

Particles were generated as per the particle size distribution curve (Fig. 3.14) within the enclosed wall at sixty percent of their final size. The smaller particles eased their placement and would grow to the defined diameters to achieve the required porosity. The biaxial numerical simulations of particles of various gradations, generated at a porosity of 0.16, were conducted to study the effect of particle gradation on the shear strength of the granular material.

Figure 3.15 shows the deviatoric stress vs. deviatoric strain for Gradations A, B, and C sheared at a confining stress of 20 kPa. Figure 3.16 shows the volumetric strain vs. deviatoric strain for these samples. While all three samples had a similar range of deviatoric stresses, the sample with Gradation A had lower strength and higher dilatancy. On the other hand, the sample with Gradation B (containing a wide range of particle sizes) showed higher strength and lower dilatancy (max ε_v = 1.0%). Small particles in Gradation B could move into the gaps between large particles to minimize the dilation. The sample with Gradation A (i.e., uniform particles) did not have smaller particles, which could enter the gaps between large particles; therefore, it dilated more. The deviatoric stress and volumetric strain behavior of the sample with Gradation C was generally bounded between the responses of the samples with Gradations A and B.

Evans *et al.* (2009) also reported the effects of particle gradation on the shear strength and the volumetric strain based on the biaxial numerical tests. In their study, they considered four gradations: linear, baseline, fine, and coarse. A well-graded sample with coarser particles had higher shear strength and dilatancy than that with finer particles. A relatively uniform, linear specimen exhibited softer stress-strain behavior at a low strain and overall more dilatant behavior. Their results were based on the samples prepared at slightly

different void ratios (0.084 to 0.132) at isotropic conditions, which could significantly affect the stress-strain behavior particularly at a small strain.

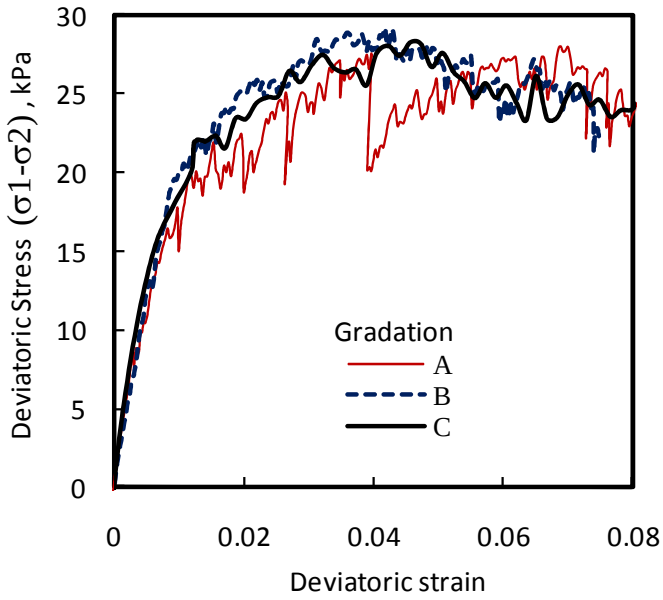

Fig. 3.15 Deviatoric stress vs deviatoric strain for different gradations (σ_2= 20 kPa)

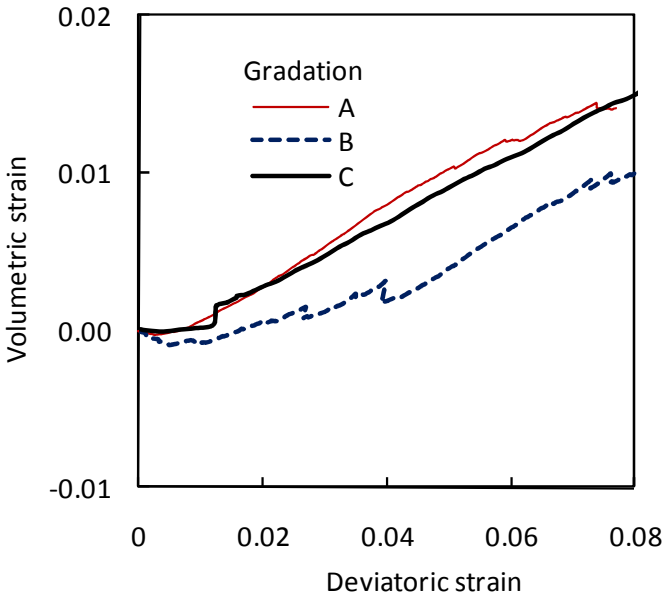

Fig. 3.16 Volumetric strain vs. deviatoric strain for different gradations (σ_2= 20 kPa)

3.4 Fabric and Force Orientations

Fabric orientation of a assembly describes the preferred orientation of the particles in a sample (Oda *et al.* 1980; Rothenburg and Bathurst 1989; Bathurst and Rothenburg 1990). The fabric orientation is an important index property for granular materials. The fabric (contact) orientation between two cylindrical particles at the contact can be calculated from the coordinate records of their centroids. Whenever the particles are in contact, the contact orientation is defined by a unit normal vector joining the centroids of the particles. The contact force between the particles can be decomposed into a normal component acting in the direction of the normal vector and a shear component acting in the contact plane (i.e. perpendicular to the normal). The information regarding the fabric (contact) and force (normal as well as shear) orientations can be extracted at any stages of a numerical simulation. In this section, the behavior of different graded assemblies in biaxial simulations is analyzed from the fabric and force orientation point of view.

3.4.1 Orientation at isotropic stress

A polar histogram of the contact forces can be obtained by collecting the contact force information at a predefined bin angle (O'Sullivan *et al.* 2008). In this study, a bin angle of 10^{o} was selected, and the polar histogram for the contact orientation was normalized using the total number of contacts. Similarly, the polar histograms for contact normal and tangential forces were normalized by the average normal force over all contacts in the assembly. The observation of the normalized contact and the contact force orientation led to the following Fourier series approximations (Rothenburg and Bathurst 1989; Bathurst and Rothenburg 1990).

$$E(\theta) = \frac{1}{2\pi}(1 + a\ cos2(\theta - \theta_a)) \quad \text{Eq. 3.7}$$

$$\overline{f_n}(\theta) = \overline{f_o}(1 + a_n\ cos2(\theta - \theta_f)) \quad \text{Eq. 3.8}$$

$$\overline{f_t}(\theta) = \overline{f_o}(-a_t\ cos2(\theta - \theta_t)) \quad \text{Eq. 3.9}$$

$$\overline{f_o}(\theta) = \frac{1}{2\pi}\int_0^{2\pi} \overline{f_n}(\theta)d\theta = \frac{1}{N}\sum_{N_c} f_n^k \quad \text{Eq. 3.10}$$

where, $E(\theta)$= the contact density distribution function;

$\overline{f_n}(\theta)$ = the average normal force density distribution function;

$\overline{f_t}(\theta)$= the average tangential force density distribution function;

$\overline{f_o}(\theta)$= the average contact forces of all contacts;

a, a_n, a_t = the magnitude of directional variation of contacts, average normal force, and average tangential force;

θ_a, θ_f, θ_t= the corresponding major principal directions of anisotropy;

N = the total number of particles;

f_n^k = the contact normal force.

Note that the integration of the contact density function over 2π radians is always 1.

Figure 3.17 shows the normalized histograms of the contact orientations for the samples with Gradations A, B, and C at an isotropic stress condition during the biaxial simulations. If the contact orientation is isotropic, θ_a should be either 0^o or 90^o which enforces $E(\theta)$ to be $1/2\pi$. This isotropic orientation is plotted with broken lines in Fig. 3.17. Since Gradation A contained only uniform particles, random generation of particles followed by a subsequent gravity deposition (preferred because of almost hexagonal packing) gave a

strong directional orientation of the contacts. The contact orientations for the samples with Gradations B and C confirmed the isotropic orientations at an isotropic stress during the biaxial simulation. Towards a well-graded particle size distribution in the assembly, the probability density function for a particle sharing a contact with another particle in any arbitrary direction becomes directional independent.

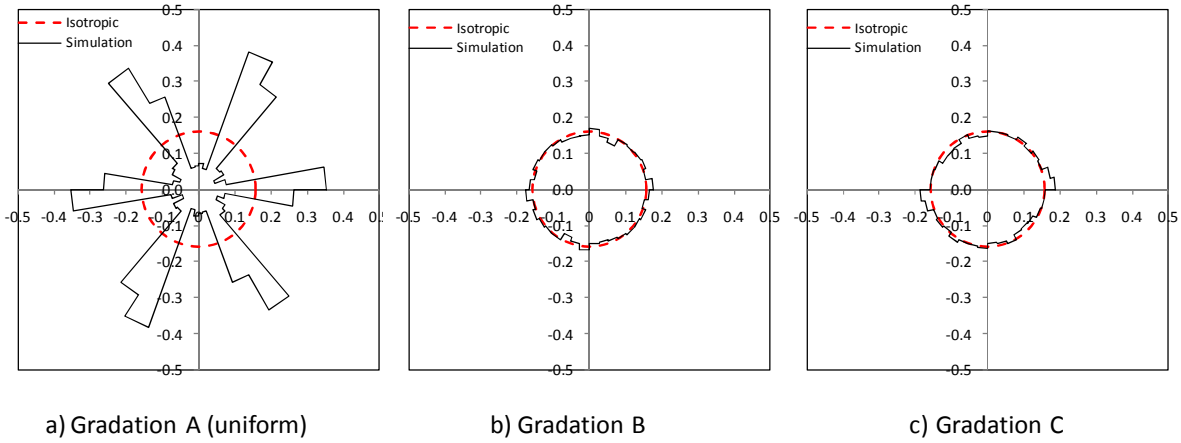

Fig. 3.17 Contact orientations at an isotropic stress (20 kPa) for different gradations

Figure 3.18 shows the normalized histograms for the normal force orientations for the samples with Gradations A, B, and C at an isotropic stress condition during the biaxial simulations. If the normal force is isotropic, θ_f should be either 0^o or 90^o and the average normal force density distribution function ($\overline{f_n}(\theta)$) is 1. The isotropic normal force distribution function was plotted as a broken line. The normal force distribution for the sample with Gradation A showed some variations from the isotropic normal force distribution. The normal force distributions for the samples with Gradations B and C showed closer approximation to the isotropic normal force distributions. The closer approximation of the normal force distribution to the isotropic normal force is the

consequence of particle gradation. Since the contact and normal force orientation for Gradations B and C are both isotropic, each contact should share a similar magnitude of force. In case of the sample with Gradation A, the contact orientation was not isotropic, while the normal force distribution was still close to the isotropic one. This isotropic normal force distribution implies that the assembly truly achieved an isotropic stress condition during the simulation. However, each contact should share a different magnitude of force because of the non-symmetric distribution of contacts illustrated in Fig. 3.18 (a).

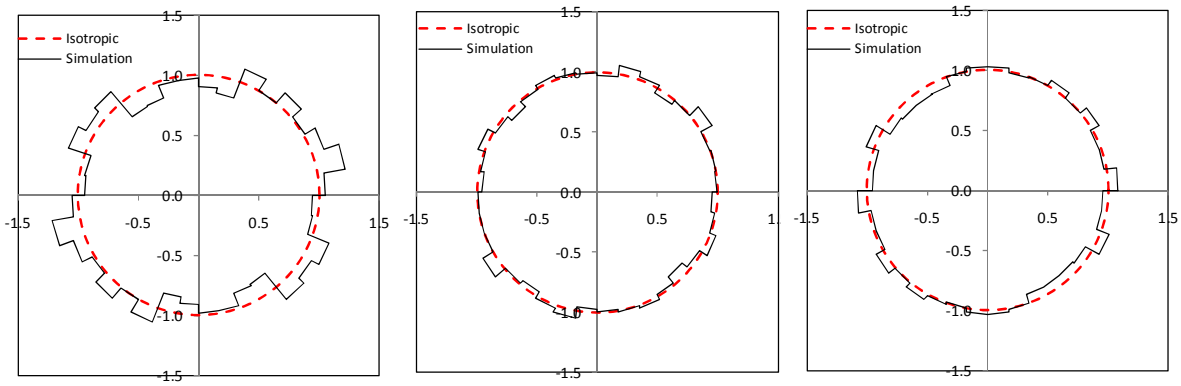

Fig. 3.18 Normal force orientations at an isotropic stress for different gradations

Figure 3.19 shows the normalized histograms of the tangential force orientations for samples with Gradations A, B, and C at an isotropic stress condition during the biaxial simulations. From mechanics, it is expected that the tangential force distributions should be close to zero when the normal force distributions are isotropic.

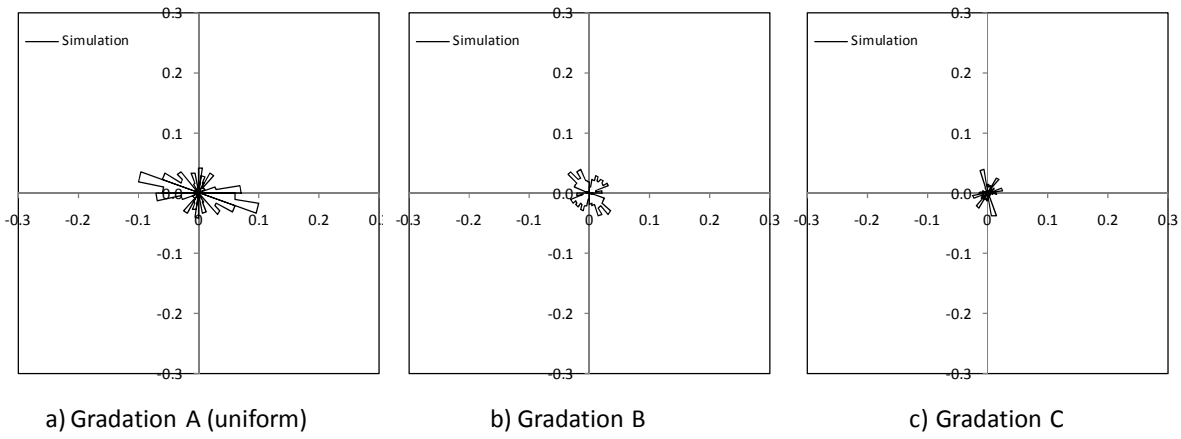

Fig. 3.19 Tangential force orientations at an isotropic stress for different gradations

3.4.2 Orientation at large strain

Figure 3.20 shows the normalized histograms of the contact orientations for the samples with Gradations A, B, and C at 8% deviatoric strain. At this strain level, particles had more contacts oriented towards the vertical direction than in the lateral direction. For Gradations B and C, the ratios of the contacts oriented towards the vertical direction to the lateral direction were approximately 2.0. Also the loss of contacts in the lateral direction and the gain towards the vertical direction was noticed for Gradation A (uniform particles). The comparison of the contact orientations at the isotropic stress (Fig. 3.17) and those at the 8% deviatoric strain (Fig. 3.20) shows that the Fourier series approximation at a higher strain was plausible if the contacts had an isotropic distribution at the isotropic stress condition (Gradations B and C). The contacts in the sample with Gradation A showed a special distribution which was untenable to the Fourier series approximation.

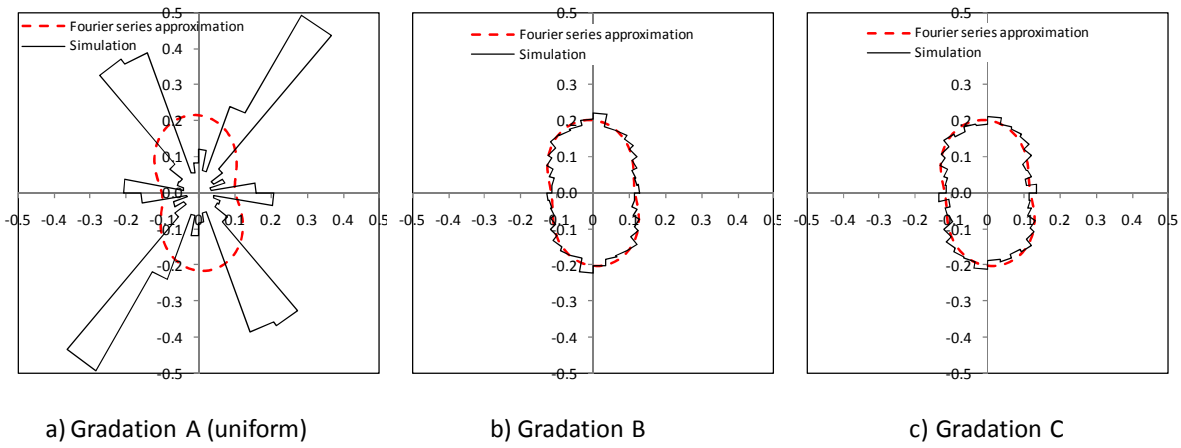

Fig. 3.20 Contact orientations at 8% deviatoric strain for different gradations

Figure 3.21 shows the normalized histograms of the normal force orientations for samples with Gradations A, B, and C at 8% deviatoric strain. Since the lateral stress was maintained at 20 kPa and the samples were sheared by increasing the vertical stress, large normal contact forces in the vertical direction were expected. The ratio of the normal contact force in the vertical direction to that in the lateral direction was approximately 2.0. This ratio was the same as the ratio observed in the contact orientations for samples with Gradations B and C. For the sample with Gradation A, a discrepancy existed between the contact orientation and the normal force orientation. Few contacts available in the vertical direction must have carried significantly high normal forces to realize this normal force distribution. A similar conclusion was drawn in Section 3.4.1 for the sample with Gradation A under the isotropic stress condition.

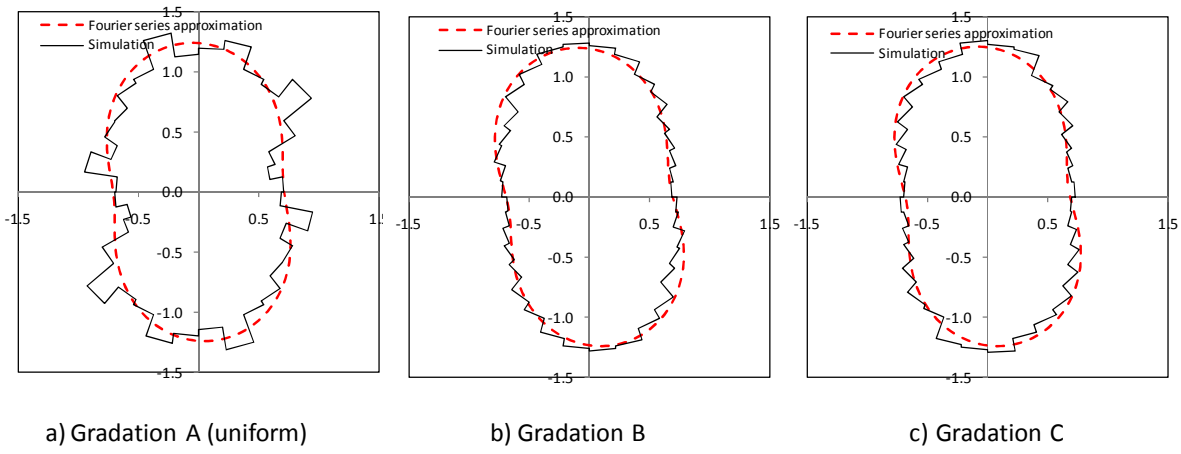

Fig. 3.21 Normal force orientations at 8% deviatoric strain for different gradations

Figure 3.22 shows the normalized histograms of the tangential force orientations for samples with Gradations A, B, and C at 8% deviatoric strain. Different from the isotropic stress condition (Fig. 3.19), the tangential force increased under the application of the deviatoric strain. The least tangential force occurred at the axis of the maximum normal force as expected.

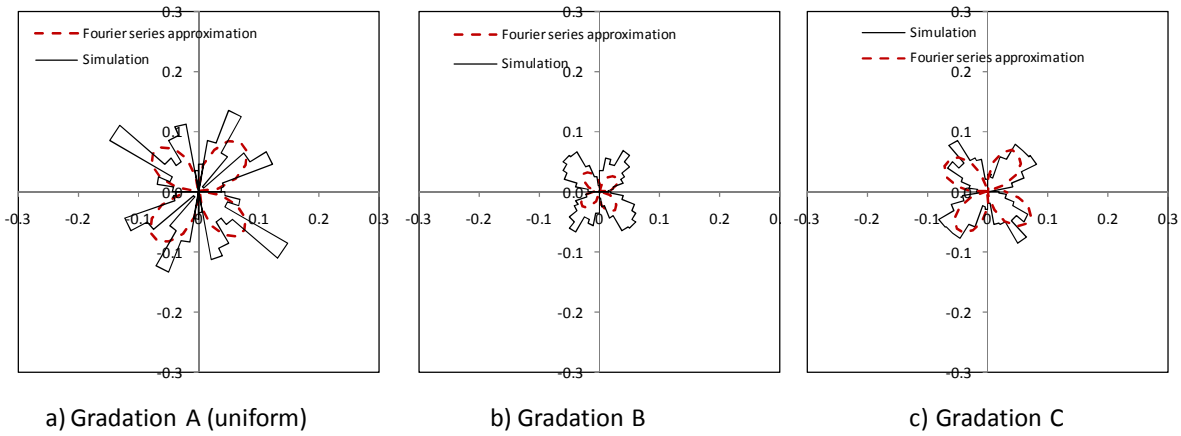

Fig. 3.22 Tangential force orientations at 8% deviatoric strain for different gradations

3.4.3 Effect of particle size on orientation

In an assembly of graded particles, large particles are believed to carry large contact forces, and small particles are believed to provide more contacts to the large particles to improve the stability. In this study, the contact and force orientations were extracted by dividing the particles into two categories: particles smaller than d_{50} and particles larger than d_{50}. The contact and force distributions were normalized by the total number of contacts (N) and the average normal contact force ($\overline{f_o}$), respectively. Figures 3.23 and 3.24 show the contact orientations for the samples with Gradations B and C, respectively. The contact orientations for the two particle sizes, smaller and larger than $d_{50,}$ were similar. The number of contacts for particles larger than d_{50} was smaller than that for particles smaller than d_{50} because the number of particles at a particular size within a constant volume depends on the square of the particle diameter. The number of contacts for either particle size was smaller than that for all particles. The observation was consistent for the samples with Gradations B and C.

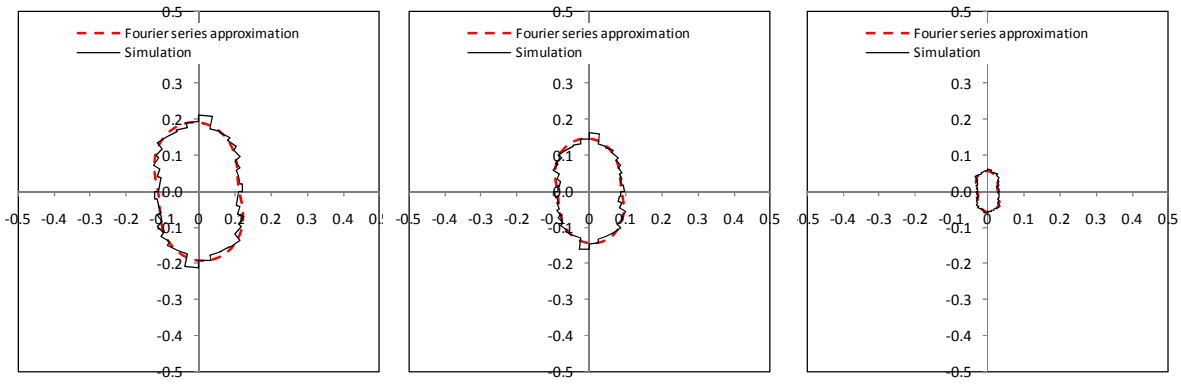

a) All particles b) Smaller than d_{50} c) Larger than d_{50}

Fig. 3.23 Contact orientations as per particle sizes at 8% deviatoric strain for Gradation B

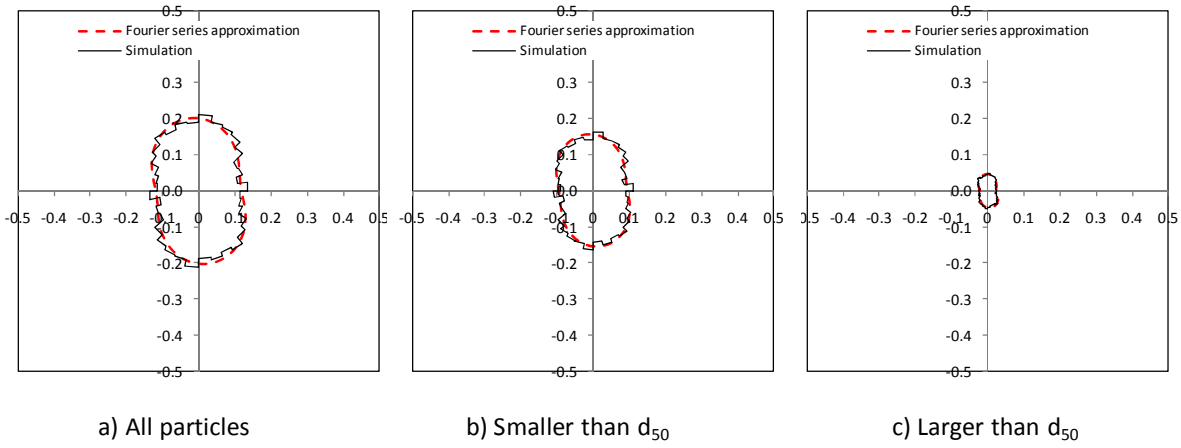

Fig. 3.24 Contact orientations as per particle sizes at 8% deviatoric strain for Gradation C

Figures 3.25 and 3.26 show the normal force orientations for the samples with Gradations B and C, respectively. In both categories (particles smaller and larger than d_{50}), large normal forces were observed in the vertical direction. Considering the distribution of the normal forces for the particles smaller than d_{50}, the ratios of the normal forces in the vertical direction to the horizontal direction were 1.6 and 1.7 for the samples with Gradations C and B. Similar ratios, while considering the distribution of forces for the particles larger than $d_{50,}$ were 2.1 and 2.2 for the samples with Gradations C and B, respectively. The larger particles in the assembly not only carried a large contact force per contact but also showed more anisotropy compared to the smaller particles.

Figures 3.27 and 3.28 show the tangential force orientations for the samples with Gradations B and C, respectively. For both gradations, larger tangential forces were observed for the particles larger than d_{50}; the distributions of the tangential forces were consistent with those of the normal forces. Table 3.1 summarizes the parameters defined in Section 3.4 for contact and force orientations in samples with Gradations B and C.

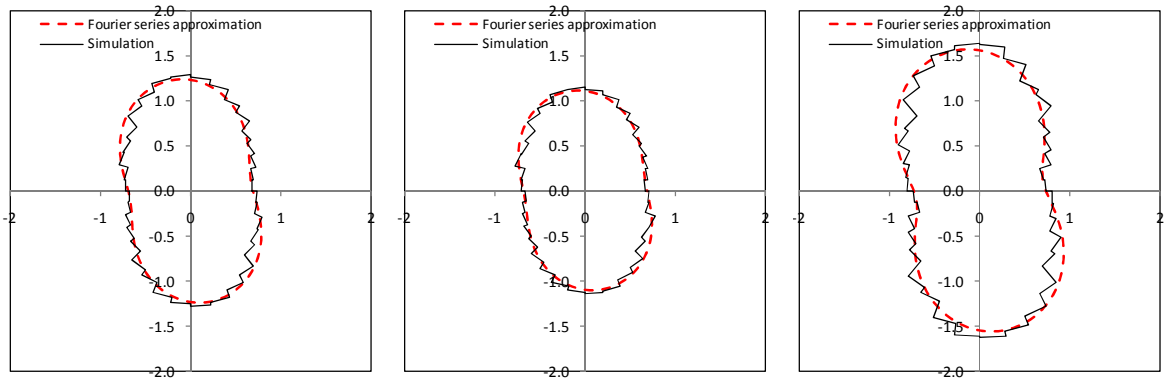

a) All particles b) Smaller than d_{50} c) Larger than d_{50}

Fig. 3.25 Normal force orientations as per particle sizes at 8% deviatoric strain for Gradation B

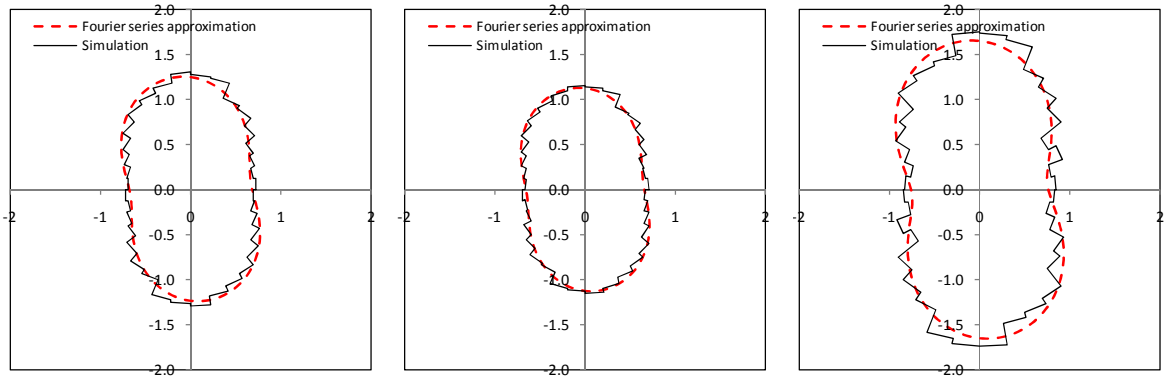

a) All particles b) Smaller than d_{50} c) Larger than d_{50}

Fig. 3.26 Normal force orientations as per particle sizes at 8% deviatoric strain for Gradation C

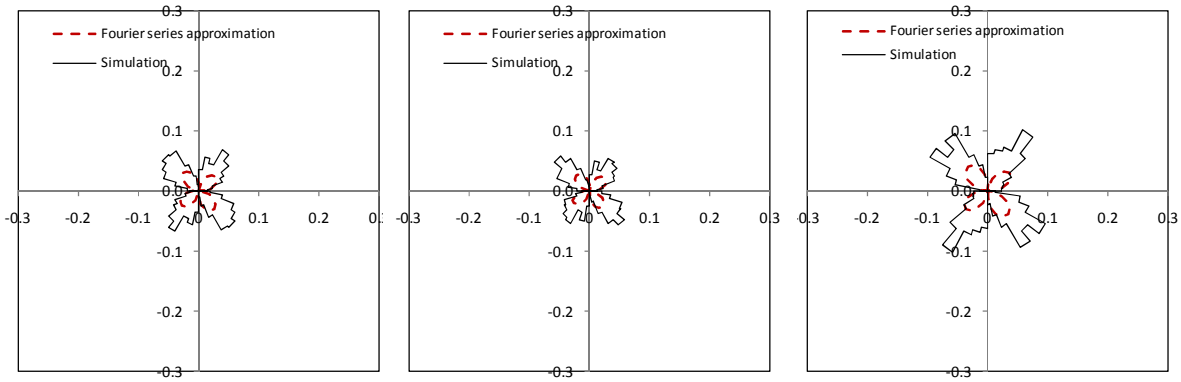

a) All particles b) Smaller than d_{50} c) Larger than d_{50}

Fig. 3.27 Tangential force orientations as per particle sizes at 8% deviatoric strain for Gradation B

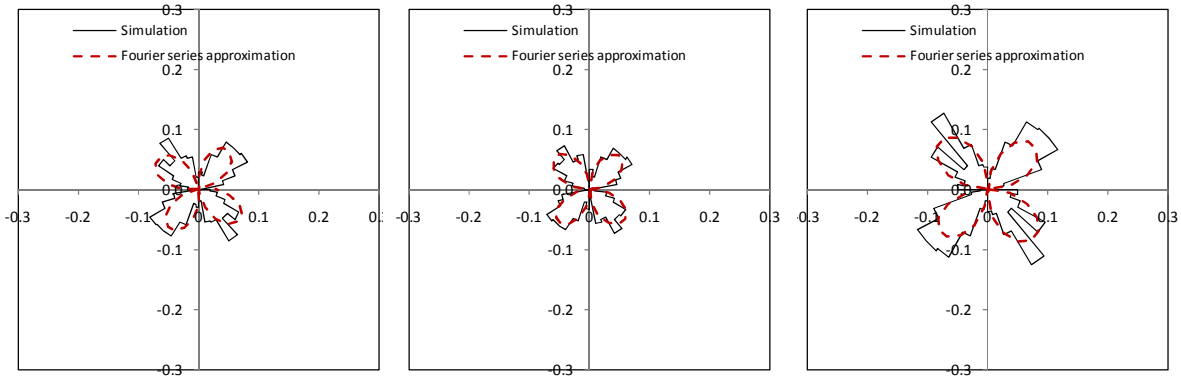

a) All particles b) Smaller than d_{50} c) Larger than d_{50}

Fig. 3.28 Tangential force orientations as per particle sizes at 8% deviatoric strain for Gradation C

Table 3.2 Coefficients of the Fourier series approximation for samples with Gradations B and C

Coefficients	Gradation B			Gradation C		
	All particles	Particles smaller than d_{50}	Particles larger than d_{50}	All particles	Particles smaller than d_{50}	Particles larger than d_{50}
a	0.044	0.028	0.015	0.043	0.031	0.012
a_n	0.285	0.222	0.436	0.290	0.239	0.452
a_t	0.038	0.033	0.049	-0.082	-0.076	-0.109
θ_a	96.5	97.4	96.5	97.7	97.9	97.7
θ_f	99.2	99.2	99.2	97.8	97.5	95.8
θ_t	83.1	83.1	84.2	83.7	82.5	84.8

3.5 Cyclic Biaxial Test

Granular materials exhibit resilient behavior when subjected to cyclic stresses lesser than their shear strengths. At each load repetition, a plastic deformation accumulates which contributes to a rut on an unbounded aggregate base. The concept of resilient modulus (M_R) has been used to describe such a cyclic behavior of the granular material. Resilient modulus is defined as:

$$M_R = \frac{\sigma_d}{\varepsilon_a^e} \qquad \text{Eq. 3.11}$$

where, σ_d = the deviatoric stress;

ε_a^e = the resilient axial strain.

Past studies have shown that the DEM simulation of cyclic tests is promising for studying the resilient behavior of granular materials (Zeghal 2004; Uthus *et al.* 2008). In fact, Zeghal (2004) demonstrated that the stress-dependent resilient behavior of the granular

materials can be studied using a relatively small number of load repetitions. Zeghal (2004) noticed that the resilient response stabilized after 20 loading and unloading cycles. The deviatoric stress significantly controlled the resilient behavior at a low confining stress but had less effect at a high confining stress.

Figures 3.29 and 3.30 show the deviatoric stress and volumetric strain plot against the deviatoric strain at different cycles for the sample with Gradation A in this study. The vertical load was changed at a constant strain rate until the target stress was achieved. The maximum axial stress was permitted to 70% of the axial strength of the sample (Fig. 3.15) and the minimum axial stress was fixed to the confining stress (20 kPa).

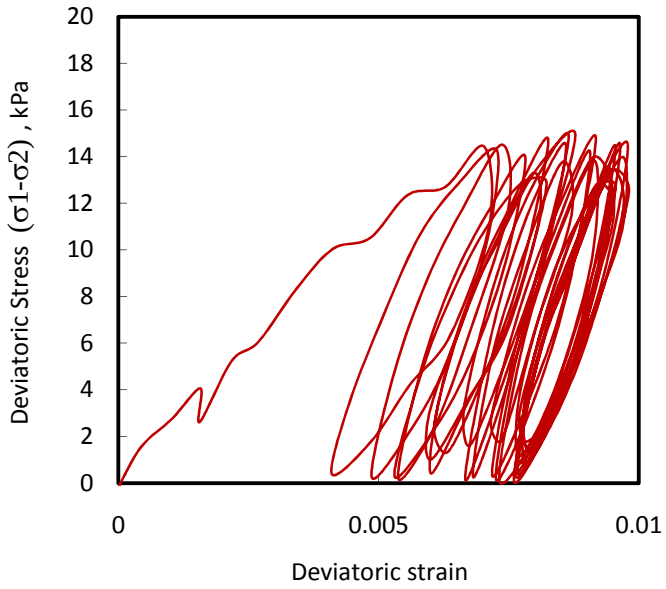

Fig. 3.29 Deviatoric stress vs deviatoric strain during cyclic biaxial test for Gradation A (σ_2= 20 kPa)

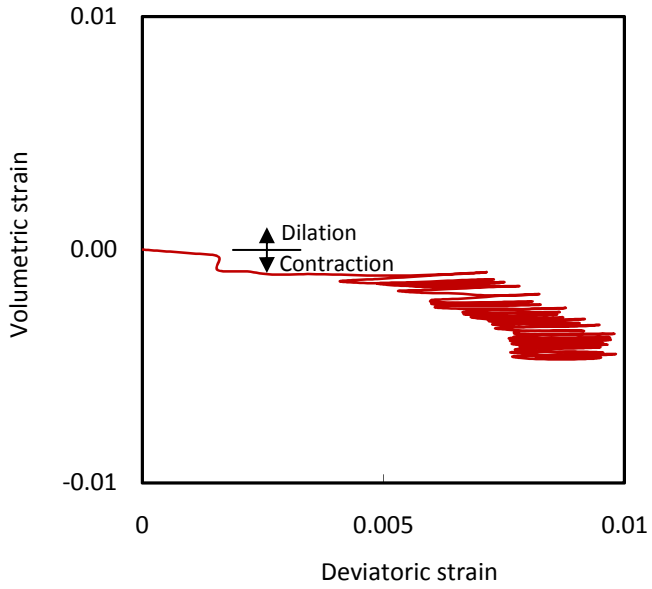

Fig. 3.30 Volumetric strain vs. deviatoric strain during a cyclic biaxial test for Gradation A (σ_2= 20 kPa)

Figures 3.31 and 3.32 show the deviatoric stress and volumetric strain plot against the deviatoric strain for the sample with Gradation B. The deviatoric stress-strain behavior was similar for both cases. The sample with Gradation A consisting of uniform particles showed volumetric contraction while the sample with Gradation B consisting of different size particles exhibited a stable volumetric response during the cyclic load simulation. The arrangement of different size particles must have contributed to the stable volumetric response for the sample with Gradation B.

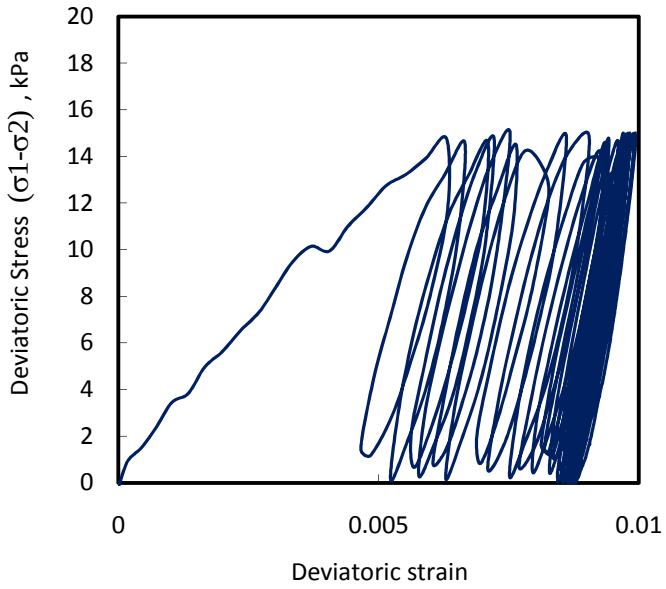

Fig. 3.31 Deviatoric stress vs. deviatoric strain during a cyclic biaxial test for Gradation B (σ_2= 20 kPa)

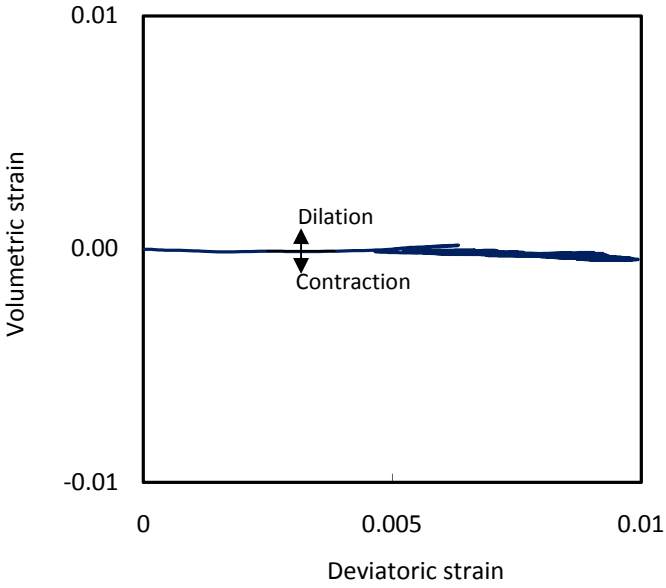

Fig. 3.32 Volumetric strain vs. deviatoric strain during a cyclic biaxial test for Gradation B (σ_2= 20 kPa)

The resilient moduli can be calculated from the presented results in Figs. 3.29 and 3.31 for the samples with Gradation A and B. The resilient axial strain was calculated as the difference between the total axial strain after loading and the remaining axial strain (plastic) after unloading. Figure 3.33 shows the resilient modulus with the number of cycles for the samples with Gradations A and B. The resilient modulus for the sample with Gradation B was approximately 50% higher than that for Gradation A. Given almost an equal peak strength for both samples in monotonic loading (Fig. 3.15), the graded sample (Gradation B) showed a significant improvement in the resilient modulus compared to the uniform sample (Gradation A).

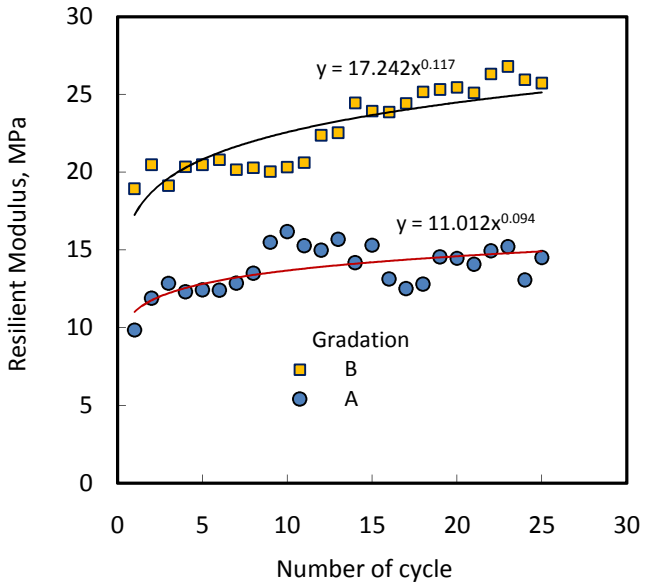

Fig. 3.33 Resilient modulus vs. number of cycles for Gradations A and B (σ_2= 20 kPa)

3.6 Calibration of Paper

Paper was used as a reinforcement in a trapdoor experiment (Chapter 4). Tension tests of the paper were conducted using the ElectroForce machine (Fig. 3.34). Four specimens were prepared from two locations of the paper. In each test, a paper specimen of 5 mm in width and 50 mm in length was subjected to a monotonically increasing load at a displacement rate of 1 mm/min. Throughout the test, the load and the displacement were recorded using a data logger. The machine was programmed to scan the data at every five seconds. In each scan, 30 data points were recorded. The tests were terminated upon the tensile failure of the specimens. Figure 3.35 shows the tensile force plotted against the strain. While the specimen obtained from the same location showed similar tensile force; variations on the tensile force were evident for the samples obtained from different locations.

The paper was modeled in the PFC^{2D} using bonded particles of 0.2 mm in diameter (thickness of the paper) for calibration. The contact bond force between the particles representing the paper specimen corresponded to its tensile strength. Similarly, the normal stiffness between the particles corresponded to the tensile stiffness at a strain of 1.5%. These deduced micromechanical parameters for the paper are provided in Table 3.3. The starting and ending particles in the row were given a small velocity (V) of 1E-8m/step and the resulting forces were measured. Figure 3.35 shows a reasonable agreement between the experimental results and the DEM simulation of the tension tests.

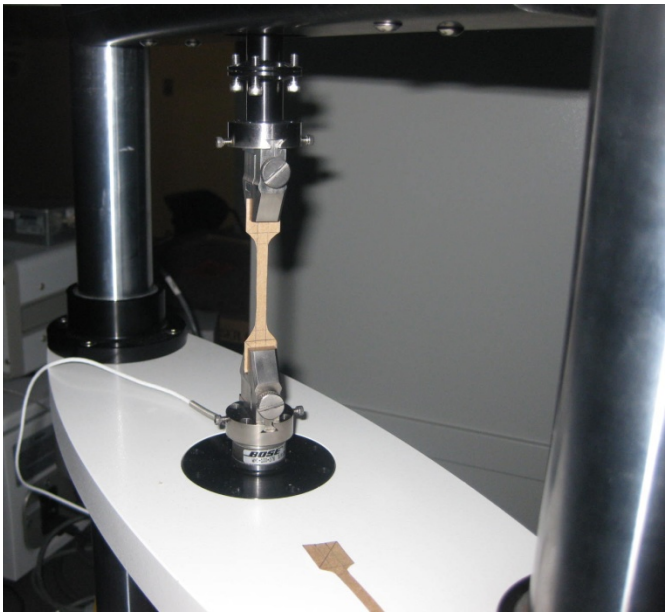

Fig. 3.34 Tension test of a paper specimen using the ElectroForce machine

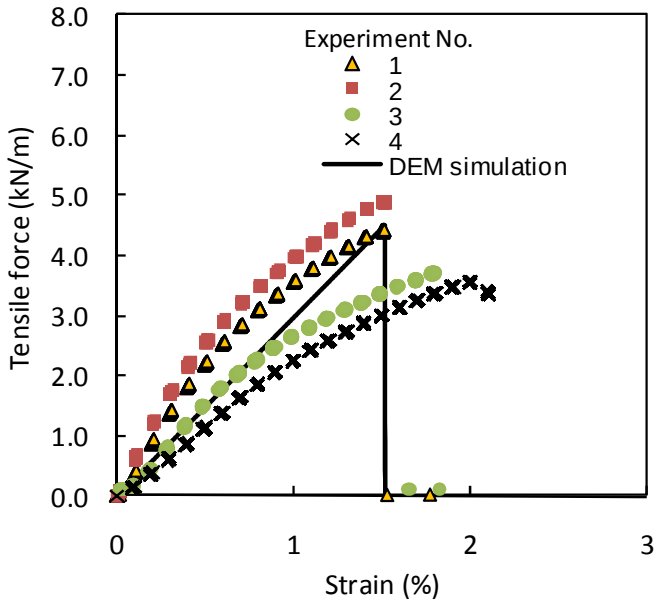

Fig. 3.35 Tensile force vs. strain for a paper specimen

3.7 Calibration of Geotextile and Geogrid

Geotextiles and geogrids were used as reinforcement in pile-supported embankments and granular bases (Chapters 5 and 6). Woven geotextile and extruded, punched-drawn biaxial geogrid were used for calibration. The geotextile were modeled using bonded particles of 1.0 mm in diameter. Similarly, the geogrid was modeled using bonded particles of 1.0 mm diameter at a rib and 2.6 mm diameter at junctions. The contact bond strengths between the particles representing the geosynthetics (geotextile and geogrid) corresponded to their tensile strengths. Similarly, the normal stiffness between the particles corresponded to their tensile stiffness at a strain of 10%. The micromechanical parameters for the geosynthetics were calibrated using tension tests. The input parameters are shown in Table 3.3. Only a portion of the particles generated for the tension test is shown in Fig. 3.36.

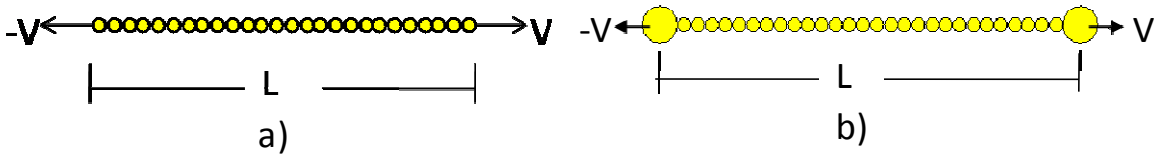

Fig. 3.36 Particle assembly for a tension test simulation a) geotextile, b) geogrid

The starting and ending particles in the row were given a small velocity (V) of 1E-8m/step and the resulting forces were measured in the model. The DEM results were compared with the strengths of the geosynthetics as mentioned on the product specifications (geotextile: HP370-Tencate Mirafi; geogrid: Tensar, BX-1500). Fig. 3.37 shows a reasonable agreement between the DEM and the experimental results. It is worth

mentioning that the stiffness of a viscoelastic material such as geosynthetics depends on the strain rate (Walters *et al.* 2002). However, the current model used an elastic spring at the contact of two particles (contact-bond model) and the viscoelastic behavior of the geosynthetics was not captured.

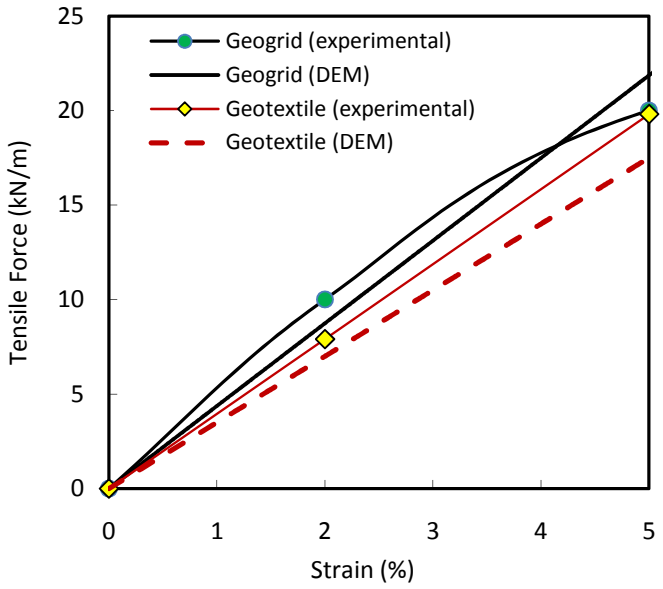

Fig. 3.37 Calibration of the geosynthetics by tension tests

Table 3.3 Micromechanical properties for DEM analysis

Material	Parameters	
Analogical soil	Young's modulus of the particle-particle contact, E_c(MPa)	150
	Ratio of normal to shear stiffness of particles, k_n/k_s	1.2
	Friction coefficient (μ)	0.85
Paper	Young's modulus of the particle-particle contact, E_c (MPa)	1491
	Ratio of normal to shear stiffness of particles, k_n/k_s	1.0
	Parameter of contact bond normal strength, ϕ_n (kN)	4.5
	Parameter of contact bond shear strength, ϕ_s (kN)	4.5
	Friction coefficient (μ)	0.68
Geotextile	Young's modulus of the particle-particle contact, E_c (MPa)	350
	Ratio of normal to shear stiffness of particles, k_n/k_s	1.0
	Parameter of contact bond normal strength, ϕ_n (kN)	47.3
	Parameter of contact bond shear strength, ϕ_s (kN)	47.3
	Friction coefficient (μ)	0.68
Geogrid	Shear stiffness of particles, k_s (MN/m)	2580
	Normal stiffness of particles, k_n (MN/m)	2580
	Friction coefficient (μ)	0.68
	Parameter of contact bond normal strength, ϕ_n (kN)	94.97
	Parameter of contact bond shear strength, ϕ_s (kN)	94.97
	Parallel bond normal stiffness, k_{np} (GN/m^3)	1290
	Parallel bond shear stiffness k_{sp} (GN/m^3)	1290
	Parallel bond normal strength, σ_{np} (MN/m^2)	94.9
	Parallel bond shear strength, σ_{sp} (MN/m^2)	94.9
	Parallel bond radius multiplier, r_{pb}	0.5

CHAPTER FOUR

TRAPDOOR EXPERIMENT AND DEM SIMULATION

This chapter describes the trapdoor experiments using analogical soil and the DEM simulation of these experiments. The trapdoor experiments have been used for a long time to study soil arching mechanisms and also to develop design methodologies for geosynthetic-reinforced earth structures that involve soil arching. However, the influence of geosynthetic reinforcement on soil arching was investigated to a less extent and often simplified in design methodologies; therefore, it deserves further research. In this study, unreinforced and paper-reinforced model embankments were constructed and investigated. The calibrated micromechanical properties of the analogical soil and the paper reinforcement in Chapter 3 were used in the DEM simulation. Simulation of the trapdoor experiments validated the modeling techniques and established a framework to study the soil arching and geosynthetic-soil interaction at a micro scale.

4.1 Equipment Design and Test Procedure

Figure 4.1 shows a model for the trapdoor experiment. The model was 900 mm long, 50 mm wide, and 350 mm high. The model was fabricated with an aluminum frame and Plexiglass on its front and rear walls. The transparent Plexiglass allowed visual observations and pictorial records for further analysis. The model was equipped with seven wooden blocks (127-mm wide), which are moveable as trapdoors independent of each other. Hereafter in this dissertation, these wooden blocks are referred as trapdoors and the trapdoors are numbered from one to seven.

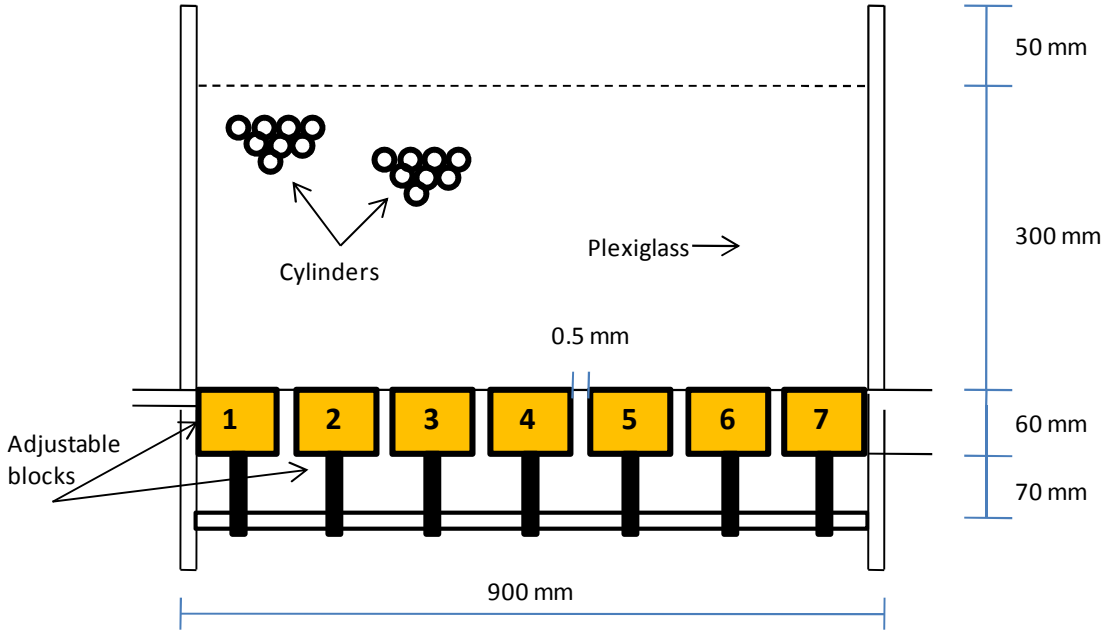

Fig. 4.1 Model of a trapdoor experiment

On top of the trapdoors, analogical soil (aluminum bars) was filled. The aluminum bars had three diameters: 5.6, 12.7, and 19.0 mm. The aluminum bars were placed manually. First the larger diameter bars were placed as desired to obtain the required gradation; the gaps between the larger diameter bars would then be filled using the smaller diameter bars. The gravimetric composition in the mix of the 5.6, 12.7, and 19.0-mm diameter bars were 81, 10, and 9 %, respectively. Different heights of embankments were prepared in this study. For the reinforced cases, paper reinforcement was placed at a height of 25 mm above the trapdoor to support the embankment. Aluminum bars of 5.6 mm in diameter were used as fill between the paper reinforcement and the trapdoor. Strain gauges were glued on the paper reinforcement to measure the strains along the paper. The trapdoor was lowered down at an increment of 2 mm. A digital-still camera was used to take the picture of the model at each stage of the trapdoor movement. These pictures were analyzed using

AUTOCAD software to measure the displacement of aluminum bars at the predefined locations. Suitable grids were drawn on the model to aid this image analysis process (Fig. 4.2). The automatic data acquisition system was used to record the displacements of the trapdoor and the strains in the reinforcement whenever paper reinforcement was used. The details of the experiments are provided in Table 4.1.

Fig. 4.2 Physical model of the analogical soil for the trapdoor study

Table 4.1 Details of the trapdoor experiments

Test No.	Height of embankments (mm)	Trapdoor No.	Reinforcement	H/B ratio
1	185	4	No	1.4
2	260	4	No	2.0
3	185	4	Yes	1.4
4	260	4	Yes	2.0
5	185	3	Yes	1.4
6	185	6	Yes	1.4
7	260	3	Yes	2.0
8	260	6	Yes	2.0

Note: H = height of embankment, B = width of trapdoor (127 mm)

4.2 Experimental Results

For the unreinforced embankments, the displacement measurements are presented. For the reinforced embankments, the displacement and strain measurements of the trapdoor experiments are presented. In most of the experiments, only the maximum vertical displacements were measured. For the trapdoor tests of soil arching interactions, the displacement profiles were also measured.

4.2.1 Unreinforced embankments

Unreinforced embankments of two heights: 185 and 260 mm were constructed. The displacements in the embankments at different stages of No. 4 trapdoor displacement were analyzed using the AUTOCAD software. First the picture of the embankment taken before lowering the trapdoor was imported to the AUTOCAD and the grids were drawn in the same pattern as were marked in the picture to create a template file. The pictures taken during subsequent trapdoor displacements were imported into the template file. The measurement of the perpendicular distances between the template grids and the picture grids obtained the displacements at different heights in the embankment. Note that a minimum displacement of 0.5 mm could be adequately measured using this technique. Any displacement smaller than 0.5 mm remained unnoticed and was insignificant for this particular problem involving large displacements in the embankment.

Figures 4.3 and 4.4 show the maximum vertical displacements in the embankments of H/B ratios at 1.4 and 2.0, respectively. For the embankment of the H/B ratio at 1.4, the vertical displacements of the aluminum bars were measureable above the central trapdoor (No. 4) throughout the embankment height even at a 2 mm displacement of the trapdoor. For the

embankment of the H/B ratio at 2.0, the vertical displacements of the aluminum bars were measureable below a height of 200 mm at a 2 mm displacement of the trapdoor. No displacement of the aluminum bars was measured at the top of the embankment at a 2 mm displacement of the trapdoor. The vertical displacement at the top of the embankments slowly increased with an increase of the trapdoor displacement until the trapdoor was lowered by 10 mm. After 10 mm displacement of the trapdoor, the vertical displacement at the top of the embankment increased rapidly. For the given trapdoor displacement, the maximum vertical displacements at the top of the embankment were smaller for the embankment of the H/B ratio at 2.0 than those for the embankment of the H/B ratio at 1.4.

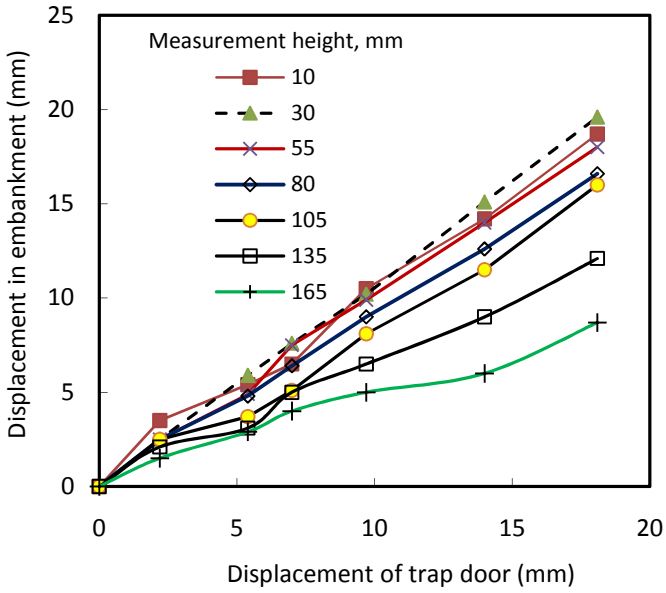

Fig. 4.3 Maximum vertical displacement in embankment vs. displacement of trapdoor (H/B = 1.4)

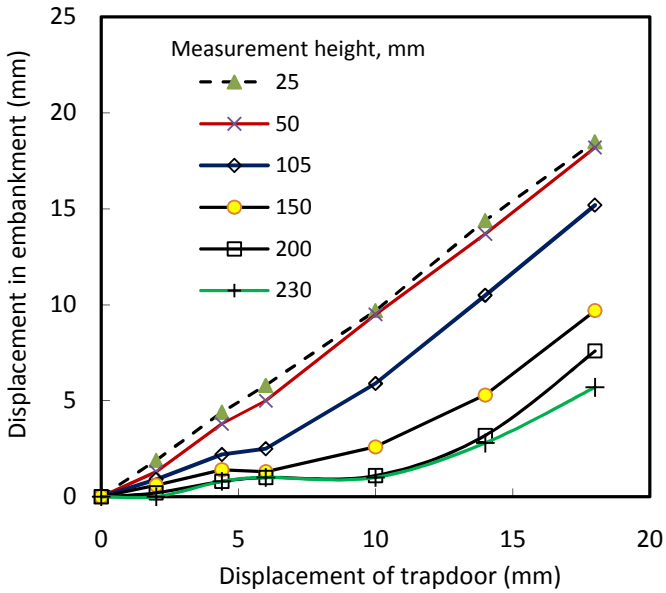

Fig. 4.4 Maximum vertical displacement in embankment vs. displacement of trapdoor (H/B = 2.0)

4.2.2 Reinforced embankments

Reinforced embankments of two heights, 185 and 260 mm, were constructed. The paper reinforcement was placed at 25 mm above the trapdoor. For the 180-mm high embankment (H/B = 1.4), the vertical displacements were measured above the trapdoor at the following heights: 25, 50, 100, 150, and 185 mm. At the heights of 150 and 185 mm, the vertical displacements in the embankment were measurable only after a 3 mm displacement of the trapdoor (Fig. 4.5). The vertical displacement at the height of 185 mm stabilized after the trapdoor displacement of 20 mm. At other intermediate heights (25, 50, 100, and 150 mm), the vertical displacements in the embankments increased with an increase of the displacement of the trapdoor.

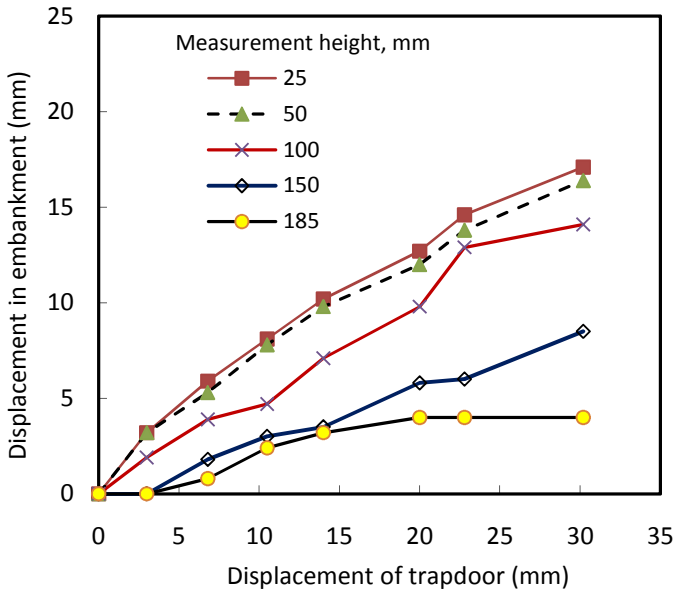

Fig. 4.5 Maximum vertical displacement in the reinforced embankment vs. displacement of the trapdoor (H/B = 1.4)

Using the grids drawn on the aluminum bars, the displacement patterns were traced. At a 3 mm displacement of the trapdoor, the region of movement of the aluminum bars could be delineated by a triangle from the rest of the embankment (Fig. 4.6 a). Therefore, the shape of the soil arch was triangular at this stage. The picture taken at a 14 mm displacement of the trapdoor clearly showed a gap between the paper reinforcement and the underlying aluminum bars above the trapdoor (Fig. 4.6 b). Further displacement of the trapdoor increased the gap between the paper and the aluminum bars but caused minimum disturbance to the embankment. It is interesting to note the change in the shape of the displacement region of aluminum bars when the displacement of the trapdoor increased from 3 mm to 14 mm. The triangular arch opened wider and extended higher to the top of the embankment with a trapezoid displacement pattern. Therefore, soil arching formed at different stages with different displacement patterns and changed with the displacement of the trapdoor. In the centrifuge tests, Costa *et al.* (2009) observed similar patterns of soil

arching and characterized the soil arching at a small displacement as an internal failure and that at a large displacement as an external failure.

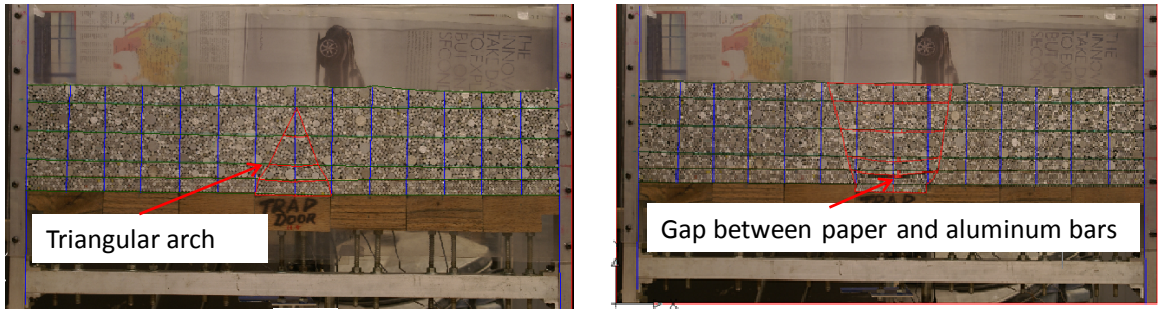

a) b)

Fig. 4.6 Reinforced embankments at (a) 3mm and (b) 14 mm displacements of the trapdoor (H/B = 1.4)

Figure 4.7 shows the maximum vertical displacements in the reinforced embankment at different stages of the trapdoor displacement in the fourth test (H/B = 2.0) listed in Table 4.1. The maximum vertical displacements were measured above the trapdoor at the following heights: 25, 50, 100, 150, 200, and 245 mm. With the onset of trapdoor displacement, the vertical displacements in the embankment were measurable at and smaller than 150 mm. A 2.5 mm displacement of the trapdoor was necessary to induce the vertical displacement in the embankment at a height of 200 mm above the trapdoor. Similar to the third test, the soil arching was triangular in shape at a small displacement and opened wider and extended higher with an increase of the displacement of the trapdoor.

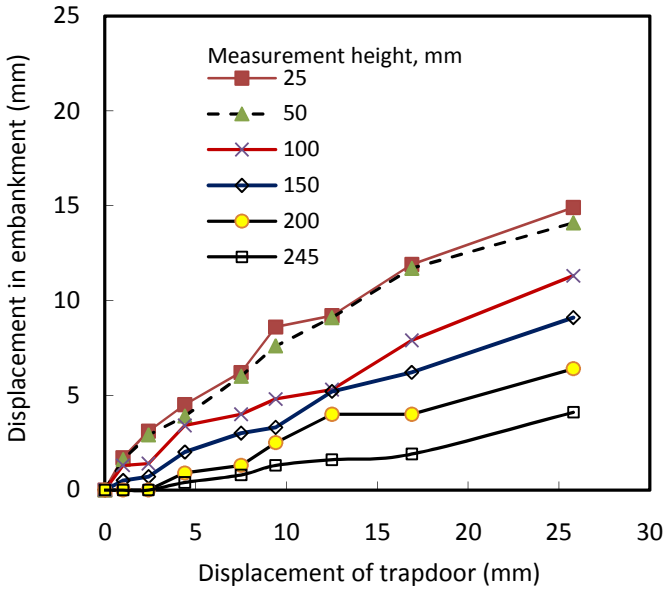

Fig. 4.7 Maximum vertical displacement in the reinforced embankment vs. displacement of the trapdoor (H/B = 2.0)

In the third test (H/B=1.4), four strain gauges were glued to the paper reinforcement and marked as C-450, R1-515, R2-580, and R3-640; the numbers indicated the location of strain gauges (in mm) measured from the left end of the test box and the letters indicated the position of the strain gauges relative to the trapdoor being lowered (C = Central, R = Right). The strain gauge (C-450) located over the center of the trapdoor measured the lowest strain. On the other hand, the strain gauge (R1-515) located over the edge of the trapdoor measured the highest strain (Fig. 4.8). Figure 4.9 shows the strain development in the paper reinforcement at different stages of trapdoor displacement. The strains in the paper reinforcement increased almost linearly up to a 15 mm displacement of the trapdoor. Thereafter, the strains in the paper reinforcement stabilized or increased slowly except R3-640. At this stage of the trapdoor displacement, the redistribution of stresses in the embankment completed. However, a lateral movement of the aluminum bars below the

paper reinforcement was observed. This lateral movement of the aluminum bars must have contributed to an additional strain in the reinforcement after the formation of the gap between the paper reinforcement and the underlying aluminum bars above the trapdoor.

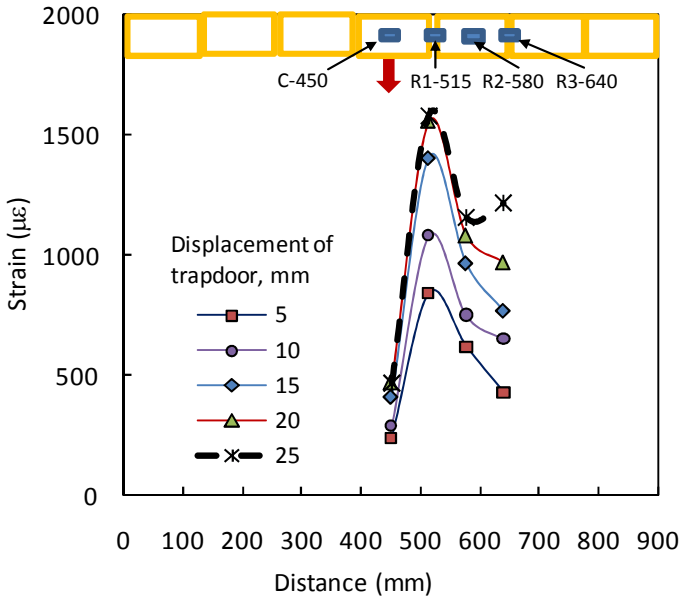

Fig. 4.8 Development of strain along the paper reinforcement (H/B = 1.4)

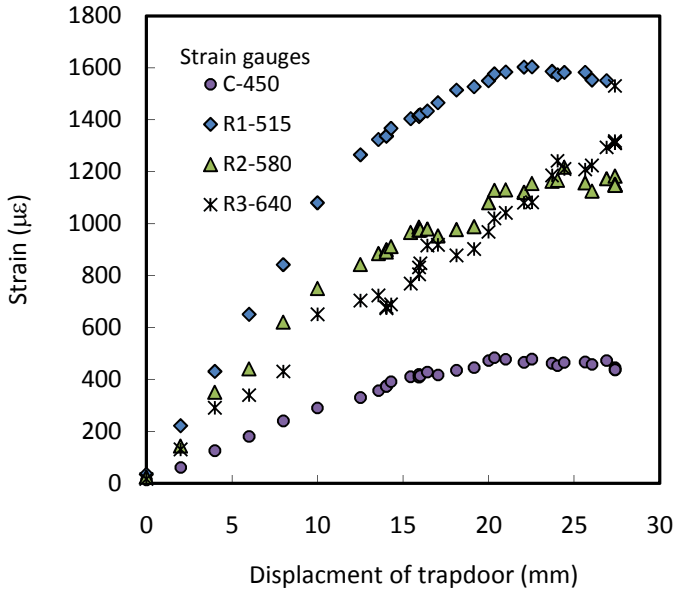

Fig. 4.9 Strain vs. displacement of trapdoor (H/B = 1.4)

Similar to the third test, four strain gauges were used in the fourth test (H/B = 2.0) but the strain gauges were glued at different locations. Accordingly, the strain gauges were named as L- 388, C-450, R1-515, and R2-580 and are shown in Fig. 4.10. The locations of strain gauges were deliberately changed in this experiment to maximize the information using the least possible strain gauges. Figure 4.10 shows the strain development along the paper reinforcement at different stages of the trapdoor displacement. Similar to the third test, the maximum strain developed next to the trapdoor edge and the minimum strain developed over the center of the trapdoor. The strain gauges installed on the paper reinforcement over both edges of the trapdoor measured similar strains since the No. 4 trapdoor, lowered in this test, was located at the center of the model. The strains in the paper reinforcement stabilized after a 10 mm displacement of the trapdoor.

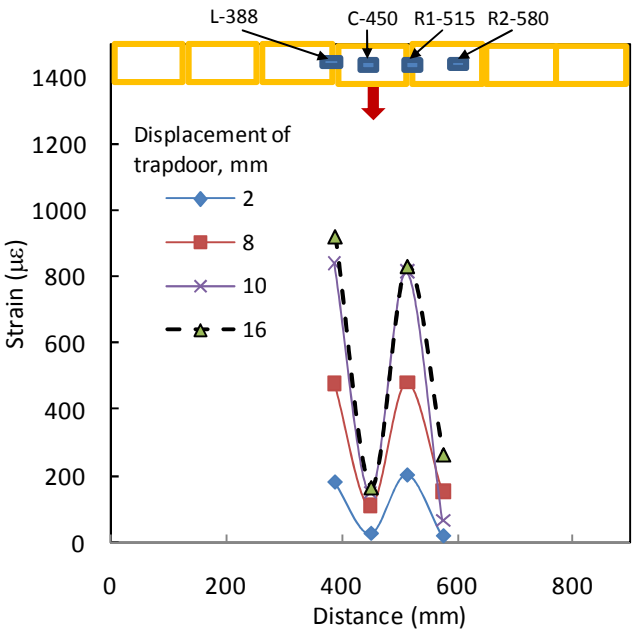

Fig. 4.10 Development of strains along the paper reinforcement (H/B = 2.0)

Smaller strains developed in the paper reinforcement for the embankment at H/B ratio of 2.0 than those in the embankment at H/B ratio of 1.4. Also smaller trapdoor displacement was required for the fourth test (H/B = 2.0) to achieve stable strains along the paper reinforcement compared to the third test (H/B = 1.4). For a same level of displacement of the aluminum bars, higher shear stress develops at the yielding (arch) zone for the embankment at H/B ratio of 2.0 than the embankment at H/B ratio of 1.4 which must be the reason for a stable strain at a smaller trapdoor for the fourth test (H/B = 2.0).

4.2.3 Interaction of soil arching

As demonstrated in the previous section, at a large trapdoor displacement, the region of displacement in the embankment extended beyond the vertical plane of the trapdoor. When two or more trapdoors are spaced closely and lowered, they may induce interaction between the neighboring regions of displacement. This interaction was evaluated for the two embankments at different heights (H/B = 1.4 and 2.0). To investigate this interaction, the trapdoors No. 3 and 6 were chosen. Note that the trapdoors No. 3 and 6 were located asymmetrical to the vertical centerline of the embankment. In these interaction tests, the No. 3 trapdoor was lowered first and then followed by lowering the No. 6 trapdoor. Subsequently, the interaction tests involving the No. 3 trapdoor were called Part 1 trapdoor test and the interaction tests involving the No. 6 trapdoor were called Part 2 trapdoor test. The fifth and sixth tests listed in Table 4.1 were one interaction test while the seventh and eighth tests were another interaction test.

Figures 4.11 and 4.12 show the maximum vertical displacements in the embankment at different stages of the interaction test for the embankment with H/B = 1.4. Similar to the previous observations for a single trapdoor test, the displacement at the top of the

embankment was measurable after a 3 mm displacement of the trapdoor and stabilized when the trapdoor displacement was between 10 to 15 mm. At other measurement heights the displacements in the embankment increased with an increase of the trapdoor displacement. After a trapdoor displacement of 15 mm, partial collapse of the aluminum bars between the paper reinforcement and the trapdoor was observed that filled the voids and caused the increased vertical displacement throughout the embankment.

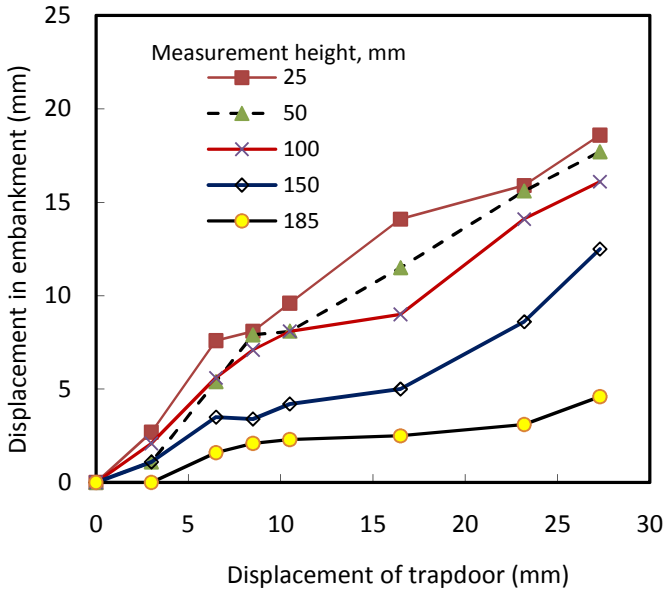

Fig. 4.11 Maximum vertical displacement in the embankments vs. displacement of the trapdoor in the fifth test (H/B = 1.4)

Figure 4.13 shows the displacement profiles at different heights in the embankment during Parts 1 and 2 trapdoor test for the embankment at H/B ratio of 1.4. The displacement profile shows that the embankment displacement in the Part 1 trapdoor test (i.e., the fifth trapdoor test) were not affected by the displacements of the Part 2 trapdoor test (i.e., the sixth trapdoor test.

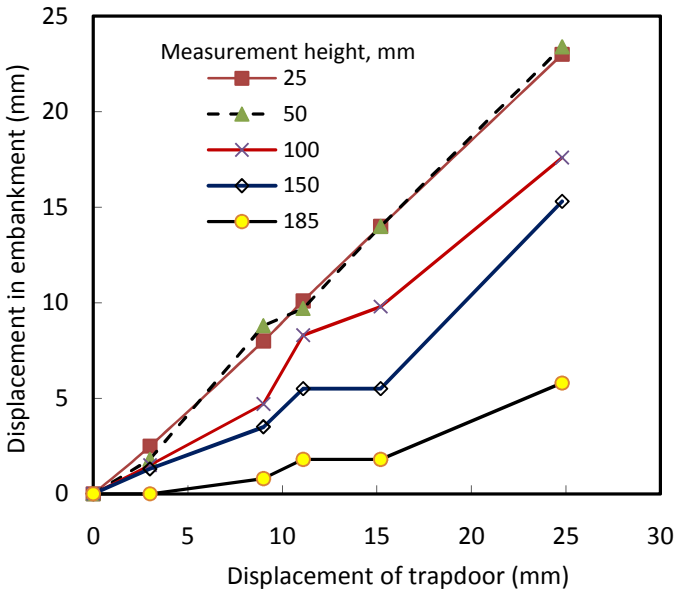

Fig. 4.12 Maximum vertical displacement in the embankments vs. displacement of the trapdoor in the sixth trapdoor test (H/B = 1.4)

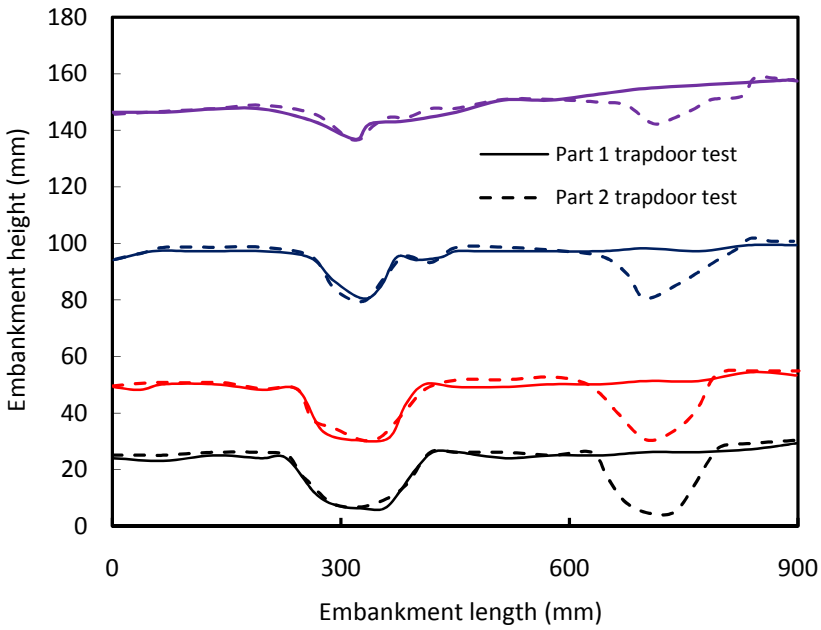

Fig. 4.13 Displacement profiles in the interaction tests (H/B = 1.4)

Figures 4.14 and 4.15 show the displacements in the embankment (H/B = 2.0) at different stages of the trapdoor interaction test including the seventh and eighth trapdoor tests. 3-mm trapdoor displacement was required to cause any displacement at the top of the embankments, which stabilized after reaching 5 to 10 mm.

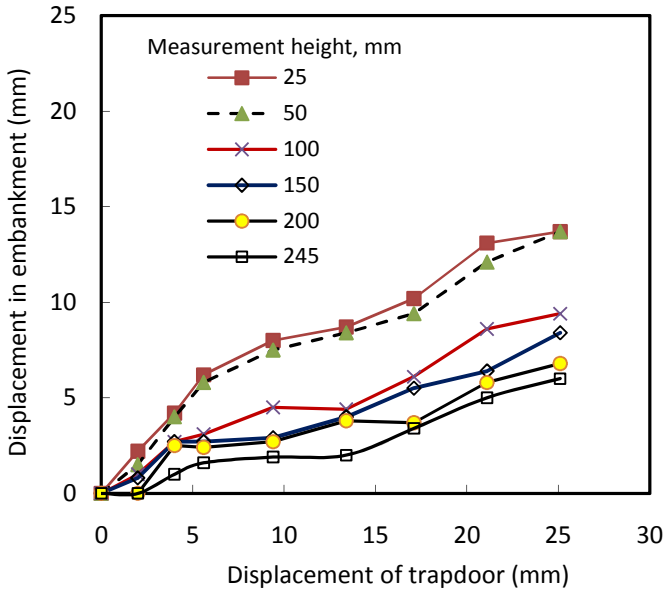

Fig. 4.14 Displacement in the embankment vs. displacement of the trapdoor in the seventh trapdoor test (H/B = 2.0)

Figure 4.16 shows the displacement profiles at different heights in the embankment during Parts 1 and 2 trapdoor test for the embankment at H/B ratio of 2.0. The embankment displacements in the Part 1 trapdoor test (i.e., the seventh trapdoor test) were not affected by the displacements of the Part 2 trapdoor test (i.e., the eighth trapdoor test). In these tests, the width of the trapdoor was 127 mm and the spacing between the third and sixth trapdoor was 254 mm. Therefore, it can be concluded that the formations of soil arching as the consequences of the Nos. 3 and 6 trapdoor displacement were not interacting.

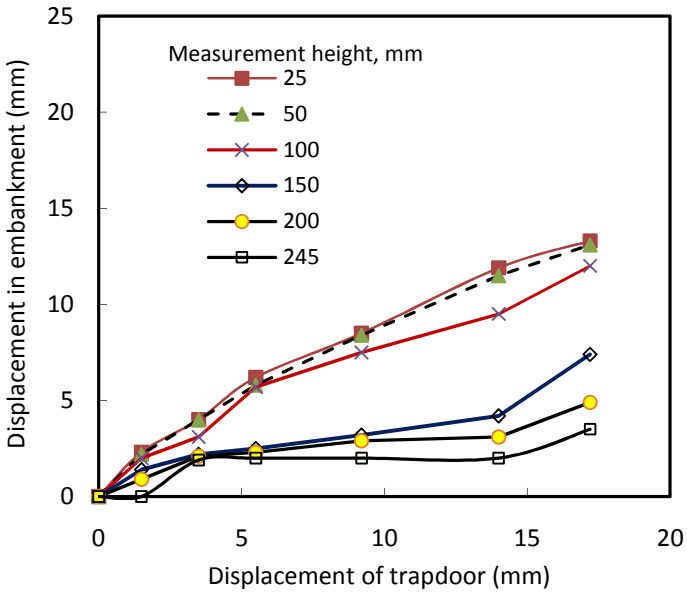

Fig. 4.15 Maximum vertical displacement in the embankment vs. displacement of the trapdoor in the eighth trapdoor test (H/B = 2.0)

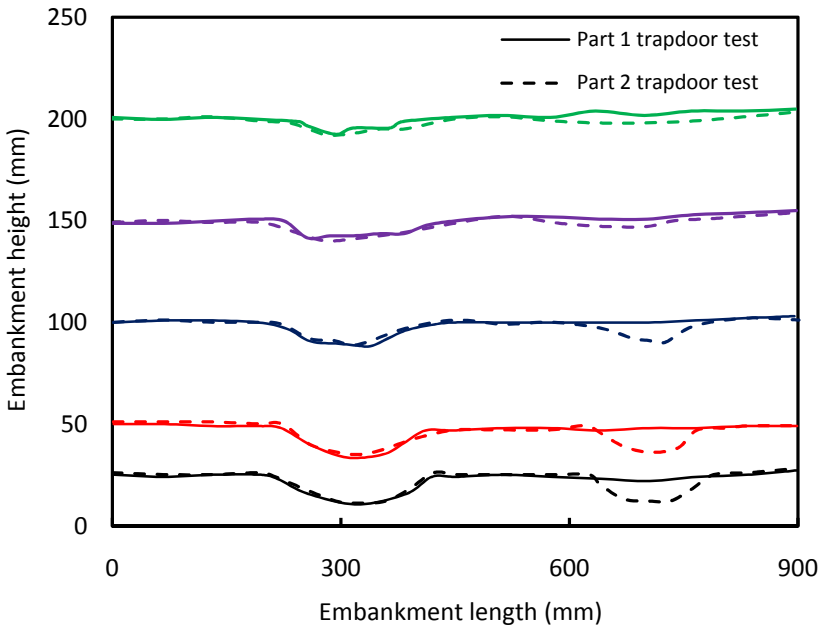

Fig. 4.16 Displacement profiles in the interaction tests (H/B = 2.0)

Figures 4.17 and 4.18 show the development of strain in the paper reinforcement with the trapdoor displacement in the fifth trapdoor test (Part 1 trapdoor test) for the embankment at H/B ratio of 1.4. Six strain gauges were glued at the distances of 320, 380, 440, 570, 630, and 700 mm from the left end of the test box. The strains in the paper reinforcement stabilized after 10 mm trapdoor displacement. A minimum strain of 466 με developed in the paper reinforcement over the center of the trapdoor when the trapdoor displacement reached 8 mm and larger. A maximum strain of 1760 με developed in the paper reinforcement next to the No. 3 trapdoor edge. The minimum and maximum strains were 17% and 10% higher than the corresponding measurements in the third test. Higher strains in this test were justified based on the location of the trapdoor. Had there been the strain gauges on the left side of the No. 3 trapdoor, less strains would be recorded since a shorter anchorage length was available on the left side of the No. 3 trapdoor.

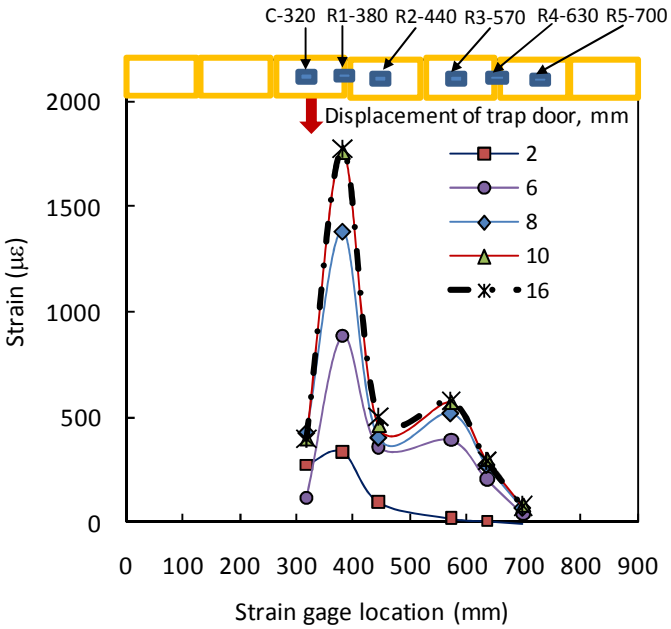

Fig. 4.17 Development of strain along the paper reinforcement in the fifth trapdoor test (H/B = 1.4)

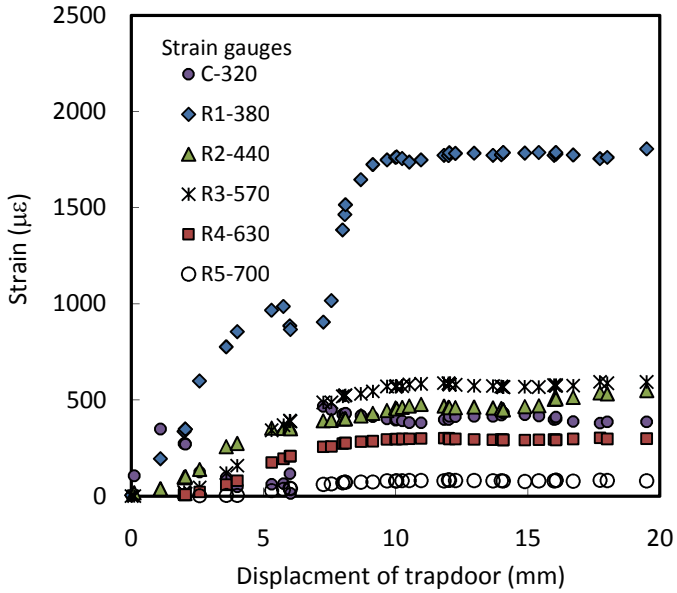

Fig. 4.18 Strain in the paper reinforcement vs. displacement of the trapdoor in the fifth trapdoor test (H/B = 1.4)

Figures 4.19 and 4.20 show the development of strains in the paper reinforcement in the sixth trapdoor test (Part 2 trapdoor test) for the embankment at H/B ratio of 1.4. Strains remained practically constant in Gauges C-320, R1-380, and R2-440 when No. 6 trapdoor was lowered. Significant strains developed next to the lowered trapdoor (No. 6) edge (Gauge R4-630). The level of the strain in the paper reinforcement depended on the pullout capacity of the paper which was limited on the right side of the No. 6 trapdoor because of a short anchorage length. Therefore, a significant strain developed in the paper reinforcement over the left edge due to load transfer. The strain was released with further displacement of No. 6 trapdoor which led to a complete anchorage failure from the right side of the embankment. Gauges R3-570 and R5-700 also experienced strain changes when No. 6 trapdoor was lowered, albeit at a slow pace. The strain gauge measurements

in Figs. 4.19 and 4.20 suggested that the displacement of No. 6 trapdoor had a marginal effect on the strains in the paper reinforcement above No. 3 trapdoor.

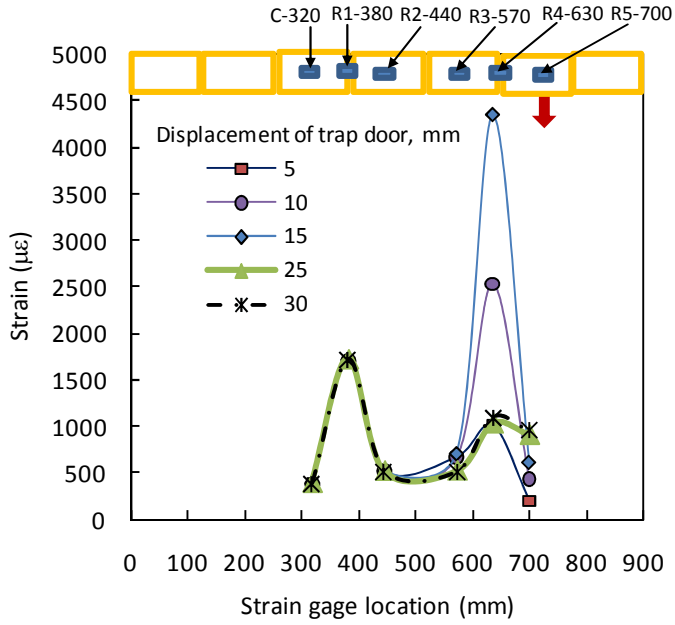

Fig. 4.19 Development of strain along the reinforcement in the sixth trapdoor test (H/B = 1.4)

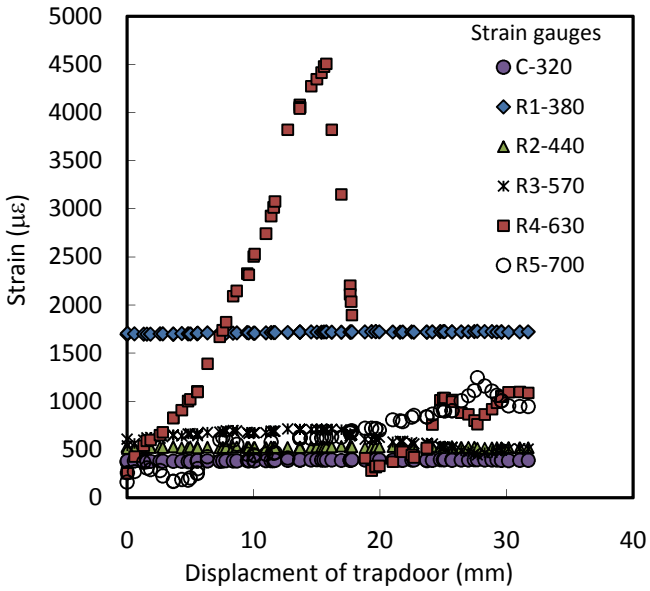

Fig. 4.20 Strain in the paper reinforcement vs. displacement of the trapdoor in the sixth trapdoor test (H/B = 1.4)

Figures 4.21 and 4.22 show the development of strain in the paper reinforcement with the trapdoor displacement in the seventh trapdoor test (Part 1 trapdoor test) for the embankment at H/B ratio of 2.0. Six strain gauges were glued at the distances of 320, 380, 440, 570, 630, and 700 mm from the left end. The strains in the paper reinforcement stabilized after 7 mm trapdoor displacement. A minimum strain of 320 με developed in the paper reinforcement over the center of the trapdoor when the trapdoor moved 8 mm and more. A maximum strain of 1110 με developed in the paper reinforcement next to the trapdoor edge. The minimum and maximum strains were higher than the corresponding measurements in the fourth trapdoor test. The difference in the available anchorage lengths of the paper reinforcement on the left side of the lowered trapdoors were the reason behind these strain variations. The maximum strain in this test (H/B = 2.0) was 63% of the maximum strain in the fifth trapdoor test (H/B = 1.4).

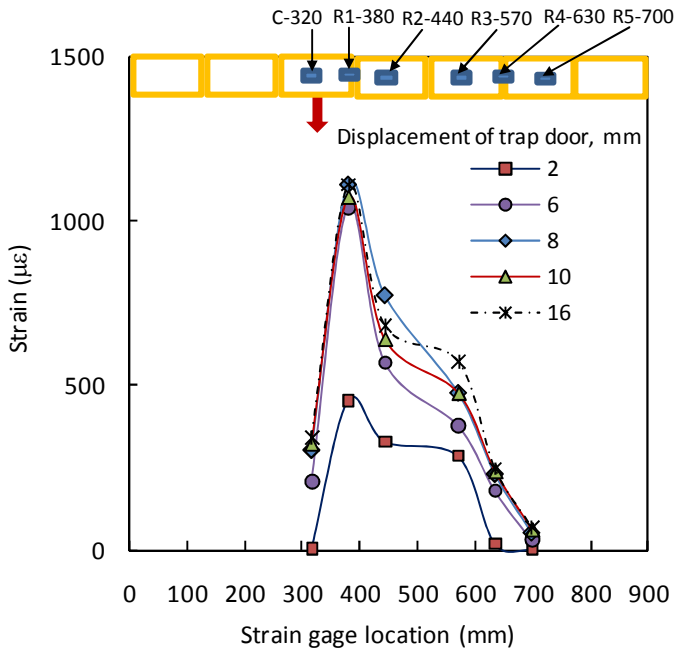

Fig. 4.21 Development of strain along the reinforcement in the seventh trapdoor test (H/B = 2.0)

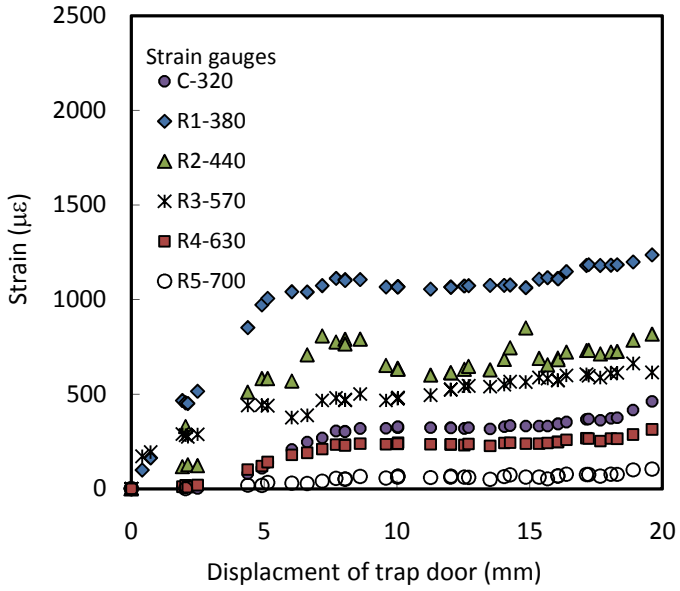

Fig. 4.22 Strain in the paper reinforcement vs. displacement of the trapdoor in the seventh trapdoor test (H/B = 2.0)

Figures 4.23 and 4.24 show the development of strain in the paper reinforcement in the eighth trapdoor test (Part 2 trapdoor test) for the embankment at H/B ratio of 2.0. The strains in the paper reinforcement remained practically constant in Gauges R1-380 and R2-440 when No. 6 trapdoor was lowered. A peak strain developed next to the trapdoor edge on the left side (Gauge R4-630) when No. 6 trapdoor was lowered down by 7 mm. It is worth noting the difference in the peak strains in this trapdoor test (H/B = 2.0) and the sixth trapdoor test (H/B = 1.4). Although the anchorage lengths were same for these two tests, the overburden stresses were different due to different embankments heights. For a given material and interface properties, pullout capacity of a reinforcement is a function of the overburden stress. Higher pullout capacity of the paper reinforcement available on the right part of the No. 6 trapdoor governed the peak strain on the paper reinforcement. The peak strain released with further displacement of the trapdoor because of the anchorage failure from the right side of the embankment. Gauges R3-570 and R5-700 also experienced strain changes when No. 6 trapdoor was lowered, albeit at a slow pace. The

strain gauge measurements in Figs. 4.23 and 4.24 suggested that the displacement of No. 6 trapdoor had a marginal effect on the strains in the paper reinforcement above No. 3 trapdoor.

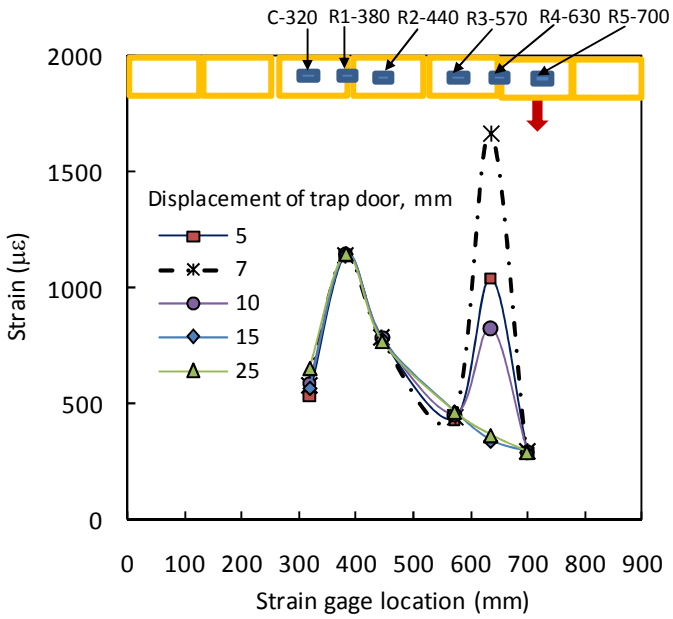

Fig. 4.23 Development of strain along the reinforcement in the eighth trapdoor test (H/B = 2.0)

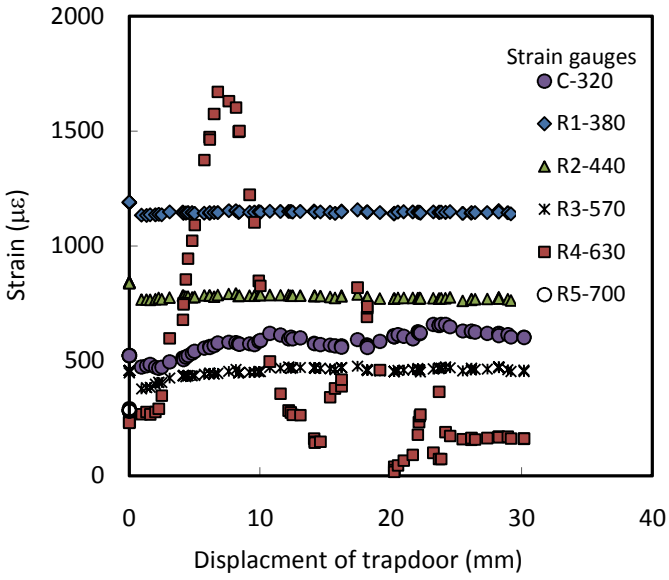

Fig. 4.24 Strain in the paper reinforcement vs. displacement of the trapdoor in the eighth trapdoor test (H/B = 2.0)

4.3 Numerical Model Preparation

The numerical DEM model of each trapdoor test was developed according to the dimensions of the corresponding physical model (900 mm in length and a variable height). Two horizontal walls and two vertical walls were created first for the test box. For the paper-reinforced cases, two additional horizontal walls were created at the elevation of the paper reinforcement to facilitate the generation of bonded particles representing the paper. Seven trapdoors were created using four walls for each trapdoor. The group of four walls representing a single trapdoor can be lowered down at a prescribed velocity to simulate a trapdoor experiment.

Enclosed inside the four model walls, 19.0-mm and 12.7-mm particles were generated at the locations identical to those in each physical experiment. Then smaller particles (5.6-mm in diameter) were randomly generated filling the embankment to achieve a required porosity. The porosities of the embankments in the physical models were measured using the image analysis technique in AUTOCAD. Though there were minor variations in the porosity within the embankments, a porosity of 0.16 was the most representative and was selected for the generation of smaller particles in the numerical modeling. Figure 4.25 shows the comparison between the physical and numerical models. The numerical model of the embankment prepared using this approach also contained local variations in the porosity. Using twenty-eight measurement circles, the local variations in the porosity of the numerical model were recorded. Figure 4.26 shows the contours of these porosities. The average porosities were 0.148 for the embankment at H/B ratio of 1.4 and 0.155 for the embankment at H/B ratio of 2.0.

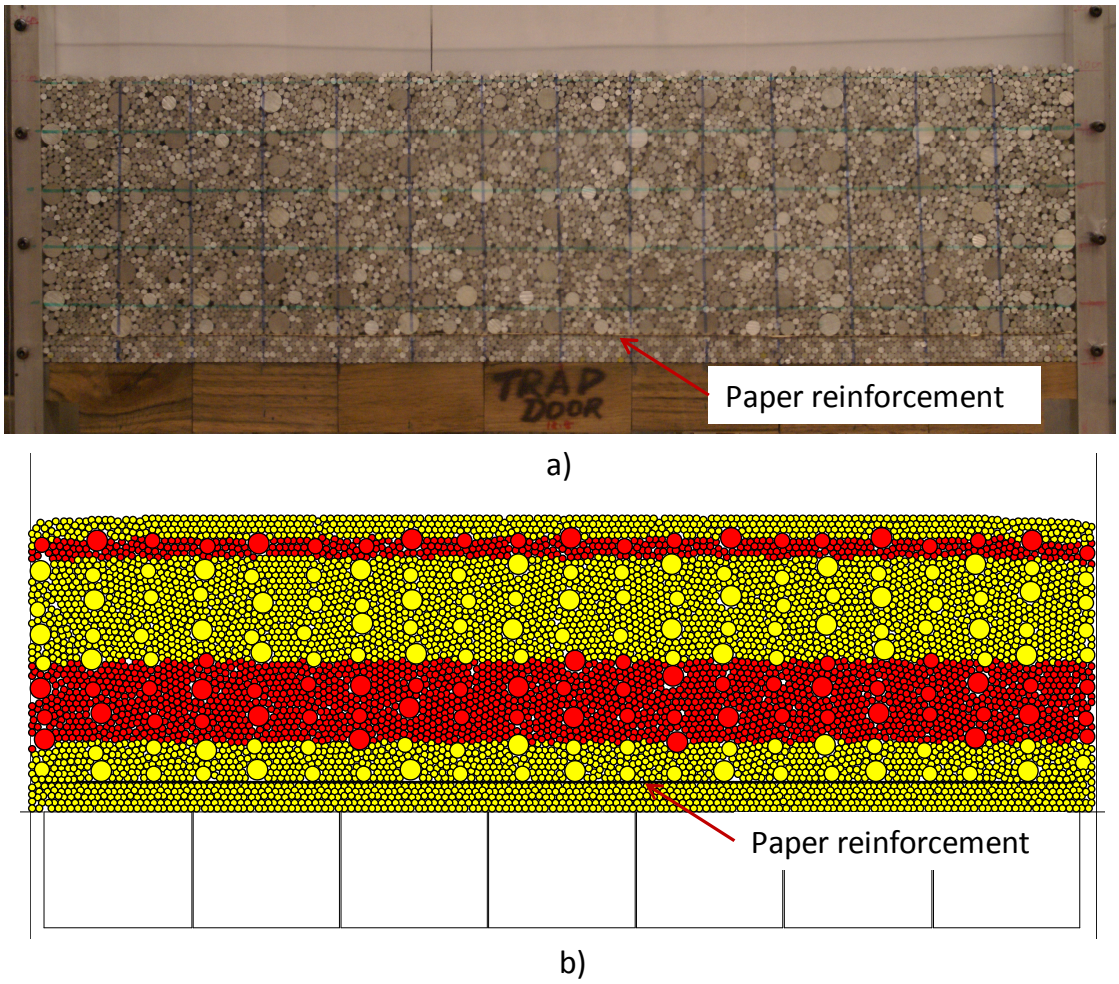

Fig. 4.25 Embankment models (H/B = 2.0): a) physical model and b) numerical model

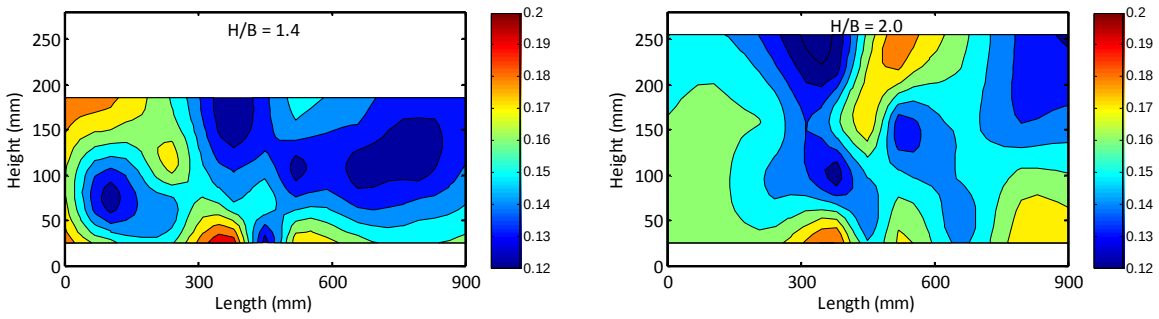

Fig. 4.26 Contours of porosity in the embankments

The calibrated micromechanical parameters of the aluminum bars and the paper reinforcement summarized in Table 3.3 were used in this study. To ensure a legitimate initial stress condition, the vertical walls were moved in the opposite directions using the numerical servo mechanism until the desired lateral wall force (equal to the lateral earth thrust at the earth pressure coefficient of 0.5) was attained. After achieving the initial stress condition, the paper reinforcement was placed by generating the bonded particles inside the guided walls and then the walls were deleted. The coefficient of friction for the particles representing the paper was set to a low value of 0.01 to minimize the frictional interaction between the paper and the aluminum bars while applying the gravitational field. This step was necessary to avoid a tension build-up in the paper reinforcement before lowering the trapdoor. When the whole system achieved the equilibrium (when the ratio of maximum unbalanced force to the maximum contact force reached the value of 0.01) under the gravitational field, the coefficient of friction for the particles representing the paper reinforcement was re-set to 0.68. The displacements of all particles were set to zero.

After the completion of the model preparation, the desired trapdoor was lowered using a velocity-controlled displacement of the walls. The wall velocity was 0.02 m/step and the time step for the simulation was 2.4E-7. For 2 mm wall displacement, 4.17E5 cycles were needed. When the walls reached an incremental displacement of 2 mm, the system was brought to the equilibrium and the coordinates of all particles were stored for the calculations of displacements and strains. This procedure was continued until the trapdoor was lowered by 26 mm.

4.3.1 Displacement field

Figure 4.27 shows the contours of the vertical displacements in the paper-reinforced embankment at H/B ratio of 1.4 at different stages of the No. 4 trapdoor displacement. The contours were plotted at an interval of 1 mm. In general, the numerical results were consistent with the experimental results presented in the previous section. At a small trapdoor displacement, only a portion of the embankment below a height of 125 mm underwent displacements. With an increase of the trapdoor displacement, the zones of the soil movement within the embankment extended higher and wider. Similar to the experimental results shown in Fig. 4.5, the maximum vertical displacement in the embankment was 10 mm at the elevation of the paper reinforcement when the trapdoor displacement was 14 mm.

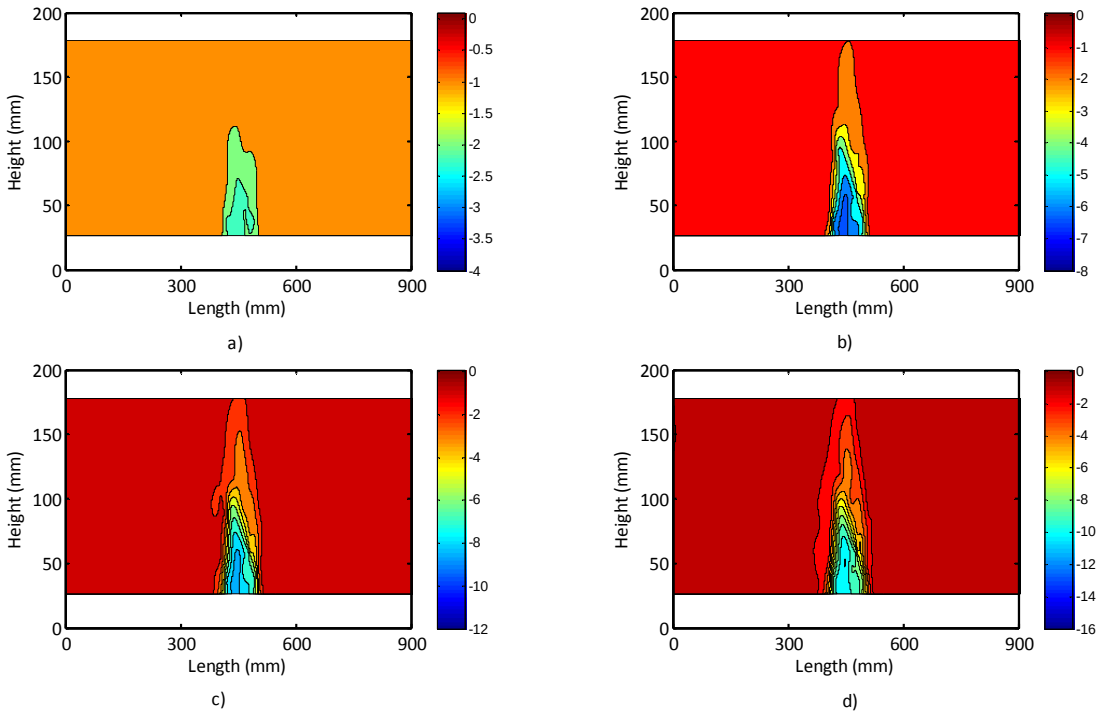

Fig. 4.27 Contours of vertical displacements (mm) within the reinforced embankment (H/B = 1.4) due to the No. 4 trapdoor displacements of a) 2 mm b) 6 mm c) 10 mm d) 14 mm

Figure 4.28 shows the contours of the horizontal displacements in the reinforced embankment at H/B ratio of 1.4 at different stages of the No. 4 trapdoor displacement. The horizontal displacements of the aluminum bars were not measured in the experiments, however, they could be computed in the numerical simulation and are presented herein for the completeness of the simulation results. The horizontal displacement vectors (positive values) on the left half of the embankment were pointing towards right and the horizontal displacement vectors (negative values) on the right half of the embankment were pointing towards left. The contours in Fig. 4.28 are nearly symmetrical indicating equal but opposite horizontal displacements of the particles about the vertical centerline of the embankment.

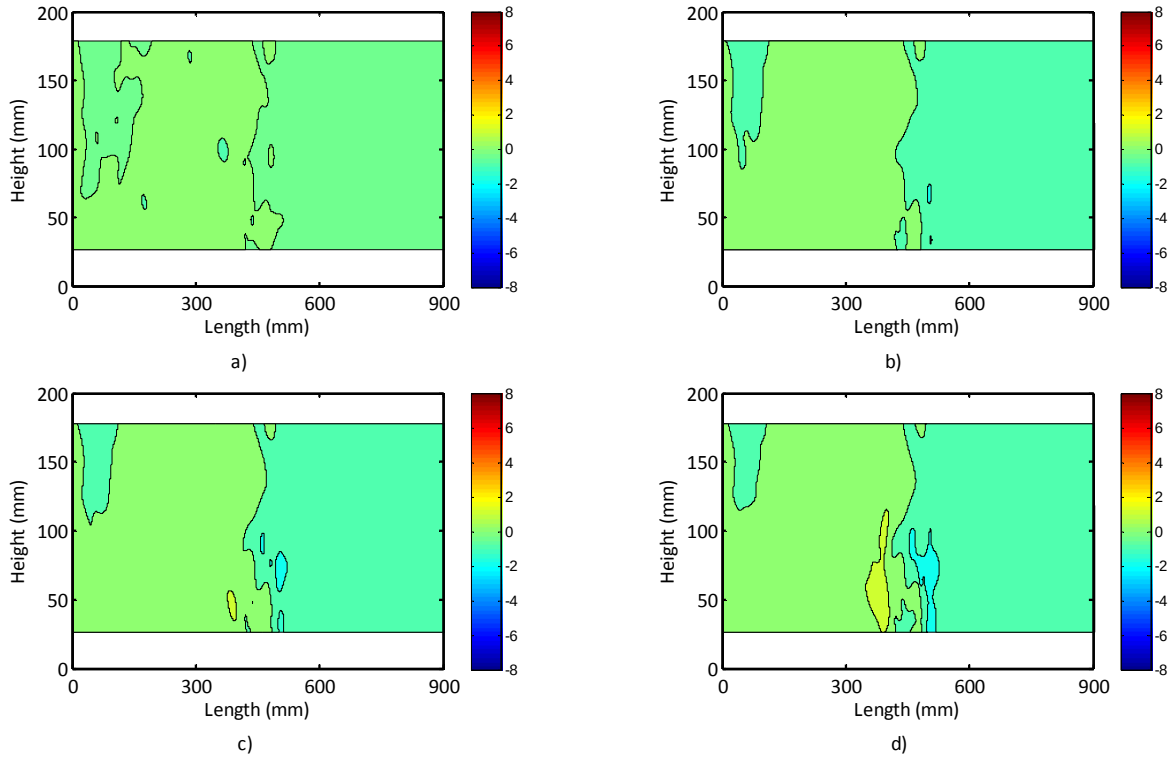

Fig. 4.28 Contours of horizontal displacements (mm) within the reinforced embankment (H/B = 1.4) due to the No. 4 trapdoor displacements of a) 2 mm b) 6 mm c) 10 mm d) 14 mm

Figure 4.29 shows the contours of the vertical displacements in the embankment at H/B ratio of 2.0 at different stages of the No. 4 trapdoor displacement. The vertical displacements obtained from the simulation results were smaller than those measured in the experiments. The horizontal displacements in this case (Fig. 4.30) were also smaller than those of the embankment at H/B ratio of 1.4 (Fig. 4.28). Unlike those in the experiments, the vertical displacements in the DEM simulation were limited to the height of 160 mm. This discrepancy between the experimental and DEM simulation results needs further research.

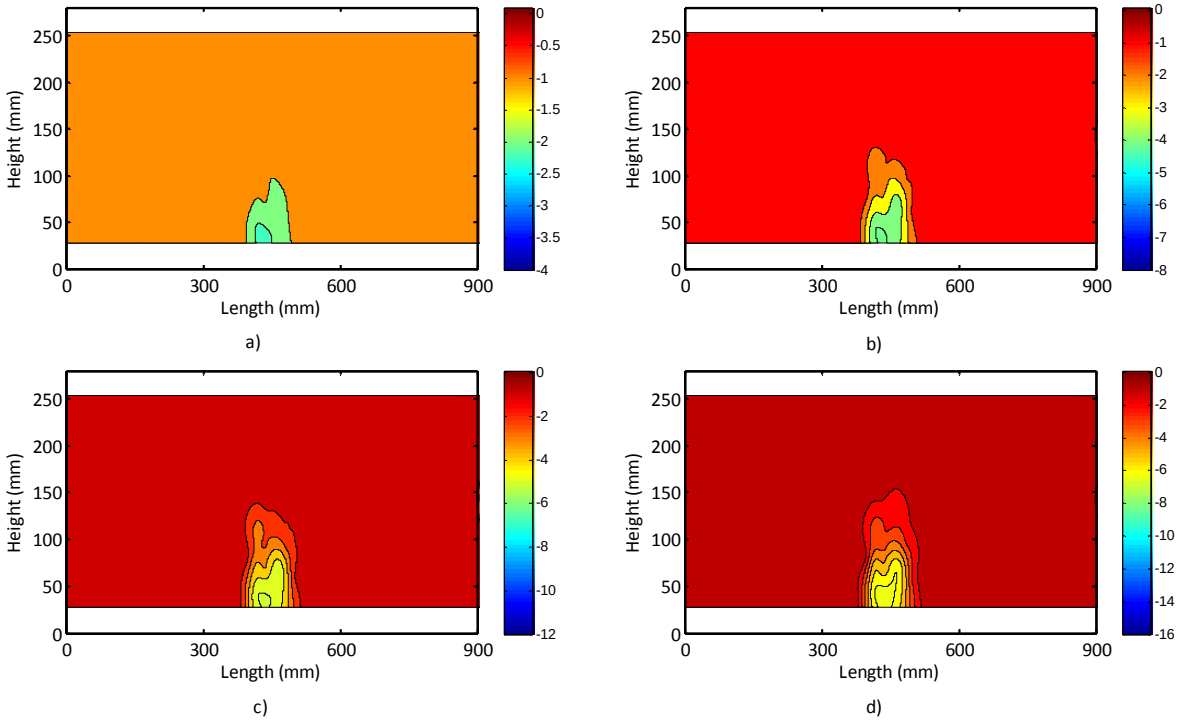

Fig. 4.29 Contours of vertical displacements (mm) within the reinforced embankment (H/B = 2.0) due to the No. 4 trapdoor displacements of a) 2 mm b) 6 mm c) 10 mm d) 14 mm

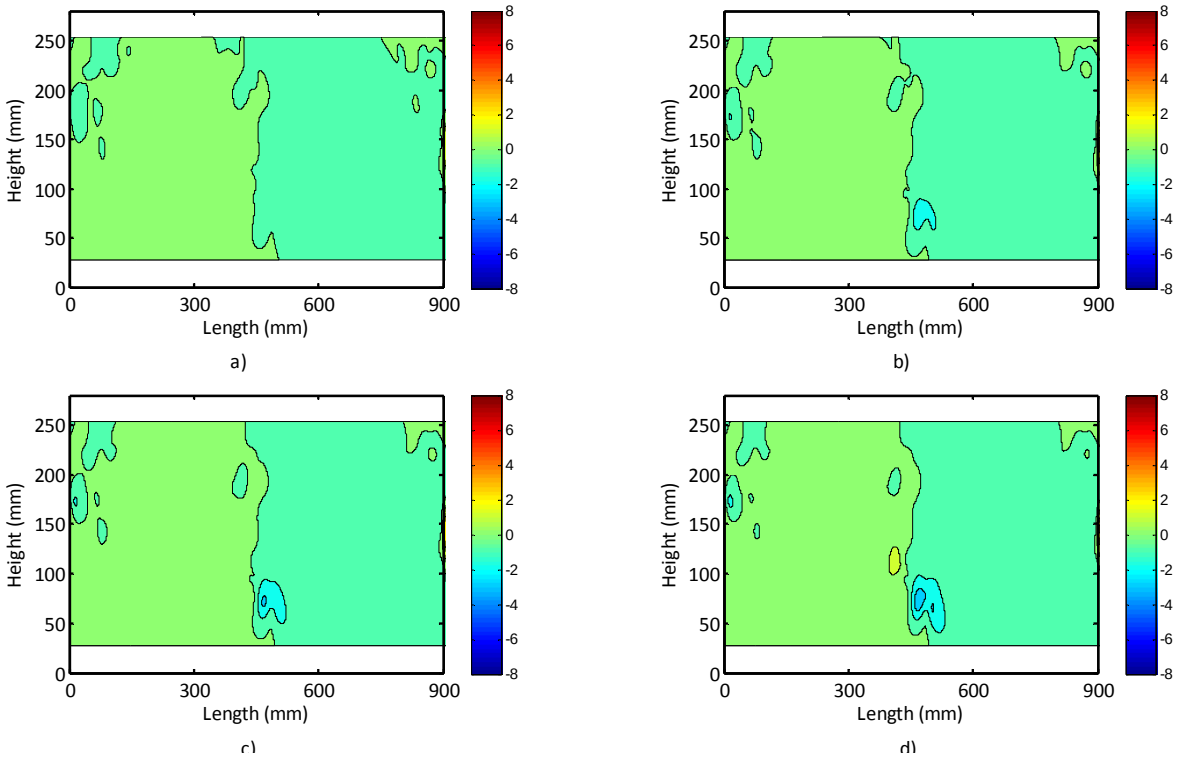

Fig. 4.30 Contours of horizontal displacements (mm) of the reinforced embankments (H/B = 2.0) due to the No. 4 trapdoor displacements of a) 2 mm b) 6 mm c) 10 mm d) 14 mm

Figures 4.31 shows the contours of the vertical displacements in the embankment at H/B ratio of 1.4 at different stages of the trapdoor displacement in the first part of the interaction test simulation. The simulation results were consistent with the experiment (i.e., the fifth trapdoor test) discussed in the previous section. At a small trapdoor displacement (2 mm), only a portion of the embankment below a height of 140 mm underwent displacements. With an increase of the trapdoor displacement, the contours extended higher and wider. The comparison of the contours in Figs. 4.27 and 4.31 shows that the vertical displacements of the particles in this test were slightly smaller than those in the single trapdoor test (the trapdoor was lowered in the center). The difference may result

from the variation of the particle arrangement during the sample preparation in the DEM simulation.

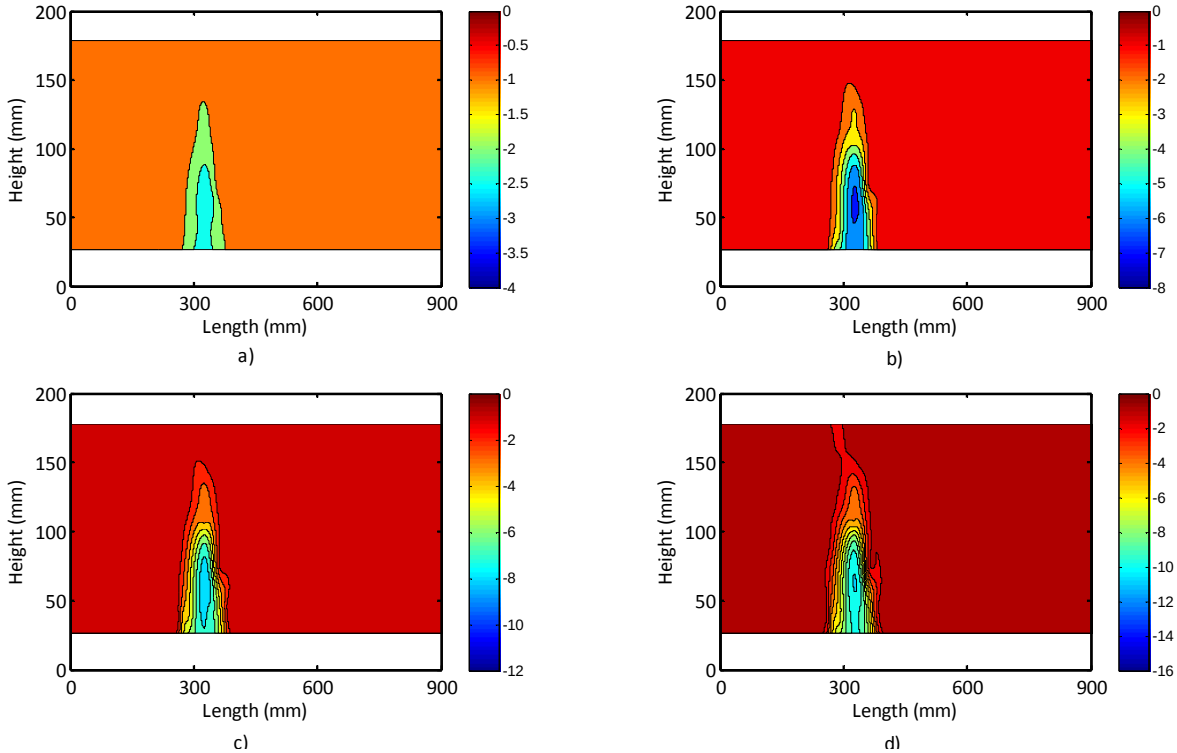

Fig. 4.31 Contours of vertical displacements (mm) in the reinforced embankment (H/B = 1.4) due to the No. 3 trapdoor displacements of a) 2 mm b) 6 mm c) 10 mm d) 16 mm

Figures 4.32 shows the contours of the horizontal displacements in the embankment at H/B ratio of 1.4 at different stages of the trapdoor displacement in the first part of the interaction test simulation. The contours of the horizontal displacements in Fig. 4.32 were almost symmetrical about the vertical centerline of the No. 3 trapdoor which was lowered.

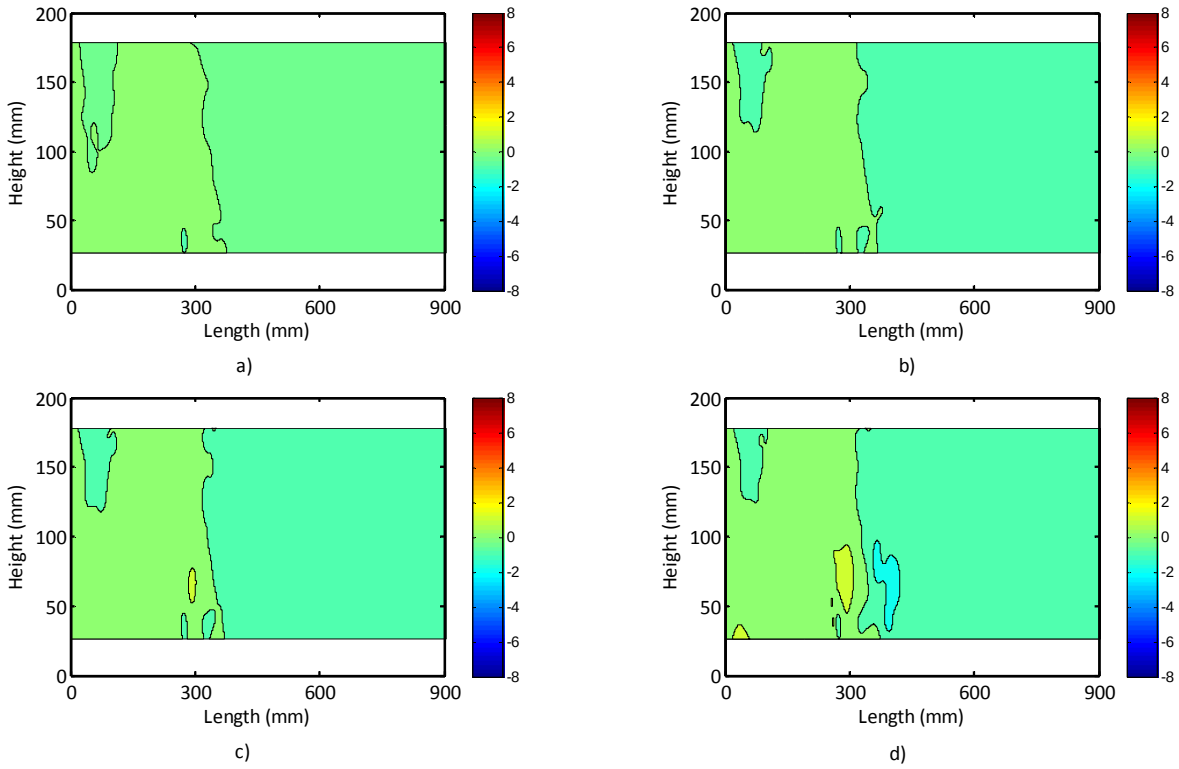

Fig. 4.32 Contours of horizontal displacements (mm) in the reinforced embankment (H/B = 1.4) due to the No. 3 trapdoor displacements of a) 2 mm b) 6 mm c) 10 mm d) 16 mm

Figure 4.33 shows the contours of the vertical displacements in the embankment at H/B ratio of 1.4 at different stages of the trapdoor displacement in the second part of the interaction test simulation. The contours of the vertical displacements extended above the lowered trapdoor (No. 6) without any distinct evidence of interaction with the displacement zone induced by lowering the No. 3 trapdoor (Part 1 trapdoor test). This finding is similar to that from the experimental study discussed in the previous section.

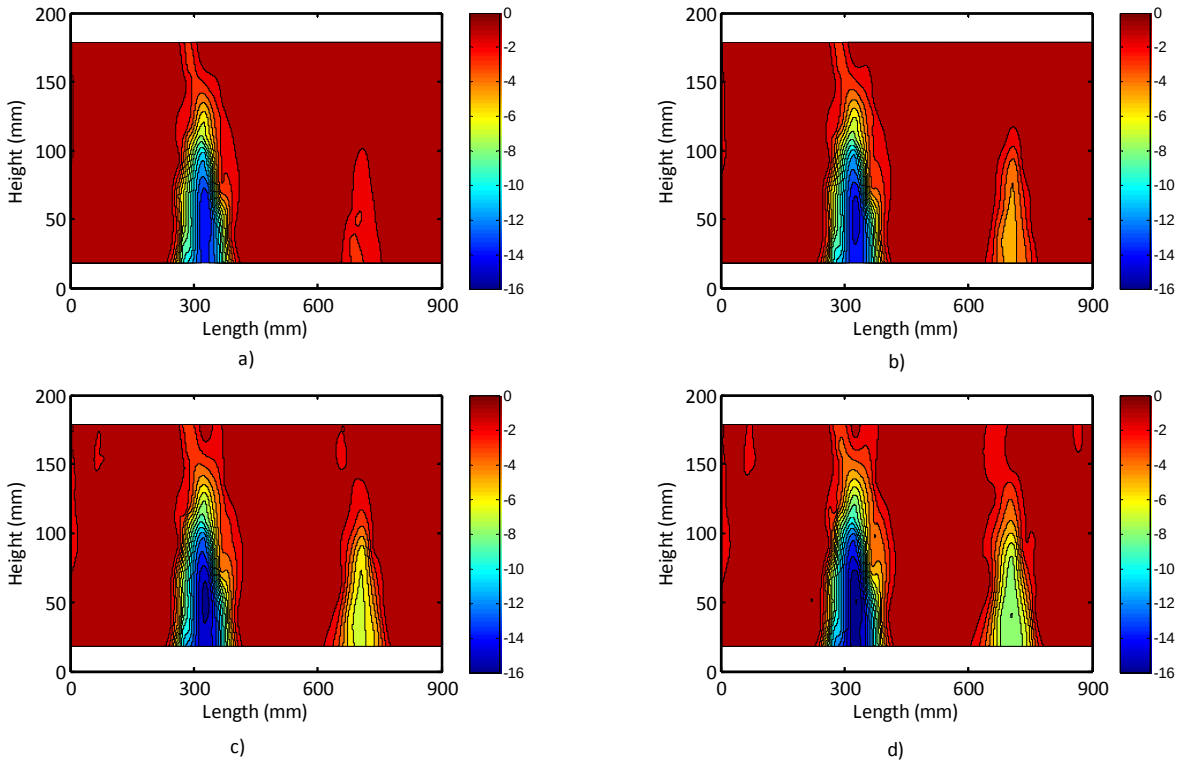

Fig. 4.33 Contours of vertical displacements (mm) in the reinforced embankment (H/B = 1.4) due to the No. 3 trapdoor displacement of 26 mm and the No. 6 trapdoor displacements of a) 2 mm b) 6 mm c) 10 mm d) 16 mm

Figure 4.34 shows the contours of the horizontal displacements in the embankment at H/B ratio of 1.4 at different stages of the trapdoor displacement in the second part of the interaction test simulation. The contours of the horizontal displacement were symmetrical about the vertical centerline of the No. 3 trapdoor but were asymmetrical about the vertical centerline of the No. 6 trapdoor. This difference is because of the proximity of the No. 6 trapdoor to the vertical wall which resulted in anchorage failure of the paper-reinforcement on the right side of the No. 6 trapdoor. This anchorage failure induced large horizontal movement of the particles towards the left.

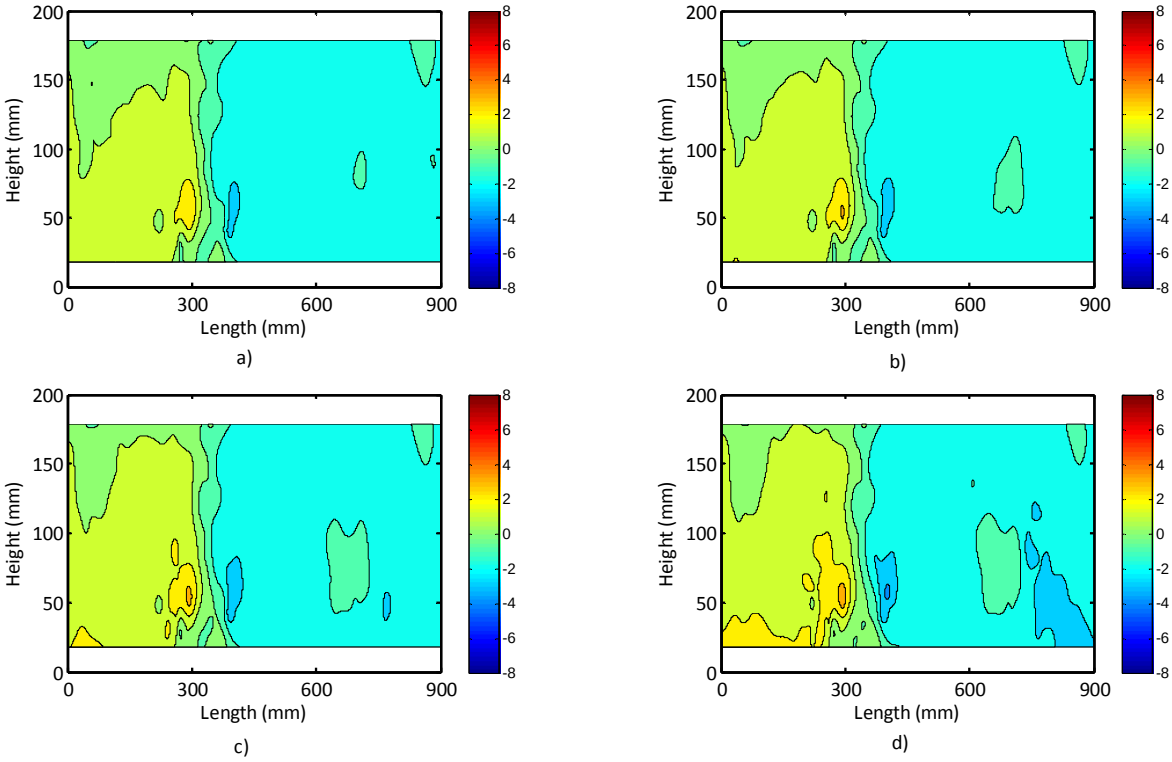

Fig. 4.34 Contours of horizontal displacements (mm) in the reinforced embankment (H/B = 1.4) due to the No. 3 trapdoor displacement of 26 mm and the No. 6 trapdoor displacements of a) 2 mm b) 6 mm c) 10 mm d) 16 mm

Figures 4.35 shows the contours of the vertical displacements in the embankment at H/B ratio of 2.0 at different stages of the trapdoor displacement in the first part of the interaction test simulation. At a small trapdoor displacement (2 mm), only a portion of the embankments below a height of 100 mm underwent displacements. With an increase of the trapdoor displacement, the contours extended higher and wider. The comparison of the displacements in the experimental and simulation results (Figs. 4.14 and 4.35) shows the same magnitude of the displacement at the level of paper reinforcement. However, the simulation displacements at the top of the embankment were smaller than those in the experiment. Similar discrepancy was noticed in the comparison between the simulation and the experimental results for the single central trapdoor.

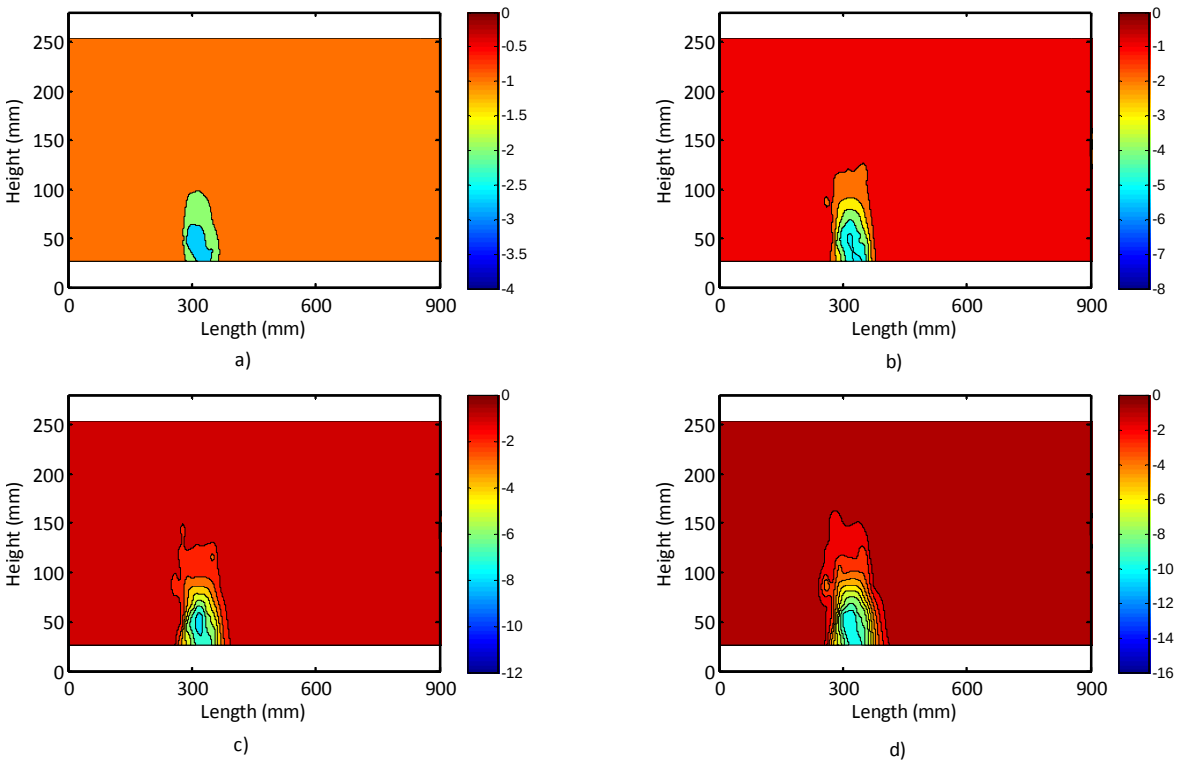

Fig. 4.35 Contours of vertical displacements (mm) in the reinforced embankment (H/B = 2.0) due to the No. 3 trapdoor displacements of a) 2 mm b) 6 mm c) 10 mm d) 16 mm

Figures 4.36 shows the contours of the horizontal displacements in the embankment at H/B ratio of 2.0 at different stages of the trapdoor displacement in the first part of the interaction test simulation. The contours of horizontal displacements were generally symmetrical about the center line of the specific trapdoor (Fig. 4.36).

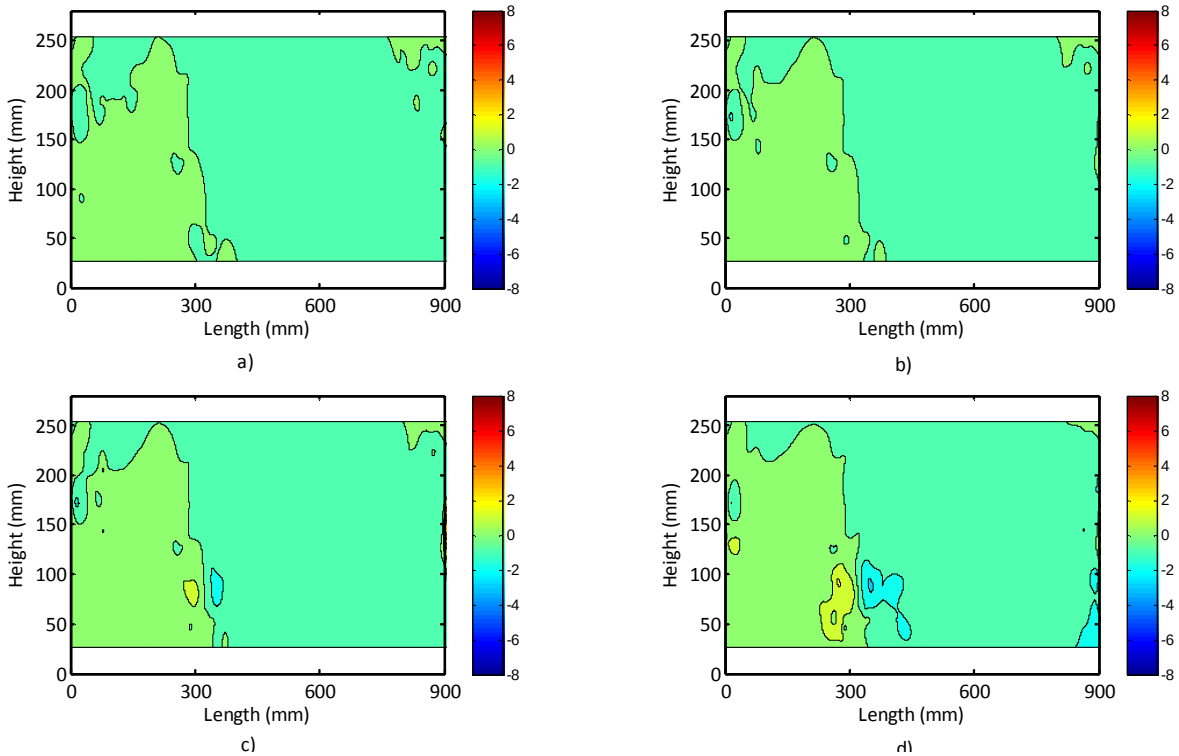

Fig. 4.36 Contours of horizontal displacements (mm) in the reinforced embankment (H/B = 2.0) due to the No. 3 trapdoor displacements of a) 2 mm b) 6 mm c) 10 mm d) 16 mm

Figures 4.37 shows the contours of the vertical displacements in the embankment at H/B ratio of 2.0 at different stages of the trapdoor displacement in the second part of the interaction test simulation. The magnitude of the vertical displacements at the level of paper reinforcement was same as that measured in the experiment. However, smaller vertical displacements were obtained from the simulation at the top of the embankment than those measured in the experiment. The contours of the vertical displacements extended above the No. 6 trapdoor without any distinct evidence of interaction with the displacement zone induced by lowering the No. 3 trapdoor.

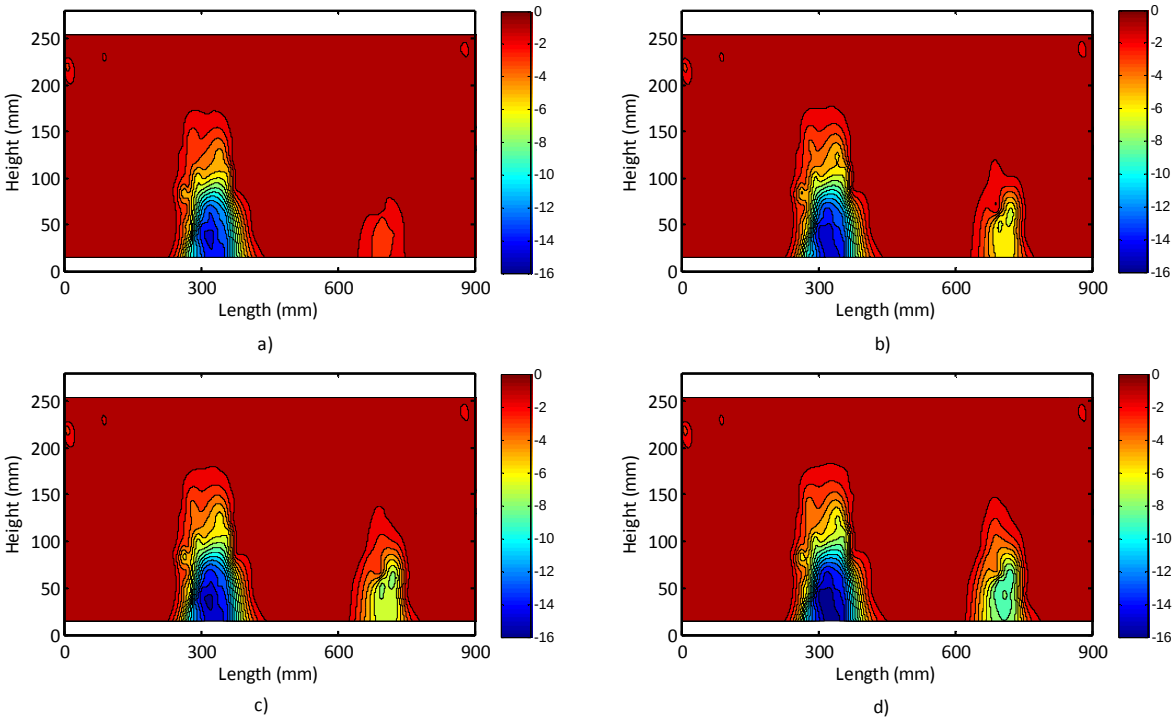

Fig. 4.37 Contours of vertical displacements (mm) in the reinforced embankment (H/B = 2.0) due to the No. 3 trapdoor displacement of 26 mm and the No. 6 trapdoor displacements of a) 2 mm b) 6 mm c) 10 mm d) 16 mm

Figures 4.38 shows the contours of the horizontal displacements in the embankment at H/B ratio of 2.0 at different stages of the trapdoor displacement in the second part of the interaction test simulation. The contours of horizontal displacements were symmetrical about the vertical centerline of the No. 3 trapdoor but asymmetrical about the vertical centerline of the No. 6 trapdoor. Similar conclusions were drawn from the interaction test simulations of the embankment at H/B ratio of 1.4.

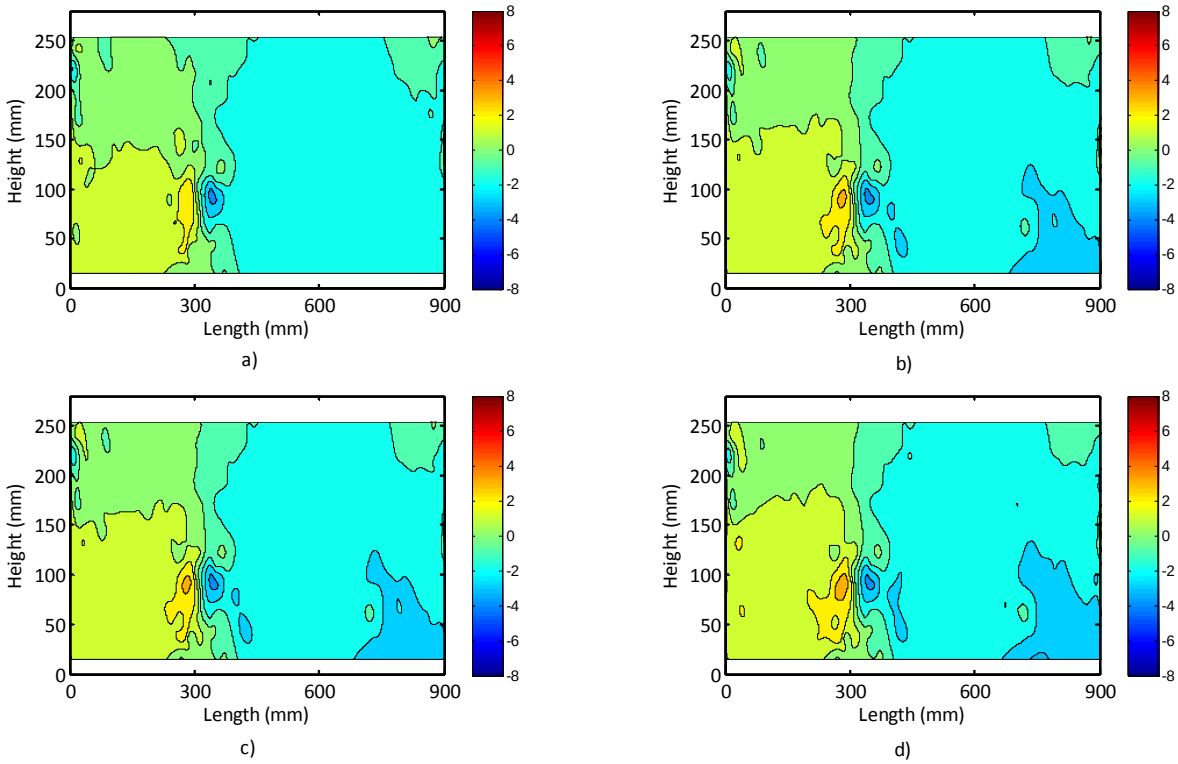

Fig. 4.38 Contours of horizontal displacements (mm) in the reinforced embankment (H/B = 2.0) due to the No. 3 trapdoor displacement of 26 mm and the No. 6 trapdoor displacements of a) 2 mm b) 6 mm c) 10 mm d) 16 mm

4.3.2 Comparison of strain in paper reinforcement

Strains in the paper reinforcement were measured at certain locations in the trapdoor experiments. In the numerical simulation of trapdoor experiments, the strains can be calculated using the stresses in the paper reinforcement. The stresses (σ_x, σ_y, and τ_{xy}) in the particles that represented the paper reinforcement were recorded at each stage of the trapdoor displacement. The principal stresses in the paper reinforcement can be calculated using the following equation.

$$\sigma_{1,2} = \frac{\sigma_x + \sigma_y}{2} \pm \sqrt{\left(\frac{\sigma_x + \sigma_y}{2}\right)^2 + \tau_{xy}^2} \quad \text{Eq. 4.1}$$

where $\sigma_{1,2}$ = the major and minor principal stresses.

Equation 4.2 relates the major principal stress (σ_1) and strain (ε_1) as follows:

$$\varepsilon_1 = \frac{\sigma_1}{E_p} \quad \text{Eq. 4.2}$$

where E_p= Young's modulus of the paper reinforcement that can be determined using Fig. 3.35.

Figure 4.39 shows the comparison of numerically computed and experimentally measured strains in the paper reinforcement at various stages of the single central trapdoor displacement for the embankment at H/B ratio of 1.4. The simulation results show that the location of the maximum strains in the paper reinforcement lied above the trapdoor edge with a rightward offset of 25 mm which is equivalent to the fill thickness below the paper reinforcement. In the DEM simulation and experimental test, the aluminum bars above the adjacent trapdoor fell into the void created by lowering the trapdoor that caused a shift in support of the paper reinforcement away from the edge of the trapdoor.

The strains in the paper reinforcement from the numerical study as well as the experimental measurements decreased from the edge of the trapdoor towards the right end of the test box. At the center of the lowered trapdoor, higher strains were obtained in the paper reinforcement from the numerical simulation than the experimental measurements.

As explained in Section 4.2.2, at a 14-mm displacement of the trapdoor a gap formed between the paper reinforcement and the aluminum bars causing a loss of support from the underlying bars for the paper reinforcement. Under these circumstances, a minor reduction of the strains in the paper reinforcement as obtained from the numerical simulation is justified based on the catenary shape of the paper reinforcement.

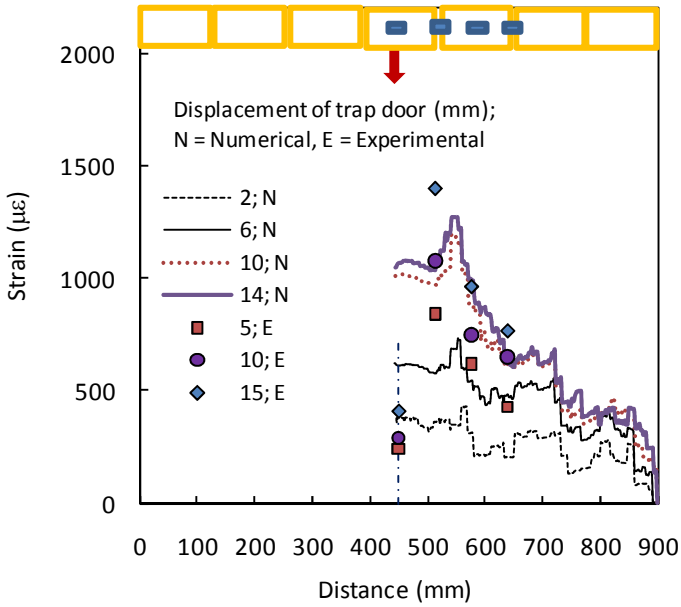

Fig. 4.39 Comparison of computed and measured strains along the paper reinforcement (H/B = 1.4)

Figure 4.40 shows the comparison of numerically computed and experimentally measured strains in the paper reinforcement at various stages of the single central trapdoor displacement for the embankment at H/B ratio of 2.0. The computed and measured peak strains in the paper reinforcement in this case were smaller than those in the embankment at H/B ratio of 1.4. The locations of the peak strains and distributions of the strains in the paper reinforcement in this case were similar to those in the embankment at H/B ratio of 1.4.

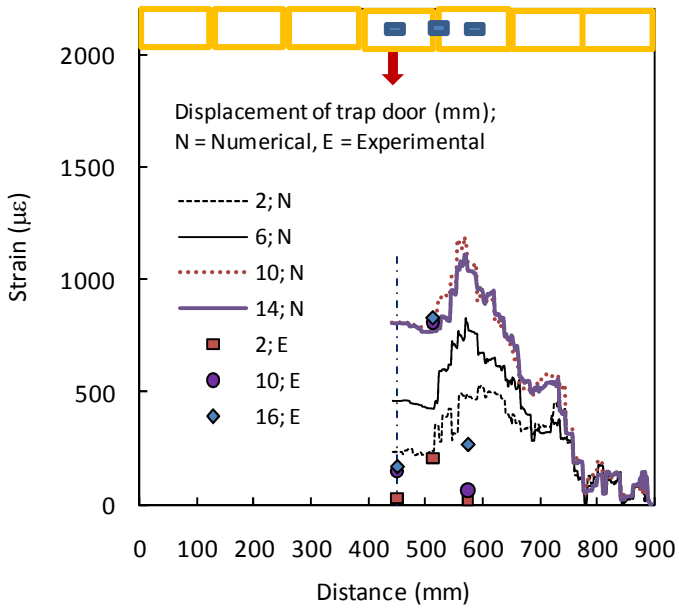

Fig. 4.40 Comparison of computed and measured strains along the paper reinforcement (H/B = 2.0)

Figure 4.41 shows the comparison of numerically computed and experimentally measured strains in the paper reinforcement at various stages of the No. 3 trapdoor displacement (Part 1 interaction test) for the embankment at H/B ratio of 1.4. The peak strains from the simulation were smaller than the experimental measurements at a given trapdoor displacement.

Figure 4.42 shows the comparison of numerically computed and experimentally measured strains in the paper reinforcement at various stages of the No. 6 trapdoor displacement (Part 2 interaction test) for the embankment at H/B ratio of 1.4. The peak strains from the simulation were smaller than the experimental measurements at a given trapdoor displacement. The strains in the paper reinforcement within the influence zone of the No. 3 trapdoor were affected by the lowering of the No. 6 trapdoor. This phenomenon was not observed in the experiment.

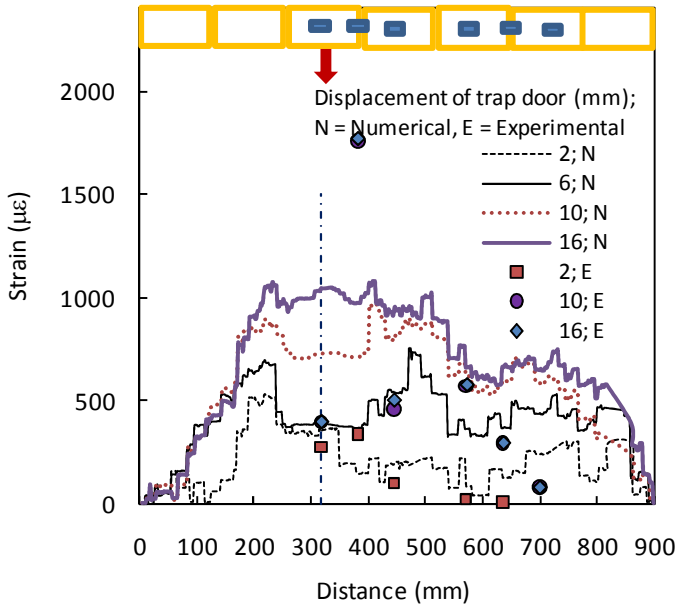

Fig. 4.41 Comparison of computed and measured strains along the paper reinforcement in the first part of the interaction test (H/B = 1.4)

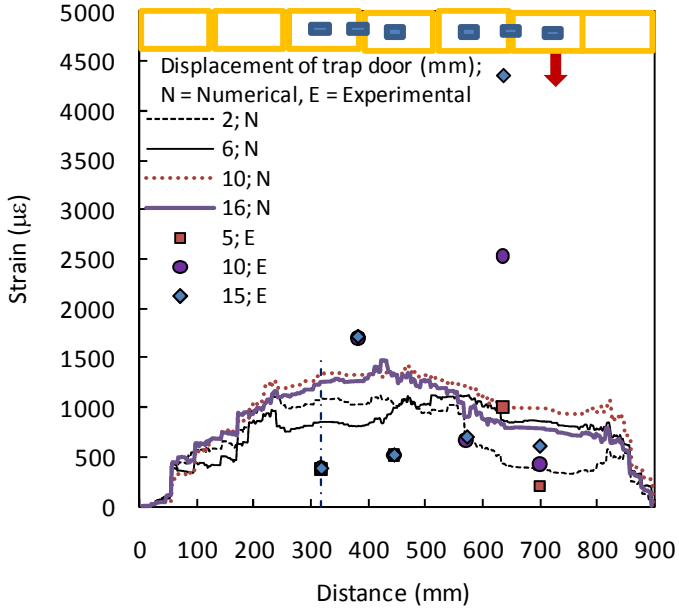

Fig. 4.42 Comparison of computed and measured strains along the paper reinforcement in the second part of the interaction test (H/B = 1.4)

Figure 4.43 shows the comparison of numerically computed and experimentally measured strains in the paper reinforcement at various stages of the No. 3 trapdoor displacement (Part 1 interaction test) for the embankment at H/B ratio of 2.0. Larger strains developed in the paper reinforcement on the right side than those on the left side of the first trapdoor since a longer anchorage length for the paper reinforcement was available on the right side than that on the left side of the No. 3 trapdoor.

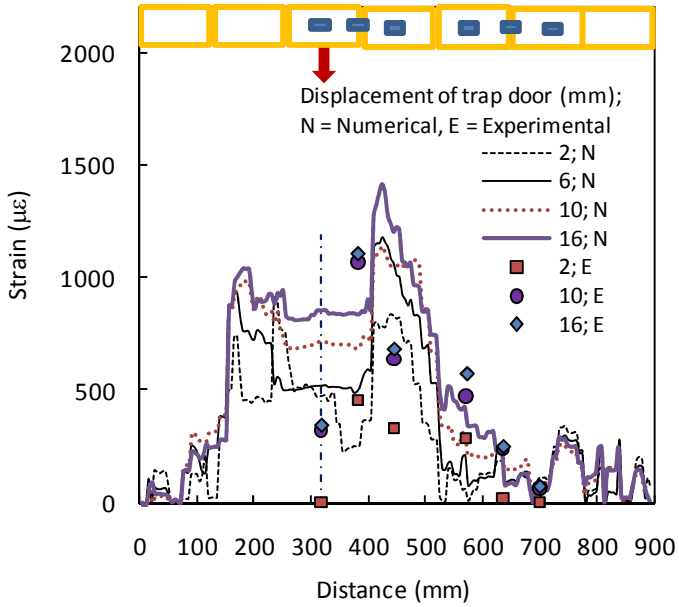

Fig. 4.43 Comparison of computed and measured strains along the paper reinforcement in the first part of the interaction test (H/B = 2.0)

Figure 4.44 shows the comparison of numerically computed and experimentally measured strains in the paper reinforcement at various stages of the No. 6 trapdoor displacement (Part 2 interaction test) for the embankments at H/B ratio of 2.0. Peak strains in the paper reinforcement developed at the left side of the No. 6 trapdoor since a longer anchorage

length was available on the left than that on the right side of the No. 6 trapdoor. Changes in the strains in the paper reinforcement above the No. 3 trapdoor were calculated when the No. 6 trapdoor was lowered. The influence of the No. 6 trapdoor displacement on the strains in the paper reinforcement above the No. 3 trapdoor was not noticed in the experiment.

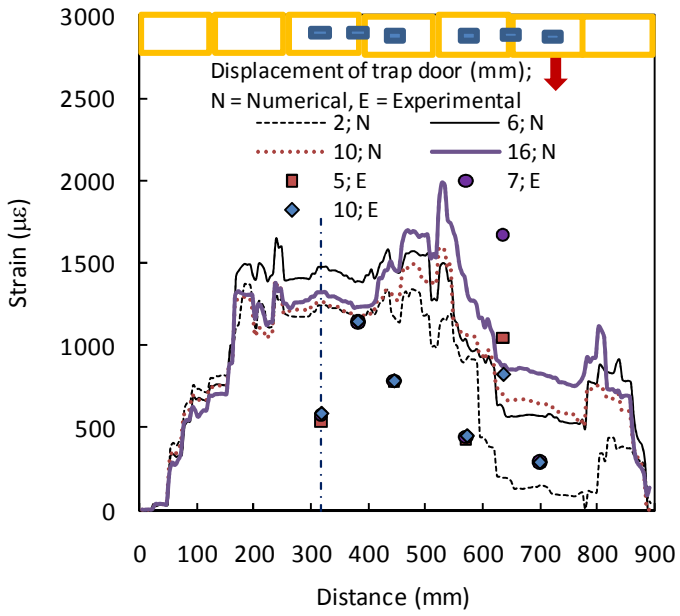

Fig. 4.44 Comparison of computed and measured strains along the paper reinforcement in the second part of the interaction test (H/B = 2.0)

CHAPTER FIVE

GEOGRID-REINFORCED PILE-SUPPORTED EMBANKMENTS

In this chapter, an application of DEM modeling to understand the behavior of geogrid-reinforced embankments supported on piles is presented. Reasonable dimensions of the embankments and the fill materials were considered. Fabric and force orientations in the embankments were presented to understand the soil arching at a microscale. Further, a cyclic load was applied on a footing resting on the top of the embankment. The change in load share between piles and soil due to the cyclic loading was studied.

5.1 Numerical Model Preparation

A 1.6 m high and 1.5 m long rectangular box was created using four walls (Fig. 5.1). Particles ranging from 9.2 mm to 20.8 mm in diameter were generated at a porosity of 0.16 using a radial expansion technique as described in Itasca (2004). The particle size distribution followed a normal distribution curve with a mean particle size (d_{50}) of 15.0 mm. The micromechanical properties of the particles are shown in Table 3.3. A model created using the radial expansion technique generates high stress which should be brought to an initial stress condition. Lateral walls were moved in opposite directions using the numerical servo mechanism until the desired lateral wall force (equal to the lateral earth thrust at the earth pressure coefficient of 0.5) was attained. After achieving the initial stress condition, a geogrid sheet was placed by generating the bonded particles (large particles of 2.6 mm in diameter on the nodes and small particles of 1.0 mm in diameter between nodes) inside the guided walls (created at 1.3 m below the top wall), which were optional depending on whether an unreinforced or reinforced case was studied. A 0.3 m x

0.3 m pile cap was placed on either side of the model using walls and the particles inside the pile caps were deleted because they do not interact with particles outside the walls. The deletion of these particles was also needed for the calculation of the unbalanced force on the walls from the particles outside. The remaining particles in the model were subjected to the gravity field and brought to an equilibrium condition (at which the ratio of the maximum unbalanced force to the maximum contact force reached the value of 0.01).

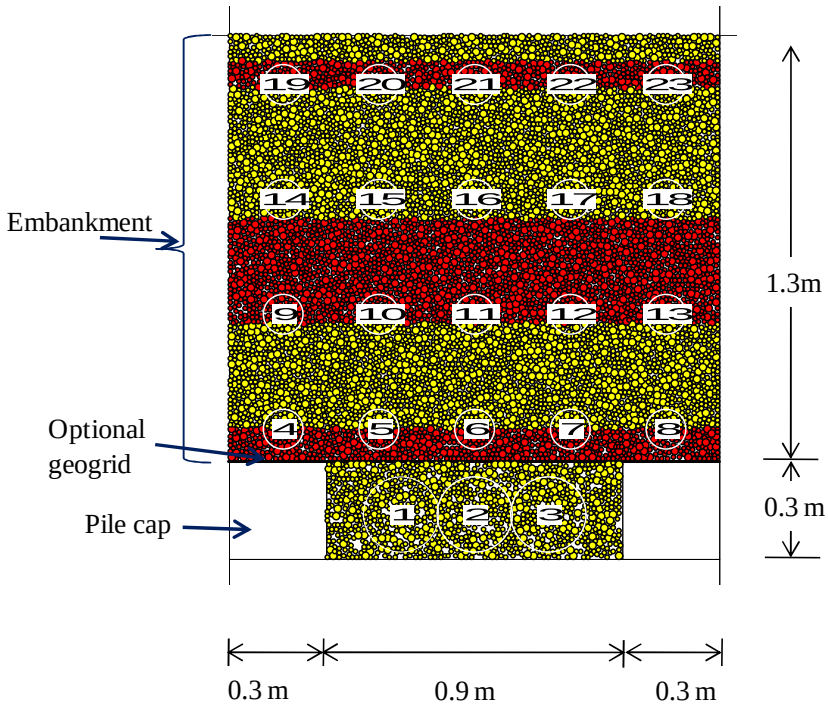

Fig. 5.1 DEM model of a geosynthetic-reinforced pile-supported embankment

Furthermore, the porosity of the assembly below 1.3 m (i.e., between the pile caps) was increased to 0.30 from an initial porosity of 0.16 by randomly deleting the particles within this zone. The high porosity within this zone was to simulate the compressible soil. Because of this compressible soil in the lower part, the embankment fill undergoes displacements to achieve a new equilibrium of the system (embankment). Twenty-three measurement circles were installed in the model as shown in Fig. 5.1 to measure the

horizontal and vertical stresses at different stages of the simulation. In this study, the ratio of the embankment height to the clear spacing of the pile caps was 1.45, which was selected based on BS8006 (1995) and Chen *et al.* (2008).

5.2 Analysis of Results

5.2.1 Stresses in embankments

Development of the soil arch in an embankment changes its stress field. However, the stresses are not readily measureable in the discrete simulation. In a discrete collection of particles, only the forces acting at the physical contacts can be computed. These forces can be converted to the equivalent continuum stresses over a measurement circle using the volume average method. Equation 5.1 relates the forces at contacts to the average stresses ($\bar{\sigma}_{ij}$) in the measurement circle (Itasca 2004):

$$\bar{\sigma}_{ij} = \left(\frac{1-n}{\sum_{N_p} V^{(p)}}\right)\left(\sum_{N_p}\sum_{N_c^p}\left(x_i^{(c)} - x_i^{(p)}\right)F_j^{(c,p)}\right) \qquad \text{Eq. 5.1}$$

where, $V^{(p)}$ = the volume of the particle;

n -= the porosity inside the measurement circle;

N_c^p = the number of contacts along the surface of particle p;

$x_i^{(c)}$ and $x_i^{(p)}$ = the locations of the centroid and the contact of particle p;

$F_j^{(c,p)}$ = the force acting on a particle p at contact c

The summation is taken over N_p particles whose centroids lie within the measurement circle.

Figure 5.2 shows the vertical and horizontal stress contours within the embankment before the development of soil arching. The particles were subjected to a gravity field and brought to an equilibrium state. The force equilibrium of the embankment was ensured when the total weight of the embankment was same as the summation of the loads transferred to the pile caps and the bottom wall. Minor fluctuations on the stresses at equal vertical heights were noticed but expected since contact forces might develop in some preferential path in the discrete simulation. Almost equally spaced vertical stress contours in Fig. 5.2 show the linear gradient of vertical stress under the influence of the gravity field. The horizontal stresses were approximately one half of the vertical stresses throughout the embankment.

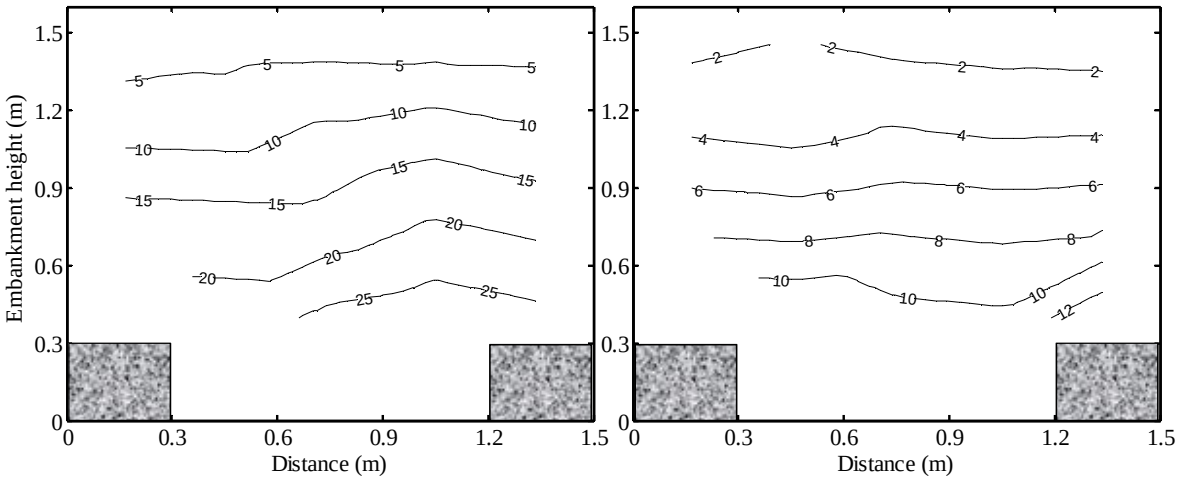

Fig. 5.2 Stress contours in the embankment before soil arching

Figure 5.3 shows the contours of vertical and horizontal stresses after the development of soil arching in the unreinforced embankment. Figure 5.4 shows similar plot for the reinforced embankment. In both cases, the vertical stresses increased significantly over

the pile caps but decreased between the pile caps. The horizontal stresses also increased over the pile caps but largely remained unaffected in the portion of the embankment between the pile caps. Therefore, the horizontal stresses follow the trend of the vertical stresses only in a loading path but behave differently in an unloading path. This effect leads to the locked-in horizontal stresses in the soil mass.

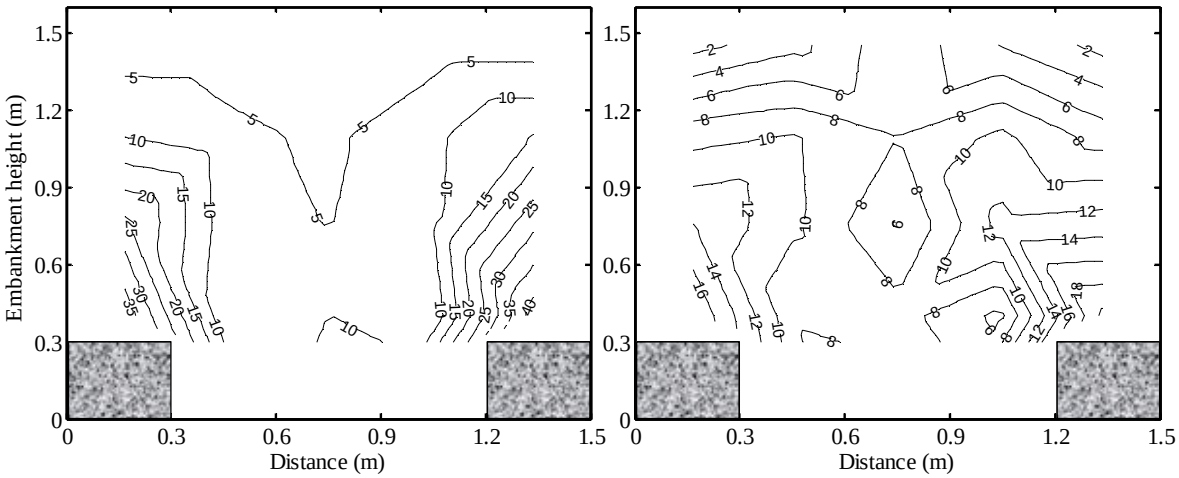

a) Vertical stress (kPa) b) Horizontal stress (kPa)

Fig. 5.3 Stress contours in the unreinforced embankments after soil arching

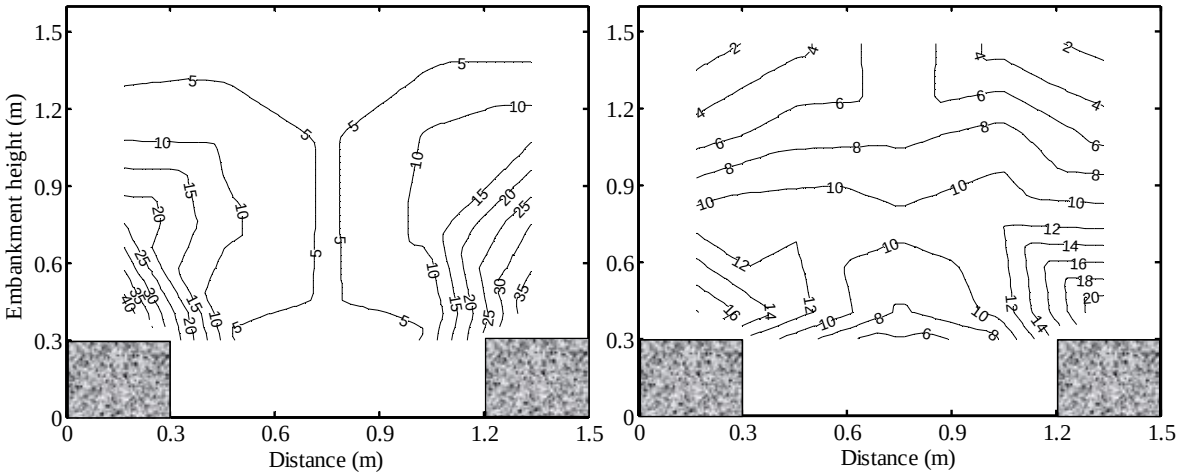

a) Vertical stress (kPa) b) Horizontal stress (kPa)

Fig. 5.4 Stress contours in the geogrid-reinforced embankments after soil arching

A ratio of the horizontal stress to the vertical stress, defined as the coefficient of lateral earth pressure (*k*), is often used to evaluate the stress condition in the soil mass. The coefficient of lateral earth pressure was calculated before and after the soil arch formation for the unreinforced and reinforced embankments as shown in Fig. 5.5. Three sections were considered at distances of 0.20 m, 0.40 m, and 0.75 m away from the left wall. Before the development of soil arching, the coefficient of lateral earth pressure fluctuated in a narrow range that can be considered "uniform" for practical purpose. The average lateral earth pressure coefficient was 0.49. The coefficient of lateral earth pressure at rest can be calculated using Jaky's formula as follows:

$$K_o = 1 - sin\emptyset = 1 - sin26^o = 0.56 \qquad \text{Eq. 5.2}$$

where, $\emptyset$ -= the friction angle of granular media. The theoretical value of K_o was reasonably close to the average value obtained from the numerical simulation.

After the development of full soil arching, the coefficient of lateral earth pressure varied in a wide range of 0.5 to 2.7 as shown in Fig 5.5. The coefficient of 2.7 is the same as the coefficient of passive earth pressure. In both unreinforced and reinforced embankments, the maximum coefficient of lateral earth pressure occurred at the top level of the embankments along the mid-span between the pile caps. Due to the development of soil arching, the vertical stresses along the mid-span of the embankment decreased significantly as shown in Figs. 5.3 and 5.4. Therefore, the reduced vertical stresses

coupled with the relatively unaffected horizontal stresses resulted in the maximum coefficient of lateral earth pressure at the top of the embankment.

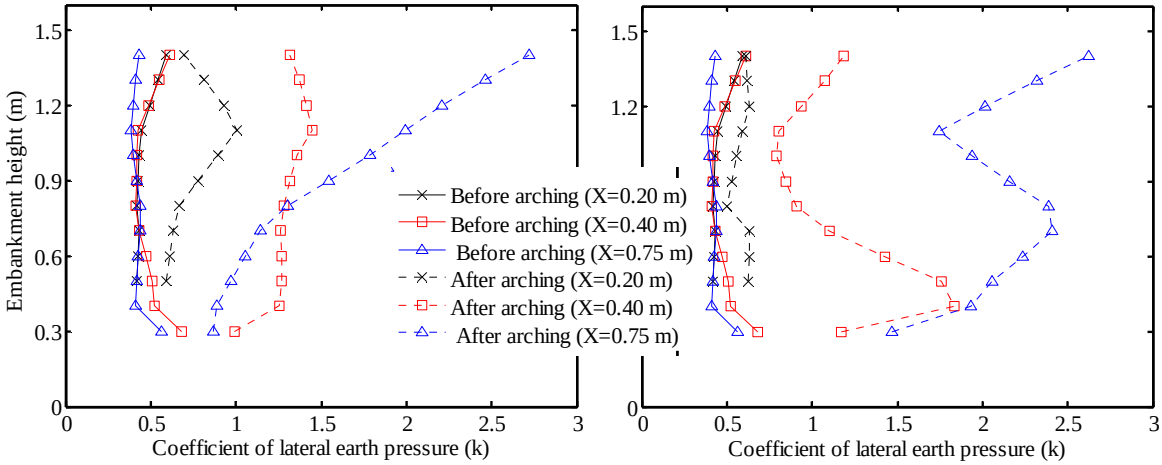

Fig. 5.5 Coefficient of lateral earth pressure at different sections of the embankment before and after soil arching

5.2.2 Contact forces and orientations

Forces in granular media transfer through the interconnected network of force chains via contact points. Figure 5.6 shows the contact force distribution for the unreinforced and reinforced embankments at full soil arching development. The contact forces were plotted on the same scale. Black lines indicate compressive contact forces and red lines indicate tensile contact forces. The thickness of lines represents the relative magnitude of contact forces. The weight of the embankment portion between the pile caps transferred to the adjacent pile caps due to the reorientation of contact forces. Therefore, the compressive contact forces were concentrated over the pile caps for both unreinforced and reinforced

embankments. The remaining weight of the embankment portion between the pile caps transferred to the underlying compressible soil in the unreinforced embankment. The geogrid transferred the remaining weight of the embankment portion between the pile caps to the pile caps through the cable action of the geogrid in case of the reinforced embankment. A negligible amount of forces transferred to the compressible soil as the geogrid barely rested over the compressible soil. Furthermore, it is evident that the contact forces at the mid-span of the embankments were increasingly aligned on a horizontal direction towards the top of the embankment. The consequence of this load transfer was the occurrence of the maximum lateral earth pressure coefficient on the top of the embankment as explained in the preceding section.

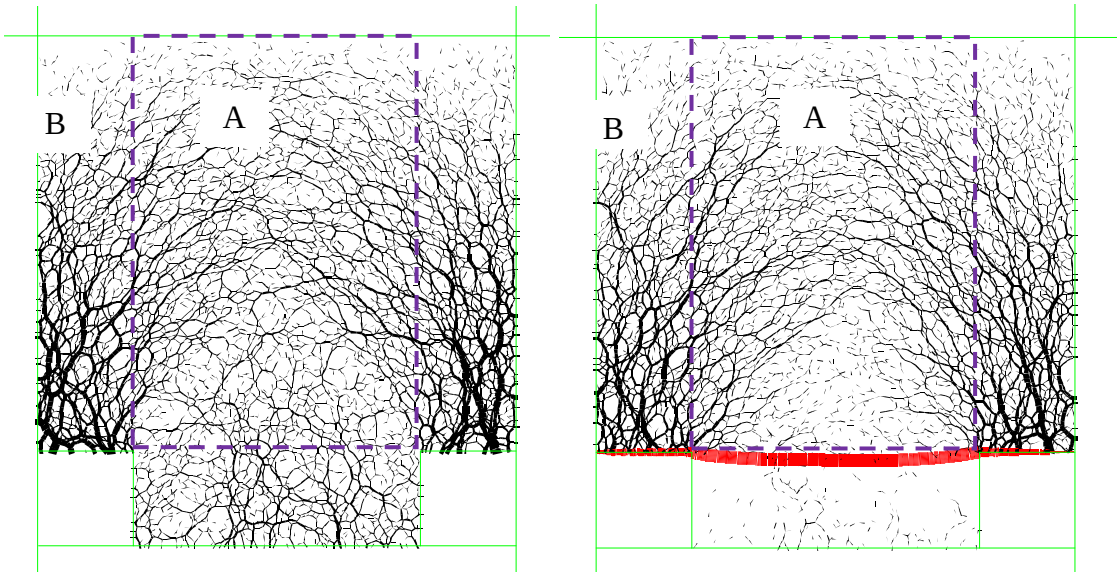

Fig. 5.6 Contact force distribution at soil arching

The polar histogram of the contact forces shown in Fig. 5.7 can be obtained by collecting the contact force information at a predefined bin angle (O'Sullivan *et al.* 2008). In this study, the bin angle of 10^{o} was selected, and the polar histogram for contact orientation

was normalized by the total number of contacts. Similarly, the polar histograms for contact normal force and tangential force were normalized by the average normal force over all contacts in the assembly. Figure 5.7 shows the normalized histogram for the contact and force orientations for the embankment at an initial equilibrium condition and after the full soil arching development for the cases of unreinforced and reinforced embankments. Figure 5.7 also shows the Fourier series approximation of these normalized contact and force orientations. Since Zone A and B in Fig. 5.7 showed different contact force orientations, the contact and force orientations were separately evaluated. The mathematical expressions for these Fourier series approximations were explained in Section 3.4.

Table 5.1 shows the coefficient of Fourier series approximation of the contact and force orientations at different stages of simulation. At the initial equilibrium under the application of the gravity field, Zones A and B in the embankment had identical density distributions for the contact and for the normal as well as the tangential forces and are shown in Fig. 5.7 a. The density distribution of contacts was isotropic, the normal contact forces had principal direction at 89.9^{o}, and the average tangential contact was zero at 94^{o}. After the development of full soil arching, Zone A developed more contacts in the horizontal direction than in the vertical direction (Fig. 5.7 b and d). The contact normal force was slightly higher in the horizontal direction than that in the vertical direction for the unreinforced embankment but was isotropic for the reinforced embankment. The isotropic distribution of the stresses beneath the soil arch was proposed for the analytical solution of piled embankment by Hewlett and Randolph (1988). Within Zone B, the inclined principal directions of the contacts and the contact normal forces developed at angles of 74.5^{o} and 86.2^{o} for the unreinforced embankment and 80.9^{o} and 83.9^{o} for the

reinforced embankment, respectively. Similarly, the directions of the zero average tangential force inclined at angles of 82.5^{o} and 81.4^{o} for unreinforced and reinforced embankments, respectively. The normalized tangential forces after the development of soil arching did not show any marked increase compared to those before the development of soil arching. The above discussion demonstrates that the load transfer of the embankment to the pile caps due to the reorientation of the major principal stresses.

Table 5.1 Coefficients of the Fourier series approximation during soil arching

Coefficients	Before soil arching	After soil arching (unreinforced embankment)		After soil arching (reinforced embankment)	
		Zone A	Zone B	Zone A	Zone B
a	0.002	-0.01	0.03	-0.02	0.04
a_n	0.32	-0.08	0.33	-0.02	0.40
a_t	0.16	-0.03	0.09	-0.02	0.13
${\theta_a}^{\mathrm{o}}$	90.0	95.4	74.5	93.1	80.9
${\theta_f}^{\mathrm{o}}$	89.9	95.4	86.2	90.0	83.9
${\theta_t}^{\mathrm{o}}$	94.0	95.1	82.5	91.1	81.4

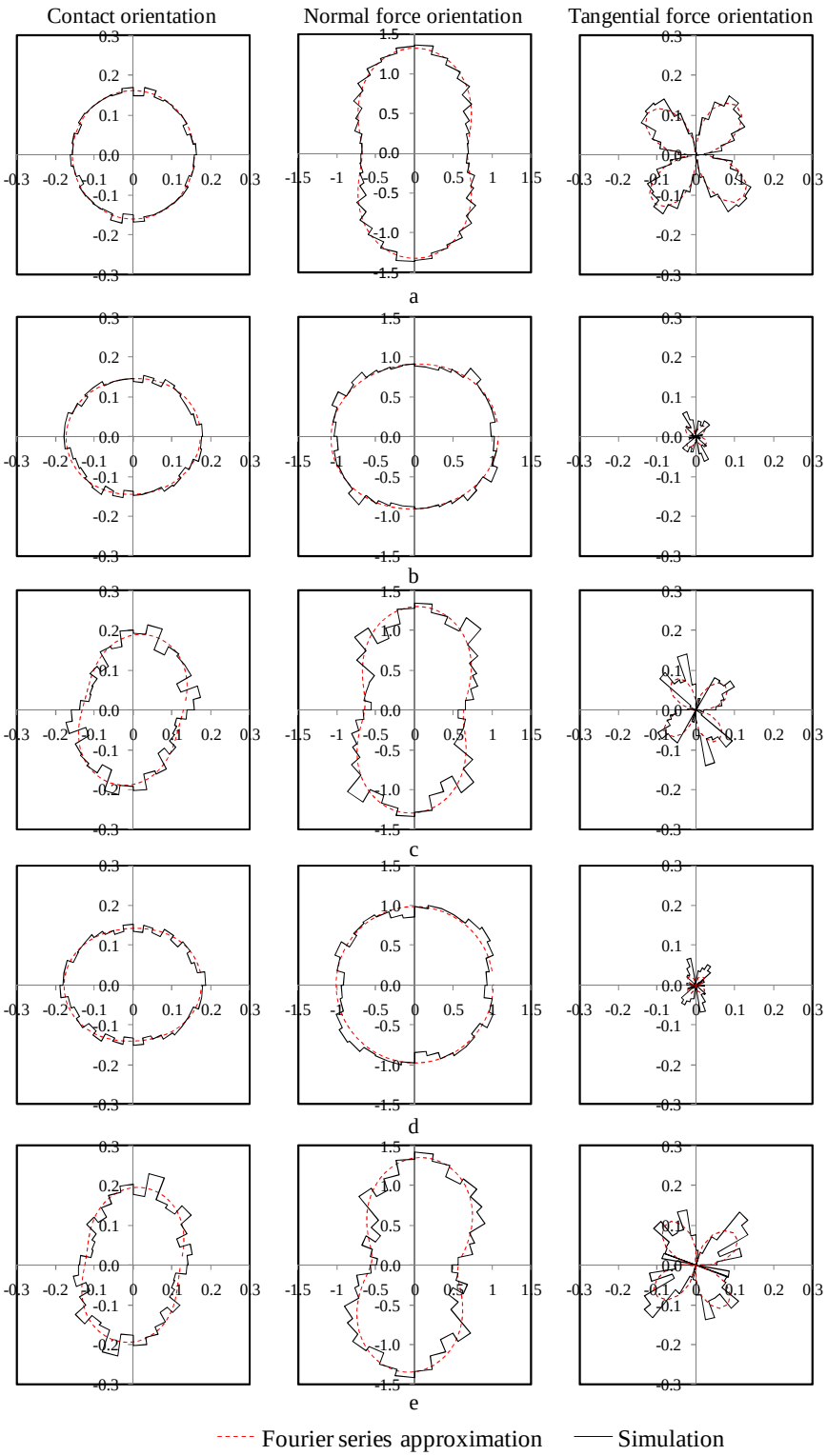

Fig. 5.7 Contact and force orientations for: a) before soil arching, b) after soil arching for Zone A; unreinforced embankments, c) after soil arching for Zone B; unreinforced embankments, d) after soil arching for Zone A; reinforced embankments, and e) after soil arching for Zone B; reinforced embankments

5.2.3 Porosity changes in embankments

Granular materials show volumetric dilation or contraction behavior under the influence of external disturbances (force field or displacement field) depending upon their initial packing conditions and external disturbances. In general, an initial densely-packed system shows volumetric dilation and a loosely-packed system shows volumetric contraction (Section 3.3.2). It is extremely challenging to experiment the volumetric changes within the embankment when the soil arching develops. However, this information can be readily obtained in a discrete element simulation. Using the porosities monitored at different measurement circles, the percentage of porosity changes in the embankment before and after the development of soil arching could be calculated and are presented in Fig. 5.8. Both the unreinforced and reinforced embankments showed increased porosities (i.e., dilation) to a maximum percentage change of 2%. The maximum dilation occurred at the mid-span between the pile caps and at the height equal to one half of the clear spacing. Higher dilation also developed near the edge of the pile caps. The influence area of the increased porosity for the unreinforced embankment was more spread out than that for the reinforced embankment. The dilation of the embankment fill due to soil arching was also reported by Costa *et al.* (2009). Had it been a three-dimensional study of the embankment over piles, less dilation would have been observed since the two-dimensional plane assembly undergoes dilation at a higher rate than the three-dimensional assembly (Rothenburg and Bathurst 1992). Rothenburg and Bathurst (1992) also pointed out that the two-dimensional assembly can dilate in one direction only.

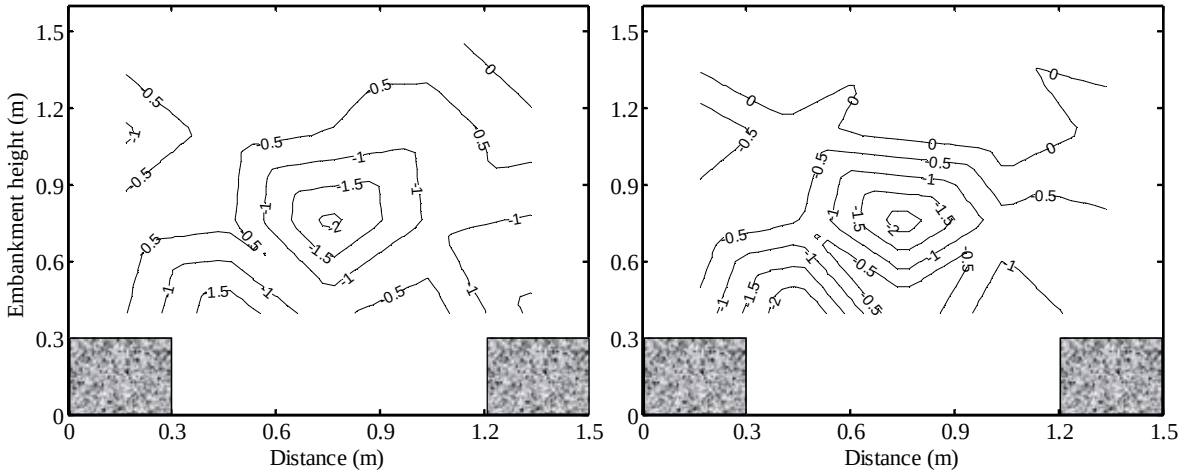

a) Unreinforced b) Geogrid reinforced

Fig. 5.8 Percentage of porosity change in the embankment due to soil arching

5.2.4 Particle displacement in embankments

The displacement vectors of the soil particles in the unreinforced and reinforced embankments are shown in Fig. 5.9. The same magnitude of the maximum displacement was used for these two figures for comparison. A triangular shape delineated a zone of larger displacements from the zone of smaller displacements in either case. Denser and longer displacement vectors illustrated larger settlements in the unreinforced embankment than those in the reinforced embankment. A gap between the displacement vectors and the top wall was distinctly observed for the unreinforced embankment that indicated the full height of the embankment was affected by the particle movement resulting from the compression of the compressible soil. The geogrid reduced the overall displacements in the reinforced embankment.

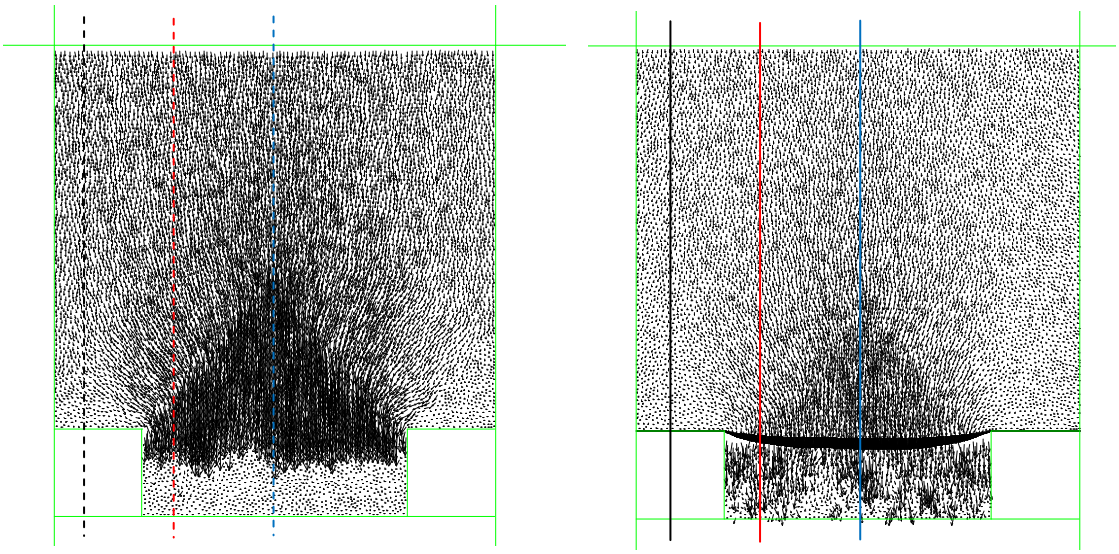

Fig. 5.9 Displacement vectors for the unreinforced and reinforced embankments

Figure 5.9 shows a triangular shape of the soil arching with a shear angle of 53.0, where the shear angle is defined as the angle formed by the shear plane relative to the horizontal plane (Van Eekelen *et al.* 2003). This angle is less than the active angle of 58.0^{o} (i.e., $45^{o}+26^{o}/2$). The triangular shape of the shear plane was observed in an experimental study of piled embankments by Van Eekelen *et al.* (2003).

Three sections were considered at distances of 0.10 m, 0.40 m, and 0.75 m away from the left wall to investigate the vertical displacement in the unreinforced and reinforced embankments. Figure 5.10 shows the vertical displacement after the development of soil arching. It is shown that vertical displacements extended to the top of the embankment. The maximum vertical displacements were 48 and 28 mm for the unreinforced and reinforced embankments respectively at the top elevation of the pile caps. On the top of the embankment, the vertical displacements were 15 and 7.5 mm for the unreinforced and the reinforced embankments, respectively. The results showed that the geogrid

reinforcement reduced the total settlement for the reinforced embankment to 50% of that for the unreinforced embankment in this study. Geogrid reinforcement also reduced the differential settlement.

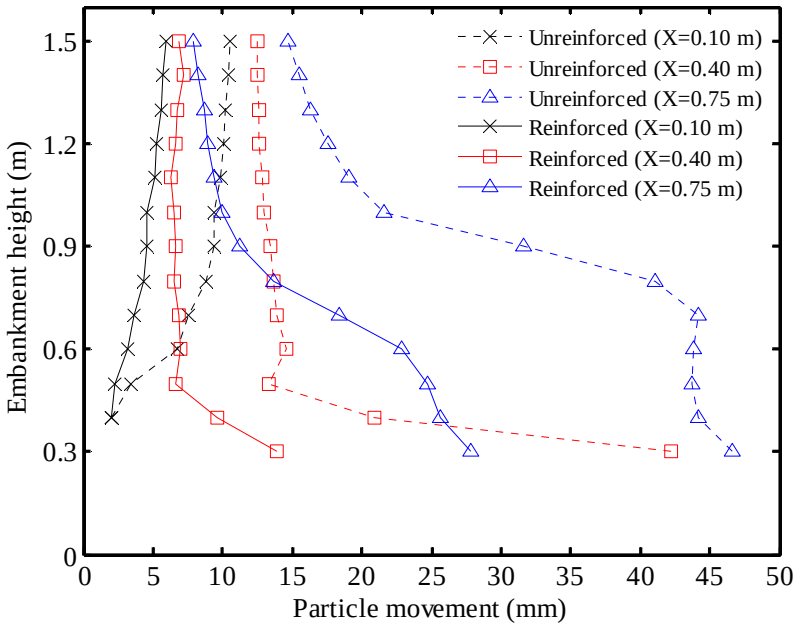

Fig. 5.10 Vertical movement of particles at soil arching

5.2.5 Deformation and tension in geogrid

Figure 5.11 shows the development of tension in the geogrid and the deformation of the geogrid along the width of the embankment at the full soil arching development. The geogrid underwent a maximum deformation of 37 mm. The geogrid attained a catenary shape as expected.

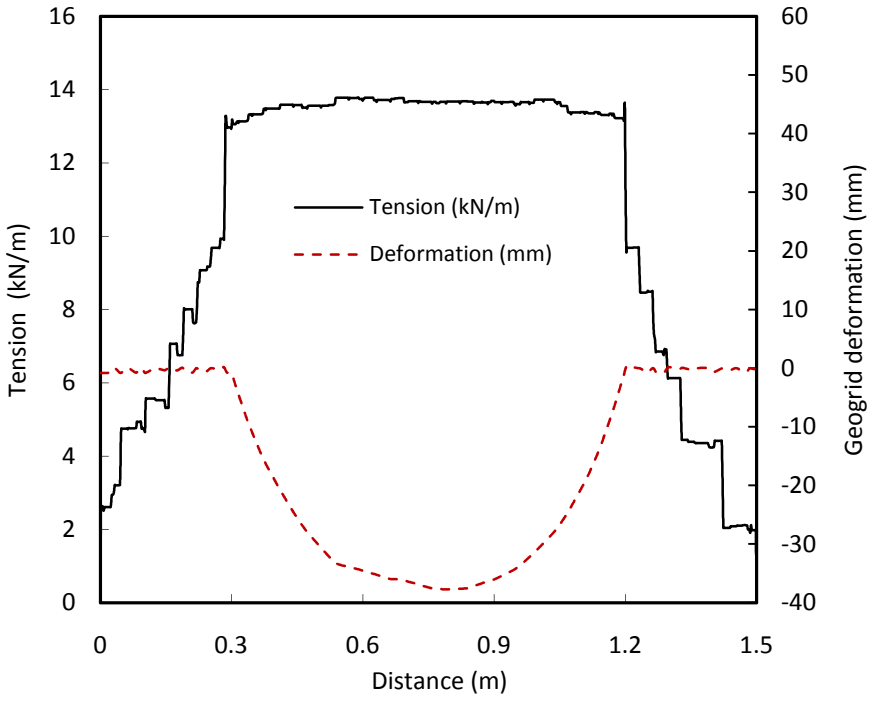

Fig. 5.11 Deformation and tension force in geogrid

The maximum tension up to 13.8 kN/m developed in the geogrid that corresponds to an approximately 3.3% strain (see Calibration of the geogrid). The maximum tension developed near the edge of the pile caps and remained constant between the pile caps. Since the geogrid barely touched the underlying compressible soil, the load could not transfer to the underlying soil. Therefore, the tension in the geogrid remained constant between the pile caps. If the geogrid gained the support from the compressible soil, the tension in the geogrid would decrease while moving toward the center of the embankment from the pile edge. On the other hand, if the geogrid does not gain any support from the compressible soil (similar to a geogrid over a void), the tension in the geogrid slightly varies according to the catenary shape of the geogrid. In this simulation, a 37 mm deformation of the geogrid over a length of 900 mm was small enough to maintain a practically constant tension between the pile caps.

5.3 Embankment under a Cyclic Load

The behavior of an embankment under a cyclic load was investigated by loading a footing at the top center of the embankment. Before the selection of the cyclic load, the load capacity of the foundation under a monotonic load should be first determined and not exceeded by the cyclic load. The monotonic load test was simulated by applying a load on a footing (300 mm wide) up to failure. The footing of 300 mm is the typical plate size used in the plate load test to simulate a traffic loading. Further, the influence depth of a strip footing extends to a depth of 4B (B is the width of footing) which implies the full embankment height being affected due to the cyclic loading. The footing was given a small velocity of 5E-8m/step in a downward direction and the resistance force offered by the unreinforced pile-supported embankment was recorded. The vertical displacement of the footing was also calculated. Figure 5.12 shows the load-deformation plot for the footing on the unreinforced and reinforced embankments. For the unreinforced embankments, the maximum load capacity was determined to be 16 kN from Fig. 5.12. A cyclic load of 10 kN (approximately 60% of the maximum load for the unreinforced embankment, equivalent to 133 kPa average contact pressure) was selected for the further analysis. This load is smaller compared to a typical wheel load of a highway truck with 80 kN axle load. The purpose of this study is to understand the behavior of a pile-supported embankment under a cyclic load rather than to model the actual embankment and vehicle conditions.

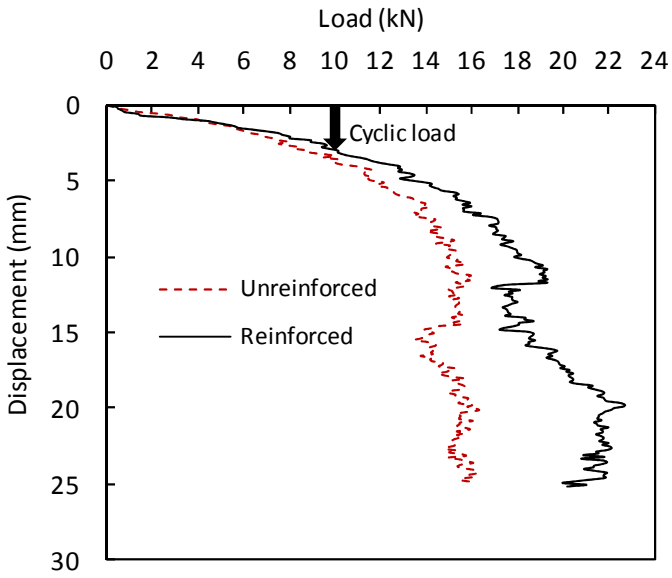

Fig. 5.12 Load vs. deformation under a monotonic load

5.3.1 Load deformation behavior

Figures 5.13 and 5.14 show the load-deformation behavior of the footing on the unreinforced and geogrid-reinforced embankments, respectively, up to 25 cycles. The deformation calculated for the geogrid-reinforced embankment was approximately 68% of that calculated for the unreinforced embankment. Figure 5.15 shows that the deformation increased with the load cycles, which can be attributed to the accumulation of plastic strain under the cyclic load. The deformation of the unreinforced and reinforced embankments increased continuously with the load cycles until the end of 25 cycles.

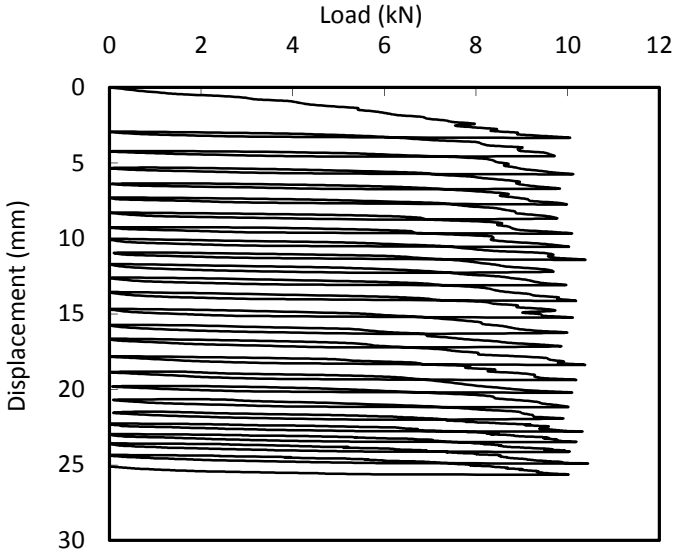

Fig. 5.13 Load vs. displacement for the unreinforced embankment under a cyclic load

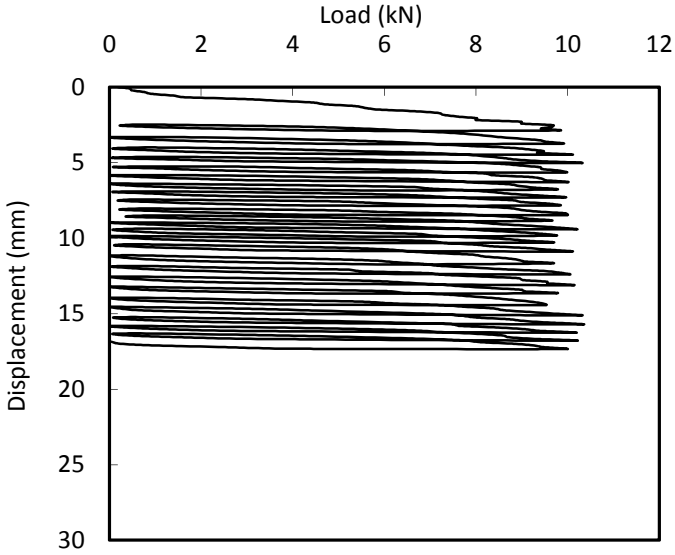

Fig. 5.14 Load vs. displacement for the geogrid-reinforced embankment under a cyclic load

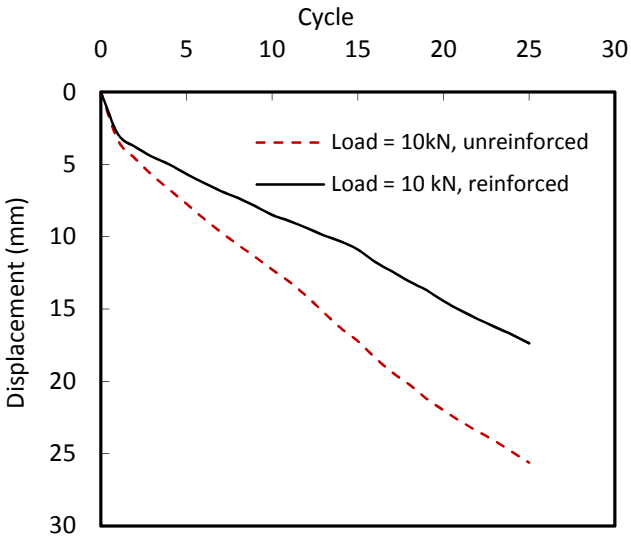

Fig. 5.15 Displacement vs. load cycle

5.3.2 Stresses on pile caps and soil

Figure 5.16 shows the evolution of the stresses on the pile caps and the soil below the level of the geogrid reinforcement (1.3 m below from the top) using a stress concentration ratio. Stress concentration ratio (n) is often used to characterize the degree of soil arching and defined as a ratio of the stress on the pile cap, σ_c, to the stress on the soil, σ_s, (Han and Gabr 2002). The initial stress concentration ratio (n) was 3.4 for the unreinforced model and 7.5 for the geogrid reinforced model (Fig. 5.16). This result is consistent with that of the Han and Gabr (2002) numerical study, in which the geosynthetic increased the stress concentration ratio as compared with the unreinforced case. The stress concentration ratio in Fig. 5.16 increased with cyclic loadings up to five cycles and decreased thereafter. The displacement plot in Fig. 5.15 as well as the stress concentration plot in Fig. 5.16 show that the cyclic loading is deteriorating existing soil arching. However, the effect of cyclic loading may depend on the ratio of the embankment height to the clear spacing of the pile

caps and the dimension of the footing. In a study of similar problem, Han and Bhandari (2009) noticed that the existing soil arching was not affected by the cyclic loading when the footing was 150 mm wide for the same dimension of embankment used in this study.

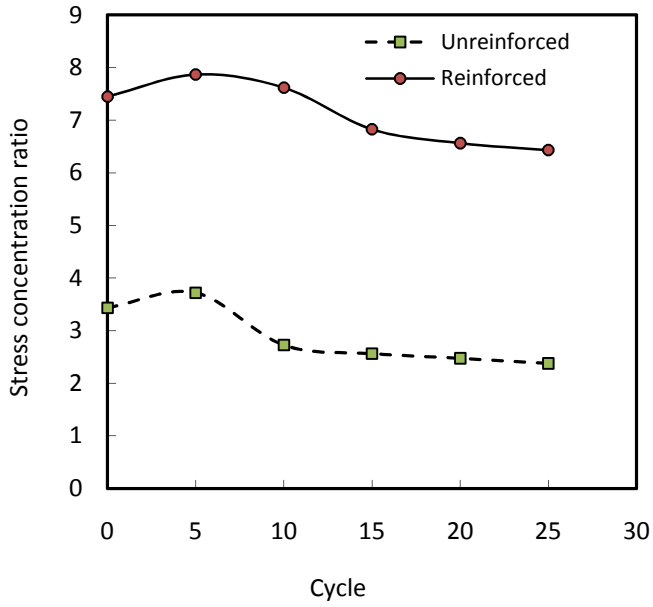

Fig. 5.16 Stress concentration ratio vs. load cycle

5.3.3 Contact forces and orientations under cyclic loading

Figure 5.17 shows the contact force distribution for the unreinforced and reinforced embankments after 25 load cycles. Similar to Fig. 5.6, black lines indicated compressive contact forces and red lines indicated tensile contact forces. The forces were plotted on the same scale for both unreinforced and reinforced embankments. Comparison of contact force distributions before and after the application of cyclic loads illustrates the effects of cyclic loading on soil arching. Cyclic loading completely disturbed the soil arching that existed before the application of cyclic loading. Table 5.2 lists the coefficient of Fourier

series approximation of the contact and force orientations before and after the application of cyclic loading.

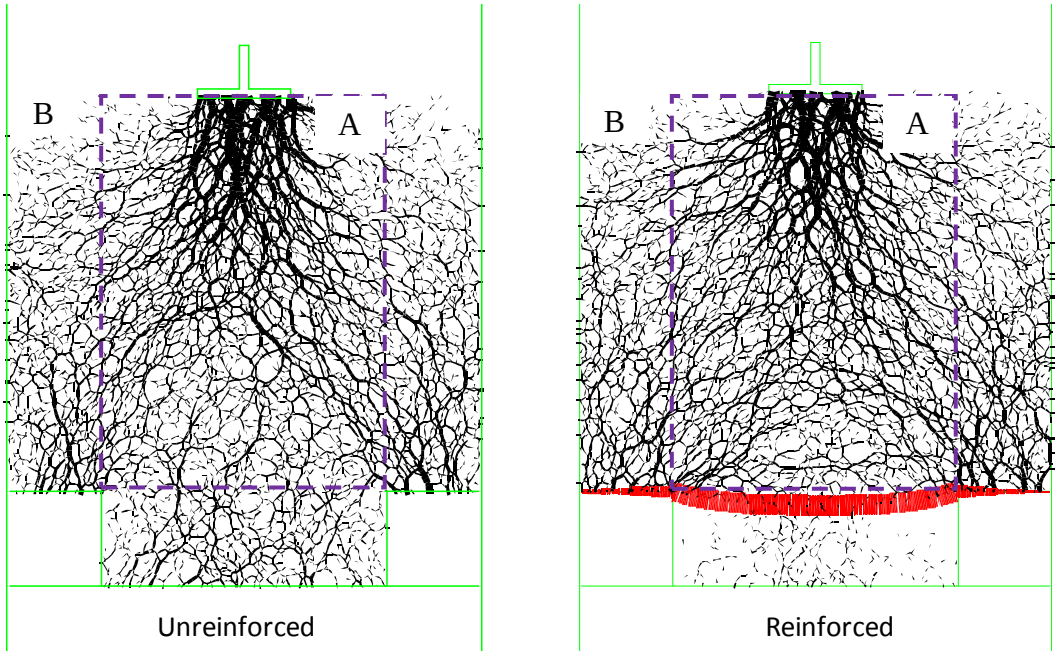

Fig. 5.17 Contact force distribution after 25 load cycles

Table 5.2 Coefficients of the Fourier series approximation before and after load cycles

Coefficients	Before cyclic loading (unreinforced)		After 25 load cycles (unreinforced)		Before cyclic loading (reinforced)		After 25 load cycles (reinforced)	
	Zone A	Zone B	Zone A	Zone B	Zone A	Zone B	Zone A	Zone B
a	-0.010	0.030	0.005	0.013	-0.02	0.040	0.001	0.017
a_n	-0.080	0.330	0.242	0.230	-0.02	0.400	0.179	0.247
a_t	-0.030	0.090	0.053	0.030	-0.02	0.130	0.049	0.035
${\theta_a}^{\circ}$	95.4	74.5	101.1	59.4	93.1	80.9	96.3	72.0
${\theta_f}^{\circ}$	95.4	86.2	96.4	68.6	90.0	83.9	99.9	74.4
${\theta_t}^{\circ}$	95.1	82.5	95.1	65.9	91.1	81.4	91.1	72.2

Figure 5.18 shows the normalized histograms for the contact and force orientations together with the Fourier series approximation for the unreinforced embankment before and after the application of 25 load cycles.

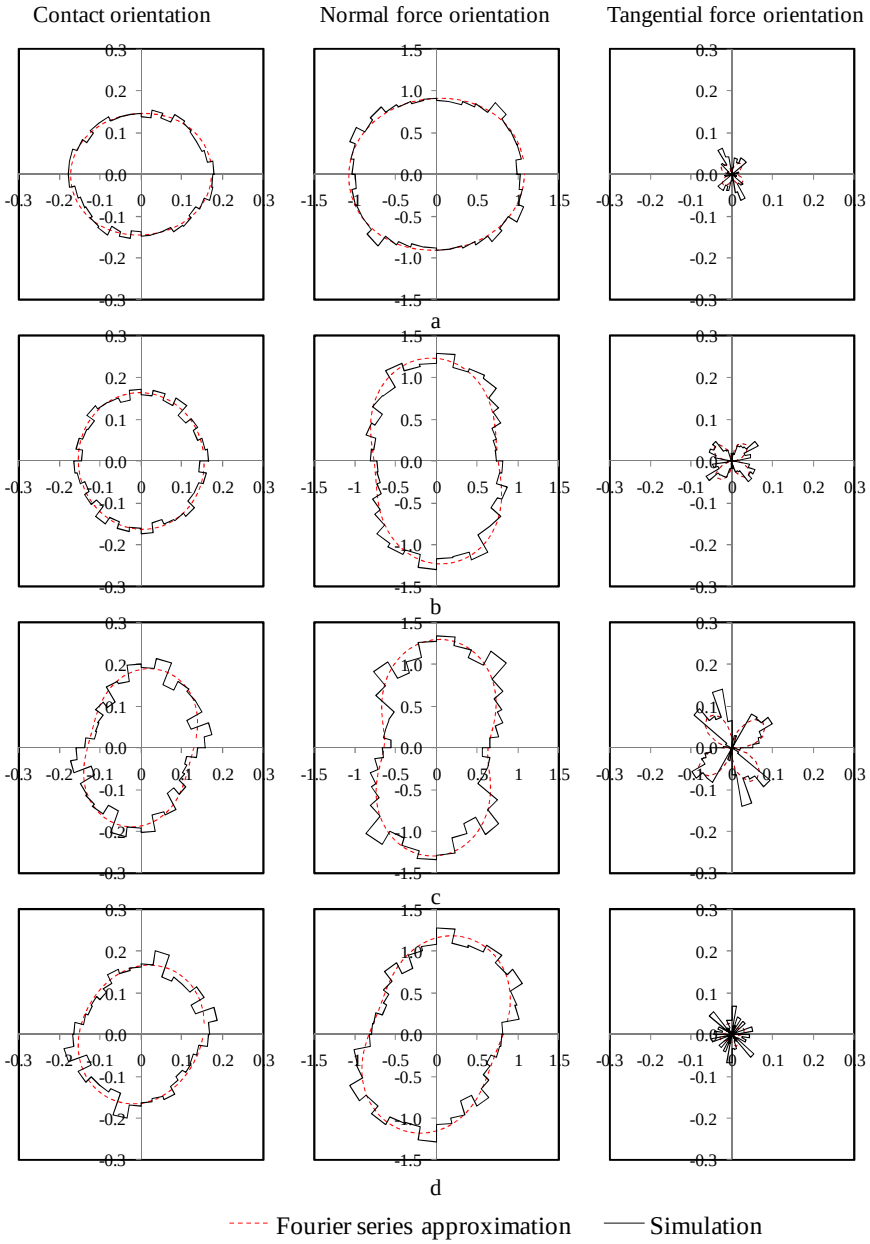

Fig. 5.18 Contact and force orientations for unreinforced embankments: a) before cyclic loading for Zone A; b) after 25 load cycles for Zone A; c) before cyclic loading for Zone B; and d) after 25 load cycles for Zone B

Figure 5.19 shows the normalized histograms for the contact and force orientations together with the Fourier series approximation for the reinforced embankment before and after the application of 25 load cycles.

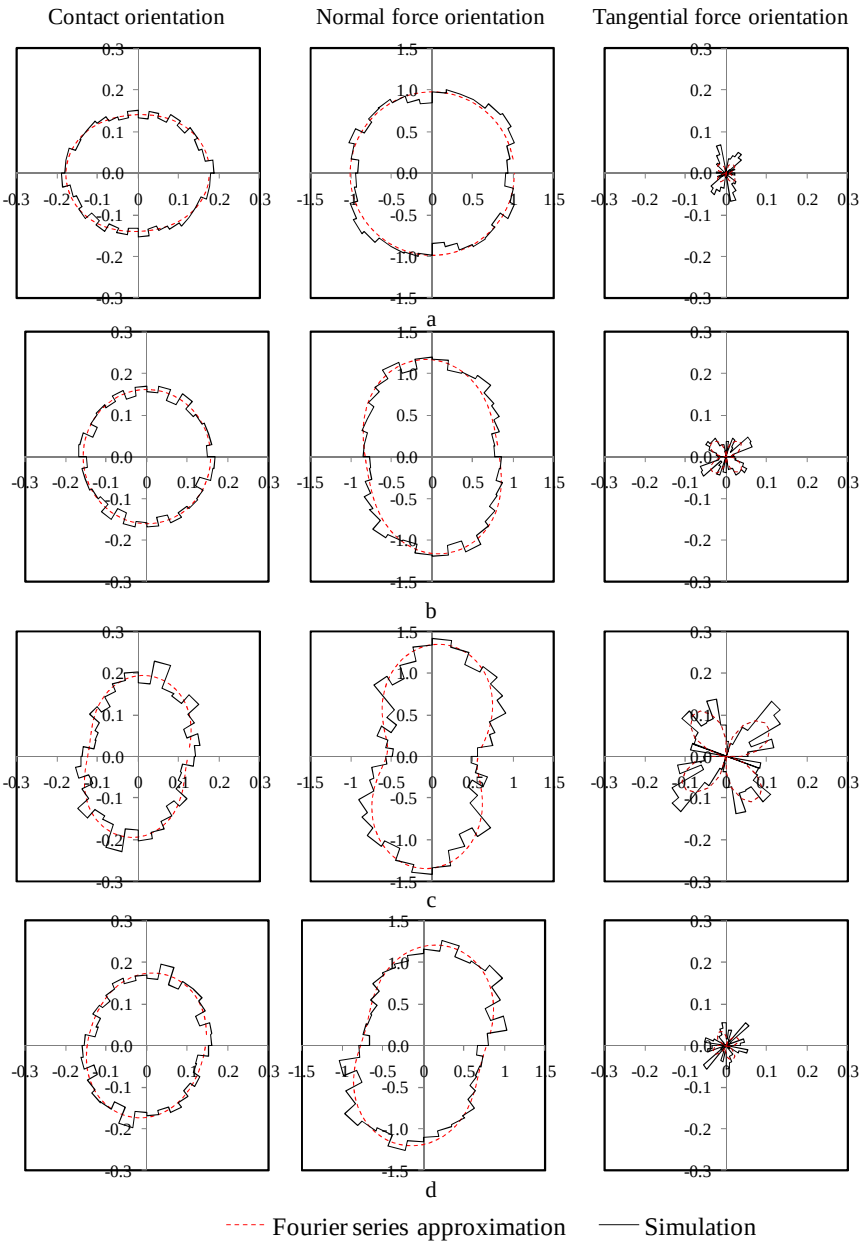

Fig. 5.19 Contact and force orientations for reinforced embankments: a) before cyclic loading for Zone A; b) after 25 load cycles for Zone A; c) before cyclic loading for Zone B; and d) after 25 load cycles for Zone B

Comparison of contact orientations indicated that Zone-A lost few contacts in the horizontal direction and gained in the vertical direction due to the application of 25 load cycles. The nearly isotropic contact force distribution before the application of cyclic loads changed orientation toward the vertical direction after the application of 25 load cycles. Within Zone-B, principal directions of the contacts and the contact normal forces inclined increasingly towards the horizontal direction as the consequence of 25 load cycles. While this observation was applicable for the unreinforced and reinforced embankments, the orientation angles of the principal directions (for contacts and forces) were different for the unreinforced and reinforced embankments as listed in Table 5.2. The changes in orientation angles of the principal directions were larger for the unreinforced embankments that the reinforced embankments. The effects of cyclic loadings were prominent in the unreinforced embankments than the reinforced embankments which were also reflected in a larger reduction of soil arching ratio presented in Fig. 5.16.

5.3.4 Tension in geogrid under cyclic loading

The tensile force distribution along the geogrid with the load cycle is shown in Fig. 5.20. There is a general tendency of an increase in the tensile force of the geogrid with the load cycle. The maximum tension occurred over the edge of the pile caps. Since the principal axis of the contact force orientation in Zone A aligned increasingly towards the vertical direction due to the application of cyclic loading as shown in Figs. 5.18b and 5.19b, the magnitude of the normal force increased in the portion of the geogrid between the pile caps. Therefore, the tensile force in the geogrid increased even between the pile caps while applying the cyclic loading.

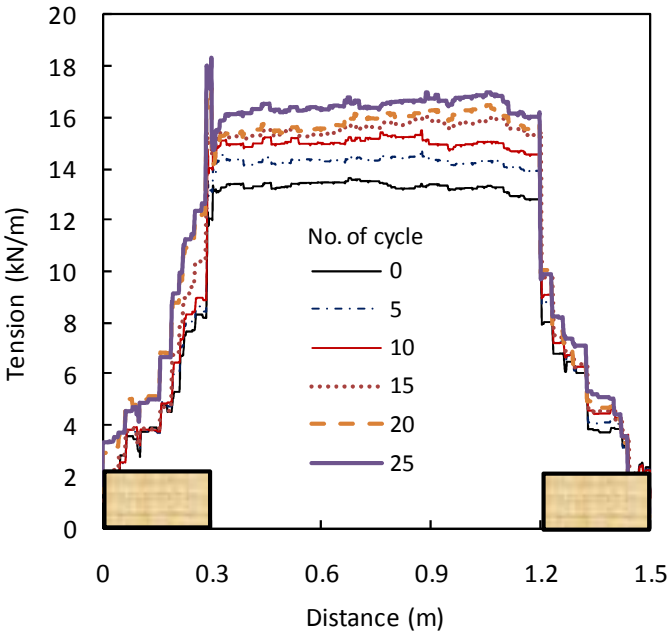

Fig. 5.20 Development of the tension in the geogrid with the load cycle

CHAPTER SIX

BEHAVIOR OF GEOSYNTHETIC-REINFORCED BASES

Improving subgrade or reinforcing base course during pavement construction and service is one of the major applications of geosynthetics. This chapter discusses the DEM study of the geosynthetic-reinforced bases subjected to cyclic wheel loading with a main focus on the interaction between geosynthetic and soil. Geotextile and geogrid-reinforced base courses were simulated. The influences of placement depth of geosynthetics, geosynthetic tensile stiffness, and geogrid aperture size on the interaction between geosynthetic and soil were investigated.

6.1 Geotextile-Reinforced Bases

The DEM analysis in this study was based on the experimental work done by Han *et al.* (2008). In their tests, the Asphalt Pavement Analyzer (APA) machine, originally used to test rutting and fatigue behavior of hot mix asphalt samples in cylinders or beams in test molds, was modified to evaluate the geosynthetic-soil interaction. The original test mold of the APA machine was modified into an aluminum box at dimensions of 0.38 m x 0.45 m x 0.10 m to enable the placement of a geosynthetic sheet in a base layer. Poorly graded, subrounded river sand with a mean grain size of 2.6 mm was used in the laboratory tests. The bases were prepared in four layers at 70.0 % relative density.

Rutting tests were conducted on the bases with and without a geotextile sheet at depths of 25.0 and 12.5 mm below the surface. A load of 88N was applied on a wheel moving on a pressured hose with a diameter of 25.0 mm for 8,000 cycles (one cycle equals to two

passes). A pressurized hose is a rubber pipe with air pressure inside, which is used to apply pressure on the base to simulate the effect of tire pressure. Rut depths were measured at different cycles. Figure 6.1 shows the plot of rut depth versus the number of cycles. It is clearly shown that the rut depth increased significantly at the initial stage of tests while it slowly increased beyond 2,000 cycles. Figure 6.1 shows the benefit of the geotextile in the reduction of the rut depth. Details of these tests can be found in the paper by Han *et al.* (2008).

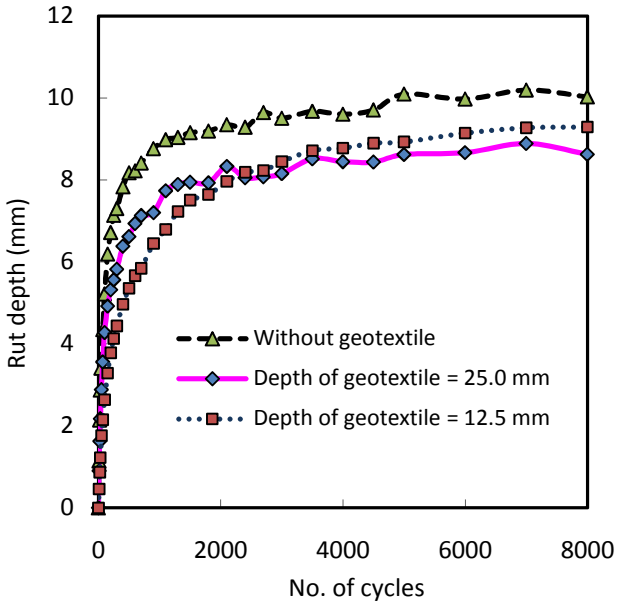

Fig. 6.1 Rut depth vs. the number of cycles (Han *et al.*, 2008a)

The above experiment evaluated the rut depth of geosynthetic-reinforced and unreinforced bases, in which the interaction between geosynthetic and sand was three dimensional in nature. The numerical modeling discussed in succeeding sections, however, is two dimensional. Therefore, the purpose of this study is not to match the experimental results;

instead, it was to qualitatively capture the mechanisms involved in this kind of test and explain the phenomena from the DEM analysis.

6.1.1 Numerical sample preparation

For the numerical simulation, a box was created with the same dimensions in length and height (0.38 m x 0.10 m) as those used in the laboratory tests (Fig. 6.2). The box was enclosed by four walls. First, the box was divided into two compartments to ease the placement of the geotextile. The dimensions of the compartments were chosen so as to mimic the location of the geotextile in the laboratory tests. Cylindrical particles (0.38 m long along the plane of paper) were generated simultaneously in both compartments. The radius expansion technique, as described in Itasca (2004), was chosen to obtain the required 2-D porosities (0.13, 0.16, and 0.19).

The geotextile layer was placed by generating the particles inside the guided walls (Fig. 6.2). After the generation of the geotextile layer, the walls were deleted and a hose was created on the top of the assembly by particles with the same size and properties as the geotextile. The particles were then subjected to the gravity loading, and the inter-particle friction was introduced at this stage. The assembly was cycled to meet the equilibrium of forces. It should be noted that the radius expansion technique generates large forces on the wall, and hence the forces should be brought to an initial at-rest condition. Lateral walls were moved in opposite directions using the numerical servo mechanism until the desired lateral wall force (equal to the lateral earth thrust at the earth pressure coefficient of 1.0) was attained. The vertical and horizontal stresses were monitored at five locations across the horizontal plane at the mid-depth of the base (50 mm). The range of coefficient of lateral earth pressure across the horizontal plane for different models was close to 1.0 and

the difference was less than 0.3. Therefore, there was some variation of the normal contact level in the horizontal direction. This result was the consequence of controlling the porosity of the assembly rather than the stress level within the sample during the numerical sample preparation. However, the wall movement required to achieve the target wall forces was very small (approximately 0.2 mm) and had a marginal effect on the porosity of the assembly. The displacements of all particles were set to zero at this stage so that the vertical displacement and the particle movement measurement would not be affected by the displacements during the sample preparation. The particles attained low velocity (max. velocity = 1E-5 m/sec) and the velocity vectors were randomly oriented ensuring the equilibrium of the assembly. The time step for the analysis was 8.3E-7 which meant the system required 8.3E7 computational cycle for an additional displacement of 0.01mm (Itasca 2004). Obviously, such a small velocity of the particles would have a negligible effect on the numerical results.

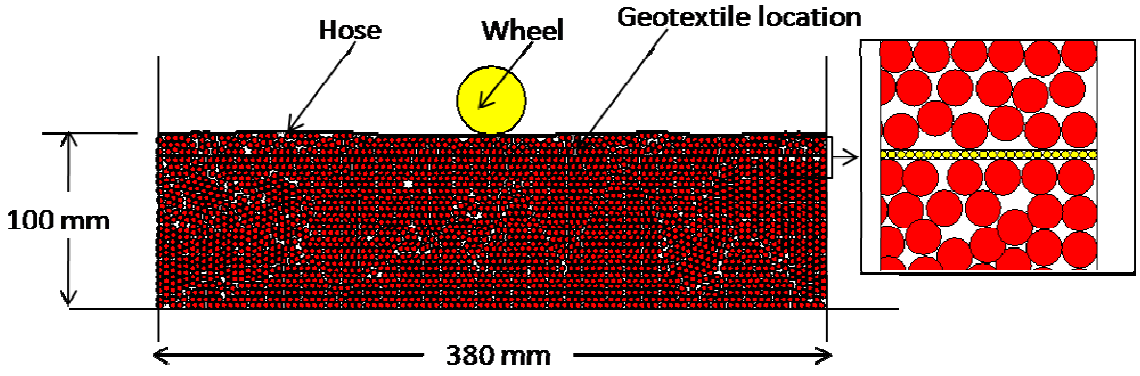

Fig. 6.2 DEM model of an APA test simulation.

6.1.2 Moving wheel load

On top of the hose, a wheel (diameter = 40 mm) was created at the mid-length to apply a cyclic load of 353 N. Higher wheel load (353N) was applied compared to the laboratory tests. It was chosen so as to observe the effects of reinforcement at relatively low number of passes (25 passes) compared to the laboratory tests. This higher wheel load with 25 passes is sufficient to show the benefits of reinforcement while economizing computational time. The moving wheel was given a very small velocity so that the unbalanced particle forces were small at every step of wheel movement. The wheel was moved from the left side of the model and allowed to reach the right side of the model. Once it reached the right end of the model, the velocity sign was changed and the wheel was moved in a reverse direction towards the left end of the model. This process was repeated for 25 passes. After each pass of the wheel, the average rut depth was monitored. To evaluate the rut depth, the positions of all particles representing the hose were measured and averaged to calculate the current height of the unreinforced or reinforced section. The change in height of the section was taken as the rut depth for a given number of passes.

Four cases were considered for the numerical simulation. In the first reference case, the geotextile was not placed and the model was run without any reinforcement. In the second case, the geotextile was placed at a depth of 12.5 mm below the top surface. In the third case, the geotextile was placed at a depth of 25.0 mm below the top surface. The particles of small diameter used to model the geotextile may create a slippage plane; therefore, their effect was studied using a sheet of tiny particles without any bonding strength at 25 mm below the top surface as the fourth case. The above four cases are named as Case I, Case

II, Case III, and Case IV, respectively and will be referred accordingly. The first three cases qualitatively represent the laboratory tests.

6.1.3 Contact forces due to a moving wheel load

The contact forces, when the wheel load was at center of the model after 25 passes, are shown in Figs. 6.3 to 6.5 for dense packing assembly (n = 0.13). Similar contact force distributions were obtained upon the application of a moving wheel load on loosely-packed bases, therefore, they are not presented herein. The thickness of force chains shows its relative magnitude. Figure 6.3 shows that the contact forces are symmetrical beneath the wheel in absence of reinforcement. The geotextile reinforcement changed the contact force distribution in the assembly. The geotextile reinforcement at 12.5 mm below the top surface caused contact forces to branch out and distribute widely. The branching and wide distribution of contact forces were less when the geotextile reinforcement was 25.0 mm below the top surface as compared to the geotextile reinforcement at 12.5 mm below the top surface. Figure 6.4 shows that geotextile reinforcement helps distribute the contact forces developed upon wheel loading to a wider area beneath the reinforcement layer.

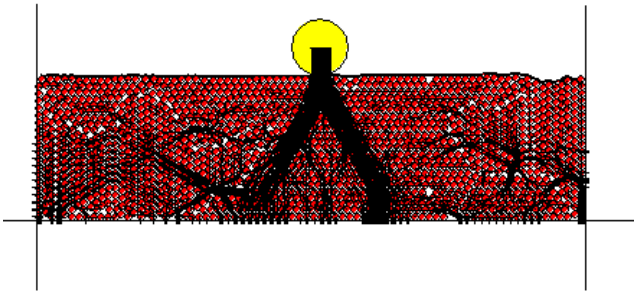

Fig. 6.3 Contact force distribution for the densely-packed unreinforced model (n=0.13)

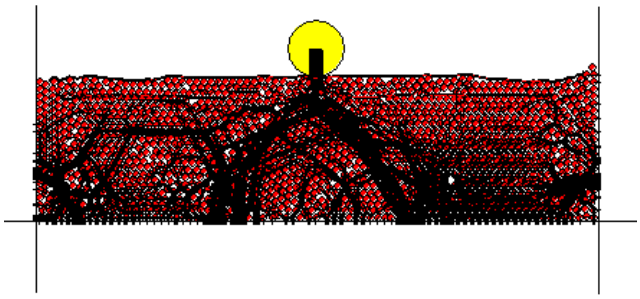

Fig. 6.4 Contact force distribution for the densely-packed model reinforced at 12.5 mm below the top surface (n=0.13)

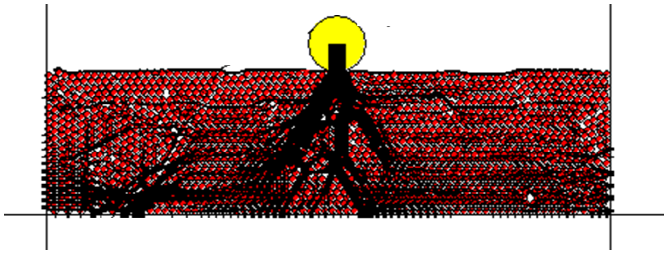

Fig. 6.5 Contact force distribution for the densely-packed model reinforced at 25.0 mm below the top surface (n=0.13)

6.1.4 Rut depths due to a moving wheel load

To evaluate the benefits of geotextile reinforcement, the rut depth was calculated at the end of each pass. The height of the unreinforced or reinforced section after the first pass of the wheel loading was taken as the reference point to alleviate any changes in thickness during the model preparation. Subsequently, rut depths were measured from this height. The rut

depth versus the number of passes is plotted for different geotextile locations as shown in Figs. 6.6 to 6.8. Similarly, the rut depth versus the number of passes is plotted for different porosities as shown in Figs. 6.9 to 6.11. The rut depths at the end of 25 passes are summarized in Table 6.1.

Table 6.1 Summary of rut depths at the end of 25 passes

2D-porosity (n)	Rut depth without geotextile (mm)	Rut depth with geotextile at 12.5 mm (mm)	Rut depth with geotextile at 25.0 mm (mm)	Rut depth with a sheet of tiny particles at 25.0 mm (mm)
0.13	0.211	0.308	0.370	0.517
0.16	0.884	0.393	0.679	0.788
0.19	1.311	1.093	1.507	1.585

Figure 6.6 shows that the unreinforced base had least rut depths than all other bases because the lateral movement is a dominate effect on the rut depths at a dense assembly and the vertical movement is minimal. The geotextile at either 12.5 or 25.0 mm deep had an effect on the rut depths; therefore, the influence depth in the dense base was more than 25.0 mm. The geotextile at 12.5 mm deep had a slightly more benefit than that at 25.0 mm.

Figure 6.7 presents the results corresponding to the behavior of medium dense bases. Under this condition, the unreinforced base had the largest rut depths because the vertical movement became important. The benefit of the tensile strength of the geotextile is demonstrated as compared with the case with a sheet of particles. In addition, the geotextile at a depth of either 12.5 mm or 25.0 mm had an effect on the rut depths; therefore, the influence depth in the medium dense base was more than 25.0 mm. The

geotextile at 12.5 mm deep had a slightly more benefit than that at 25mm. These DEM results are consistent with those from the experimental tests shown in Fig. 6.1. Therefore, the medium dense base at a porosity of 0.16 will be used for analysis in the succeeding sections.

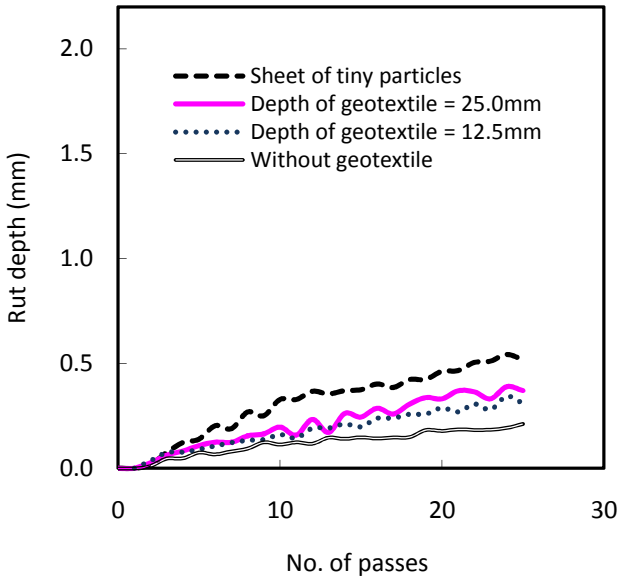

Fig. 6.6 Rut depth vs. the number of passes at n=0.13

Figure 6.8 presents the results corresponding to the behavior of loose bases, which is not common in practice. Under this condition, obviously vertical movement of particles is dominant. Unlike the medium dense condition, the cases with the geotextile and the sheet of particles at 25.0 mm deep had very similar rut depths as the unreinforced base. The geotextile at 12.5mm deep significantly reduced the rut depths as compared with the unreinforced base. Therefore, the influence depth of the wheel loading on a loose base was between 12.5 to 25.0 mm due to local deformation and failure, which is less than those in dense and medium dense bases. The significant benefit of the geotextile at 12.5 mm is attributed to the reduction of contact forces below the geotextile as shown in Fig. 6.4.

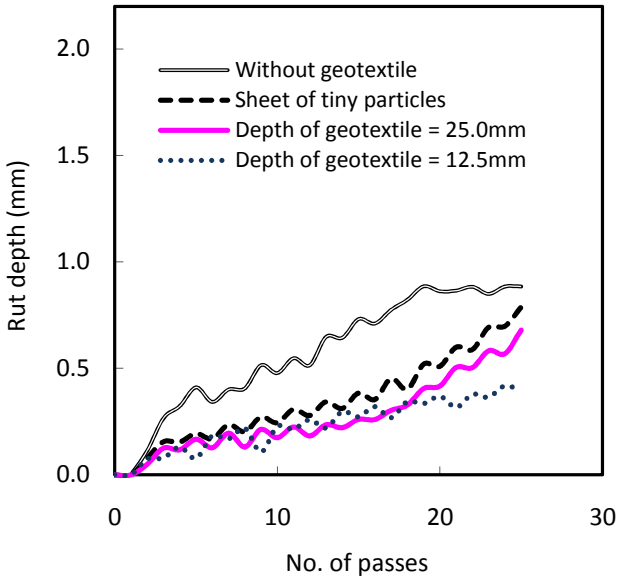

Fig. 6.7 Rut depth vs. the number of passes at n=0.16

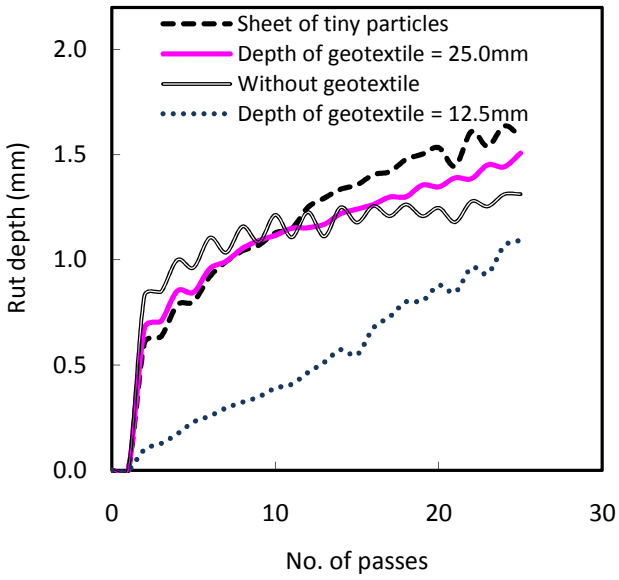

Fig. 6.8 Rut depth vs. the number of passes at n=0.19

Upon wheel loading, particles can move in the vertical and horizontal directions. Both movements can induce rutting on the surface. The geotextile can minimize particle vertical movement; however, it can promote particle horizontal movement due to slippage. The overall rutting depends on the magnitudes of vertical and horizontal movements. In addition, the density of soil would affect the mode of deformation or failure. It is well known that a local failure likely occurs in loose sand while a general failure likely occurs in dense sand. The local failure has a shallower influence depth while the general failure has a deeper influence depth. These phenomena can be found from the DEM results in Figs. 6.6 to 6.8. Comparing the results with a sheet of particles to those with the geotextile at the same depth (25.0mm), the geotextile with a tensile (bonding) strength had less rut depths than the sheet of particles without any tensile strength. This comparison implies that the tensile stress develops in the geotextile due to the sliding of particles above the geotextile. The geotextile can resist the tensile force; the sheet of particles without any bond cannot resist the tensile force required to minimize the vertical movement of particles. Comparing the results with a sheet of particles to those without geotextile (particles randomly distributed), the existence of a sheet of particles significantly increased the rut depths due to the slippage at the sheet of particles.

Particle porosity has significant effects on rut depths which can be observed from Table 6.2 and Figs. 6.9 to 6.11. For low packing density, i.e., high porosity (n = 0.19), the rut depth was highest. The increase in density from medium dense to dense marginally reduced the rut depths. Under the conditions shown in Figs. 6.9 to 6.11, the base with a sheet of tiny particles had the highest rut depths because of the ease in vertical and lateral displacements.

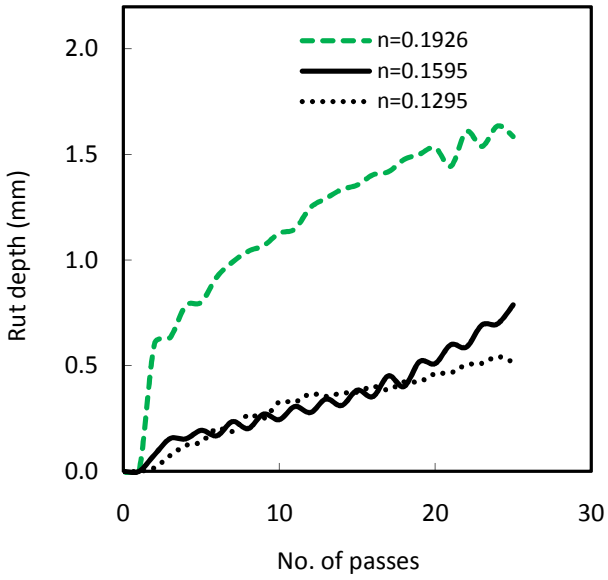

Fig. 6.9 Rut depth vs. the number of passes with a sheet of particles

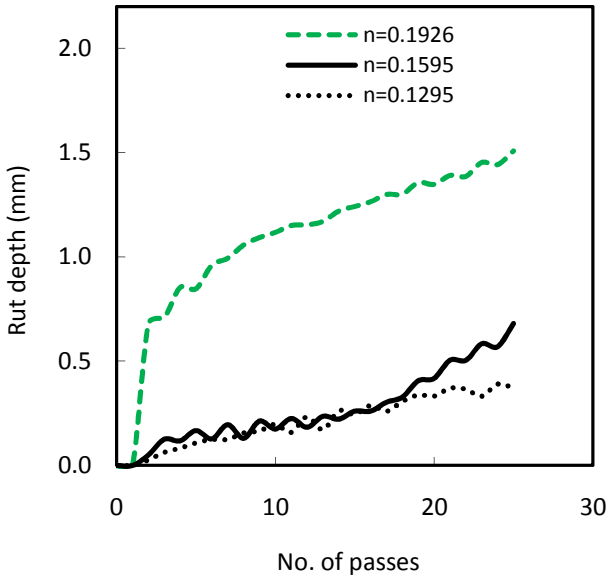

Fig. 6.10 Rut depth vs. the number of passes with the geotextile at depth of 25.0 mm

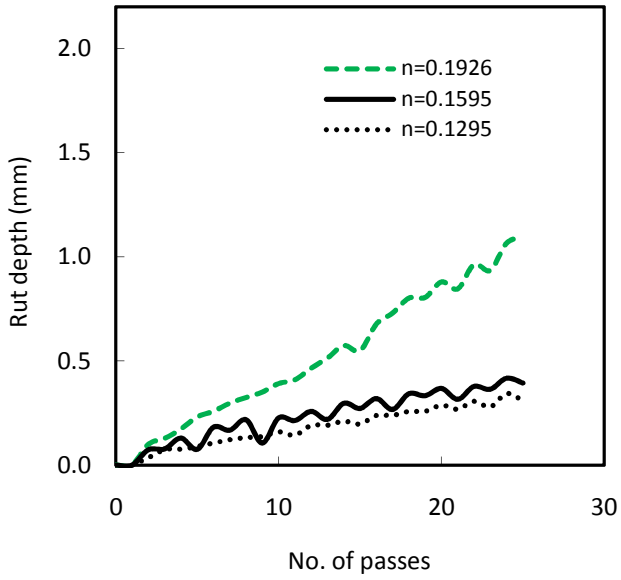

Fig. 6.11 Rut depth vs. the number of passes with the geotextile at depth of 12.5 mm

6.1.5 Vertical wheel load

In the previous section, the behavior of the unreinforced and geotextile-reinforced bases at different porosities was investigated when the bases were subjected to a moving wheel load. However, the two-dimensional model of a moving wheel load closely simulated a compactive effort than a localized failure beneath the hose that was observed in the experiments. Therefore, the medium dense bases (n = 0.16) were subjected to a cyclic wheel load in the vertical direction. The wheel had a restriction on movement in the horizontal direction. The contact normal shear stiffness values of this wheel were the same as those of the particles. The dead load of the wheel was 36.5 N (note that the cylinderical particles were 0.38 m long along the plane of paper, and the iron wheel (density ρ = 7800kg/m^3) was considered). Hence in the cyclic model test, the wheel load was 389.5 N under a loading condition and 36.5 N under an unloading condition.

A 353 N load was applied to the wheel on the assembly. The assembly was solved until the ratio of the maximum unbalanced force to the maximum contact force reached the value of 0.01 (default in the PFC^{2D}). The load was removed from the wheel and the assembly was again solved in the similar way. This loading and unloading process was repeated for 25 cycles (i.e. 25 loadings and 25 unloadings). Note that 25 cycles is equivalent to 50 passes. The number of cycles was chosen after some initial trials that would achieve a constant displacement. On each loading and unloading of the wheel, the vertical displacement was calculated. To evaluate the vertical displacement, the new position of the loading wheel was monitored.

The stiffness of the geotextile was changed in a parametric study to investigate its effect on the geotextile-soil interaction. For all numerical models, the same procedure was followed to prepare the samples so that the results can be compared without any adverse effect of model preparation. As random generation of particles was used to create the numerical models, the uniqueness of the results can be questionable. The uniqeness of the results was verified by creating the another random assembly with same material properties, boundary, and loading conditions to achieve the same numerical results.

6.1.6 Vertical permanent displacement

The vertical permanent displacement vs. the number of cycles is shown in Fig. 6.12. The model with a sheet of tiny particles (Case IV) had the maximum deformation followed by those with the geotextile at a depth of 25.0 mm (Case III), without a geotextile (Case I), and with the geotextile at a depth of 12.5 mm (Case II). In the experimental study (Han *et al.* 2008), the geotextile placed at a depth of 25.0 mm (Case III) resulted in less deformation than the unreinforced case (Case I) while in the numerical study, the

geotextile placed at a depth of 25.0 mm had higher deformation than the unreinforced case (Case I). The reason for this difference may be attributed to different particle shapes and size distributions. Angular particles with different sizes in the experiment tend to interact with the geotextile better to minimize lateral movement of particles.

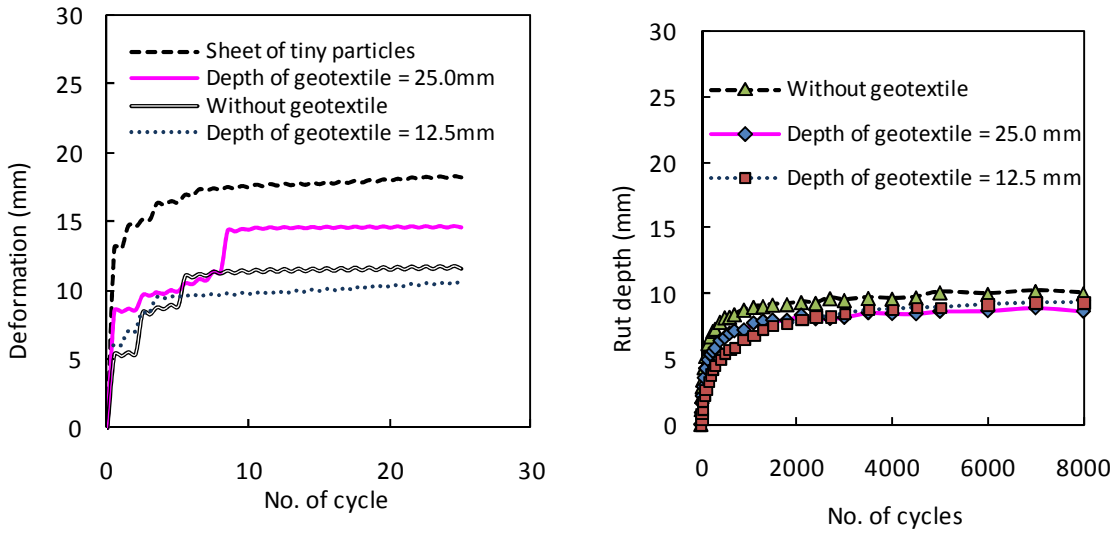

a) Simulation result

b) Experimental result

Fig. 6.12 Comparison of numerical results at particle porosity of n=0.16 (medium dense sand) with experimental results

Figure 6.12a shows the curves with steps in the two cases with the geotextile placed at a depth of 25.0 mm (Case III) and without a geotextile (Case I). These results could be due to a limited number of particles and a formation of a quasi-stable configuration of the particles during simulation, which collasped with additional loading and unloading steps. The use of large number of particles is expected to improve the smoothness of the curves but require significant computation time. Towards the end of simulation, an increase of cycles did not increase the deformation. This phenonemon shows that 25 loading-

unloading cycles adopted in this study are adequate to achieve a stable deformation state. In the discrete element analysis of railway degradation, Lobo-Guerrero and Vallejo (2006) noticed a stable permanent deformation after 60 cycles, which are higher than that obtained in this study. Different model heights, loading conditions, and porosities may result in this difference. Guerrero and Vallejo (2006) used a 0.6-m high model generated at a porosity (n) of 0.2, which required more cycles for a stable permanent deformation than that in this study.

The loading-unloading cycles for the two cases with the maximum and minimum vertical deformations are shown in Figs. 6.13 and 6.14. In both cases, the initial cycles consist of elastic and plastic deformations. With an increase of cyles, the elastic deformations became dominant and the hysteresis behavior diminished. The load-deformation behavior as depicted in Figs. 6.13 and 6.14 shows that the geotextile at a depth of 12.5 mm doubled the stiffness of the model as compared with a sheet of tiny particles. A similar comparison, when the geotextiles were placed at depths of 12.5 and 25.0 mm, shows the stiffness ratio ($k_{12.5}/k_{25.0}$) of 1.42, where $k_{12.5}$ and $k_{25.0}$ are the stiffness of the models when reinforced with a geotextile at the depths of 12.5 mm and 25.0 mm respectively.

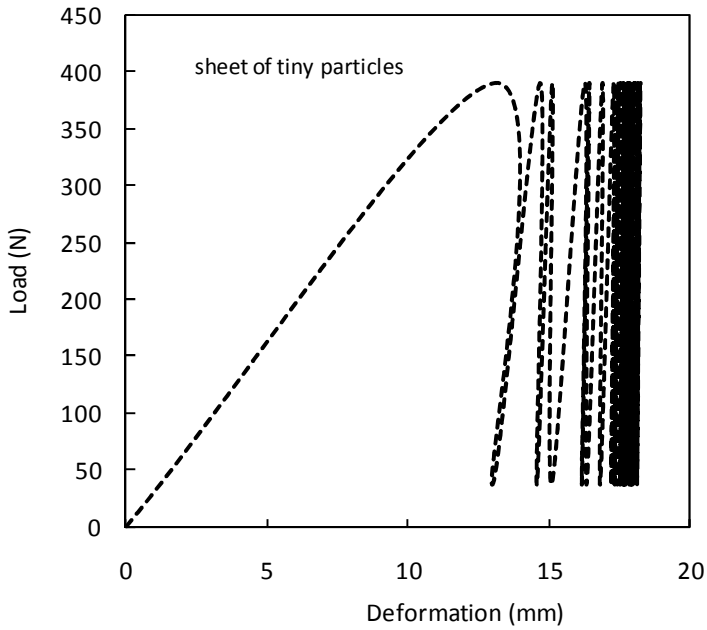

Fig. 6.13 Loading-unloading cycles for the model with a sheet of tiny particles at a depth of 25 mm

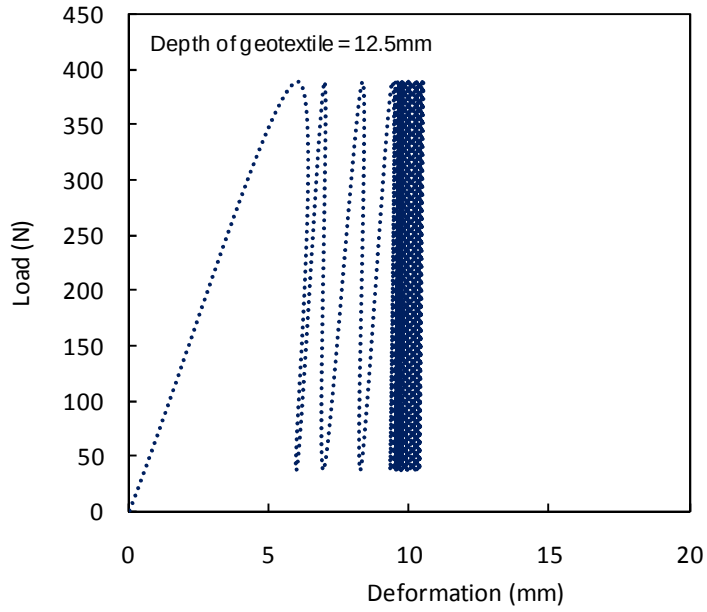

Fig. 6.14 Loading-unloading cycles for the model with a geotextile at a depth of 12.5 mm

6.1.7 Stresses in geotextile

Whenever a geotextile was used, the principal stresses of the particles that represented the geotextile were calculated. The stresses (σ_x, σ_y, and τ_{xy}) in the particles that represented the geotextile were recorded at the end of 25 cycles (a loading stage). The tension in the getextile can be calculated using these stresses as explained in Section 4.3.2.

The variation of the tension in the geotextile along the width of the model is shown in Fig. 6.15. The maximum tension in the geotextile increased by 2.3 times when it was placed at a depth of 12.5 mm as compared with that at a depth of 25.0 mm.

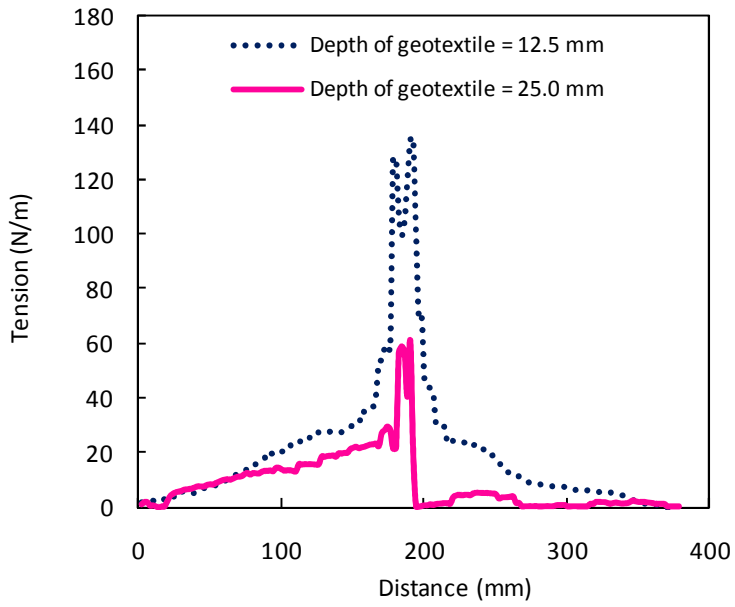

Fig. 6.15 Maximum tension in the geotextiles

The tensile strain of the geotextile is related to its tensile stress by the following relation:

$$\varepsilon_1 = \frac{\sigma_1}{E} = \frac{\sigma_1}{(J/t)} \qquad \text{Eq. 6.1}$$

where, ε_1 = the tensile strain;

σ_1 = the tensile stress;

J = the tensile stiffness;

t = the thickness of the geotextile.

The maximum tensile strains developed in the geotextiles were 0.038 and 0.0174% when the geotextiles were placed at depths of 12.5 and 25.0 mm, respectively. This result proves that only a small fraction of the geotextile strength was mobilized in the reinforced base under the simulated cyclic loading. The computed strains in the geotextile in this study were lower than those of Miura *et al.* (1990) and Hufenus *et al.* (2006) as previously discussed in Chapter Two. The reasons for the lower strains in this study are (1) a lower vertical load of 353 N was applied and (2) the subgrade was firm. Under such a low strain, the benefit of the geotextile as a tensioned membrane is minor. Therefore, the contribution of the geotextile in the base is to provide vertical confinement to particles above the geotextile, i.e., separation, which will be discussed in the following section.

6.1.8 Role of the geotextile in particle movement

Figures 6.16 to 6.19 present displacement vectors of soil particles due to the cyclic wheel loading for four cases. The magnitudes of the displacement vectors were based on the same scale as that in the worst case (Case IV), which had the maximum vertical

deformation. Figure 6.16 shows that the soil particles in the unreinforced section under the load moved downward and laterally, in which a large portion of particles moved downward. However, Figures 6.17 and 6.18 both show that the geotextile helped minimize vertical movement of particles as compared with that in the unreinforced section in Fig. 6.16. The enlarged view of the particle displacement vectors clearly illustrates the role of geotextile in preventing the vertical movement of particles (Fig. 6.17). When the geotextile was placed at a depth of 12.5 mm, the geotextile attained a curved shape and the vertical displacement of the particles continued beneath the geotextile layer. However, the contact bond between particles that represented the geotextile remained intact (Fig. 6.18). The enlarged view of the displacement vectors in Fig. 6.18 also shows a slippage of particles towards the left side of the model. As shown in Fig. 6.19, the largest particle movement occurred when a sheet of tiny particles with a smaller contact friction (0.8 times the contact friction of sand) and zero bonding strength existed. This result is anticipated because the sheet of tiny particles with weaker friction contact facilitates horizontal as well as vertical movements of particles. The case with the sheet of tiny particles does not exist in the field, however, it sets up a baseline for understanding the mechanisms involved in the geotextile.

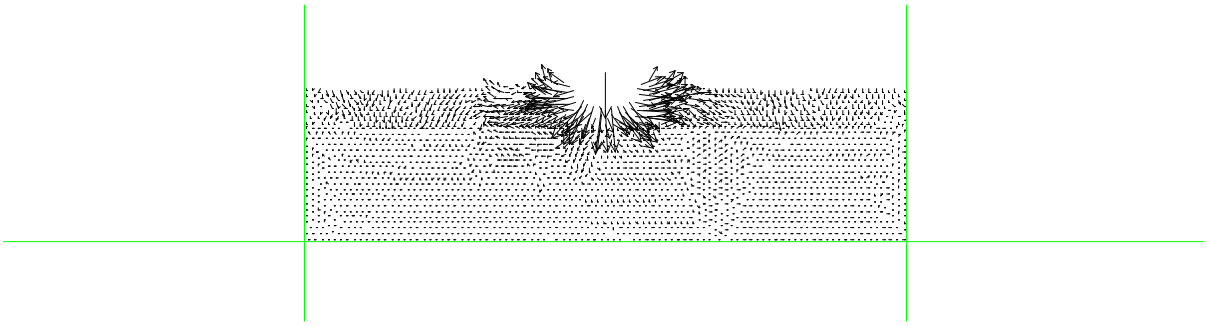

Fig. 6.16 Displacement vectors of particles in the base without a geotextile (the maximum displacement = 13.3 mm and the deformation under the wheel =11.7 mm)

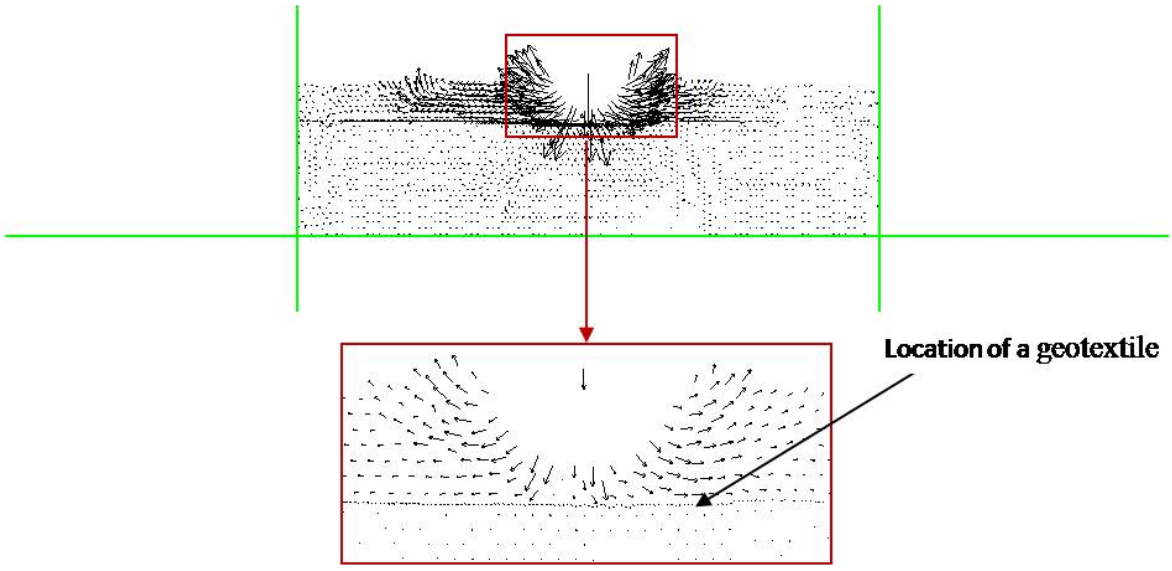

Fig. 6.17 Displacement vectors of particles in the base with a geotextile at a depth of 25 mm (the maximum displacement = 15.7 mm and the deformation under the wheel =14.6 mm)

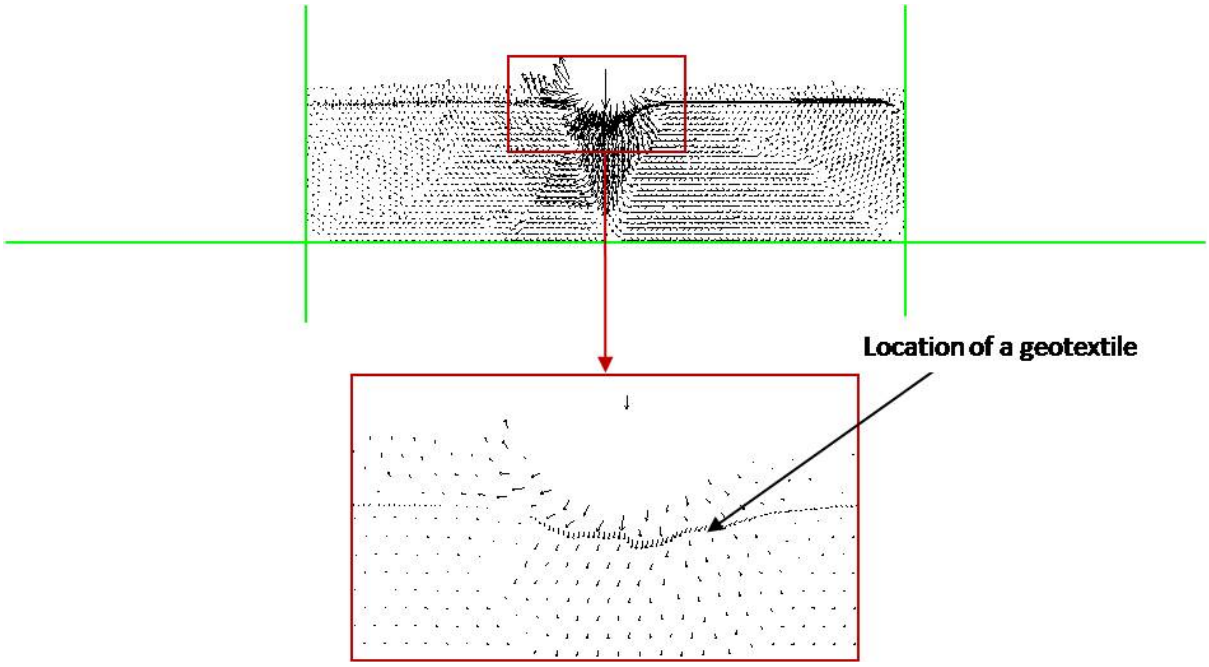

Fig. 6.18 Displacement vectors of particles in the base with a geotextile at a depth of 12.5 mm (the maximum displacement = 11.8 mm and the deformation under the wheel =11.7 mm)

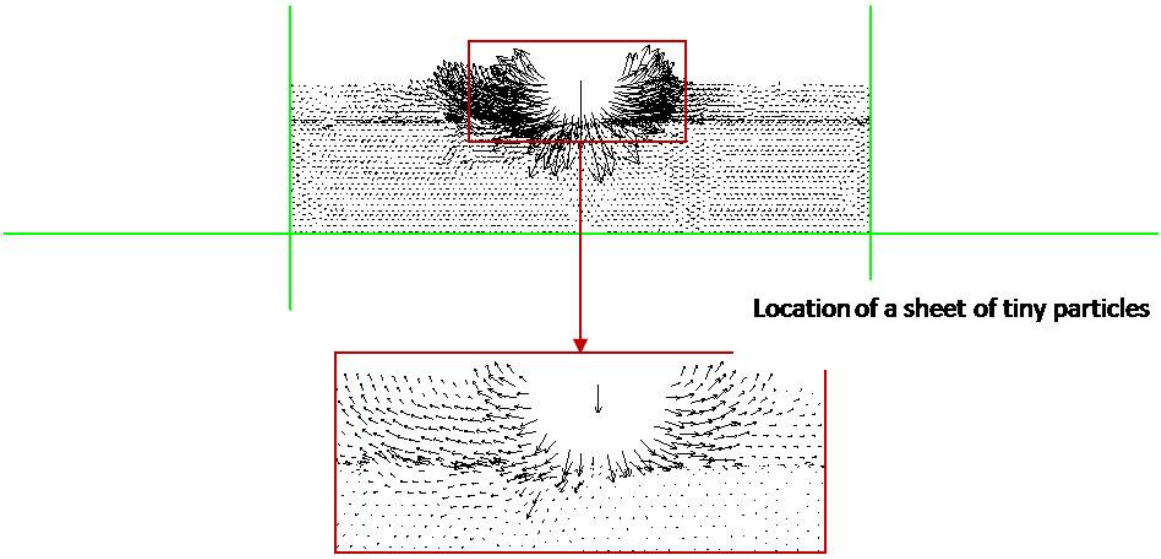

Fig. 6.19 Displacement vectors of particles in the base with a sheet of tiny particles at a depth of 25.0 mm (the maximum displacement = 20.4 mm and the deformation under the wheel =18.3 mm)

In the geotextile-reinforced base, the geotextile had a relatively strong bonding strength but weak friction resistance. As a result, two opposing mechanisms existed: restricting the vertical movement of particles and facilitating the horizontal movement of particles. If the vertical movement of particles restricted by the geotextile is larger than that due to the facilitated horizontal movement of particles, less deformation would occur (for example, the geotextile placed at a depth of 12.5 mm (Case II)) and vice versa (for example, the geotextile placed at a depth of 25 mm (Case III)). When the geotextile was placed at a depth of 25.0 mm (Case III), the vertical deformation on the surface was mostly cumulative from the soil above the geotextile. Therefore, the effect of the geotextile in reducing the vertical deformation is limited. However, when the geotextile was placed at a depth of 12.5 mm (Case II), the vertical deformation on the surface was cumulative from

the soil above and below the geotextile. Therefore, the existence of the geotextile at this depth prevents the particles from moving upward outside the loading area and downward within the loading area, thus reducing the vertical deformation.

6.1.9 Influence of the stiffness of a geotextile on interaction

During the DEM analysis, it was observed that the geotextile particles always held together and the tensile failure of the geotextile was not an issue. Therefore, stiffness of the geotextile is more relevant than the bond strength to the performance of the geotextile-reinforced sand.

Figure 6.20 shows the effect of the stiffness of a geotextile on the vertical deformation under the cyclic load. To investigate the effect of the stiffness of a geotextile, the stiffness in the baseline case (J=350 kN/m at 10% strain) was increased by 10 and 100 times. The plotted vertical deformations were obtained at the end of 25 cycles (the loading stage) at different stiffness ratios as compared with those in the baseline case. The tenfold-increase in the stiffness of the geotextile had a marginal benefit on minimizing the vertical deformation for the geotextile either at a depth of 12.5 or 25.0 mm. Further increase of the stiffness of the geotextile by 100 times showed an improved benefit on minimizing the vertical deformation. However, the benefit was less significant for the geotextile at 25.0 mm deep as compared with that at 12.5 mm deep.

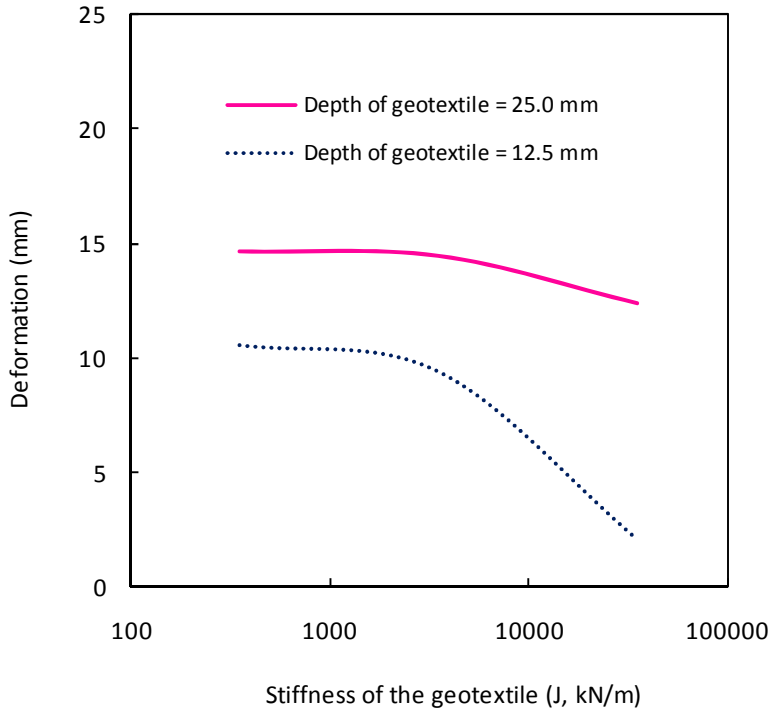

Fig. 6.20 Deformation vs. stiffness of the geotextile

Figure 6.21 shows loading-unloading cycles of the reinforced base with hundred-fold stiffness of the geotextile placed at a depth of 12.5 mm. As compared with the geotextile placed at the same depth (12.5 mm) in the baseline case (Fig. 6.14), Fig. 6.21 shows both elastic and plastic deformations developing within the entire loading-unloading cycles. Even though the geotextile with a high stiffness could control the plastic deformation at the initial loading-unloading cycles, the hysteresis behavior continued up to the end of the analysis due to the continuous re-arrangement of the particles. Therefore, the stiffer geotextile promoted continuous re-arrangement of the particles.

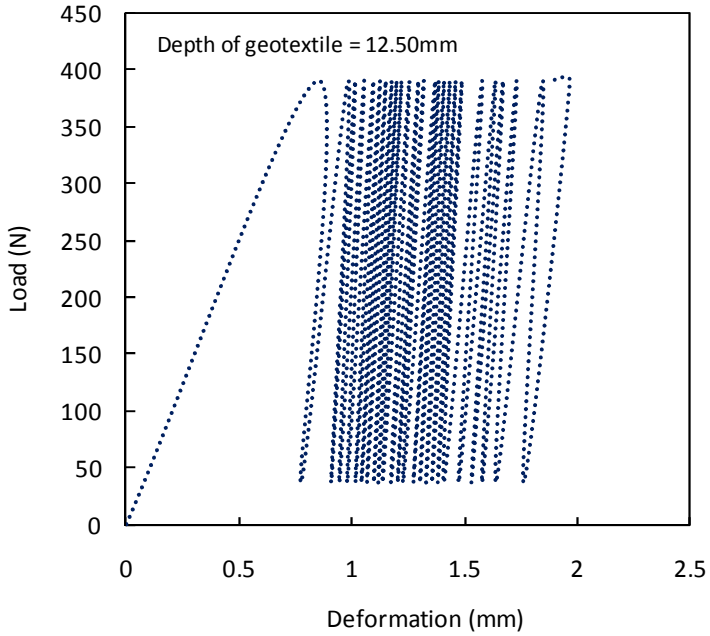

Fig. 6.21 Loading-unloading cycles for the geotextile with 100J at a depth of 12.5 mm

6.2 Geogrid-Reinforced Base

It is well accepted that the interlocking of the aggregates with the geogrid is the primary factor responsible for the improved performance of the geogrid-reinforced aggregate (base) (Konietzky *et al.* 2004; Leng and Gabr 2006; McDowell *et al.* 2006, Qian *et al.* 2010). However, the mechanisms of the geogrid-aggregate interaction under wheel loading are not well understood. It was expected that the DEM model of the geogrid-reinforced base would provide better understanding of the distribution of contact forces and the resilient behavior under this condition.

6.2.1 Numerical sample preparation

An unpaved road with a rigid subgrade was selected for the simulation in this study. To investigate the interaction of the geogrid and the aggregate, the influence of the subgrade was excluded from the analysis in this study. A 2.5 m wide and 0.303 m high box was created by four walls. First, the box was divided into two compartments to ease the placement of the geogrid. The dimensions of the compartments were chosen so as to place the geogrid at one of two depths of the base. Particles were generated simultaneously in both compartments. The radius expansion technique, as described in Itasca (2004), was chosen to obtain the required 2-D porosity (n=0.16). Uniform particles were selected in this study. The mechanical behavior of the uniform particles was discussed in Section 3.3.3.

After the particles were generated, the assembly was cycled to meet the equilibrium of forces. It should be noted that the radius expansion technique generates large lateral forces on the wall, and hence the forces should be brought to an initial at-rest condition. Lateral walls were moved in opposite directions using the numerical servo mechanism until the desired lateral wall force (equal to the lateral earth thrust at the earth pressure coefficient of 1.0) was attained. The wall movement required to achieve the target wall forces was very small (approximately 1.5% of the wall width in each direction) and had a marginal effect on the porosity of the assembly. The displacements of all particles were set to zero at this stage so that the vertical deformation and the particle movement measurement would not be affected by the displacements during the sample preparation. The particles attained a low velocity (1E-5m/step) and the velocity vectors were randomly oriented ensuring the equilibrium of the assembly. Such a low velocity would have a negligible

effect on the numerical solution. Therefore, the velocity of the particles was not set to zero.

The geogrid layer was placed by generating the particles inside the guided walls, and the inter-particle friction was introduced at this stage. The walls that enclosed the geogrid were deleted. A string of bonded particles, 5 mm in diameter, was generated on the top of the assembly with an equivalent cohesive strength of 20 kPa. This thin top layer shown in Fig. 6.22 created a stable surface of the unpaved road to prevent particles from flying away during the cyclic loading. In absense of this top layer, the escaping particles would increase the computational time. A relatively small cohesion of 20 kPa allowed the string of top layer to break the bond under the applied load just beneath the wheel while maintaining the integrity away from the wheel. For simplicity, the properties of the particles comprising the top layer were maintained same as those of the aggregates in the base layer other than the contact bond strength.

A 300 mm diameter wheel was created on top of the assembly at the mid-length to apply a cyclic load. The cyclic wheel load was applied vertically and no horizontal movement was allowed. The contact normal and shear stiffness values of this wheel were the same as those of the aggregate particles. Further, the frictional coefficient of the wheel was identical with the aggregate particles. The dead load of the wheel was 451N (note that the cylinders were 0.25 m long along the plane of paper for this model, and the wheel density (ρ) was 2600kg/m^3). The cylinders of 0.25 m long were selected so that the resulting stress due to a 40-kN load simulate the typical tyre pressure applied to the roadways.

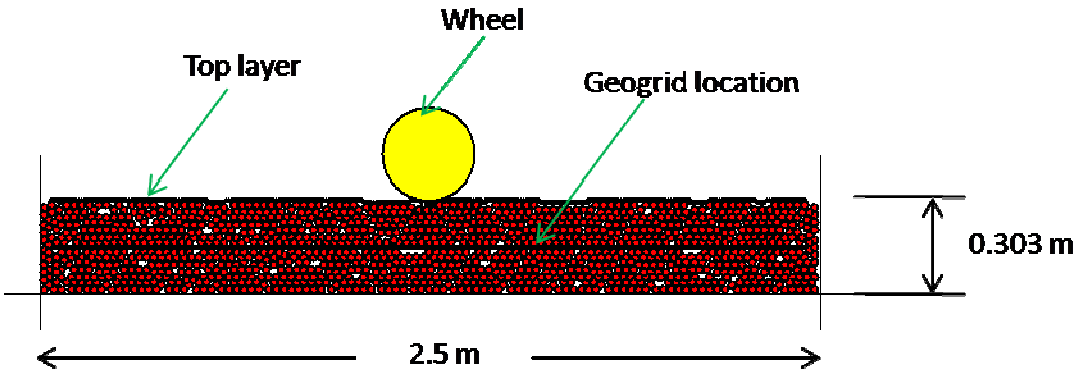

Fig. 6.22 DEM model of a geogrid-reinforced base

After the load was applied to the wheel on the assembly, the assembly was solved until the ratio of the maximum unbalanced force to the maximum contact force reached the value of 0.01 (default in the PFC^{2D}). The load was removed from the wheel and the assembly was again solved in the similar way. This loading and unloading process was repeated for 25 cycles (i.e. 25 loading and 25 unloading). The total number of steps for each simulation depended on the location of the geogrid and the applied load. The approximate steps for achieving equilibrium during the sample preparation were 1.5E6. When 40.45 kN cyclic load was applied for 25 cycles, the assembly required an additional 2.3E6 steps to complete the simulation. On the other hand, when 5.45 kN cyclic load was applied for 25 cycles, the assembly required an additional 1.3E6 steps to complete the simulation. Therefore, the approximate loading frequencies for the numerical simulation were 1.9E-5 and 1.5E-5 cycles/step for the 40.45 and 5.45 kN applied loads respectively. On each loading and unloading cycle of the wheel, the vertical deformation was calculated. To evaluate the vertical displacement, the new position of the wheel was monitored. In this study, three cases were considered for the numerical simulation. In the first reference case, no geogrid was placed and the model was run without any reinforcement. In the second

case, the geogrid was placed at 303 mm below the top layer (i.e., on top of the subgrade). In the third case, the geogrid was placed at 152 mm below the top layer. The selection of these two depths of the geogrid was based on the typical practice for base reinforcement, i.e., the geogrid reinforcement is mostly placed at the bottom of the base course or at the mid-depth of the base course.

The principal stresses of the particles that represent the geogrid were monitored using a user written FISH function. The principal stresses were used to calculate the tensile forces on the geogrid. The vertical load on the wheel, including the weight of the wheel, was varied in the range of 5.45 to 40.45 kN for the parametric study. For all numerical models, the same procedure was followed to prepare the samples so that the results can be compared without any adverse effect of the model preparation.

6.2.2 Vertical displacement

The string of particles installed at the top of the assembly was proposed to break away the bond during the loading and unloading cycles. The model observation at the end of the simulation verified the assumption. To study any effects this thin layer imparts on the response of the base during the cyclic loading, simulations were conducted without creating the thin layer. Since the purpose of the simulation was to investigate how the presence of the thin layer changes the response of the base, the smallest cyclic load of 5.45 kN was selected.

Figure 6.23 compares the vertical displacements of the wheel for a base reinforced with geogrid at a depth of 152 mm considering the presence and the absence of the top thin layer. The figure shows a peak and a trough in a loading-unloading cycle. The peak of the

vertical displacement corresponds to the loading stage while the trough of the vertical displacement corresponds to the unloading stage. Higher vertical displacement occurred in the absence of the top thin layer compared to the case that included the top thin layer. The differences on the vertical displacements for these two cases are expected to diminish as the applied load increases. Importantly the global nature of the displacement response where initial cycles caused a significant plastic displacement was witnessed in all cases. These simulation results favor the use of uniform base with the top thin layer to study the mechanism of geogrid-reinforced bases since the simulation time was significantly reduced without compromising the global behavior of the base.

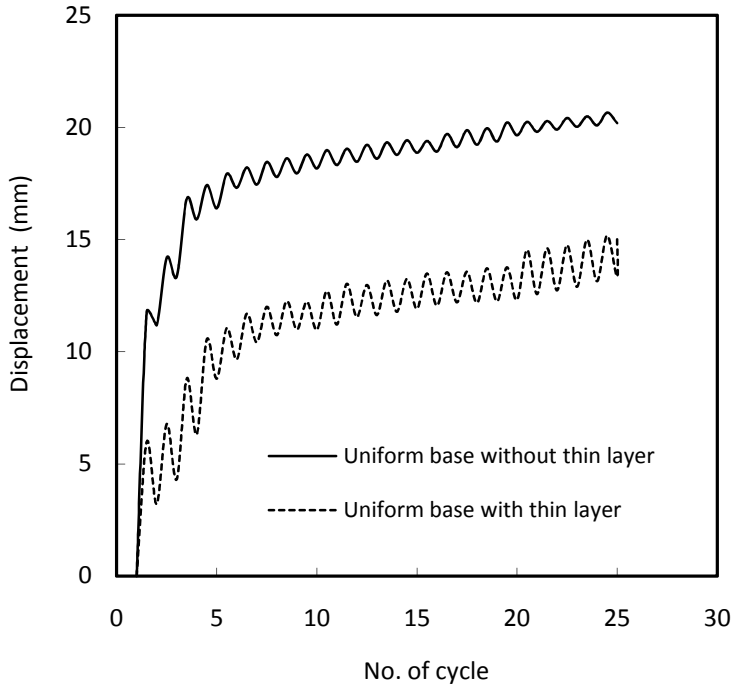

Fig. 6.23 Displacement vs. the number of cycles due to a 5.45 kN wheel load

Vertical displacements of the wheel at different loading-unloading cycles are shown in Fig. 6.24. The wheel was subjected to a vertical load of 40.45 kN during the loading stage and 0.45 kN (self weight of the wheel) during the unloading stage. Based on the projected area of the wheel on a plane, the equivalent pressure due to a 40.45 kN load would be 540 kPa, which is the typical tire pressure of a highway truck with 80 kN axle load. The total vertical displacement for a base reinforced with the geogrid at a depth of 303 mm was 119 mm. The performance of the base was improved when the geogrid was placed at a depth of 152 mm with the total vertical displacement of 104 mm. The vertical displacements at initial cycles mainly contributed to the difference in the entire performance of these two cases. During the initial loading and unloading cycles, the geogrid interacted with the aggregate particles and helped interlock the aggregate particles. The placement depth of the geogrid governed the interactions with the aggregate particles and controlled the vertical displacements at the initial cycles. Once interlocking between the geogrid and the aggregate particles completed, subsequent loading and unloading of the geogrid-reinforced bases produced approximately the same vertical displacements irrespective of the geogrid placement depths.

The base without any reinforcement could not support the 40.45 kN load since the wheel reached the bottom wall (i.e., the top of the subgrade) in the first loading cycle. Since the modeled aggregates were cylindrical in shape, interlocking between the aggregates was minimal and the unreinforced base could not support the applied 40.45 kN load. This comparison demonstrates the benefit of the geogrid in minimizing the vertical displacement by providing confinement to the particles.

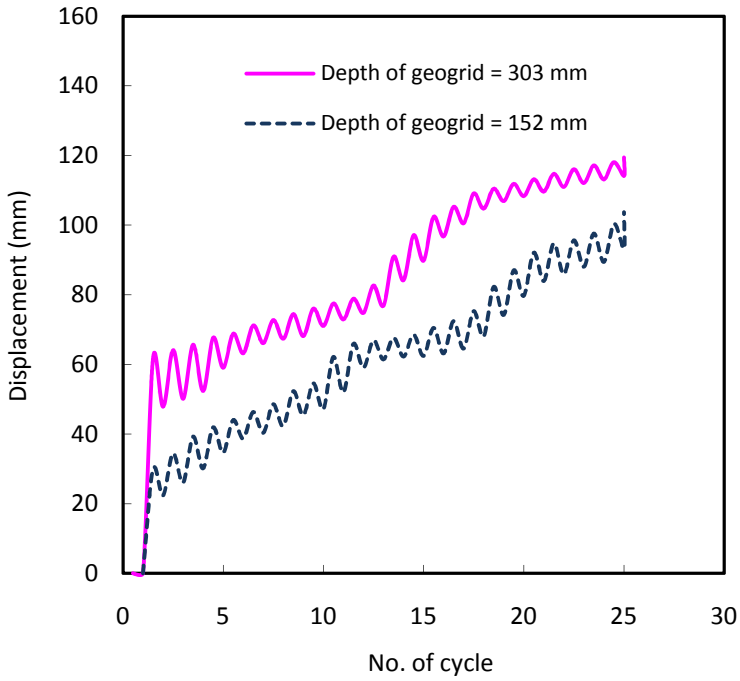

Fig. 6.24 Displacement vs. the number of cycles due to a 40.45 kN wheel load

The load-displacement cycles for two reinforced cases are shown in Figs. 6.25 and 6.26. Figure 6.25 shows the cyclic behavior of the reinforced base when the geogrid was placed at a depth of 303 mm while Fig. 6.26 shows similar behavior when the geogrid was placed at a depth of 152 mm. These two figures show that the displacement of the base under the cyclic wheel load consists of elastic and plastic portions. Large plastic displacement developed during the initial loading-unloading cycles but more elastic displacement occurred during the later cycles. The definition of the elastic and plastic displacement was used to calculate the elastic displacement from the recorded total displacements during each loading and unloading cycle. For instance, the recorded displacement during the loading cycle is the total displacement; the displacement during the subsequent unloading cycle is the plastic displacement. The difference between the total and plastic displacement is the elastic displacement. Thus the percentage of elastic displacement to

the total displacement was calculated and is plotted against the cycles in Fig. 6.27. Though there was a scatter in the calculated percentage of elastic displacement, a noticeable trend could be seen for both cases. The logarithmic trend lines show that the elastic displacement achieved approximately 80% of the total displacement at the end of 25 cycles. Additional plastic displacement would cease when 100% of the displacement for a cycle was elastic. Figure 6.27 shows that the base with the geogrid at a depth of 152 mm had more elastic displacement than that with the geogrid at a depth of 303 mm. This comparison implies that the geogrid placed at the mid-depth of the base layer is more beneficial as compared with that placed at the bottom of the base layer when subjected to heavier traffic loads.

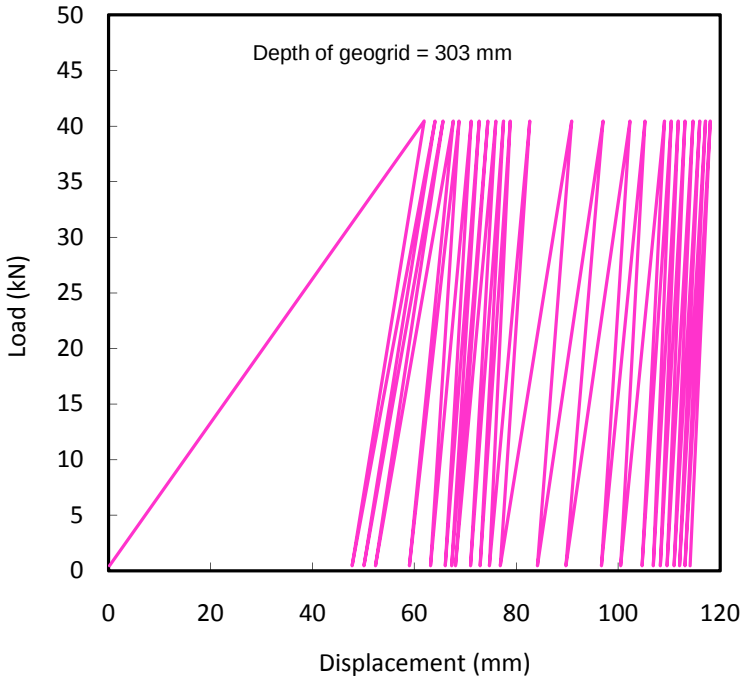

Fig. 6.25 Loading-unloading cycles for the base with a geogrid at a depth of 303 mm due to a 40.45 kN wheel load

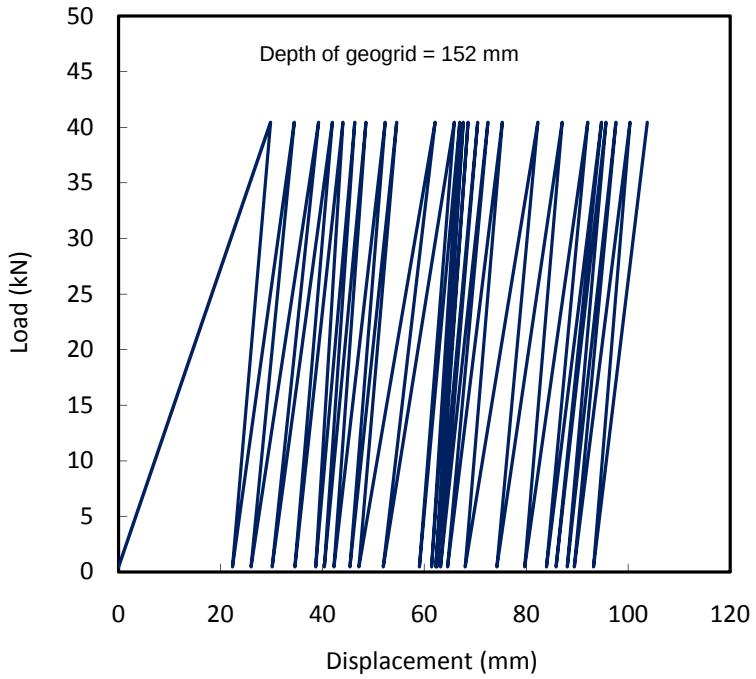

Fig. 6.26 Loading-unloading cycles for the base with a geogrid at a depth of 152 mm due to a 40.45 kN wheel load

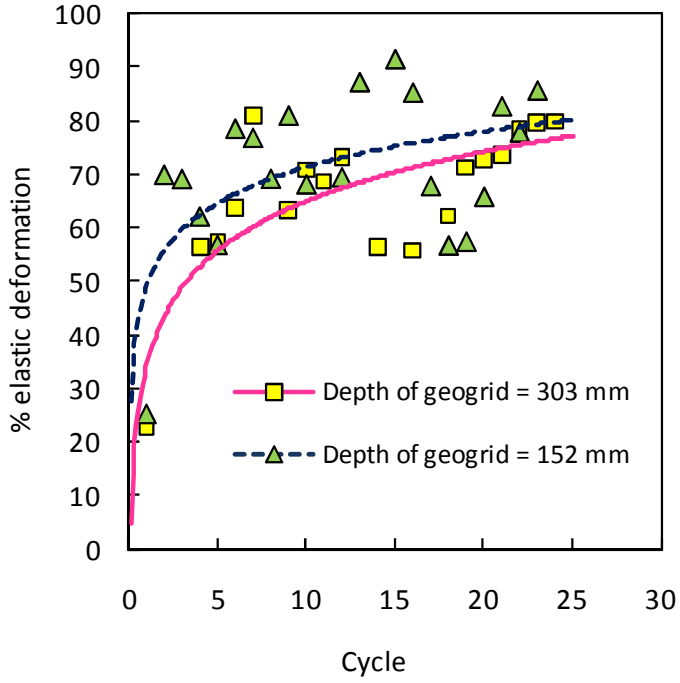

Fig. 6.27 Percentage of elastic displacement vs. cycles due to a 40.45 kN wheel load

6.2.3 Contact force due to vertical wheel load

The contact force chains are used to show how an applied force is transmitted through the particles. Figure 6.28(a) shows the contact forces in the geogrid-reinforced base, in which the geogrid was placed at a depth of 303 mm. A similar plot for the base reinforced by the geogrid at a depth of 152 mm is shown in Fig. 6.28(b). The black lines indicate compressive contact forces while the green lines indicate tensile contact forces. The line thickness represents the relative magnitude of the forces. These plots correspond to the 25^{th} loading cycle. Compared to the geogrid placed at a depth of 303 mm, the geogrid placed at a depth of 152 mm caused a wider distribution of the contact forces. A similar finding was presented in Section 6.1.3 using a moving wheel load over a geotextile-reinforced base.

The geogrid deformed in a curved shape as a tensioned membrane due to the vertical deformation of the base after the sufficient number of repeated loads. This tension membrane effect was prominent when the geogrid was placed at a depth of 152 mm (Fig. 6.28 b). The geogrid must have also provided the lateral confinement benefit since the unreinforced base could not sustain the same applied load. When the geogrid was placed at a depth of 303 mm (i.e., above the rigid subgrade), there was no tensioned membrane effect, therefore, the lateral confinement was the only controlling factor to increase the load capacity of the reinforced case. In general, the mobilization of the lateral confinement does not require a significant deformation; however, a significant deformation is needed for the tensioned membrane effect.

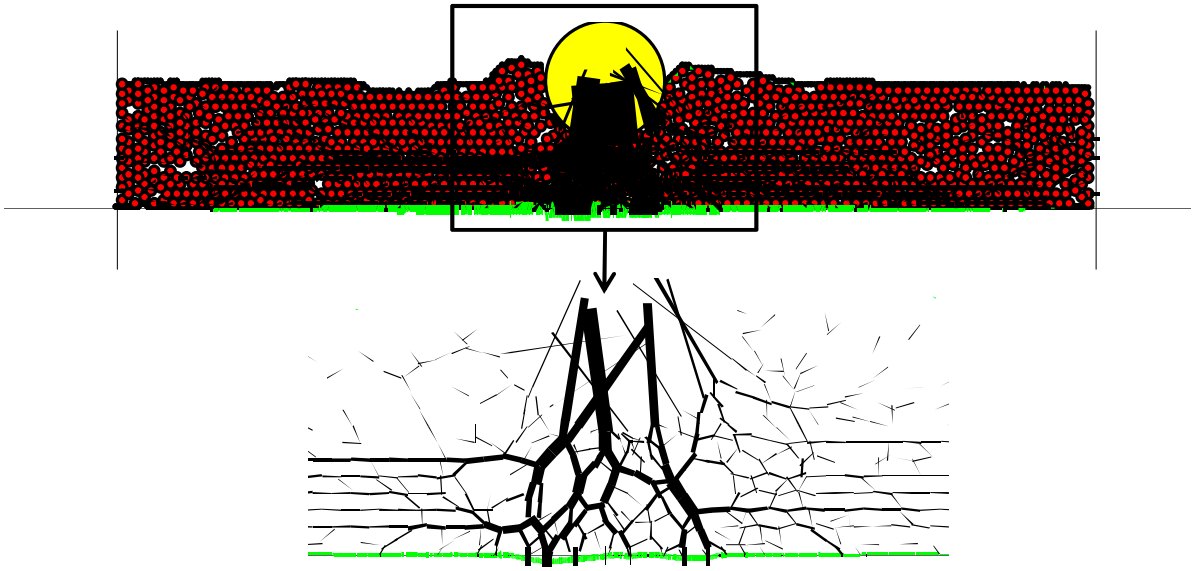

(a)

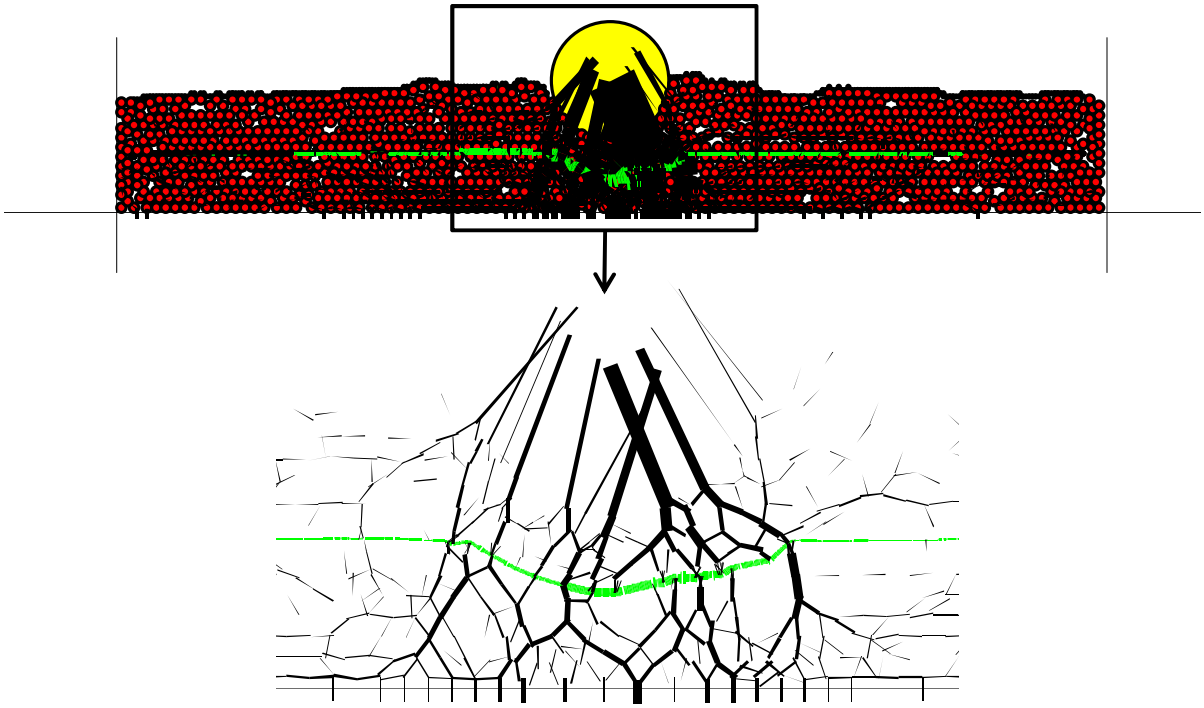

(b)

Fig. 6.28 Contact force chains due to a 40.45 kN wheel load: a) the geogrid at a depth of 300 mm, b) the geogrid at a depth of 152 mm

6.2.4 Tension in the geogrid

The stresses (σ_x, σ_y, and τ_{xy}) in the particles that represented the geogrid were recorded at the end of 25 cycles during a loading stage. These principal stresses were used to calculate the tension in the geogrid in the similar approach used for the geotextile. The variation of the tension along the width of the model is shown in Fig. 6.29. The location of the peak tension was beneath the wheel. A higher peak tension was calculated in the geogrid placed at a depth of 152 mm than the geogrid placed at a depth of 303 mm.

In Fig. 6.29, maximum tension corresponded to approximately 2 to 3% strain in the geogrid based on the stress-strain relation in Fig. 3.37. This strain in the geogrid is higher than that reported in the literature from full-scale field tests (Fannin and Sigurdsson 1996; Hufenus et al. 2006), typically 1-2%, because the computed strain in the geogrid corresponded to a higher surface displacement (100 to 120 mm) than that in the field (typically less than 75 mm). Figure 6.29 also shows that the geogrid at the deeper location had a wider tension distribution than that at the shallower location due to the stress distribution. However, the non-zero tension forces developed along a similar length of the geogrid in both models. A 2.1 m length of the 2.5 m long geogrid was under tension. The tension spanned approximately 3.5 times the diameter of the wheel in either side of the wheel. This result shows that a substantial length of the geogrid was in tension under a wheel load.

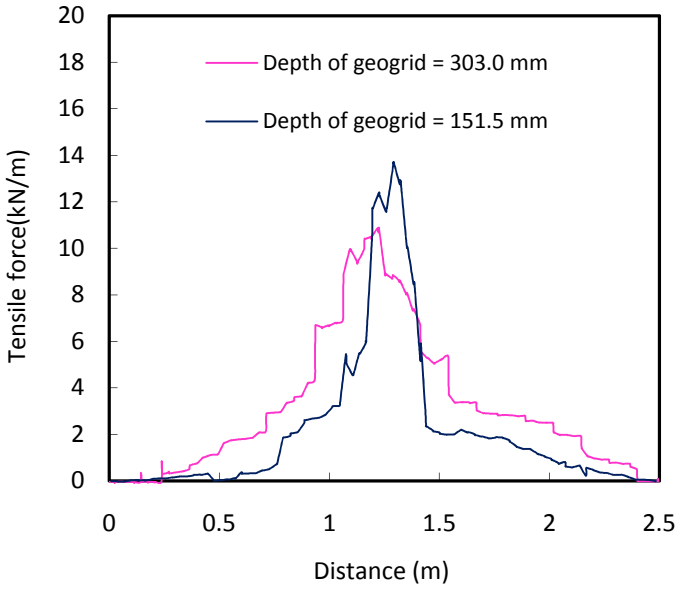

Fig. 6.29 Maximum tension in the geogrid due to a 40.45 kN wheel load

6.2.5 Influence of load on vertical displacement

The unreinforced base could not sustain either a 40.45 kN or 20.45 kN load in the DEM model as discussed in the vertical displacement section. Therefore, the comparative behavior of the unreinforced and reinforced bases was investigated at lower loads. Figure 6.30 shows the vertical displacements of the bases (unreinforced and reinforced) at the end of 25 cycles under the influence of a 5.45 to 40.45 kN vertical load. The load-displacement behavior in Fig. 6.30 shows that the unreinforced base could sustain a 10.45 kN load. Furthermore, the benefits of using the geogrid to significantly reduce the vertical displacement were similar for the load up to 20.45 kN, irrespective of the geogrid placement depth. Only for the higher load of 40.45 kN was the geogrid placed at a depth of 152 mm more beneficial in minimizing the vertical displacement than the geogrid placed at a depth of 303 mm.

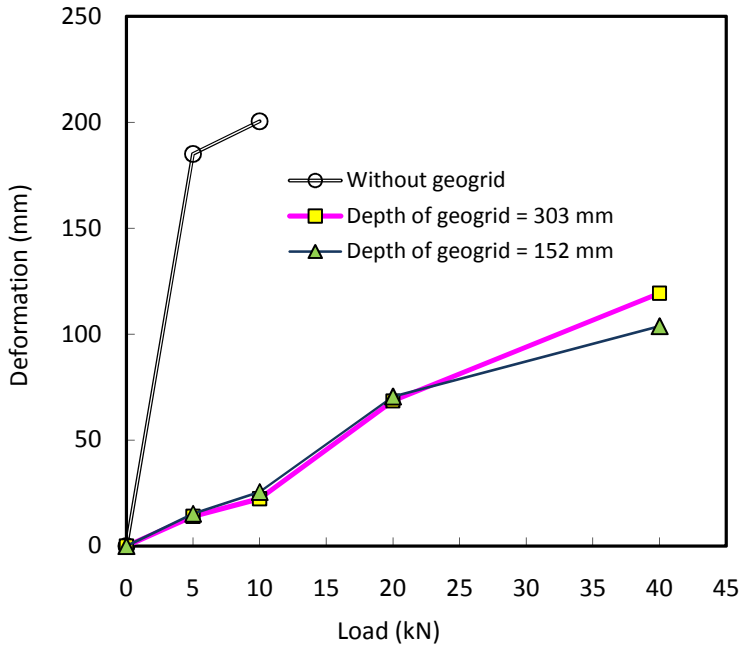

Fig. 6.30 Load vs. permanent displacement at the end of 25 cycles of load

The percentages of the displacements that were elastic are plotted in Fig. 6.31 for the reinforced and unreinforced bases subjected to a 10.45 kN load. At this lower load, the base reinforced with the geogrid at a depth of 300 mm was most effective in achieving a high percentage of elastic displacement (approaching 100%). The percentages of elastic displacement for the base reinforced with the geogrid at a depth of 152 mm and for the unreinforced base were 95% and 90%, respectively. This comparison shows that the vertical displacement of the unreinforced base would increase at a faster rate with additional load cycles than that of the reinforced base. Compared with the cases in Fig. 6.27, the reinforced bases under a heavier load had lower percentages of elastic displacement (i.e., higher percentages of plastic displacement). Therefore, the reinforced

bases under a heavier load experience permanent displacement at a faster rate than those under a lighter load.

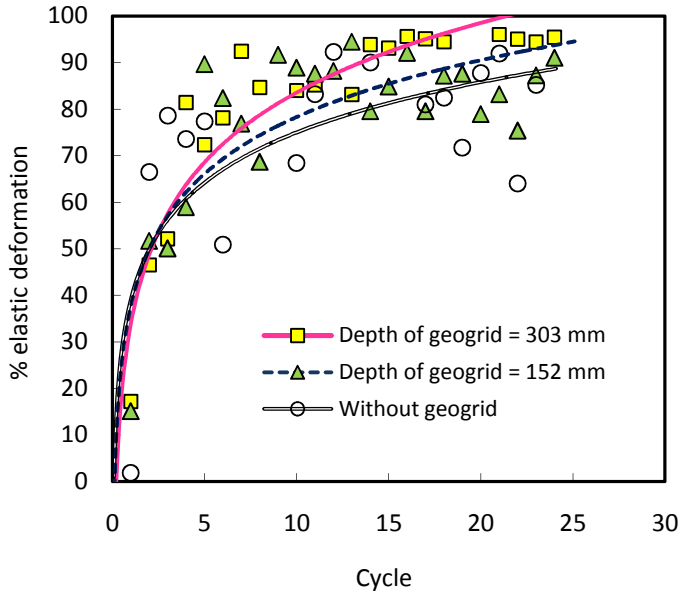

Fig. 6.31 Percentage of elastic displacement vs. cycle at a 10.45 kN wheel load

6.3 Influence of Geogrid Aperture Size

Experimental studies of geogrid-reinforced aggregates have shown an optimum aperture size of the geogrid for a given size of aggregates to maximize the performance of the geogrid-reinforced system (Jewell *et al.* 1984; Brown *et al.* 2007). Jewell *et al.* (1984) observed that the aperture size of the geogrid should be three to four times the particle diameter to achieve the maximum benefit. In a Composite Element Test (CET) of geogrids and aggregates using a cyclic load at a frequency of 2 Hz, Brown *et al.* (2007) observed the minimum settlement of the aggregate base when the geogrid had an aperture size of 65-80 mm for the 50 mm in diameter aggregates (Fig. 6.32). Therefore, the ratio of

the aperture size to the aggregate diameter was 1.3-1.6 for the optimum performance of the geogrid-reinforced system. In Fig. 6.32, the first number indicates the tensile strength (kN/m) of the geogrid and the second number indicates the aperture size. Brown *et al.* (2007) used a steel beam measuring 0.7 m in length and 0.25 m in width to apply a 20 kN cyclic load. The equivalent contact pressure on the aggregate base was 107kPa. Brown *et al.* (2007) also investigated the effect of tensile strength and, by association, stiffness of the geogrid on the performance of the reinforced base. Their experimental results suggested a much smaller effect, if any of the geogrid tensile strength on minimizing the settlement of the base.

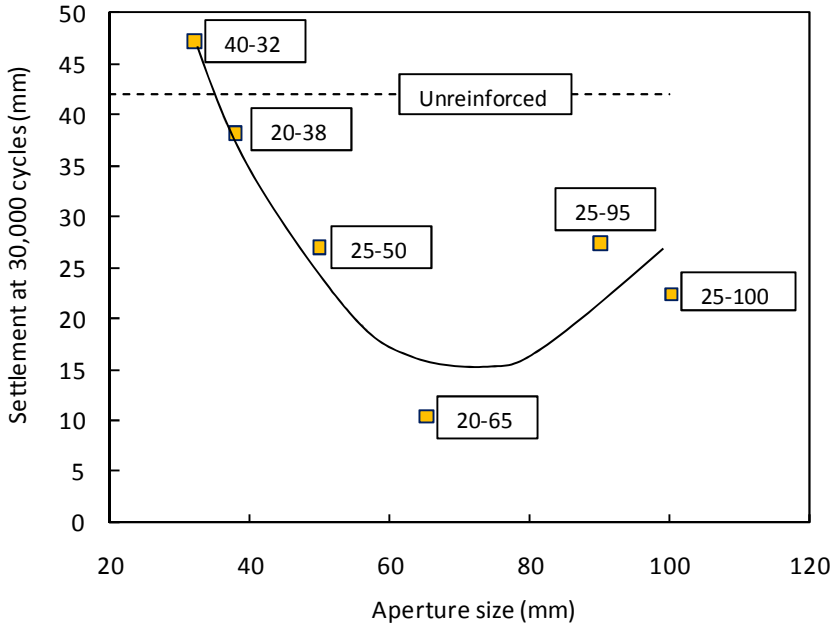

Fig. 6.32 Influence of aperture size on settlement (after Brown *et al.*, 2007)

Numerical simulation of pull-out tests using three-dimensional models also indicated an optimum aperture size of the geogrid to enhance the pull-out force (McDowell *et al.* 2006). Beyond the simulation of these pull-out tests, there lacks the understanding of how

different geogrid aperture sizes affect the performance of geogrid-reinforced bases. This study investigates the influence of geogrid aperture size on the performance of base courses.

6.3.1 Numerical sample preparation

An unpaved base section with a rigid subgrade was selected for simulation. A 2.50 m wide and 0.30 m high box was created by four walls. The geogrid calibrated in Section 3.7 had an aperture size of 30 mm. In line with the findings of Brown *et al.* (2007), the diameter of the particles was selected as 19 mm, thereby confirming the optimum ratio (1.3-1.6) between the aperture sizes to the particle diameter. The mechanical properties of the uniform particles (Gradation A) were investigated in Section 3.3.3. Other than the particle size, the procedure for the sample preparation was same as described in Section 6.2.1. The base section had the porosity of 0.16 at the time of particle generation. The geogrid was installed at the mid depth (152 mm) of the base section.

After the preparation of the model, a load was applied in the vertical direction with an equivalent frequency of 0.76 Hz. This loading frequency is commonly used in the experiments of low-volume unpaved roads. The use of higher loading frequency (2 Hz) described in the preceding section was relevant for railroad application. A 10-kN cyclic ramp load was applied using a wheel of 0.3 m in diameter and the resulted surface displacement was calculated. This load pulse had a 0.3 second linearly increasing load from 0 to 10 kN, followed by a constant 10 kN load for 0.2 second, a linearly decreasing load to 0 kN over a 0.3 second period, and then a 0.5 second pause at 0 kN before the next loading cycle (Fig. 6.33).

The responses of both unreinforced and geogrid-reinforced bases were investigated in this study. The same micromechanical properties were used for the geogrids of different aperture sizes. Maintaining the same micromechanical properties was necessary to isolate the effect of the geogrid strength on the performance of the reinforced base.

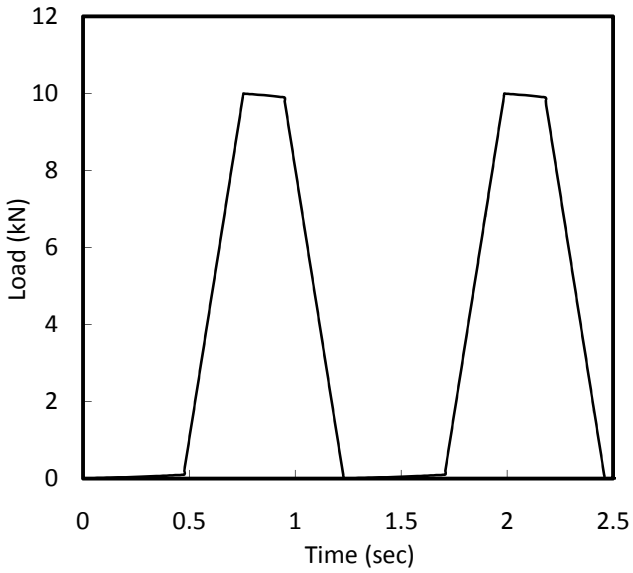

Fig. 6.33 Cyclic load scheme

6.3.2 Vertical displacement due to ramp load

Figure 6.34 shows the displacements of base courses with time when subjected to the cyclic ramp load. The numerical study was terminated once the displacement was beyond 100 mm since the acceptable rut depth of an unpaved road is typically 50-100 mm (Giroud and Han 2004). Increase and decrease in the displacement correspond to the rising and falling ramps of the load cycle. As shown in Fig. 6.34, the unreinforced base with uniform particles only sustained the ramp load for three cycles before the displacement reached 100 mm. On the other hand, the geogrid-reinforced bases with uniform particles sustained the

ramp load for more than three cycles. The number of additional load cycles that the geogrid-reinforced base could sustain before reaching the termination criterion depended on the geogrid aperture size when all other parameters remained same.

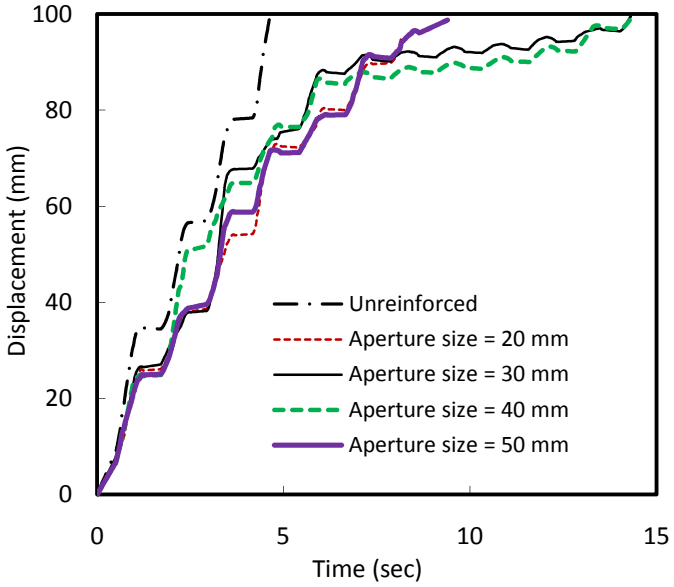

Fig. 6.34 Displacement vs. time

Figure 6.35 shows the sustained load cycles at the displacement of 100 mm for the aperture sizes of geogrids: 20, 30, 40, and 50 mm. Minimum displacement of the reinforced bases with uniform aggregates (diameter =19mm) was obtained when the geogrid aperture size ranged between 30 to 40 mm. Therefore the optimum ratio of aperture size to the aggregate diameter can be calculated as 1.5 to 2.0. Even though the experimental problem studied by Brown *et al.* (2007) and the numerical simulation conducted in this study have different geometry and loading conditions, the existence of the optimum aperture size and the range is strikingly similar.

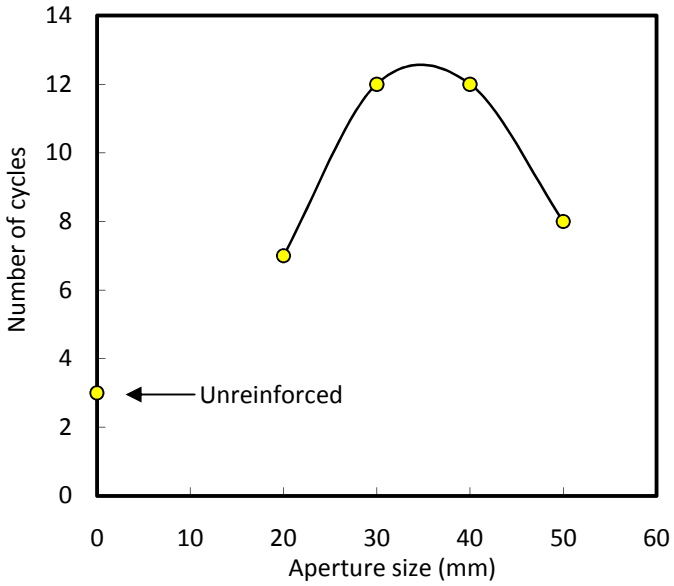

Fig. 6.35 Sustained cycles at 100mm displacement for different aperture sizes of geogrid

6.3.3 Tension in geogrid due to ramp load

The aperture size of the geogrid had a profound effect on the performance of the geogrid-reinforced base. It is imperative to evaluate the tension in the geogrid at the loading and the unloading stages to explain the improved performance. Recording the geogrid stresses, we can compute the tension force developed in the geogrid at any stages during the simulation. Figures 6.36 and 6.37 show the tension in the geogrid of 30 mm aperture size at different loading and unloading cycles. Non- symmetrical tensile force developed in the geogrid after the first loading cycle which may be attributed to some local inhomogeneity of the sample. The tension in the geogrid was evolving towards a symmetrical distribution when additional cyclic ramp loads were permitted. Compared to the geogrid tension at the first cycle, wider stretch of the geogrid was affected at the fifth cycle. Moving from the

fifth to eleventh cycle, the peak tension force in the geogrid increased but the stretch of the geogrid under tension decreased.

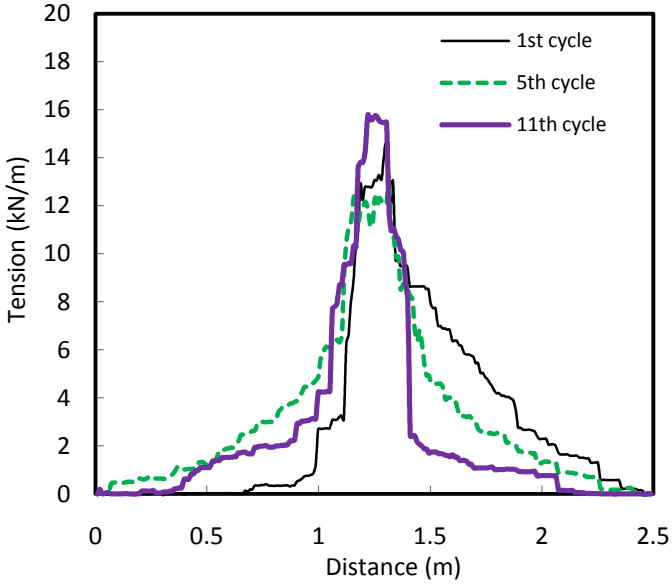

Fig. 6.36 Tension in geogrid at different loading cycles (aperture size of geogrid = 30 mm)

The tension in the geogrid significantly dwarfed during the unloading cycles (Fig. 6.37). Only 12 percent of the peak tension developed during the loading cycles remained in the geogrid during the unloading cycles. It is interesting to note that a less tension remained in the geogrid below the wheel location than in the neighborhood during the unloading cycles.

Figure 6.38 shows the tension in the geogrid of different aperture sizes during the fifth loading cycle. The maximum tensile peak force developed in the geogrids of aperture sizes of 30 mm and 40 mm. Also these aperture sizes corresponded to a wider stretch of tensile force in the geogrid. Therefore, the distribution of tensile force in the geogrids of different aperture sizes confirmed a better interaction between the geogrids and the particles for the particular geogrid aperture sizes. This observation is consistent with the

additional load cycles sustained by the base when the geogrid of aperture sizes of 30 and 40 mm were used compared to the other aperture sizes.

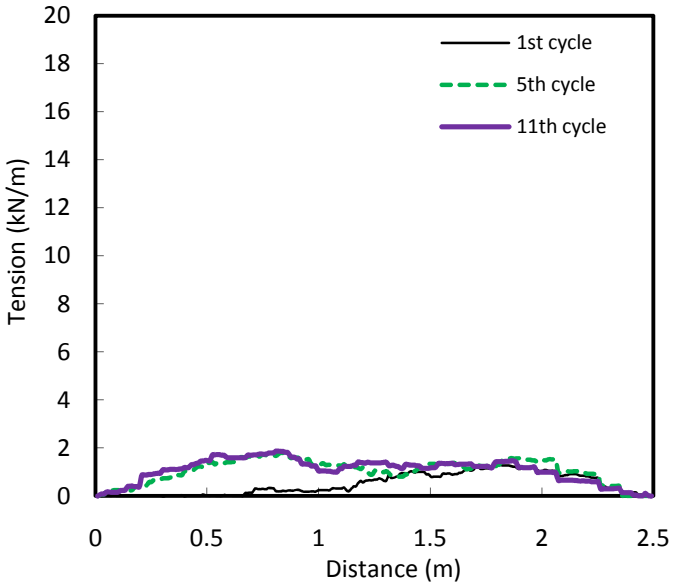

Fig. 6.37 Tension in geogrid at different unloading cycles (aperture size = 30 mm)

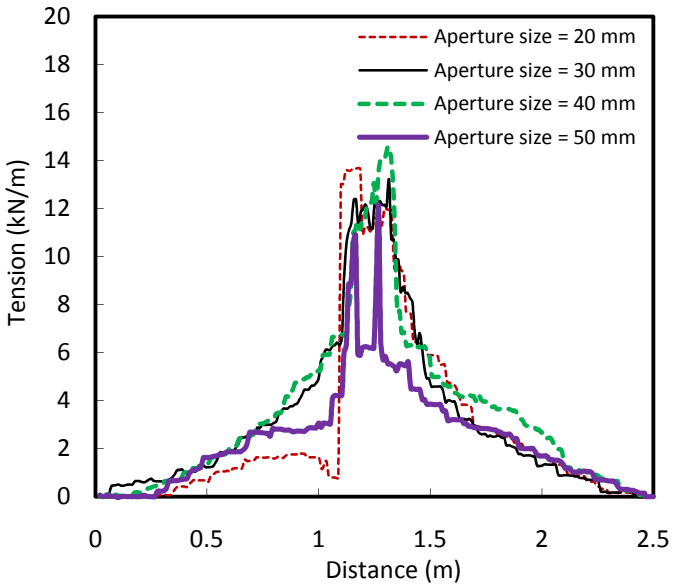

Fig. 6.38 Tension in geogrid of different aperture size (5th loading cycle)

Figure 6.39 shows the tension in the geogrid of different aperture sizes during the fifth unloading cycle. Again, only a fraction of peak tensile force developed during the loading cycles remained on the geogrids during the unloading cycle. Not only during the loading cycles but also during the unloading cycles, the geogrids of aperture sizes of 30 and 40 mm had larger tensile force compared to the other aperture sizes considered in this study.

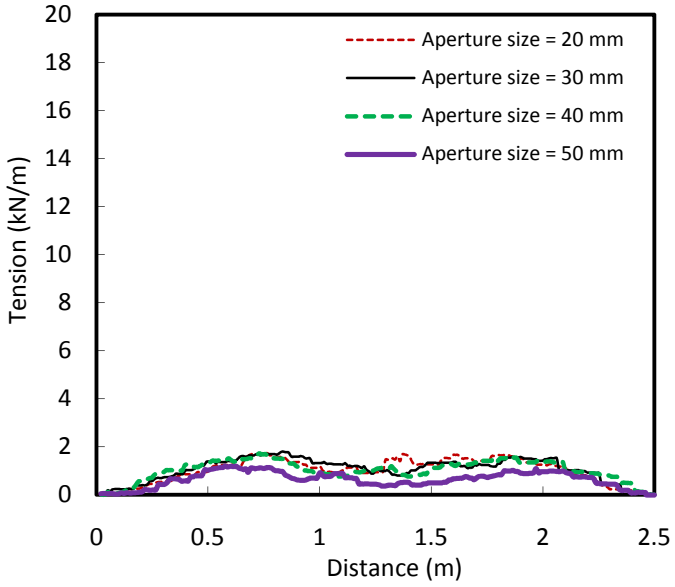

Fig. 6.39 Tension in geogrid of different aperture size (5th unloading cycle)

6.3.4 Particle rotational field

Aggregates displace under the action of external loading and the field of particle rotation is important for the understanding of the shear localization (Misra and Jiang 1997; Pena *et al.* 2007; Sibille and Froiio 2007). Figure 6.40 shows the normalized frequency distribution of the particle rotation for the unreinforced base during the first loading and unloading cycle. The rotations of the all particles were extracted and grouped into different bin

angles at an interval of 3.34^{o} to obtain the normalized frequency distribution. The number of particles at zero rotational angle diminished during the unloading compared to that during the loading. Furthermore, the particles had larger rotational angles during the unloading compared to that during the loading. The frequency distribution of the particle rotation signifies that the particles continuously rotated in the same direction even during the unloading. Similar findings were reported earlier by Lu and McDowell (2007) from their numerical study on spherical ballast particles subjected to a sinusoidal pulse load.

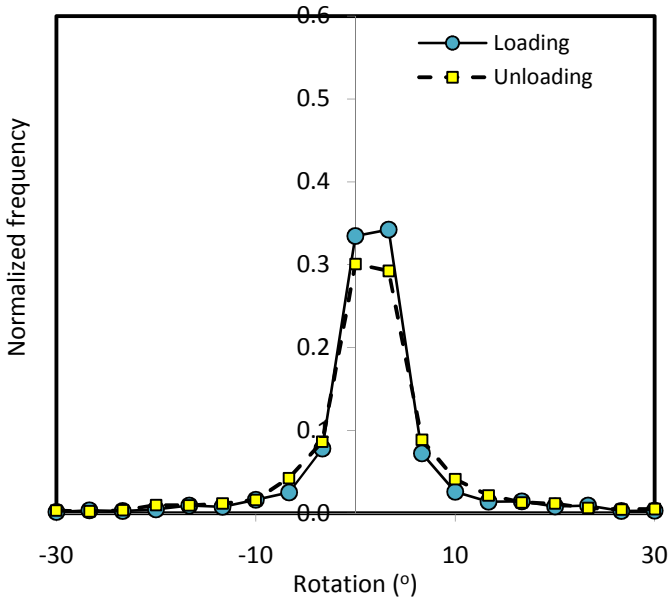

Fig. 6.40 Normalized frequency distributions of particle rotation for the unreinforced base at the first cycle

Comparison of Figs. 6.40 to 6.41 shows that the geogrid-reinforced base had less particle rotation than the unreinforced base, which demonstrates the benefit of geogrid reinforcement on minimizing the particle rotation. The geogrid with an aperture size of 30 mm had a narrowed distribution of particle rotation. Similar to the unreinforced base, the particles in the geogrid-reinforced base continuously rotated in the same direction during

the unloading stage as during the loading stage. However, the geogrid hindered the rotation of particles during the unloading. Therefore, the normalized frequency distributions during the loading and unloading nearly coincided to each other.

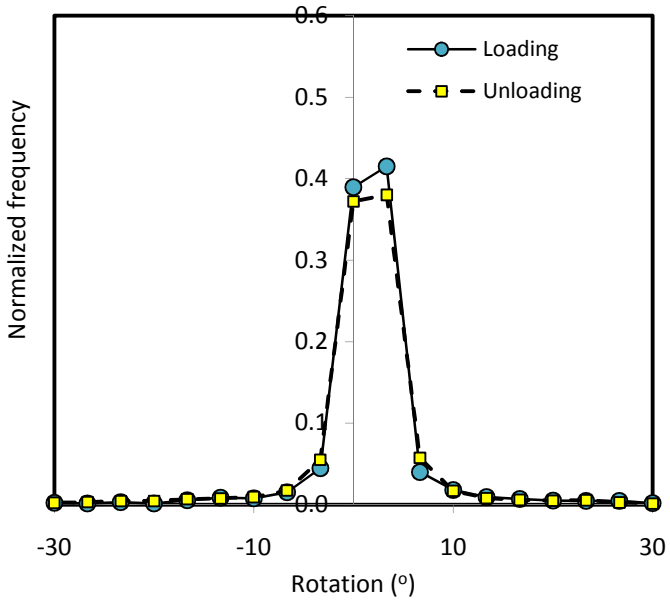

Fig. 6.41 Normalized frequency distributions of particle rotation for the reinforced base (aperture size = 30 mm) at the first cycle

Figures 6.42 and 6.43 show the normalized frequency distribution of particle rotation during the loading and unloading stages when the geogrid of 30 mm-aperture size was used. The difference on the frequency distributions at the loading and unloading stages was only noticeable during the first cycle. After the fifth cycle, the frequency distribution during the loading and unloading stages almost coincided with each other. Note that the displacement of the base course also increased slowly after the fifth cycle. However, the particle rotation did not cease and continued with additional loading cycles and had a wider rotational distribution at the eleventh cycle.

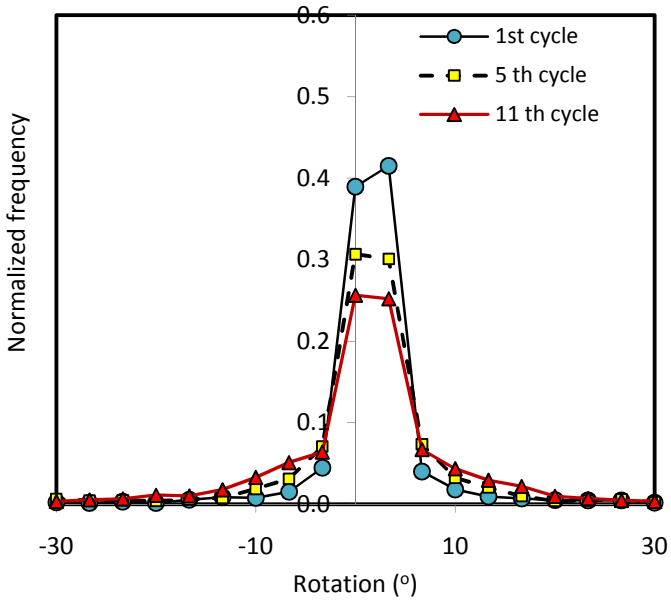

Fig. 6.42 Normalized frequency distributions of particle rotation for the reinforced base (aperture size = 30 mm) at different loading cycles

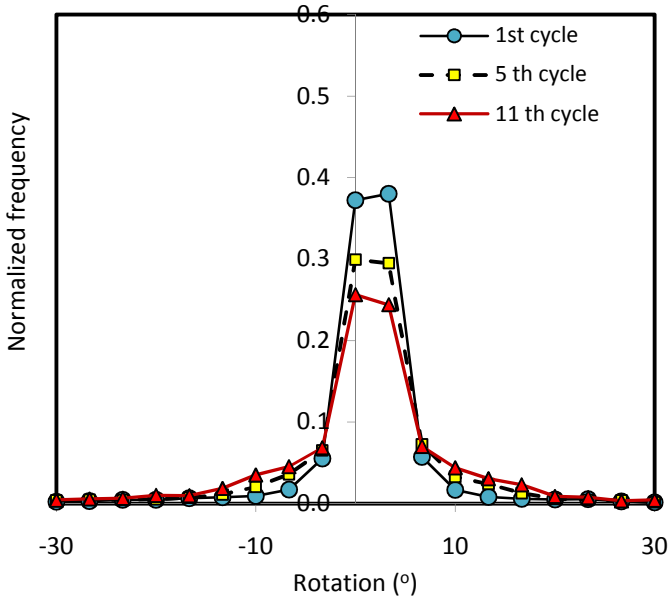

Fig. 6.43 Normalized frequency distributions of particle rotation for the reinforced base (aperture size = 30 mm) at different unloading cycles

CHAPTER SEVEN

CONCLUSIONS AND RECOMMENDATIONS

Geosynthetics are commonly used in the construction of embankments and roadways. Sound design of these structures depends on a holistic understanding of the interaction between geosynthetic and soil. Many studies have been done in the past to understand the geosynthetic-soil interaction using experimental and numerical techniques. However, the mechanisms were not well studied at a microscale. The microscale study of the interaction between geosynthetic and soil subjected to monotonic and/or cyclic loadings is expected to furnish additional information. The major findings from this study are summarized and recommendations are made for future research.

7.1 Conclusions

This research focused on understanding the behavior of granular material with particular emphasis on the interaction between geosynthetic and granular material (soil) under different loading conditions. The findings from this study are discussed below according to their potential applications and are summarized below.

Behavior of granular material

1) The porosity of soil had a strong influence on the shear strength of the soil. Under a monotonic loading condition, particle gradation had a limited influence on the shear strength of the soil. In a graded soil, large-diameter particles carry more contact forces and small-diameter particles help improve the stability providing more contacts to the large-diameter particles. Directional anisotropy on the contact

forces was prominent for large-diameter particles compared to the small-diameter particles when the soil underwent considerable a deviatoric strain. While particle gradation had a minor effect on the shear strength of soil under monotonic loading conditions, a well-graded soil had a 50% higher resilient modulus compared to a uniformly-graded soil under cyclic loading conditions. Therefore, a graded base is essential for the construction of durable roadways.

Soil arching in the trapdoor experiments

1) Soil arching is essentially a meta-stable condition and changes with the extent as well as the shape of arch with a displacement of the trapdoor. In the two-dimensional model studies conducted in this research, a plane of equal settlement was not observed upto the experimented range of H/B (the embankment height divided by the trapdoor width) ratio of 2.0.

2) The inclusion of reinforcement in the embankments minimized the total as well as differential settlements measured on the top of the embankments. A significant strain developed in the paper reinforcement and extended in the lateral direction beyond the vertical plane of the trapdoor. The lateral extent of the strain implies a relative movement between the embankment fill and reinforcement beyond the vertical plane of the trapdoor. The location of a peak strain in the paper-reinforcement was governed by the fill thickness between the reinforcement and the trapdoor. In general, the location of the peak strain in the paper reinforcement shifts laterally outward by a distance equal to the fill thickness between the reinforcement and the trapdoor; the lateral shift distance being measured from the edge of the trap door.

3) In the two-dimensional trapdoor tests, the formation of soil arching due to the displacement of two trapdoors did not interact with each other in a kinematic sense when the trapdoors were separated by a distance equal to twice the width of the trapdoor for the embankment fill (aluminum bars) of a low friction angle. On the other hand, the displacement of the second-lowered trapdoor separated by the same distance had marginal effects on the development of strains in the reinforcement within the influence zone of the first-lowered trap door. The anchorage failure of the reinforcement also controlled the development of the peak strain particularly in the low embankments and should be considered in the design.

Behavior of geosynthetic-reinforced pile-supported embankments

1) During the development of soil arching, vertical stresses on the embankment fill decreased above the compressible soil and increased above the pile caps. Horizontal stresses also increased above the pile caps but remained unaffected above the compressible soil. The coefficient of lateral earth pressure after the development of soil arching varied from 0.5 to 2.8 within the embankment fill compared to an average value of 0.49 before the development of soil arching. Isotropic polar histograms of the contact normal forces showed that the embankment fill had isotropic stresses above the compressible soil when soil arching developed. On the other hand, the polar histograms of the contact normal forces above the pile caps showed that the principal stresses reoriented due to the formation of soil arching. Polar histograms of the shear force did not show any marked increase during the soil arching. Therefore, the embankment load transfers to the pile caps due to the reorientation of the principal stresses.

2) The embankment fill showed dilation during soil arching. Maximum dilation of 2% was observed in the unreinforced as well as reinforced embankments. The maximum dilation occurred at the mid-width of the embankment and located at an approximate distance of one half of the pile cap spacing above the boundary between the embankment and the compressible soil. The influence zone of dilation extended higher for the unreinforced embankment compared to the reinforced embankment.

3) The displacement vectors of the embankment fill suggested a triangular shape of the maximum settlement zone. The geogrid-reinforced pile-supported embankments had 50% less total settlement on the top of the embankment as compared with the unreinforced pile-supported embankments. Geogrid reinforcement reduced total as well as differential settlements on the top of the embankment. The geogrid attained a catenary shape and developed a maximum tension of 13.8 kN/m which corresponded to 3.3% strain in the geogrid.

4) There was an accumulation of plastic strain in the embankment fill under the cyclic load. For the conditions evaluated, the geogrid-reinforced embankment had a 68% deformation of the unreinforced embankment under cyclic loadings. The stress concentration ratio for the geogrid-reinforced embankment was higher than that of the unreinforced embankment. The tensile force in the geogrid increased with the load cycles.

Behavior of geosynthetic-reinforced bases

1) The geosynthetic reinforcement helped distribute the forces to a wider area. When the bases were reinforced with geotextile, two different mechanisms were observed

for the particle movement in the bases. The geotextile provided vertical confinement but promoted lateral sliding of the particles since it had lower frictional resistance to the soil particles when rolling and sliding on the geotextile. The overall rut depth depended on the magnitudes of particle movements in the vertical and lateral directions. The particle movements in the vertical and lateral directions were governed by the depth of the geotextile. The density of base course had a profound effect on a rut depth. The dense base had a deeper influence depth but less rut depth under wheel loading than the loose base.

2) The simulation of geotextile-soil interaction tests showed that tensile stresses developed in the geotextile under wheel loading which helped improve the performance of the reinforced section. The geotextile placed at a depth of 25.0 mm had small tensile stresses and was less effective in minimizing the surface deformation caused by the cyclic wheel load as compared with the geotextile placed at a depth of 12.5 mm. For the geotextile at either depth, a low tensile strain developed in the geotextile under cyclic wheel loading. An increase in the stiffness of the geotextile showed a marginal improvement of the performance, particularly when the geotextile was placed at a depth of 25.0 mm. Therefore, a very stiff geotextile is not necessary to improve the performance of the base.

3) The simulation of the geogrid-reinforced base course showed that the geogrid reinforcement was effective in improving the bearing capacity of the base course. The unreinforced base could not sustain a typical wheel load of 40.45 kN while a reinforced base with the geogrid placed at a depth of 152 or 303 mm could carry this load. The reinforced bases had a higher percentage of elastic displacement than that of the unreinforced base. The contact force distribution showed that the

geogrid helped widen the distribution of contact force chains. The higher load capacity, elastic displacement, and contact force distribution of the reinforced bases were attributed to the lateral confinement and tensioned membrane effects by the geogrid. The placement depth of the geogrid had a greater influence on limiting the permanent displacement of the base under a heavier load. Under the typical wheel load (40kN), the maximum tension developed in the geogrid ranged from 10.0 to 13.5 kN/m, which corresponds to approximately 2 to 3% strain.

4) At a prescribed displacement of 100 mm, the simulation results of bases showed that the geogrid reinforcement increased the number of load cycles. The rotation field of the particles in both unreinforced and reinforced bases indicated that the particles continuously rotated in the same direction during the loading and unloading. The geogrid hindered the rotation of particles and narrowed the normalized frequency distribution of particle rotations. The performance of the reinforced base depended on the size of the geogrid aperture. Minimum displacement of the reinforced bases with uniform aggregates (diameter =19mm) was obtained when the geogrid aperture size ranged between 30 to 40 mm. The maximum tensile peak force developed in the geogrids of aperture sizes 30 mm and 40 mm. Also these aperture sizes corresponded to a wider stretch of tensile force in the geogrid. Therefore, the distribution of tensile force in the geogrids of different aperture sizes confirmed a better interaction between the geogrids and the particles for the particular geogrid aperture sizes. From this study, the optimum ratio of the aperture size to the aggregate diameter was 1.5 to 2.0.

7.2 Recommendations for Future Study

1) The studies in this dissertation considered uniform and graded particles which were circular (disk) in shape. The similar studies considering the irregular shape of the particles with the provision of particle breakage are recommended.

2) In the trapdoor experiments of soil arching, the displacements of the aluminum bars were measured using the AUTOCAD software. Better resolution photography and their digital image processing are recommended to measure the kinematic field of the aluminum bars which can be compared with the DEM simulation results.

   The studies in this dissertation considered the two-dimensional models to investigate the geosynthetic-soil interaction. While the results from two dimensional models were useful and revealed important mechanisms on geosynthetic-soil interaction, a three-dimensional study of these problems is strongly recommended to verify/improve the numerical results obtained in this study.

References

Abu-Farsakh, M., Coronel, J., and Tao, M. (2007). "Effect of soil moisture content and dry density on cohesive soil-geosynthetic interactions using large direct shear tests." *Journal of Materials in Civil Engineering*, 19(7), 540-549.

Abu-Farsakh, M. Y., Almohd, I., and Farrag, K. (2006). "Comparison of field and laboratory pullout tests on geosynthetics in marginal soils." *Transportation Research Record*, 1975, 124-136.

Adams, M. T. and Collin, J. G. (1997). "Large model spread footing load tests on geosynthetic reinforced soil foundations." *Journal of Geotechnical and Geoenvironmental Engineering*, 123(1), 66-72.

Allen, J. J. (1973). *The effects of non-constant lateral pressures on the resilient response of granular materials*, Ph.D. Dissertation, University of Illinois at Urbana-Champaign, United States -- Illinois.

Almohd, I., Abu-Farsakh, M., and Farrag, K. (2006). "Geosynthetic reinforcement-cohesive soil interface during pullout." American Society of Civil Engineers, Reston, VA 20191-4400, United States, Milwaukee, WI, United States, 40-49.

Athanasopoulos, G. A. (1993). "Effect of particle size on the mechanical behavior of sand-geotextile composites." *Geotextiles and Geomembranes*, 12, 255-273.

Bardet, J. P. (1998). "Introduction to computational granular mechanics." In: *Behaviour of Granular Materials*, B. Cambou, ed., Springer-Verlag, Wien, New York.

Barksdale, R. D. and Itani, S. Y. (1989). "Influence of aggregate shape on base behavior." *Transportation Research Record*, 1227, 173-181.

Bathurst, R. J. and Rothenburg, L. (1988). "Micromechanical aspects of isotropic granular assemblies with linear contact interactions." *Journal of Applied Mechanics, Transactions ASME*, 55(1), 17-23.

Bathurst, R. J., and Rothenburg, L. (1990). "Observations on stress-force-fabric relationships in idealized granular materials." *Mechanics of Materials*, 9(1), 65-80.

Bhandari, A. and Han, J. (2009). "DEM study of shallow foundation under vertical loading." In: M. Iskander, D.F. Laefer, and M.H. Hussein, Eds., *ASCE Geotechnical Special Publication No. 187, Contemporary Topics in Ground Modification, Problem Soils, and Geo-Support*, Orlando, Florida, 465-472.

Bhandari, A. and Han, J. (2010). "Investigation of geotextile-soil interaction under a cyclic vertical load using the discrete element method." *Geotextiles and Geomembranes*, 28(1), 33-43.

Bhandari, A., Han, J., and Wang, F. (2009). "Micromechanical analysis of soil arching in geosynthetic-reinforced pile supported embankments." In: X. Zhang, J. Zhang, X. Yu, and H. Fu (Eds.), *ASCE Geotechnical Special Publication No. 189, Characterization, Modeling, and Performance of Geomaterials: Selected Papers From the 2009 GeoHunan International Conference*, GeoHunan, China, 47-52.

Bourdeau, P. L. (1989). "Modeling of membrane action in a two-layer reinforced soil system." *Computers and Geotechnics*, 7(1-2), 19-36.

Brown, S. F., Kwan, J., and Thom, N. H. (2007). "Identifying the key parameters that influence geogrid reinforcement of railway ballast." *Geotextiles and Geomembranes*, 25(6), 326-335.

Carlsson, B. (1987). *Reinforced Soil, Principles for Calculation*. Terratema AB, LinkÖping

Chang, C. S. and Misra, A. (1989). "Theoretical and experimental study of regular packings of granules." *Journal of Engineering Mechanics*, 115(4), 704-720.

Chang, C. S. and Misra, A. (1990). "Packing structure and mechanical properties of granulates." *Journal of Engineering Mechanics*, 116(5), 1077-1093.

Chang, D. T.-T., Chang, F.-C., Yang, G.-S., and Yan, C.-Y. (2000). "Influence factors study for geogrid pullout test." *Clamps, Clamping Techniques, and Strain Measurement for Testing of Geosynthetics*, *ASTM Special Technical Publication*, 1379, 129-142.

Chareyre, B. and Villard, P. (2003). "Discrete element modeling of curved geosynthetic anchorages with known macro-properties." In Konietzky (ed.), *Proceedings of the First International PFC Symposium on Numerical Modeling in Micromechanics via Particle Methods*, Gelsenkirchen, Germany, 197-203.

Chareyre, B. and Villard, P. (2005). "Dynamic spar elements and discrete element methods in two dimensions for the modeling of soil-inclusion problems." *Journal of Engineering Mechanics*, 131(7), 689-698.

Chen, Y. M., Cao, W. P., and Chen, R. P. (2008). "An experimental investigation of soil arching within basal reinforced and unreinforced piled embankments." *Geotextiles and Geomembranes*, 26(2), 164-174.

Cheng, Y. P. (2004). *Micromechanical Investigation of Soil Plasticity*, Ph.D. Dissertation, University of Cambridge, United Kingdom.

Cheng, Y. P., Bolton, M. D., and Nakata, Y. (2004). "Crushing and plastic deformation of soils simulated using DEM." *Geotechnique*, 54(2), 131-141.

Costa, Y. D., Zornberg, J. G., Bueno, B. S., and Costa, C. L. (2009). "Failure mechanisms in sand over a deep active trapdoor." *Journal of Geotechnical and Geoenvironmental Engineering*, 135(11), 1741-1753.

Cowell, M. J. and Sprague, C. J. (1993). "Comparison of pull-out performance of geogrids and geotextiles." *Proceedings of Geosynthetics '93 Conference, IFAI*, Vancouver, Canada, 579 – 592.

Cundall, P. A. and Hart, R. D. (1992). "Numerical modelling of discontinua." *Engineering Computations*, 9, 101-132.

Cundall, P. A. and Strack, O. D. L. (1979). "A discrete numerical model for granular assemblies." *Geotechnique*, 29(1), 47-65.

DeMerchant, M. R., Valsangkar, A. J., and Schriver, A. B. (2002). "Plate load tests on geogrid-reinforced expanded shale lightweight aggregate." *Geotextiles and Geomembranes*, 20(3), 173-190.

Douglas, R. A. and Valsangkar, A. J. (1992). "Unpaved geosynthetic-built resource access roads. Stiffness rather than rut depth as the key design criterion." *Geotextiles and Geomembranes*, 11(1), 45-59.

Evans, T. M., Hamed, M., Charles, C., and Akhtar, A. T. (2009). "Grain size distribution effects in 2D discrete numerical experiments." In: M. Iskander, D. F. Laefer, and M. H. Hussein (Eds.) *ASCE Geotechnical Special Publication No. 186, Contemporary Topics in In-Situ Testing, Analysis, and Reliability of Foundations*, Orlando, Florida, 58-65.

Fannin, R. J. and Sigurdsson, O. (1996). "Field observations on stabilization of unpaved roads with geosynthetics." *Journal of Geotechnical Engineering*, 122(7), 544-553.

Farrag, K., Acar, Y. B., and Juran, I. (1993). "Pull-out resistance of geogrid reinforcements." *Geotextiles and Geomembranes*, 12(2), 133-159.

Fuller, W. and Thompson, S. E. (1907). "The laws of proportioning concrete." *Transactions of the American Society of Civil Engineers*, 1053, 67-143.

Gardiner, B. S. and Tordesillas, A. (2005). "Micromechanical constitutive modelling of granular media: Evolution and loss of contact in particle clusters." *Journal of Engineering Mathematics*, 52(1-3), 93-106.

Giroud, J. P., Bonaparte, R., Beech, J. F., and Gross, B. A. (1990). "Design of soil layer-geosynthetic systems overlying voids." *Geotextiles and Geomembranes*, 9(1), 11-50.

Giroud, J. P. and Han, J. (2004). "Design method for geogrid-reinforced unpaved roads. I. Development of design method." *Journal of Geotechnical and Geoenvironmental Engineering*, 130(8), 775-786.

Guerrero, S. L. and Vallejo, L. E. (2005). "Discrete element method evaluation of granular crushing under direct shear test conditions." *Journal of Geotechnical and Geoenvironmental Engineering*, 131(10), 1295-1300.

Haeri, S. M., Noorzad, R., and Oskoorouchi, A. M. (2000). "Effect of geotextile reinforcement on the mechanical behavior of sand." *Geotextiles and Geomembranes*, 18, 385-342.

Hainbuchner, E., Potthoff, S., Koneitzky, H., and Kamp, L. (2003). "Particle based modeling of shear box tests and stability problems for shallow foundations in sand." In Konietzky (Ed.), *Proceedings of the First International PFC Symposium on Numerical Modeling in Micromechanics via Particle Methods*, Gelsenkirchen, Germany, 151-156.

Han, J. and Bhandari, A. (2009). "Evaluation of geogrid-reinforced pile-supported embankments under cyclic loading using discrete element method." In J. Han, G. Zheng, V.R. Schaefer, and M. Huang, *ASCE Geotechnical Special Publication No. 188, Advances in Ground Improvement*, Orlando, Florida, 73-82.

Han, J. and Gabr, M. A. (2002). "Numerical analysis of geosynthetic-reinforced and pile-supported earth platforms over soft soil." *Journal of Geotechnical and Geoenvironmental Engineering*, 128(1), 44-53.

Han, J., Zhang, Y., and Parsons, R. L. (2008a). "Development of a performance-based laboratory test method for evaluating geosynthetic-soil confinement." In: *CD-Rom Publication, the 87th TRB Annual Meeting, January 13 to 17, Washington, DC*, Washington, DC.

Han, J., Yang, X. M., Leshchinsky, D., and Parsons, R. L. (2008b). "Behavior of geocell-reinforced sand under a vertical load." *Journal of Transportation Research Board*, 2045, 95-101.

Hartl, J. and Ooi, J. Y. (2008). "Experiments and simulations of direct shear tests: Porosity, contact friction and bulk friction." *Granular Matter*, 10(4), 263-271.

Hatami, K. and Raymond, G. P. (2006). "Influence of soil strength on optimal embedment depth of geosynthetic reinforcement layer in granular-reinforced foundations." *Transportation Research Record* (1975), 155-162.

Hewlett, W. J. and Randolph, M. F. (1988). "Analysis of piled embankments." *Ground Engineering*, 21(3) 12-18.

Hossain, Z., Indraratna, B., Davre, F., and Thakur, P. K. (2007). "DEM analysis of granular ballast breakage under cyclic loading." *Geomechanics and Geoengineering*, 2(3), 175-181.

Hufenus, R., Rueegger, R., Banjac, R., Mayor, P., Springman, S. M., and Bronnimann, R. (2006). "Full-scale field tests on geosynthetic reinforced unpaved roads on soft subgrade." *Geotextiles and Geomembranes*, 24(1), 21-37.

Indraratna, B. and Salim, W. (2003). "Deformation and degradation mechanics of recycled ballast stabilised with geosynthetics." *Soils and Foundations*, 43(4), 35-46.

Itasca. (2004). *Particle Flow Code in Two Dimensions*, Itasca Consulting Group, Inc., Minnesota.

Jacobson, D. E., Valdes, J. R., and Evans, T. M. (2007). "A numerical view into direct shear specimen size effects." *Geotechnical Testing Journal*, ASTM, 30(6), 1-5.

Jenck, O., Dias, D., and Kastner, R. (2007). "Two-dimensional physical and numerical modeling of a pile-supported earth platform over soft soil." *Journal of Geotechnical and Geoenvironmental Engineering*, 133(3), 295-305.

Jenck, O., Dias, D., and Kastner, R. (2009). "Discrete element modelling of a granular platform supported by piles in soft soil - validation on a small scale model test and comparison to a numerical analysis in a continuum." *Computers and Geotechnics*, 36(6), 917-927.

Jewell, R. A., Milligan, G. W. E., Sarsby, R. W., and Dubois, D. (1984). "Interaction between soil and geogrids." *Polymer Grid Reinforcement*, 18-30.

Kelly, D., Fairfield, C., and Sibbald, A. (1995). "Geosynthetics for the improvement of unpaved roads." *Highways and Transportation*, 42(7-8), 13-15.

Kempfert, H.-G., GÖbel, C., Alexiew, D. and Heitz, C. (2004). "German recommendation for reinforced embankments on pile-similar elements." *EuroGeo3-Third European Geosynthetic Conference, Geotechnical Engineering with Geosynthetics,* 279-284.

Koerner, R. M. (1998). *Designing with Geosynthetics*, 4th Ed., Prentice Hall, Upper Saddle River, N.J.

Konietzky, H., te Kamo, L., Groeger, T., and Jenner, C. (2004). "Use of DEM to model the interlocking effect of geogrids under static and cyclic loading." *Numerical Modeling in Micromechanics via Particle Methods*, Taylor and Francis Group, London, 3-11.

Latha, G. M. and Murthy, V. S. (2007). "Effects of reinforcement form on the behavior of geosynthetic reinforced sand." *Geotextiles and Geomembranes*, 25, 23-32.

Le Hello, B. and Villard, P. (2009). "Embankments reinforced by piles and geosynthetics-numerical and experimental studies dealing with the transfer of load on the soil embankment." *Engineering Geology*, 106(1-2), 78-91.

Lekarp, F., Isacsson, U., and Dawson, A. (2000). "State of the art. I: Resilient response of unbound aggregates." *Journal of Transportation Engineering*, 126(1), 66-75.

Leng, J. and Gabr, M. A. (2006). "Deformation-resistance model for geogrid-reinforced unpaved road." *Transportation Research Record*, 1975, 146-154.

Lim, W. L. and McDowell, G. R. (2005). "Discrete element modelling of railway ballast." *Granular Matter*, 7, 19-29.

Ling, H. I. and Tatsuoka, F. (1992). "Nonlinear analysis of reinforced soil structures by Modified CANDE (M-CANDE)." In: J. T. H. Wu (Ed.), *Geosynthetic-Reinforced Soil Retaining Walls, Proceedings of the International Symposium on Geosynthetic-Reinforced Soil Retaining Walls*, Denver, 279-296.

Ling, H. I. and Tatsuoka, F. (1994). "Performance of anisotropic geosynthetic-reinforced cohesive soil mass." *Journal of Geotechnical Engineering*, 120(7), 1166-1184.

Ling, H. I., Wang, J. P., and Leshchinsky, D. (2008). "Cyclic behaviour of soil-structure interfaces associated with modular-block reinforced soil-retaining walls." *Geosynthetics International*, 15(1), 14-21.

Liu, C.-N., Ho, Y.-H., and Huang, J.-W. (2009). "Large scale direct shear tests of soil/pet-yarn geogrid interfaces." *Geotextiles and Geomembranes*, 27(1), 19-30.

Liu, S. H. (2006). "Simulating a direct shear box test by DEM." *Canadian Geotechnical Journal*, 43, 155-168.

Lobo-Guerrero, S. and Vallejo, L. E. (2006). "Discrete element method analysis of railtrack ballast degradation during cyclic loading." *Granular Matter*, 8(3-4), 195-204.

Lobo-Guerrero, S. and Vallejo, L. E. (2007). "Influence of pile shape and pile interaction on the crushable behavior of granular materials around driven piles: DEM analyses." *Granular Matter*, 9(3-4), 241-250.

Lu, M. and McDowell, G. R. (2007). "The importance of modelling ballast particle shape in the discrete element method." *Granular Matter*, 9(1-2), 69-80.

Mallick, S. B., Zhai, H., Adanur, S., and Elton, D. J. (1996). "Pullout and direct shear testing of geosynthetic reinforcement: State-of-the-art report." *Transportation Research Record*, 1534, 80-90.

Matsuoka, H. and Yamamoto, S. (1994). "Microscopic study on shear mechanism of granular materials by DEM." *Journal of Geotechnical Engineering, JSCE*, 487 (26), 167-175.

McDowell, G. and Stickley, P. (2006). "Performance of geogrid-reinforced ballast." *Ground Engineering*, 39(1), 26-30.

McDowell, G. R., Harireche, O., Konietzky, H., Brown, S. F., and Thom, N. H. (2006). "Discrete element modelling of geogrid-reinforced aggregates." *Geotechnical Engineering*, 159(GEI), 35-48.

McKelvey, J. A., III. (1994). "Anatomy of soil arching." *Geotextiles and Geomembranes*, 13(5), 317-329.

Misra, A. (1991). *Constitutive Relationships for Granular Solids with Particle Slidings and Fabric Changes*, Ph.D. Dissertation, University of Massachusetts Amherst, United States.

Misra, A. and Cheung, J. (1999). "Particle motion and energy distribution in tumbling ball mills." *Powder Technology*, 105(1-3), 222-227.

Misra, A. and Jiang, H. (1997). "Measured kinematic fields in the biaxial shear of granular materials." *Computers and Geotechnics*, 20(3-4), 267-285.

Miura, N., Sakai, A., Taesiri, Y., Yamanouchi, T., and Yasuhara, K. (1990). "Polymer grid reinforced pavement on soft clay grounds." *Geotextiles and Geomembranes*, 9(1), 99-123.

Munjiza, A. (2004). *The Combined Finite-discrete Element Method*, John Wiley & Sons, England.

Nakamura, T., Mitachi, T., and Ikeura, I. (2003). "Estimating method for the in-soil deformation behavior of geogrid based on the results of direct box shear test." *Soils and Foundations*, 43(1), 47-57.

Nogami, T. and Yong, T. Y. (2003). "Load-settlement analysis of geosynthetic-reinforced soil with a simplified model." *Soils and Foundations*, 43(3), 33-42.

O'Sullivan, C., Cui, L., and O'Neill, S. C. (2008). "Discrete element analysis of the response of granular materials during cyclic loading." *Soils and Foundations*, 48(4), 511-530.

Oda, M., Konishi, J., and Nemat-Nasser, S. (1980). "Some experimentally based fundamental results on the mechanical behaviour of granular materials." *Geotechnique*, 30(4), 479-495.

Pena, A. A., Garcia-Rojo, R., and Herrmann, H. J. (2007). "Influence of particle shape on sheared dense granular media." *Granular Matter*, 9(3-4), 279-291.

Perkins, S. W. (1999). *Geosynthetic Reinforcement of Flexible Pavements: Laboratory Based Pavement Test Sections*, Report No. FHWA/MT-99/8106-1. Washington, DC: US Department of Transportation, Federal Highway Administration, 140 pp.

Perkins, S. W. and Cortez, E. R. (2005). "Evaluation of base-reinforced pavements using a heavy vehicle simulator." *Geosynthetics International*, 12(2), 86-98.

Perkins, S. W. and Ismeik, M. (1997). "Synthesis and evaluation of geosynthetic-reinforced base layers in flexible pavements: Part I." *Geosynthetics International*, 4(6), 549-604.

Pokharel, S. K., Han, J., Parsons, R. L., Qian, Y., Leshchinsky, D., and Halahmi, I. (2009). "Experimental study on bearing capacity of geocell-reinforced bases." In: E. Tutumleur and I. L. Al-Qadi (Eds.), *Proceedings of the 8th International Conference on the Bearing Capacity of Roads, Railways, and Airfields*, Champaign, Illinois, 1159-1167.

Potyondy, D. O. and Cundall, P. A. (2004). "A bonded-particle model for rock." *International Journal of Rock Mechanics and Mining Sciences*, 41(8 SPECISS), 1329-1364.

Qian, Y., Han, J., Pokharel, S. K., and Parsons, R. L. (2010). "Experimental study on triaxial geogrid-reinforced bases over weak subgrade under cyclic loading." *ASCE Geotechnical Special Publication No. 199*, 120-128.

Raju, D. M. and Fannin, R. J. (1997). "Monotonic and cyclic pull-out resistance of geogrids." *Geotechnique*, 47(2), 331-337.

Raju, D. M. and Fannin, R. J. (1998). "Load-strain-displacement response of geosynthetics in monotonic and cyclic pullout." *Canadian Geotechnical Journal*, 35(2), 183-193.

Raymond, G. and Ismail, I. (2003). "The effect of geogrid reinforcement on unbound aggregates." *Geotextiles and Geomembranes*, 21(6), 355.

Reid, W. M. and Buchanan, N. W. (1984). "Bridge approach support piling." In proceedings of the conference on *Piling and Ground Treatment*, London, England, 267-274.

Rogbeck, Y., Gustavsson, S., Södergren, I. and Lindquist, D. (1998). "Reinforced piled embankments in Sweden-design aspects." *Proceedings of the Sixth International Conference on Geosynthetics*, 755-762

Rothenburg, L. and Bathurst, R. J. (1989). "Analytical study of induced anisotropy in idealized granular materials." *Geotechnique*, 39(4), 601-614.

Rothenburg, L. and Bathurst, R. J. (1989). "Analytical study of induced anisotropy in idealized granular materials." *Geotechnique*, 39(4), 601-614.

Rothenburg, L. and Bathurst, R. J. (1992). "Micromechanical features of granular assemblies with planar elliptical particles." *Geotechnique*, 42(1), 79-95.

Rothenburg, L. and Bathurst, R. J. (1993). "Influence of particle eccentricity on micromechanical behavior of granular materials." *Mechanics of Materials*, 16(1-2), 141-152.

Saad, B., Mitri, H., and Poorooshasb, H. (2006). "3d fe analysis of flexible pavement with geosynthetic reinforcement." *Journal of Transportation Engineering*, 132(5), 402-415.

Selig, E. T. (1987). "Tensile zone effects on performance of layered systems." *Geotechnique*, 37(3), 247-254.

Selig, E. T. and Roner, C. J. (1987). "Effects of particle characteristics on behavior of granular material." *Transportation Research Record*, 1131, 1-6.

Shahin, H. M., Nakai, T., Hinokio, M., Kurimoto, T., and Sada, T. (2004). "Influence of surface loads and construction sequence on ground response due to tunnelling." *Soils and Foundations*, 44(2), 71-84.

Shahin, H. M., Sung, E., Nakai, T., Hinokio, M., Kikumoto, M., Yamamoto, M., and Tabata, Y. (2006). "2D model tests and numerical simulation in shallow tunneling considering existing building load." In: Z. Hehua, Z. Feng, C. D. Eric, C. Chung-

Tien, and Z. Dongmei (Eds.), *ASCE Geotechnical Special Publication No. 155, Underground Construction and Ground Movement: Part of GeoShanghai 2006,* Shanghai, China, 304-311.

Sibille, L. and Froiio, F. (2007). "A numerical photogrammetry technique for measuring microscale kinematics and fabric in schneebeli materials." *Granular Matter*, 9(3-4), 183-193.

Skermer, N. A. and Hillis, S. F. (1970). "Gradation and shear characteristics of four cohesionless soils." *Canadian Geotechnical Journal*, 7(1), 62-68.

Subaida, E. A., Chandrakaran, S., and Sankar, N. (2008). "Experimental investigations on tensile and pullout behaviour of woven coir geotextiles." *Geotextiles and Geomembranes*, 26(5), 384-392.

Terzaghi, K. (1943). *Theoretical Soil Mechanics*, J. Wiley and Sons, New York.

Thornton, C. and Zhang, L. (2003). "Numerical simulations of the direct shear test." *Chemical Engineering Technology*, 26(2), 153-156.

Tien, H.-J. S. (2001). *The Arching Mechanism on the Micro Level Utilizing Photoelasticity Modeling*, Ph.D. Dissertation, University of Massachusetts Lowell, United States.

Tingle, J. S. and Jersey, S. R. (2005). "Cyclic plate load testing of geosynthetic-reinforced unbound aggregate roads." *Transportation Research Record*, 1936, 60-69.

Uthus, L., Hopkins, M. A., and Horvli, I. (2008). "Discrete element modelling of the resilient behaviour of unbound granular aggregates." *International Journal of Pavement Engineering*, 9(6), 387-395.

Vallejo, L. E., Lobo-Guerrero, S., and Hammer, K. (2006). "Degradation of a granular base under a flexible pavement: DEM simulation." *International Journal of Geomechanics*, 6(6), 435-439.

Van Eekelen, S. J. M., Bezuijen, A., and Oung, O. (2003). "Arching in piled embankments; experiments and design calculations." In Proceedings of the *BGA International Conference on Foundations, Innovations, Observations, Design and Practice,* Dundee, United Kingdom, 885-894.

Villard, P. and Chareyre, B. (2004). "Design methods for geosynthetic anchor trenches on the basis of true scale experiments and discrete element modeling." *Canadian Geotechnical Journal*, 41, 1193-1205.

Villard, P., Chevalier, B., Le Hello, B., and Combe, G. (2009). "Coupling between finite and discrete element methods for the modelling of earth structures reinforced by geosynthetic." *Computers and Geotechnics*, 36(5), 709-717.

Walters, D. L., Allen, T. M., and Bathurst, R. J. (2002). "Conversion of geosynthetic strain to load using reinforcement stiffness." *Geosynthetics International*, 9(5-6), 483-523.

Wang, J., Gutierrez, M. S., and Dove, J. E. (2007). "Numerical studies of shear banding in interface shear tests using a new strain calculation method." *International Journal for Numerical and Analytical Methods in Geomechanics*, 31(12), 1349-1366.

Wang, F., Han, J., Miao, L.C., and Bhandari, A. (2009). "Numerical analysis of geosynthetic-bridged and drilled shaft-supported embankments over large sinkhole." *Geosynthetics International Journal*, 16(6), 408-419.

Webster, S. L. (1992). *Geogrid Reinforced Base Courses for Flexible Pavements for Light Aircraft: Test Section Construction, Behavior under Traffic, Laboratory Tests, and Design Criteria*. U.S. Department of Transportation and Federal Aviation Administration.

Zeghal, M. (2004). "Discrete-element method investigation of the resilient behavior of granular materials." *Journal of Transportation Engineering*, 130(4), 503-509.

Zhang, J., Yasufuku, N., and Ochiai, H. (2008). "A few considerations of pullout test characteristics of geogrid reinforced sand using DEM analysis." *Geosynthetics Engineering Journal*, 22, 103-110.

Zhang, L. and Thornton, C. (2007). "A numerical examination of the direct shear test." *Geotechnique*, 57(4), 343-354.